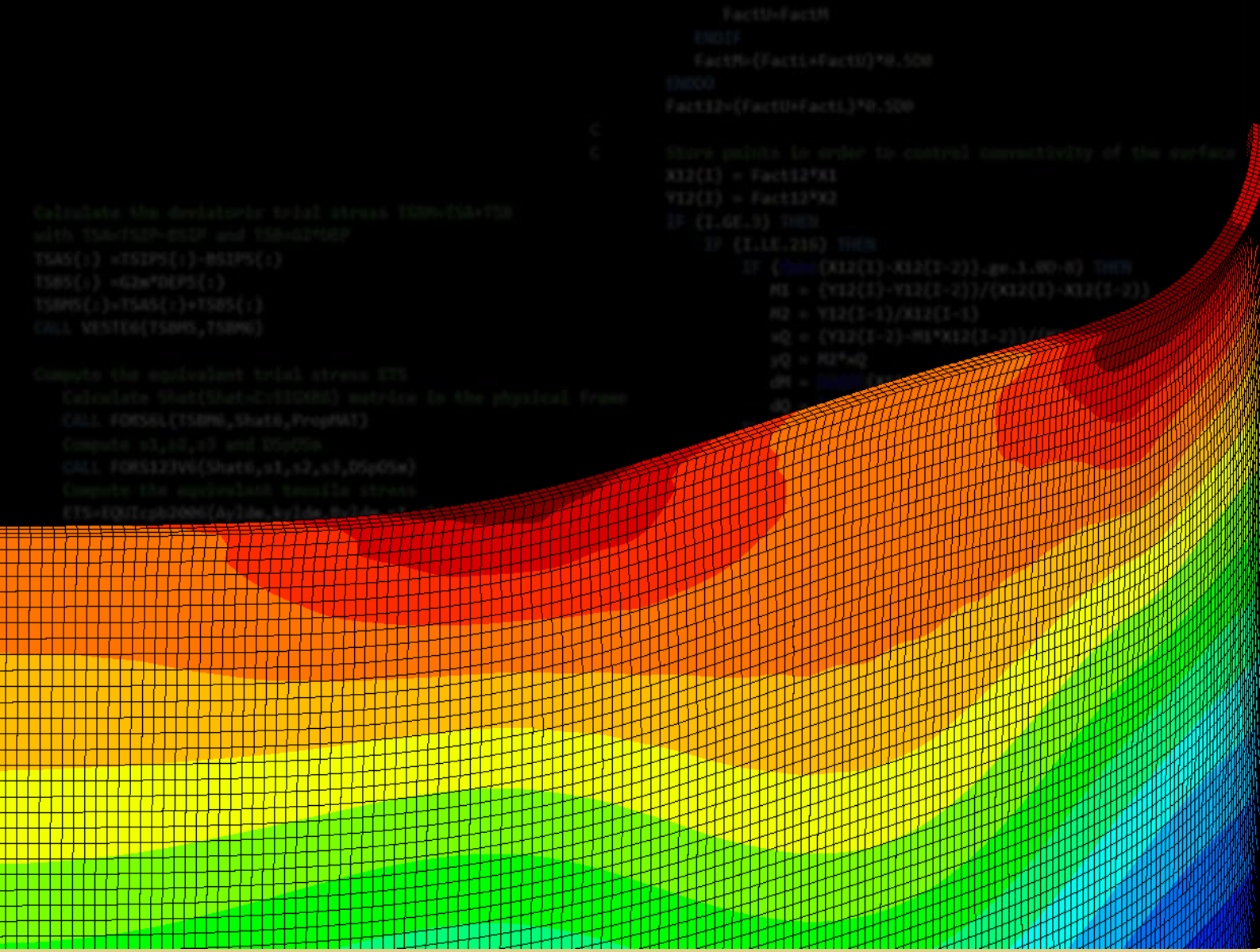

Pedro Daniel Pleno Rascão de Barros

Numerical Simulation of the Deep-Drawing of Cylindrical Cups

Orthotropy and Tension-Compression Asymmetry Modelling

Doctoral Thesis in Mechanical Engineering, branch of Production Technologies, supervised by Professor Marta Cristina Cardoso de Oliveira and Professor António Gil d'Orey de Andrade Campos, submitted to the Department of Mechanical Engineering, Faculty of Sciences and Technology of the University of Coimbra

August 2017

· U C ·

Universidade de Coimbra

Numerical Simulation of the Deep-Drawing of Cylindrical Cups:

Orthotropy and Tension-Compression Asymmetry Modelling

Thesis submitted to the Department of Mechanical Engineering of the University of Coimbra in partial fulfillment to the requirements for the doctoral degree in Mechanical Engineering

Pedro Daniel Pleno Rascão de Barros

Scientific advisers:

Prof. **Marta Cristina Cardoso de Oliveira,** University of Coimbra, Portugal

Prof. **António Gil d'Orey de Andrade Campos,** University of Aveiro, Portugal

Department of Mechanical Engineering

Faculty of Sciences and Technology

University of Coimbra

Coimbra, August 2017

“A lot of people think I'm naturally brilliant, but that's not true.
Nobody thinks that.”

Rob DenBleyker

(Page intentionally left blank)

Acknowledgements

The work presented in this Ph.D. thesis is the genuine result of a combination of hard work, failure, patience, persistence, more failure, despair, sleepless nights, success, a pinch of luck and good guidance. I guess this is just how research work is supposed to be.

First, my sincere gratitude goes to Professor Marta Oliveira. Her guidance and scientific expertise, allied with a true love for science, allowed to always look further and do better in this field – or any other field, for that matter. Also, I always find it strangely inhuman the availability, patience and (general) good mood presented every day.

To Professor António Andrade-Campos, thanks for the support during these years and believing in this work. Thank you for the availability and precious teachings that helped this manuscript to eventually appear.

Special thanks are due to Professor José Luís Alves for the scientific discussions and guidance within the framework of this thesis. His open-mind and fearless way of approaching new subjects in definitively an inspiration.

I am also grateful for the supported given by CEMMPRE – Centro de Engenharia Mecânica, Materiais e Processos (Centre for Mechanical Engineering, Materials and Processes), chaired by Professor Bruno Trindade, for giving me all the necessary resources to develop my research work.

To my colleagues within the office, thank you for the scientific discussions and just general talk and non-sense – it sure helps to know everyone has a certain degree of

insaneness. To my friends outside the research world, thank you for the time well spent and the opportunity to grow up as a person.

Finally, my deepest gratitude and admiration goes to my family and to Vânia. Though not a single sentence was written by them, I assure anyone reading these lines that, well, you wouldn't be reading them if not for their effort. Their support and patience through all these years could make anything possible, and this work is a perfect example of that.

Coimbra, August 2017

This work was sponsored by national funds from the Portuguese Foundation for Science and Technology (FCT) via the projects with reference PTDC/EMS-TEC/0702/2014 (POCI-01-0145-FEDER-016779) and PTDC/EMS-TEC/6400/2014 (POCI-01-0145-FEDER-016876) and by UE/FEDER funds through the program COMPETE 2020 under the project CENTRO-01-0145-FEDER-000014 (MATIS).
This work was also supported by a Ph.D. grant provided by the Portuguese Foundation for Science and Technology (FCT) with reference SFRH/BD/98545/2013. All supports are gratefully acknowledged.

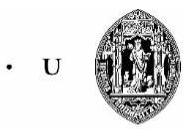

Abstract

Sheet metal forming processes are nowadays widely used in the manufacturing industry of metallic sheets, mainly due to its high production rates and the excellent mechanical properties of the final products. However, the forming process is only considered successful if the final part is free of defects. The development of a process, which may involve multi-stage operations, that ultimately produces parts free of any defects can be a costly and time-consuming task, mainly due to the experimental trial-and-error procedure involved in the determination of both the tools' shape and process conditions. Thus, the finite element method emerges as a way to perform virtual try-outs, predicting stamping defects, mainly those related with geometry and surface problems, while also allowing its integration with optimization tools in order to build more robust forming processes. Still, reliable numerical simulation results are dependent on the ability of the models to accurately describe the material's mechanical behavior since metallic sheets used in sheet metal forming processes typically exhibit orthotropic behavior, due to their crystallographic structure and the rolling process from which they are obtained.

Therefore, the main objective of this work is to analyze the influence of an accurate description of the material's mechanical behavior, as well as the process conditions, in the numerical simulation of sheet metal forming processes, using the in-house finite element code DD3IMP. The description of the material's orthotropic behavior is performed considering phenomenological yield criteria, with particular emphasis given to the highly flexible CB2001 and the CPB06 yield criterion, which allows describing both the in-plane orthotropic behavior as well as the tension-compression asymmetry.

Specific methodologies were developed and implemented in DD3MAT in-house code, for the parameters identification of both CB2001 and CPB06 yield criteria. The validation of the identification procedures developed for the CPB06 yield criterion was

performed using the four-point bending test of beams of zirconium and of a magnesium alloy, known for presenting a strong tension-compression asymmetry.

The deep drawing of cylindrical cups is thoroughly studied, since both the earing profile and the wall thickness are known to be sensitive to both the material's yield stresses and *r*-values in-plane directionalities. In fact, it is shown that the compression yield stresses directionalities play a major role in both the earing and thickness prediction. In this context, the adoption of a flexible yield criterion, such as the CB2001, allows a proper prediction of the earing profile, but the trend for the thickness distribution is not accurate, since it imposes the same tensile and compression yield stresses directionalities. On the other hand, when adopting an associated flow rule, the CPB06 may not be flexible enough to allow the simultaneous description of both the *r*-values and yield stresses directionalities for highly anisotropic materials. Therefore, the CPB06 considering two linear transformations, CPB06ex2, was implemented in DD3IMP and a parameters identification procedure was developed and implemented in DD3MAT. The comparison between the CPB06ex2 and the CB2001 yield criteria demonstrates the interconnection between the process conditions and the yield criteria adopted, particularly the influence that small changes in the stress state have in the directions of the plastic strain rates predicted.

Keywords: Deep-drawing, Numerical simulation, Metal sheets, Constitutive models, Orthotropy, Tension-compression asymmetry.

Resumo

Hoje em dia, os processos de estampagem de chapa são amplamente usados na industria de chapas metálicas, principalmente devido às elevadas taxas de produção e às excelentes propriedades mecânicas dos produtos obtidos. No entanto, o processo de estampagem só é considerado bem sucedido se a peça obtida se encontrar livre de defeitos. O desenvolvimento de um processo, que pode incluir varais etapas, que, em última instância, produza peças livres de qualquer defeito pode ser caro e consumir demasiado tempo, principalmente devido ao método *trial-and-error* envolvido na determinação das formas das ferramentas bem como das condições do processo. Deste modo, o método dos elementos finitos surge de modo a possibilitar *try-outs* virtuais, prevendo defeitos de estampagem principalmente geométricos e de superfície, permitindo ainda a sua integração com ferramentas de otimização de modo a construir processos mais robustos. Porém, resultados fiáveis de simulação numérica dependem da capacidade dos modelos em descrever com precisão o comportamento mecânico dos materiais, visto que as chapas metálicas usadas em processos de estampagem tipicamente exibem comportamento ortotrópico, devido à sua estrutura cristalina e ao processo de laminagem a partir do qual são obtidas.

O objetivo principal deste trabalho consiste em analisar a influência de uma correta descrição do comportamento mecânico do material, bem como das condições de processo, na simulação numéricas de processos de estampagem de chapas metálicas, usando o código de elementos finitos DD3IMP. A descrição o comportamento ortotrópico é feito considerando critérios de plasticidade fenomenológicos, com ênfase no critério CB2001, como elevada flexibilidade, e no critério CPB06 que permite a descrição do comportamento ortotrópico bem como de assimetria tensão-compressão.

Foram desenvolvidas e implementadas metodologias específicas no código DD3MAT para a determinação de parâmetros de anisotropia para os critérios CB2001 e CPB06. A validação do procedimento de identificação para o CPB06 foi efetuada usando o teste de flexão em quatro pontos, usando barras de Zircónio e barras de uma

liga de magnésio, ambos os materiais apresentando uma forte assimetria tensão-compressão.

A estampagem de taças cilíndricas foi estudada, uma vez que tanto os perfis de orelhas bem como a distribuição de espessuras na peça são sensíveis às direccionalidades no plano das tensões de cedência e coeficientes de anisotropia. De facto, é apontado que as tensões de cedência à compressão maioritariamente influenciam as previsões dos perfis de orelhas e espessuras. Neste contexto, a adoção de um critério extremamente flexível, como o CB2001, permite uma boa previsão do perfil de orelhas, mas a tendência prevista para as espessuras não é precisa, visto que impõe as mesmas tensões de cedência para tensão e para compressão. Por outro lado, com a adoção de uma lei de plasticidade associada, o critério CPB06 não é suficientemente flexível para permitir a descrição simultânea das tensões de cedência e coeficientes de anisotropia para materiais com elevada anisotropia. Deste modo, o critério CPB06 considerando duas transformações lineares, CPB06ex2, foi implementado no programa DD3IMP e uma metodologia específicas determinação de parâmetros de anisotropia foi implementada no código DD3MAT. A comparação de resultados entre o CPB06ex2 e o CB2001 demonstra a interdependência entre as condições de processo e o critério de plasticidade adoptado, em particular a influência que pequenas alterações no estado de tensões têm na direcção prevista para o tensor velocidade de deformação plástica.

Palavras-chave: Estampagem, Simulação numérica, Chapas metálicas, Modelos constitutivos, Ortotropia, Assimetria tensão-compressão.

Contents

Acknowledgements ... iii
Abstract ... v
Resumo ... vii
Contents ... ix
List of Figures ... xi
List of Tables ... xv
Acronyms and Nomenclature ... xvii
Acronyms ... xvii
Nomenclature ... xviii
Chapter 1 General Introduction ... 1
1.1. Motivation ... 3
1.1.1. DD3IMP ... 10
1.1.2. DD3MAT ... 11
1.1.3. DD3OSS ... 11
1.1.4. DD3TRIM ... 12
1.1.5. DD3LT ... 12
1.2. Objectives and Achievements ... 12
1.3. Thesis Outline ... 14
Chapter 2 Constitutive Modeling ... 17
2.1. Introduction ... 19
2.2. Hardening Law ... 26
2.2.1. Isotropic Hardening ... 27
2.2.2. Kinematic Hardening ... 29
2.3. Yield Surface ... 31
2.3.1. Isotropic yield criteria ... 32
2.3.1.1. Tresca (1864) ... 32
2.3.1.2. von Mises (1913) ... 33
2.3.1.3. Drucker (1949) ... 34
2.3.1.4. Hershey and Hosford (1972) ... 35
2.3.2. Anisotropic yield criteria ... 36
2.3.2.1. Hill (1948) ... 37
2.3.2.2. Barlat's yield criteria ... 39
2.3.2.3. Karafillis and Boyce (1993) ... 44
2.3.2.4. Drucker + L (2001) ... 45
2.3.2.5. Cazacu & Barlat (2001) ... 47
2.3.2.6. Cazacu yield criteria accounting SD effects ... 49
2.3.2.7. Yoshida (2013) ... 55
2.4. Final Remarks ... 56
Chapter 3 Material Parameters Identification ... 59

3.1. Introduction 61
3.2. Objective function 66
3.3. Optimization algorithms 68
3.4. Experimental Tests 71
3.4.1. Uniaxial Tensile Test 71
3.4.2. Uniaxial Compression Test 74
3.4.3. Disc Compression Test 75
3.4.4. Shear Test 77
3.4.5. Plane Strain Tensile Test 78
3.4.6. Biaxial Tensile Test 79
3.4.7. Hydraulic Bulge Test 81
3.5. Final Remarks 83
Chapter 4 Contributions to the numerical simulation of the drawing of cylindrical cups 85
4.1. DD3IMP, 3D fully implicit finite element solver: implementation of CB2001 yield criterion 87
4.2. Modeling of tension–compression asymmetry and orthotropy on metallic materials: Numerical implementation and validation 121
4.3. Study on the effect of tension-compression asymmetry on the cylindrical cup forming of an AA2090-T3 alloy 139
4.4. Numerical prediction of the earing in the cup drawing of an AA3104 aluminum alloy: process conditions *versus* yield criterion 151
Chapter 5 Conclusions and Perspectives 207
5.1. Conclusions 209
5.2. Recommendations and Perspectives 211
Appendix A Cazacu and Barlat (2001) yield criterion anisotropy parameters identification 213
A.1 Introduction 215
A.2 Yield surface convexity test 215
A.3 General algorithm implemented in DD3MAT 217
Appendix B Other publications resulting from the presented work 221
B.1 Introduction 223
B.2 Journal articles 223
B.3 Conference proceedings 225
Overall list of references 233

List of Figures

Figure 1.1. Metal formed parts and products. (a) Hydroformed bicycle frame tubes, (b) stamped B-pillar, (c) forged spanners and (d) extruded profiles. 3

Figure 1.2. Simplified deep drawing process (Copyright © CustomPartNet). 4

Figure 1.3. Common defects of formed metal parts (adapted from www.me-mechanicalengineering.com). 5

Figure 1.4. Forming simulation results for an engine hood inner, including (a) drawing, (b) trimming and (c-d) springback stages. (Courtesy of Volkswagen Autoeuropa). 8

Figure 2.1. Geometrical representation of a plastic state of stress in the principal stress space. A yield criterion independent of the hydrostatic component of stress is represented by the curve *C* in the π-plane (adapted from Hill, (1950)). 22

Figure 2.2. Schematic representation of the: (a) associated and (b) non-associated flow rules. 26

Figure 2.3. Schematic representation of the plastic behavior of materials in tension-compression on the $\sigma_1 - \sigma_2$ plane and corresponding stress *vs.* plastic strain curves. (a) Isotropic hardening; (b) Kinematic hardening; (c) Mixed isotropic-kinematic hardening (adapted from Prates (2014)). 27

Figure 2.4. Hardening behavior during a tension-compression test, highlighting the stages associated with the Bauschinger effect (adapted from Yoshida and Uemori (2003)). 29

Figure 2.5. Schematic of the yield surface's shape evolution according to the HAH model. 31

Figure 2.6. Tresca and von Mises yield surfaces in the $\sigma_1 - \sigma_2$ plane (left) and π-plane (right). 34

Figure 2.7. Drucker's yield surfaces in the $\sigma_1 - \sigma_2$ plane (left) and π-plane (right) for different values of c 35

Figure 2.8. Hosford's yield surfaces in the $\sigma_1 - \sigma_2$ plane (left) and π-plane (right) for different values of the exponent m 36

Figure 2.9. Normalized anisotropic Hill'48 yield surfaces in the $\sigma_1 - \sigma_2$ plane (left) and π-plane (right) for the AKDQ steel and the AA2090-T3 aluminum alloy. 38

Figure 2.10. Experimental and numerically predicted yield stresses and *r*-values for the (a) AKDQ steel and (b) AA2090-T3 aluminum alloy. 39

Figure 2.11. Schematic representation of the linear transformation of the yield surface of the anisotropic material to the equivalent isotropic one (adapted from Karafillis and Boyce, 1993).....39

Figure 2.12. Normalized anisotropic YLD91 yield surfaces in the $\sigma_1 - \sigma_2$ plane (left) and π-plane (right) for the AKDQ steel and AA2090-T3 aluminum alloy.....41

Figure 2.13. Experimental and YLD91 predicted yield stresses and *r*-values for the (a) AKDQ steel and (b) AA2090-T3 aluminum alloy. 41

Figure 2.14. Normalized anisotropic KB93 yield surfaces in the $\sigma_1 - \sigma_2$ plane (left) and π-plane (right), for the AKDQ steel and AA2090-T3 aluminum alloy.....45

Figure 2.15. Experimental and KB93 predicted yield stresses and *r*-values for the (a) AKDQ steel and (b) AA2090-T3 aluminum alloy. 45

Figure 2.16. Normalized anisotropic Drucker+L yield surfaces in the $\sigma_1 - \sigma_2$ plane (left) and π-plane (right) for the AKDQ steel and AA2090-T3 aluminum alloy. 46

Figure 2.17. Experimental and Drucker+L predicted yield stresses and *r*-values for the (a) AKDQ steel and (b) AA2090-T3 aluminum alloy. 47

Figure 2.18. Normalized anisotropic CB2001 yield surfaces in the $\sigma_1 - \sigma_2$ plane (left) and π-plane (right) for the AKDQ steel and AA2090-T3 aluminum alloy. 49

Figure 2.19. Experimental and CB2001 predicted yield stresses and *r*-values for the (a) AKDQ steel and (b) AA2090-T3 aluminum alloy. 49

Figure 2.20. Normalized isotropic CPB06 yield surfaces in the $\sigma_1 - \sigma_2$ plane (left) and π-plane (right) for different values of k. 51

Figure 2.21. Normalized anisotropic CBP06 yield surfaces in the $\sigma_1 - \sigma_2$ plane (left) and π-plane (right) for the AKDQ steel and AA2090-T3 aluminum alloy.....52

Figure 2.22. Experimental and CPB06 predicted yield stresses and *r*-values for the (a) AKDQ steel and (b) AA2090-T3 aluminum alloy. 53

Figure 2.23. Normalized anisotropic CPB06ex2 yield surfaces in the $\sigma_1 - \sigma_2$ plane (left) and π-plane (right) for the AKDQ steel and AA2090-T3 aluminum alloy. 55

Figure 2.24. Experimental and CPB06ex2 predicted yield stresses and *r*-values for the (a) AKDQ steel and (b) AA2090-T3 aluminum alloy. 55

Figure 3.1. (a) Experimental stress-strain curves obtained from different tests and (b) example of an adjusted hardening law, enabling the description of the experimental results when combined with an appropriate yield criterion. ...61

Figure 3.2. Schematic representation of the type of experimental tests and their correlation with both classical and non-classical inverse identification strategies.....66

Figure 3.3. Common experimental tests used for sheet metal characterization (adapted from Yin et al., 2014).....71

Figure 3.4. (a) Specimen for the tensile test performed for a direction θ in the plane of the metal sheet and corresponding (b) experimental stress-strain curves for three directions and (c) experimental strains for *r*-value calculation. 72

Figure 3.5. Usual uniaxial compression tests considering: (a) a specimen with small length-to-thickness ratio (Tritschler et al., 2014), (b) an anti-buckling device (Kuwabara et al., 2009), (c) pilled specimens (Barlat et al., 1997a) and (d) a single-sided grooved specimen (Zhou et al., 2016). 75

Figure 3.6. Discs' geometry, for increasing values of deformation, obtained from the disc compression test (Barlat et al., 2005). 76

Figure 3.7. Specimens' geometry developed by (a) Miyauchi (1984) (as extracted from Hußnätter and Merklein (2008)) and (b) Genevois (1992) (as extracted from Yoon et al. (2005)). 78

Figure 3.8. Plane strain specimens as developed by (a) Bron and Besson (2004), (b) Wagoner (1981) and (c) Kuwabara (2007). 79

Figure 3.9. (a) Biaxial testing setup (Kuwabara et al., 1998) and (b) cruciform specimen example (Prates, 2014). 80

Figure 3.10. Schematic representation of the hydraulic Bulge test (Koç et al., 2011). 81

Figure A.1. Schematic representation of the convexity test for the v plane: (a) points of the yield surface used for the convexity test defined and (b) geometrical analysis for the convexity test..... 216

(Page intentionally left blank)

List of Tables

Table 2.1. Yield criteria implemented in the DD3IMP in-house code and respective parameters for the general 3D case as well as for thin metallic sheets..... 57

Table 3.1. Yield criteria implemented in the DD3MAT in-house code and respective range for the parameters of the yield criteria. 70

Table A.1. General scheme for the convexity test algorithm.....217

Table A.2. Scheme of the anisotropy parameters identification procedure implemented in DD3MAT, highlighting the integration of the convexity test algorithm. ...219

(Page intentionally left blank)

Acronyms and Nomenclature

Acronyms

AFR	Associated Flow Rule
BCC	Body Centered Cubic
CB2001	Cazacu-Barlat (2001) yield criterion
CB2004	Cazacu-Barlat (2004) yield criterion
CEMMPRE	Centro de Engenharia Mecânica, Materiais e Processos
CPB06	Cazacu, Plunkett and Barlat (2006) yield criterion
CPB06ex2	Cazacu, Plunkett and Barlat (2006) yield criterion considering two linear transformations
DD3IMP	Deep-Drawing 3D IMPlicit code
DD3MAT	Deep-Drawing 3D MATerial code
DD3LT	Deep-Drawing 3D Learning and Teaching
DD3OSS	Deep-Drawing 3D One Step Springback
DD3TRIM	Deep-Drawing 3D TRIMming
DIC	Digital Image Correlation
FCC	Face Centered Cubic
FEA	Finite Element Analysis
FEM	Finite Element Method
FEMU	Finite Element Model Update
HAH	Homogeneous Anisotropic Hardening
HCP	Hexagonal Close Packed
IPE	Isotropic Plastic Equivalent stress state
KB93	Karafillis and Boyce (1993) yield criterion
RD, TD, ND	Rolling, Transverse and Normal Directions of the sheet metal plane (axis of orthotropy in the rolled metal sheet)
SD	Strength Differential effect

SEM	Scanning Electron Microscope
VFM	Virtual Fields Method
YLD91	Barlat et al. (1991) yield criterion

Nomenclature

α	Weighting parameter for the combined isotropic hardening laws: Swift - Voce and Swift - Hockett & Sherby
α_{k_1}	Set of scalar parameters associated with the yield criterion selected
α_{k_2}	Set of scalar parameters associated with the hardening function selected
Δr	Normal anisotropy coefficient
$\boldsymbol{\varepsilon}^{\mathrm{p}}$	Plastic strain tensor
$\bar{\varepsilon}^{\mathrm{p}}$	Equivalent plastic strain
θ	Angle from rolling direction
$\dot{\lambda}$	Plastic multiplier
$\boldsymbol{\Sigma}$	Effective stress tensor
φ	Loading angle on the yield surface
$\boldsymbol{\sigma}$	Cauchy stress tensor
$\boldsymbol{\sigma}'$	Deviatoric Cauchy stress tensor
σ_θ	Yield stress determined from the uniaxial tensile test for an angle θ with the rolling direction
$\bar{\sigma}$	Equivalent stress
$\sigma'_1, \sigma'_2, \sigma'_3$	Deviatoric principal stresses
σ_{b}	Yield stress in biaxial tension
$\sigma^{\mathrm{T}}, \sigma^{\mathrm{C}}$	Yield stress in tension and in compression
τ	Shear stress
$\mathbf{A}$	Vector of anisotropy parameters
$\mathbf{A}^{\mathrm{I}}_{\mathrm{v_{min}}}$	Anisotropy parameters set determined in iteration I of the convexity test algorithm

$a_i \ (i = 1 \text{ to } 6)$,	Parameters of the CB2001 and CB2004 yield criteria
$b_i \ (i = 1 \text{ to } 11)$	
$\mathbf{C}$	Linear transformation anisotropy tensor for the CPB06 yield criterion
c	Parameter of the KB93, Drucker+L, CB2001 and CB2004 yield criteria
$c_i \ (i = 1, \ldots, 6)$	Parameters of the YLD91, KB93 and Drucker +L yield criteria
C_{12}, C_{13}, C_{22}, C_{23}, C_{33}, C_{44}, C_{55}, C_{66}	Parameters of the CPB06 and the CPB06ex2 and yield criterion
C'_{12}, C'_{13}, C'_{22}, C'_{23}, C'_{33}, C'_{44}, C'_{55}, C'_{66}	Parameters of the CPB06ex2 yield criterion
C_x	Parameter of the Armstrong and Frederick kinematic hardening law: Saturation rate
C_Y, H, Y_S, Y_{sat}	Parameters of isotropic hardening laws
$\mathbf{D}^{\text{p}}$	Plastic strain rate tensor
e	Thickness of the shear specimen gauge area
$\mathcal{F}$	Function defining the yield condition
$F(\mathbf{A})$	Objective function
F, G, H, L, M and N	Parameters of the Hill'48 yield criterion
$\mathcal{G}$	Function defining the plastic potential
$\mathbf{H}$	Hessian matrix
I_1, I_2, I_3	First, second and third invariants of the Cauchy stress tensor $\boldsymbol{\sigma}$
ItnMAX	Maximum number of iterations for DD3MAT code
J'_1, J'_2, J'_3	First, second and third invariants of the deviatoric stress tensor $\boldsymbol{\sigma}'$
K	Parameter of the isotropic hardening law: hardening modulus

k	Parameter of the KB93, CPB06 and CPB06ex2 yield criteria
k'	Parameter of the CPB06ex2 yield criterion
$\mathbf{L}$	Linear transformation, anisotropy tensor
m	Parameter of the YLD91 yield criterion
n	Parameter of the isotropic hardening law: hardening coefficient
P_{φ}	Points used for the CB2001 yield surface convexity test algorithm
r	Anisotropy coefficient or *r*-value
$\overline{r}$	Normal anisotropy coefficient
r_{b}	Anisotropy coefficient in biaxial tension
r_{θ}	Anisotropy coefficient determined from uniaxial tensile test for an angle θ with the rolling direction
$\mathbf{s}$	Stress tensor obtained from the linear transformation $\mathbf{s} = \mathbf{L}\boldsymbol{\sigma}'$
$w_{\sigma_{\theta}^{\mathrm{T}}}$, $w_{\sigma_{\theta}^{\mathrm{C}}}$, $w_{r_{\theta}^{\mathrm{T}}}$, $w_{r_{\theta}^{\mathrm{T}}}$, $w_{\tau_{\theta}}$, $w_{\sigma_{\mathrm{b}}}$ $w_{r_{\mathrm{b}}}$	Weighting coefficients used in the objective function
$\mathbf{X}$	Backstress tensor
X_{sat}	Parameter of the Armstrong and Frederick kinematic hardening law: saturation value
Y	Flow stress

Chapter 1

General Introduction

The following chapter presents the framework for the topics covered in this thesis. An overview of sheet metal forming processes is presented followed by the importance of finite element analysis and numerical tools for its development. In this context, the need for accurate modeling of both material mechanical behavior and process conditions is highlighted. Further, the objectives of the work and the main achievements are highlighted, followed by a brief outline of the manuscript.

(Page intentionally left blank)

1.1. Motivation

Metal forming processes are nowadays widely used in the manufacturing industry. These technological processes consist in modifying the original geometry of the material by applying external forces, under a combination of tensile and compressive conditions, which induce plastic deformation of the material. Depending on the specifications of the final component, the selected forming process should provide a product with the proper function and properties at the lowest cost (DIN 8582). In addition, metal forming processes allow producing parts with superior mechanical properties. Figure 1.1 presents some examples of metal formed parts and products obtained by different forming processes.

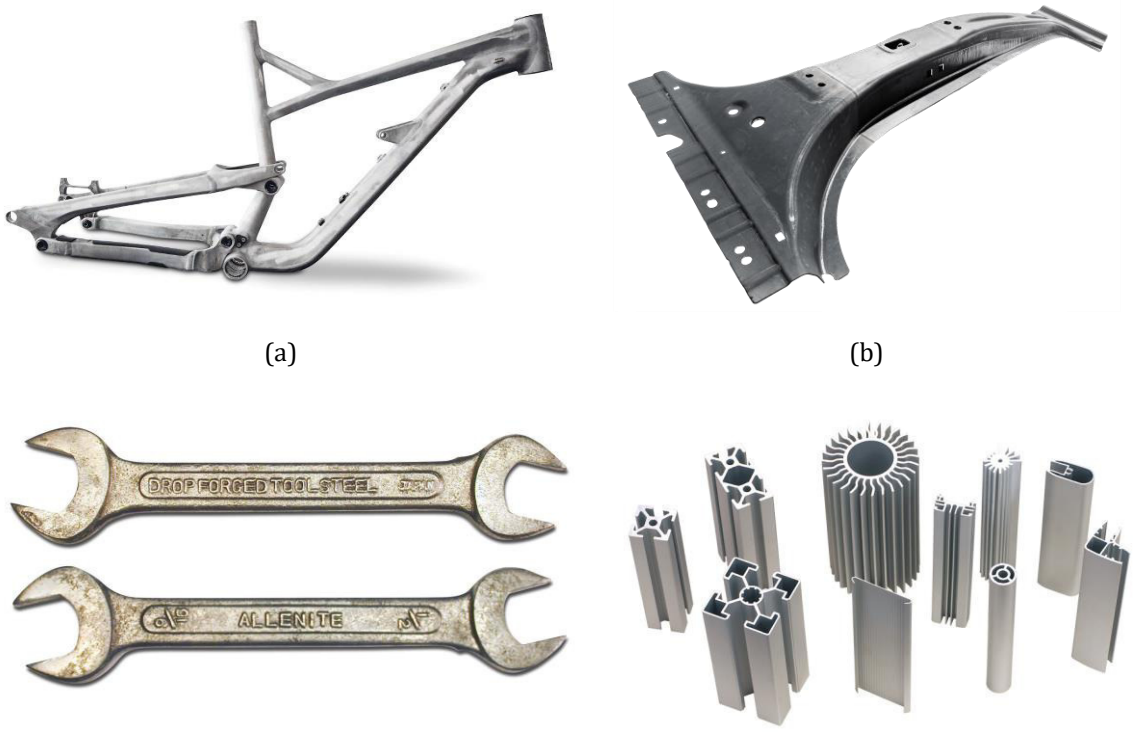

(a) (b)

(c) (d)

Figure 1.1. Metal formed parts and products. (a) Hydroformed bicycle frame tubes, (b) stamped B-pillar, (c) forged spanners and (d) extruded profiles.

In general, metal forming processes are divided into two main categories, according to the ratio between the in-plane dimensions and the thickness of the initial

shape. Small ratios lead to mass deformation while large ratios are categorized as sheet deformation, for which plane stress conditions can be assumed. Sheet metal forming processes consist in giving to a thin metallic sheet, initially flat, a desired shape. Generally, the process is considered a deep drawing when the depth of the drawn part exceeds its diameter, while in the other cases it is commonly referred only as drawing or stamping (DIN 8582). This process allows high rate production of sheet metal parts of different complexities. Thus, sheet metal forming processes are used in a wide range of production areas such as household appliances, domestic and decorative elements, electrical and electronics, aerospace, naval, and, one of the most important due to its large production volumes and large variety of components, the automotive industry.

The sheet metal forming process usually makes use of three distinct tools: (i) a punch, (ii) a die and (iii) a blank-holder, as schematically shown in Figure 1.2. In the first phase, the flat sheet metal, called blank, is clamped between the die and the blank-holder, which is usually controlled considering a pre-determined force in order to control the material flow. After this phase, the punch displacement forces the blank into the die cavity, giving the sheet its final shape. The last phase consists in removing all the forming tools.

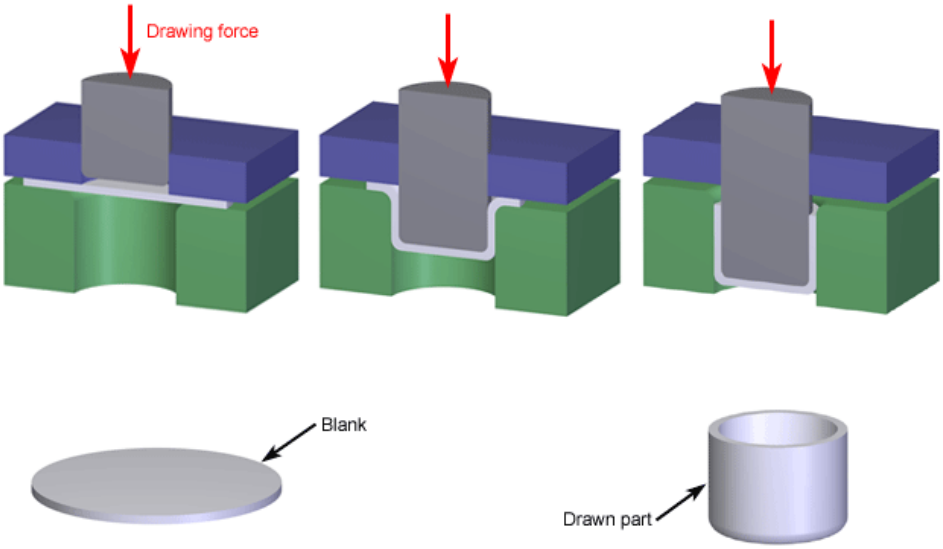

Figure 1.2. Simplified deep drawing process (Copyright © CustomPartNet).

The large amount of elastic energy stored in the material is released in this last phase, which is the main reason behind the springback phenomenon (Narasimhan and Lovell, 1999; Wagoner and Li, 2007). This phenomenon is defined as the dimensional

difference between the final stamped part and the geometry achieved before the tools' removal. In addition, the final shape of the formed component depends on the forming tools geometry, process parameters, and material behavior, which dictate the internal stresses in the component after the forming.

The success of any sheet metal forming process is, among other relevant specifications, strongly dependent on the final components shape. The main defects that occur are usually related to fracture, excessive thinning, wrinkling, buckling, springback and other surface defects, as illustrated in Figure 1.3.

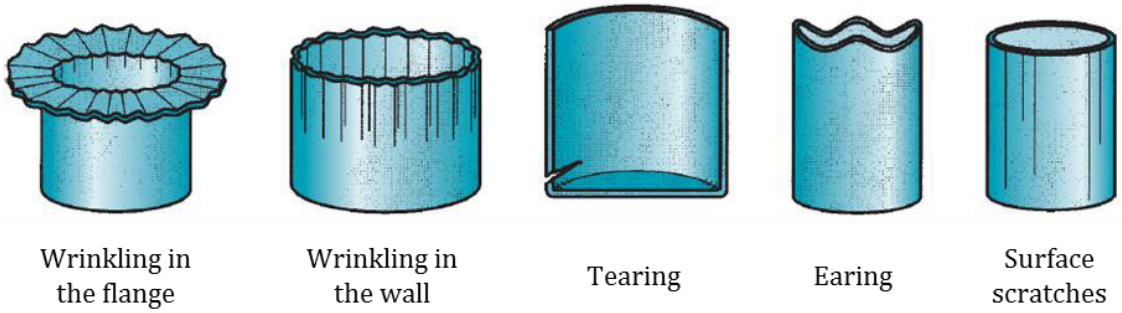

Figure 1.3. Common defects of formed metal parts (adapted from www.me-mechanicalengineering.com).

To avoid defects on the final component, the shape of the blank, the tools' geometry and the contact conditions, mainly related to lubrication and holding force, may be tweaked. In order to improve the control of the material flow, drawbeads[1] can be built-in in the stamping tool. The placement and geometry of the drawbeads allows the control of the material flow, being used to tune the success of the stamping process by balancing the amount of expansion in the central part of the blank, submitted to the action of the punch, and the amount of drawing in the external part (Alves et al., 2005). The contact conditions also have a strong impact on the success of the forming process, since the sheet's flow is restrained by the friction conditions with the tools. However, there is a strong interaction between tribological and mechanical properties of the contacting bodies, which renders increasing difficulties in the development of analytical expressions to support the design of the sheet metal forming process.

In brief, when developing a successful sheet metal forming process there are many material, geometrical and process parameters that need to be defined, in order to attain

[1] Small semi-cylindrical protrusions appearing on the die surface, with a negative cavity on the opposite tool (blank-holder or binder).

the success of the forming operation. Moreover, depending on the complexity of the final component, it may be necessary for multiple stamping steps to obtain the desired shape without defects. For a multi-step process, several tool sets need to be defined, one for each step, as well as the process parameters. In fact, the number of necessary steps is one of the most important and difficult design variables to be determined for sheet metal formed parts, since the only restriction is the desired final shape.

In the former days, the design of a formed component was performed using a trial-and-error experimental approach. In fact, after defining the final component's shape, the project was based on a series of analytical and/or empirical rules resulting from accumulated experience (Rocha and Duarte, 1993). Then, a series of prototype tools were made and iteratively modified until the result was considered satisfactory. The final tools were then built and the final try-out tests were performed. Any changes made in this try-out stage are always extremely costly and time-consuming.

With the development of computational tools, the numerical simulation of technological processes arises. The first works considering the numerical simulation of sheet metal forming processes appear in the 60's with Woo (1968), with a numerical solution using the finite differences method, limited to 2D cases. The numerical simulation of sheet metal forming processes truly emerged due to the development of the finite element method, with pioneering studies by Wifi (1976), Gotoh and Ishisé (1978) and Wang and Budiansky (1978) considering static formulations. 3D formulations were introduced by Tang et al. (1982) and Toh and Kobayashi (1983) with dynamic formulations emerging with the work from Belytschko (1977). From this time forward, in the second half of the 90's, enormous investments have been made in this area, with a massive adoption of computer programs for the numerical simulation of forming processes by the industry. The numerical simulation allows performing the virtual try-outs, thus decreasing the number of expensive experimental testing necessary to fine-tune the process. In this context, the numerical simulation should predict forming defects, mainly those related to geometry and surface quality. Thus, numerical simulation tools have been constantly evolving in order to give faster and more accurate results, while also allowing its integration with optimization tools in order to build more robust forming processes (see, *e.g.* Bonte, (2007)).

Sheet metal forming processes are nowadays designed and optimized virtually using finite element analysis (FEA). Such virtual try-out approach is consensually accepted as the main reason for the huge decrease in the time-to-market life cycle and for the notable savings in terms of money, time and effort in the design, production and process set-up of new formed parts.

The robustness of finite elements solvers in the design and optimization of sheet metal formed parts is, however, strongly dependent on the ability to accurately describe the material's mechanical behavior, as well as the global process conditions. The development of FEA involves several scientific fields from continuum mechanics to numerical analysis, which contribute to obtain accurate results. Several models, more or less complex, are used in order to predict the contact with friction between the tools and the blank, and the elastoplastic response of metal sheets. Nowadays, several commercial finite element solvers are available to simulate sheet metal forming processes. The AutoForm™ is the most commonly used in the automotive industry adopting a static-implicit approach. LS-DYNA™ adopts a dynamic-explicit approach and it is a general-purpose finite element program, originally developed to perform crash simulations. PAM-STAMP™ is another commonly used solver with the same characteristics of LS-DYNA™. Typically, these solvers allow, among others features, material cost estimation, springback prediction and tools compensation, surface defects prediction and virtual prototyping of the full forming process chain. Figure 1.4 presents an example of forming simulation results for a car engine hood inner, including drawing, trimming and springback stages, using the AutoForm™ finite element code.

The automotive industry is the most important driving force to the development of numerical simulation tools for sheet metal forming processes. This industry faces challenges dictated by consumers that desire lighter vehicles, with a more appealing design, usually meaning geometries that are more complex and more often, *i.e.* with a decreased life cycle. Safer and more efficient vehicles are also demanded, which also brings new challenges to the design process. This fact is also aggravated by the introduction of new materials (lightweight materials for fuel savings), for which the design process is more demanding since there is no empirical knowledge to support the success of the forming process. The can industry is another one that benefits from

numerical simulation tools. In fact, 1 billion cans are produced worldwide on a daily basis, with various shapes and sizes. In this context, a minimal improvement in material usage has a massive ecological and monetary impact. Even though a can may seem a simple component, the process conditions and slight material behavior variability can compromise the forming process.

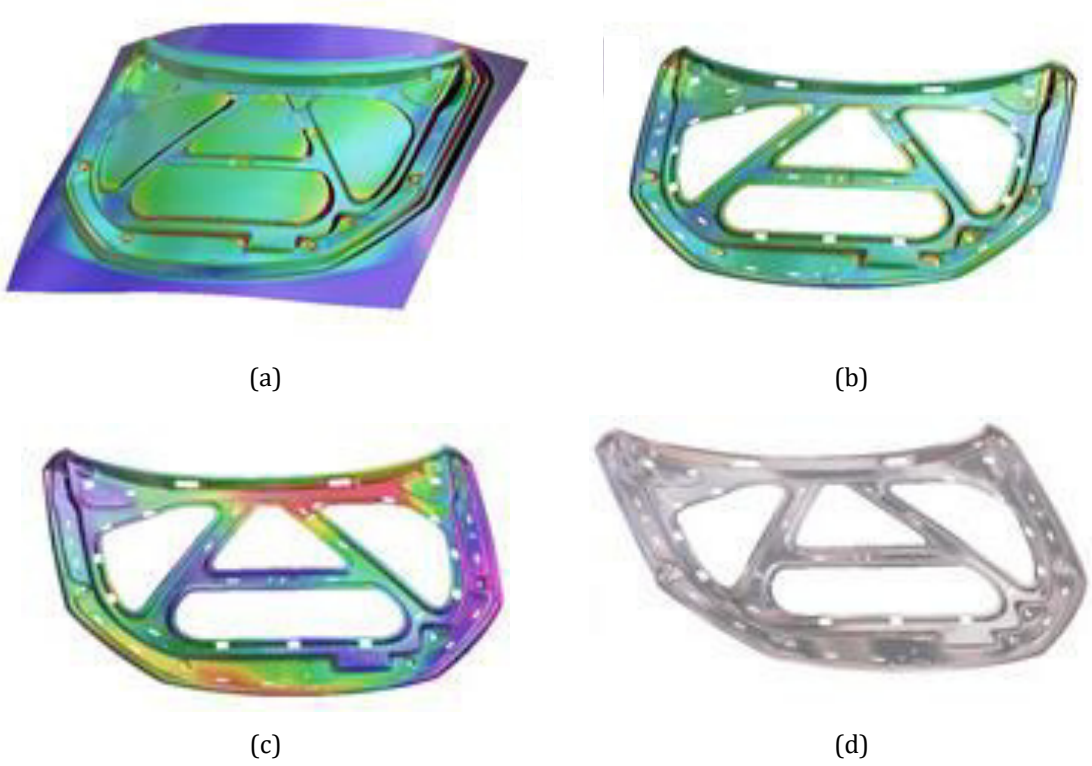

(a) (b)

(c) (d)

Figure 1.4. Forming simulation results for an engine hood inner, including (a) drawing, (b) trimming and (c-d) springback stages. (Courtesy of Volkswagen Autoeuropa).

Metal sheets, due to their crystallographic structure and the way they are obtained, generally exhibit anisotropic behavior. In fact, the rolling process induces a particular anisotropy characterized by the symmetry of the mechanical properties with respect to the three orthogonal planes, *i.e.* orthotropy (Banabic, 2010). As this process makes the metal sheets orthotropic, different mechanical behaviors are expected for different loading directions. Moreover, sheet metal forming processes are carried out with inhomogeneous deformation and under multiaxial strain paths, which influence the hardening behavior.

Phenomenological models are the most widely used to describe the elastoplastic response of metallic sheets, since these are computationally more inexpensive when

compared to micromechanical models, *i.e.* based on crystal plasticity and texture description. Furthermore, it is common to adopt an associated flow rule, meaning that the material's orthotropic behavior is modeled by a yield surface, which describes both the yielding and the plastic flow of the material. This dual role of the yield surface requires particular care and accuracy in its modeling and numerical implementation. In addition, the evolution of the yield criterion with plastic deformation is described by the hardening law. In fact, phenomenological models consist of empirical mathematical functions used to describe the macroscopic materials' mechanical behavior, which rely on adjustable material parameters to capture it.

A recent trend is the use of lightweight materials that, besides orthotropy, may also present significant tension-compression asymmetry, *i.e.* different yielding for tension and compression (also referred to as strength differential (SD) effect). Materials presenting hexagonal closed packed (HCP) crystal structure are known for presenting this effect, like magnesium and titanium alloys. However, materials with cubic structure may also present a small asymmetry (Barlat et al., 1991b). For these materials, a yield criterion capable of describing this asymmetry is required as, for example, the one proposed by Cazacu et al. (2006). In fact, the constant development and use of new materials particularly pushes the complexity of the mathematical formulations. This also requires more experimental data since models that are more complex involve a higher number of material parameters to fit. Therefore, the experimental characterization of the material is more challenging and needs a significant number of experimental tests.

The identification of the materials' parameters is generally formulated as an optimization problem, in which the goal is the minimization of an objective function that evaluates the difference between the values estimated by the selected model and the experimental ones. The most usual experimental tests consider monotonous strain paths (namely tensile, bulge and shear tests), with homogeneous deformation in the measurement region. However, due to several experimental limitations, a fundamental problem is that most of the stress space is left unexplored when fitting the parameters of the selected model (Zhang et al., 2015). Regardless of the complexity of the mathematical formulation selected, both the experimental data available and the parameters identification strategies influence largely the description of the mechanical

behavior of sheet metals. The material parameters identification is indeed a challenge, much due to its dependence on the experimental data available and the users' input and expertise.

In the early 90s, an in-house fully implicit finite element code was developed to simulate sheet metal forming processes, using a quasi-static implicit formulation (Menezes and Teodosiu, 2000). Since then, this code, named DD3IMP (Deep Drawing 3D IMPlicit), has been continuously developed, as well as a set of additional tools, which constitute the so-called DD3 family of codes. The DD3IMP code has been internationally recognized for the accuracy of its predictions (see *e.g.* Yoon et al. (2013)). The work presented here contributes to the continuous development of this family of codes, particularly for the DD3IMP and DD3MAT.

1.1.1. DD3IMP

The DD3IMP in-house code (Menezes and Teodosiu, 2000; Neto et al., 2015; Oliveira et al., 2008), which is implemented in Fortran 90/95, uses a mechanical model that takes into account the large elastoplastic deformations and rotations of the deformable body. The plastic behavior of the material is described by a yield criterion, a work hardening law, and an associated flow rule. This code uses a quasi-static formulation so that inertia effects are not taken into account in the equilibrium equations. Several work hardening laws and yield criteria have been implemented, allowing a better description of the different material mechanical behavior. The forming tools can be assumed as rigid or deformable bodies (Neto, 2014) while the frictional contact between the sheet and the tools is described by the Coulomb's classical law. The contact with friction problem is treated with an augmented Lagrangian approach (Alart and Curnier, 1991). A fully implicit algorithm of Newton-Raphson type is used to solve the nonlinearities related to the frictional contact problem and the elastoplastic behavior of the deformable body(ies). The forming tools can be modeled with Bézier or Nagata patches (Neto et al., 2014). The later guarantees that a surface smoothing procedure is applied to the faceted mesh description (Neto et al., 2013). This code uses 3D solid finite elements allowing an accurate estimate of the through thickness stress gradients, as well as the thickness evolution and contact forces.

1.1.2. DD3MAT

The DD3MAT in-house code, also developed and implemented in Fortran 90/95, is used for determining yield criterion parameters that adjust a given material experimental behavior (Barros et al., 2016). This is relevant since there are several yield criteria implemented in the DD3IMP in-house. In this context, it allows a direct comparison between the different yield criteria, contributing to the selection of the one that gives the best compromise between the model's accuracy and the computational effort. The procedure adopted is based on the minimization of an objective function, which evaluates the difference between the estimated values and the experimental ones, using a downhill simplex method. User-defined weighting factors can be used to balance the influence of the experimental data. As inputs, the user can provide the *r*-values and the yield stresses obtained from various experimental tests, such as the uniaxial tensile test, shear test (both can be obtained for a specific orientation with respect to the rolling direction), equibiaxial test and disc compression test. The flow stresses can be defined for a predetermined plastic work, assuming a previously adjusted hardening law.

1.1.3. DD3OSS

The main goal of the DD3OSS code is to predict the part's geometry after the removal of the forming tools and predict the springback effect. This code is based on the instantaneous removal of all forming tools, contrasting with the strategy that inverts the tools' displacement based on the reproduction of the real process. This corresponds to assuming that all constraints imposed by the tools at the end of the forming phase disappear at the beginning of the unloading phase meaning that all patches that define the tools as candidates to contact with the blank sheet are eliminated and, consequently, all contact forces are set to zero. This algorithm is commonly designated by "one step springback", and allows simulating springback in just one increment. Due to its enormous advantages in computational time, this code is now fully integrated in DD3IMP (Alves, 2003).

1.1.4. DD3TRIM

This code allows the trimming of 3D solid finite element meshes and the remapping of the state variables. These are fundamental operations to accurately simulate multistep processes. The global DD3TRIM algorithm allows finite element removal, remeshing and state variables remapping in the areas affected by the trimming operations. It also allows the part reposition for subsequent multistep operations (Baptista, 2006; Neto et al., 2016). The equilibrium of the formed part after the trimming operation is then performed into DD3IMP.

1.1.5. DD3LT

The DD3LT platform was developed to support the learning and teaching of virtual try-out of sheet metal forming processes, based on the awareness of problems associated with the careless use of finite element analysis codes (Heleno, 2012). It integrates an interactive application, in order to help the model's pre and post-processing, as well as an extensive database of sheet metal forming benchmark problems. Thus, the DD3LT platform enables the modification of the selected model through a friendly user interface. After selecting a problem, several options are displayed including the selection of the finite element mesh, the constitutive model of the material of the deformable body, the process parameters, the contact conditions and the numerical parameters. The DD3LT platform launches the DD3IMP code, providing the process variables (*e.g.* forces exerted by tools at each increment) and enabling the analysis of the simulated problem.

1.2. Objectives and Achievements

The focus of this work is to analyze the influence of the description of the material's mechanical behavior, as well as the process conditions, in the numerical simulation of sheet metal forming processes. Since the main focus is on the description of the orthotropic behavior, including or not tension-compression asymmetry, the cylindrical cup is used as a benchmark. A classical procedure is adopted for the identification of

the anisotropy parameters, in order to explore a similar stress space, whatever the yield criteria adopted.

The orthotropic behavior of the materials is described using a yield criterion known for its flexibility - the CB2001. The results show that the accuracy of the earing profile prediction is strongly influenced by the description of both the *r*-values and yield stresses in-plane directionalities. Additionally, for materials with a strong anisotropic behavior of the *r*-values, the earing profile is influenced by the global process modeling, particularly the contact conditions in the flange area. This is related with the uneven thickness strain distribution in the sheet's plane, leading to a non-uniform contact force distribution. However, the convexity conditions for this yield criterion are not established, which required the implementation of a specific methodology for its material parameters identification.

As previously mentioned, the analysis of the numerical results obtained with the CB2001 yield criterion highlights the impact of both the *r*-values and yield stresses, which for the cylindrical cup are mainly the ones related with the compression stress state (Yoon et al., 2011). This leads to the implementation in DD3MAT of a specific methodology for the parameters identification of the CPB06 yield criterion, which allows describing both tension–compression asymmetry and orthotropy of the plastic flow. The developed procedure was validated with the four-point bending test, considering different orientations of the beam, *i.e.* of the hard/soft to deform direction relatively to the loading direction. Two materials were tested: zirconium and a magnesium alloy. The results show the ability of the CPB06 to describe the strain fields, including the shift of the neutral layer, which is a consequence of the SD effect that the CB2001 yield criterion is unable to capture.

The developed procedure for the identification of the CPB06 anisotropy parameters was also used to describe the mechanical behavior of an AA2090-T3 alloy, since the experimental data available includes both tension and compression yield stress in-plane distributions (Barlat et al., 1991a). Different sets of parameters were identified for the CPB06, taking or not into account the strength differential (SD) effect, highlighting that the compression yield stresses directionalities play a major role in both the earing and thickness predictions. The adoption of a flexible yield criterion, such as the CB2001, allows a proper prediction of the earing profile, but fails to capture

the trend for the thickness distribution since it imposes the same trend for the tensile and compression yield stresses directionalities. Nevertheless, the CPB06 may not be flexible enough to allow the simultaneous description of both the *r*-values and yield stresses directionalities.

Following these conclusions, the CPB06 considering two linear transformations, CPB06ex2, was implemented in DD3IMP and a parameters identification procedure was developed and implemented in DD3MAT. The procedure developed was used to describe the mechanical behavior of an Alcoa AA3104 commercial bodystock alloy sheet, using tensile, bulge and disk compression experimental tests. The mechanical behavior was also modeled with the CB2001. The numerical simulation of the deep drawing of a circular cup was performed, considering also different values of the friction coefficient. The results confirm that the trend of the earing profile is mainly dictated by the in-plane yield stress and *r*-values directionalities. However, the prediction of the cup height requires an accurate description of the directions of the plastic strain rate, in function of the loading direction, for the tension-compression stress state.

All the results previously mentioned are compiled in the manuscripts which constitute Chapter 4: Contributions to the numerical simulation of the drawing of cylindrical cups. Since most of the works cited in the manuscripts are also mentioned in the literature review, an overall list of references is presented at the end of this document.

1.3. Thesis Outline

This thesis is organized into five main chapters and two appendices. In order to facilitate the reading, the current section presents a brief description of the topics considered in each chapter and appendix.

Chapter 2: The main fundamentals for the constitutive modeling of the plastic behavior of thin metallic sheets are introduced. Concepts like flow rule, hardening law and yield surface are presented as well as different models for describing the material's mechanical behavior.

Chapter 3: Some details regarding the procedures commonly adopted for the identification of the anisotropy parameters of yield criteria are discussed, including some remarks about the experimental tests and extracted data commonly used to characterize the materials' mechanical behavior.

Chapter 4: The papers that present the innovative research conducted within the framework of this thesis are presented.

Chapter 5: A summary of the main conclusions of the present work are highlighted, with emphasis on its contributions. Suggestions and recommendations for future works in this field are also presented and briefly discussed.

Appendix A: The strategies developed for the CB2001 yield criterion anisotropy parameters identification are presented, including the test used to check the convexity of the surface defined by a determined set of anisotropy parameters.

Appendix B: Other publications resulting from the conducted research are presented, featured in international journals, proceedings of international conferences and invitations for special issues.

(Page intentionally left blank)

Chapter 2

Constitutive Modeling

This chapter focuses on the fundamentals of the constitutive modeling of the plastic behavior of metallic sheets. First, a general introduction is presented regarding the theory of plasticity and its application to metallic sheets. Afterwards, an overview of some hardening laws and yield criteria is presented, emphasizing the ones implemented in the DD3IMP in-house code. Finally, some remarks and considerations are presented regarding the use of constitutive models in the numerical simulation of forming processes.

(Page intentionally left blank)

2.1. Introduction

One of the most important aspects in the numerical simulation of sheet metal forming processes is the constitutive modeling of the materials' plastic behavior. This is commonly performed considering the theory of plasticity, which corresponds to the mathematical study of stress and strains in plastically deformed solids, especially metals. This follows the well-established precedent set by the theory of elasticity, which deals with the study of stress and strains in elastically deformed solids (Hill, 1950). In fact, when considering metallic sheets, both theories are used in order to describe the material elastoplastic behavior.

The starting point for the theory of plasticity is the experimental observations of the macroscopic behavior of a plastic solid in uniform states of combined stresses. According to Hill (1950), the tasks of the theory are: first, to construct explicit relations between stress and strain agreeing with the observations as closely and as universally as needed; and second, to develop mathematical techniques for calculating non-uniform distributions of stress and strain in bodies permanently distorted in any way. The introduction of the finite element method strongly contributed to the development of the second task, grounded on the foundations of the continuum mechanics and the theory of plasticity for metals.

The most interesting attribute of metals, when compared with other plastic solids, is their capacity for cold-working. This means that, at ordinary temperatures, a dimensional change can be easily obtained with a ductile metal. Thus, the theory of plasticity is especially concerned with the technological forming processes mentioned in Chapter 1, with the purpose of determining the external loads and the non-uniform strain and hardening due to the cold-working.

As previously stated, the theory of plasticity for metals is based on experimental observations of their plastic properties. This analysis can be performed considering single crystals or polycrystalline aggregates, in order to improve knowledge concerning the physical aspects of plastic deformation. The knowledge of these aspects

enables establishing the relation between stress and strain in the microscopic domain and extend it to the macroscopic one. Although this approach, based on crystal plasticity models (see, *e.g.* Raabe et al., 2005; Zhao et al., 2004), has become more competitive, it is still computationally less efficient than the one based on phenomenological models. The later resort to mathematic laws to describe the phenomena observed in the macroscopic plastic behavior of metals, being also easier to understand from the point of view of classical mechanics. Phenomenological models are, in fact, the most widely used to describe the elastoplastic response of metallic sheets and, consequently, they are the focus of this chapter.

The models adopted in this work do not consider the influence of time and, consequently, are valid only at temperatures for which recovery, creep and thermal phenomena can be neglected. Size effects, related to grain size or inclusions, for example, are also neglected. It is considered that, if an element of the ideal solid is plastically deformed and then unloaded, it will recover elastically. The simpler approach assumes that the change of strain, upon unloading, depends linearly on the change of stress, according to the elastic modulus, which is assumed to remain invariant. However, other models have been implemented to take into account the influence of the previous plastic work in the "apparent modulus", some of which describing the hysteresis loop that can be observed during unloading and reloading (Eggertsen et al., 2011). In any case, it is supposed that upon reloading along the same path to the original stress state, the element recovers its original shape. The reloading may also be carried out with a different combination of stresses, each of which will eventually produce further plastic strain if the stress components are increased monotonically. The law defining the limit of elasticity under any possible combination of stresses is known as a yield criterion (Hill, 1950).

The plastic yielding can depend only on the magnitude of the three principal stress components and not on their directions. Therefore, any yield criterion can be assumed as a function of the three invariants (J_1, J_2 and J_3) of the Cauchy stress tensor $\boldsymbol{\sigma}$. Experimental observations have shown that the yielding of metals is, in a first approximation, unaffected by moderate hydrostatic stress, either applied alone or superposed on some state of combined stresses. Thus, it can be assumed that yielding

depends only on the principal components of the deviatoric Cauchy stress tensor $\boldsymbol{\sigma}'$, *i.e.* on its two invariants (J_2' and J_3'). A further restriction is commonly adopted, corresponding to the assumption that the magnitude of the yield stress is the same in tension and in compression. Since J_3' changes sign when the stresses are reversed, it follows that, in that case, the yield criterion must be an even function of J_3' (Hill, 1950).

Figure 2.1 presents a geometrical representation of the stress state in the commonly referred as the Haigh-Westergaard space. A generic stress state is completely defined by the values of the principal stresses (σ_1, σ_2 and σ_3) and is represented by the vector where they are taken as Cartesian coordinates. The vector defined by the deviatoric principal stresses (σ_1', σ_2' and σ_3') always lies in the π-plane, defined by the equation $\sigma_1+\sigma_2+\sigma_3=0$. On the other hand, the vector defining the hydrostatic component is always perpendicular to the π-plane. The yield criterion can be regarded as a surface in this space. However, since the yielding is independent of the hydrostatic component of stress, the surface must have a cylindrical shape with generators perpendicular to the π-plane and cut it in some curve *C*. The axis of the cylinder is defined by the condition $\sigma_1=\sigma_2=\sigma_3$. Thus, when defining the yield criterion, it is sufficient to discuss possible forms for this curve, which defines the yield *locus*, *i.e.* to consider only stress states whose hydrostatic component is zero. When considering an isotropic behavior for the material, the shape of the *locus* can be defined only for a 30º segment since the others can be obtained by reflection (Hill, 1950).

A metal in which the grains are oriented randomly can be considered isotropic. However, plastic deformation induces the grains of a polycrystal to rotate to some limiting orientation, leading to a preferred orientation or texture. If the orientations of the individual grains are not randomly distributed, the yield stress and the macroscopic stress-strain relations vary with the loading direction. In such case, the yield surface must be able to describe this anisotropy in mechanical properties, which is typically due to the crystallographic texture that develops during plastic deformation, such as in the rolling process used to produce metallic sheets. In such case, it is usual to consider states of anisotropy that possess three mutually orthogonal planes of symmetry at every point; the intersections of these planes are known as the

principal axes of anisotropy. In a specimen cut from a cold-rolled sheet, the principal axis lie in the rolling direction (RD), transversely in the sheet plane (TD), and normal to this plane (RD) (Klinger and Sachs, 1948). In case of metallic sheets, in which a pronounced preferred orientation is present, it is commonly accepted that any further change in the orientation can be neglected (see *e.g.* Kuwabara et al., 1998). Thus, the shape of the yield surface does not change during continued deformation.

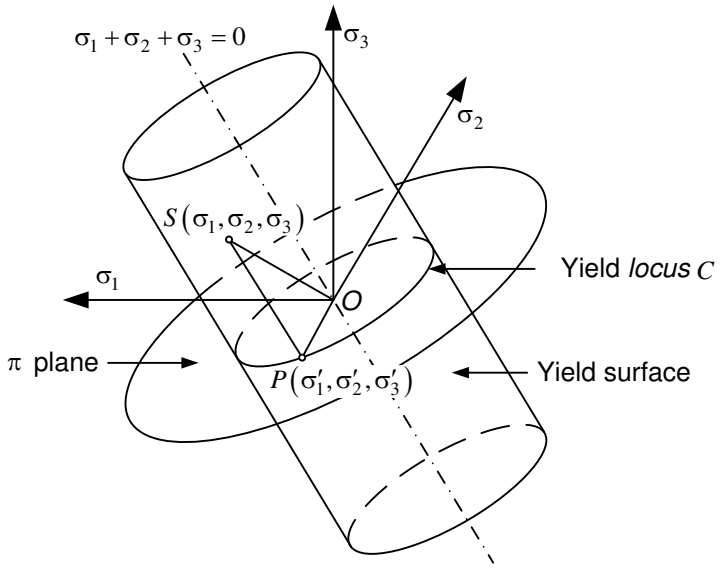

Figure 2.1. Geometrical representation of a plastic state of stress in the principal stress space. A yield criterion independent of the hydrostatic component of stress is represented by the curve *C* in the π-plane (adapted from Hill, (1950)).

Based on the observation of stress-strain curves, it is clear that the yield surface must depend on the complete previous process of plastic deformation. The more commonly adopted assumption is that, no matter by what strain-path a certain stress state is reached, the final yield *locus* is the same. Thus, the yield locus is uniquely defined by the final plastic state of stress (equivalent stress, $\bar{\sigma}$). In this sense, it can be assumed that the degree of hardening is a function of the total plastic work, *i.e.* independent of the strain-path. The assumption that hardening occurs if, and only if, plastic work is done, is consistent with the fact that purely elastic strains do not produce hardening. In this context, the equivalent plastic strain $\bar{\varepsilon}^{\mathrm{p}}$ is introduced to define the same invariant function of the components of the increment of the plastic strain tensor $\mathrm{d}\boldsymbol{\varepsilon}^{\mathrm{p}}$, as $\bar{\sigma}$ is for the components of the deviator stress tensor. The equivalent plastic strain, integrated over the strain-path, provides a measure of the

plastic work. On the other hand, if no plastic work is done by the hydrostatic component, then, for consistency, there is no plastic or irrecoverable change of volume imposed by it ($\mathrm{d}\varepsilon_{ii}^{\mathrm{p}} = 0$) (Hill, 1950). The function defining how the yield criterion evolves with the amount of plastic deformation is named hardening law, $Y\left(\bar{\varepsilon}^{\mathrm{p}}\right)$. This function defines the yield stress corresponding to each equivalent plastic strain value, also called flow stress. If the material presents the same flow stress when it is submitted to a reverse strain path change, the Bauschinger effect can be neglected and, consequently, an isotropic hardening law can be assumed. Otherwise, the most common approach used to describe the Bauschinger effect is to include a kinematic hardening law, which describes the evolution of the backstress tensor $\mathbf{X}$ based on the strain-path of the material point (Chaboche, 2008; Yoshida et al., 2002; Yoshida and Uemori, 2002). More recently, other models have been proposed that imply the distortion of the yield surface (Barlat et al., 2011).

Generally, the yielding condition is described by a function $\mathcal{F}$, such that

$$\mathcal{F}\left(\boldsymbol{\sigma}' - \mathbf{X}, \bar{\varepsilon}^{\mathrm{p}}, \alpha_{k_i}\right) = \bar{\sigma}\left(\boldsymbol{\sigma}' - \mathbf{X}, \alpha_{k_1}\right) - Y\left(\bar{\varepsilon}^{\mathrm{p}}, \alpha_{k_2}\right), \tag{2.1}$$

where $\bar{\sigma}\left(\boldsymbol{\sigma}' - \mathbf{X}, \alpha_{k_1}\right)$ is the equivalent stress given by the yield criterion and $Y\left(\bar{\varepsilon}^{\mathrm{p}}, \alpha_{k_2}\right)$ is the hardening law representing the evolution of the yield stress during deformation. α_{k_1} is a set of scalar parameters associated with the yield criterion selected and α_{k_2} is a set of scalar parameters associated with the hardening function selected. $\bar{\varepsilon}^{\mathrm{p}}$ corresponds to the internal variable of the hardening model, *i.e.* the equivalent plastic strain. In the yield condition, defined in Eq. (2.1) and in the following, it is assumed that the constitutive model is formulated in the objective frame, and thus all tensorial quantities are invariant.

The yield condition defines not only the set of permissible stress states but also the conditions for which plastic deformation can continue to occur. Whereas all elastic stress states are located inside the yield surface and defined uniquely by the elastic strain, plastic deformation can occur as long as the stress point is located on the yield

surface. This is expressed by the so-called consistency condition, which states that the time derivative of $\mathcal{F}$, $\dot{\mathcal{F}}$, is null.

When a material point is loaded from a neutral state, elastic strains develop. The relationship between the strain and the stress state is given by the generalized Hooke's law, when considering a linear elastic behavior, as it is commonly accepted for metallic materials. As the loading increases and the material begins to yield, plastic strains will also develop. In the plastic regime, there is no unique relation between the stress and total strains, because it will depend on the loading history. Thus, in order to establish a stress-strain relationship, it is more convenient to consider only the plastic strain increment $\mathrm{d}\boldsymbol{\varepsilon}^{\mathrm{p}}$, or in a more general way, the plastic strain rate tensor, $\mathbf{D}^{\mathrm{p}}$. Assuming that $\mathcal{G}$ is a function describing the plastic potential, the plastic strain rate tensor can be derived from it, imposing the normality condition (Genevois, 1992; Stoughton, 2002):

$$\mathbf{D}^{\mathrm{p}} = \dot{\lambda}\frac{\partial \mathcal{G}}{\partial \boldsymbol{\Sigma}}, \tag{2.2}$$

where $\boldsymbol{\Sigma}$ is the effective stress tensor, defined as $\boldsymbol{\sigma}' - \mathbf{X}$. Similarly to $\mathcal{F}$, the $\mathcal{G}$ function describes a surface in the stress space. Thus, the normality condition imposes that the plastic strain rate tensor is normal to the surface defined by $\mathcal{G}$, *i.e.* defines the direction of $\mathbf{D}^{\mathrm{p}}$.The scalar $\dot{\lambda}$ is the plastic multiplier defining the magnitude of the plastic strain rate tensor. In a general context, the expression for $\mathcal{G}$ should be determined based on experimental results, in a similar way to the yield function $\mathcal{F}$ (Hill, 1950). The adoption of the condition that $\mathcal{G}$=$\mathcal{F}$ is called associated flow rule (AFR), since the same function is used to describe the yielding conditions (yield surface) and the plastic strain rate (plastic potential). In contrast, the non-associated flow rule (non-AFR) considers that $\mathcal{G} \neq \mathcal{F}$.

The use of an associated flow rule is a cornerstone in the theory of plasticity since it leads to relevant results, such as the necessity of a convex yield surface and the compliance with the Drucker's stability postulate (Hill, 1950). Moreover, it can be demonstrated that the plastic multiplier, $\dot{\lambda}$ is equal to the plastic strain increment $\mathrm{d}\boldsymbol{\varepsilon}^{\mathrm{p}}$. Therefore, the dominant theory in metal plasticity assumes an AFR to calculate

the relation between the stress and the strain increment. In this case, the direction of the increment of the plastic strain tensor is normal to the yield surface at the loading point, which is commonly designated as normality condition (see Figure 2.2 (a)). The adoption of the AFR is based on experimental observations, where the presence of a high hydrostatic pressure was shown to not influence the yielding of the material (Bridgman, 1952, 1947). Also, negligible permanent volume change was shown to exist allowing the use of the same yield function as plastic potential (Khan and Huang, 1995). However, the use of the same function for both yielding and plastic potential means that the use of more flexible yield criteria is needed, mainly for highly anisotropic materials. The use of a non-AFR allows describing the plastic flow independently from the yield stress (see Figure 2.2 (b)) while also describing the behavior of materials with a pressure-dependent plastic behavior. In fact, Spitzig and Richmond (1984) report a small pressure-sensitivity in the yield criterion, for aluminum and steel, that is not accompanied by an expected plastic dilatancy, as required by the AFR. In addition, the use of a non-AFR model appears as an alternative to the use of more complex yield criteria, in order to achieve a more accurate description of the anisotropic behavior. In fact, similar results in the prediction of the earing profile of a cylindrical cup can be attained using a complex AFR yield criterion or a non-AFR using a simpler yield criterion (Safaei et al. 2013). Stoughton (2002) proposed a non-AFR formulation that accurately predicts both the *r*-values and yield stresses for directions of $0º$, $45º$ and $90º$ from the RD. Later, Stoughton and Yoon (2004) presented a non-AFR based on a pressure sensitive yield criterion with isotropic hardening capable of predicting the strength differential effect observed in tension and compression tests. Stoughton and Yoon (2009) presented a non-AFR enabling the accurate prediction of the hardening curves for directions of $0º$, $45º$ and $90º$ from the RD as well as for the balanced biaxial stress state. Taherizadeh et al. (2010) used a non-AFR with mixed isotropic-kinematic hardening improving cylindrical cups' height and springback of U-bends' predictions. It should be mentioned that although the adoption of non-AFR can avoid the necessity of more complex yield criteria, it requires the definition of the plastic potential. Therefore, its implementation is more complex and can lead to instabilities (Stoughton and Yoon, 2009).

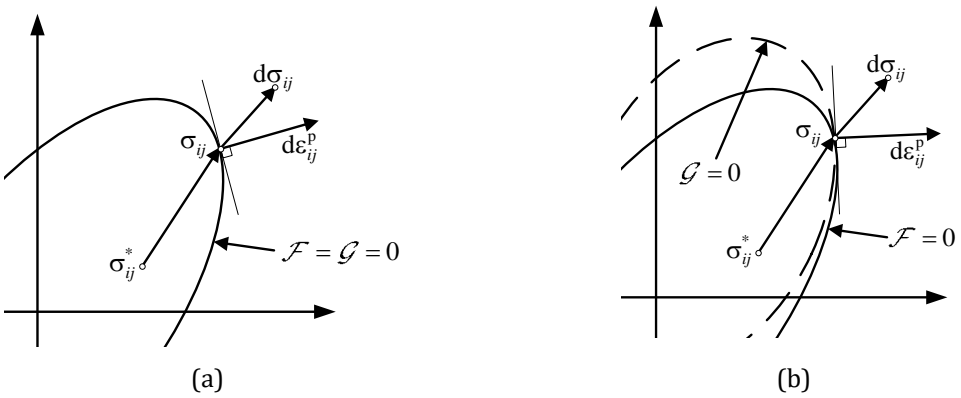

Figure 2.2. Schematic representation of the: (a) associated and (b) non-associated flow rules.

In brief, the plastic behavior of polycrystalline metallic materials is generally described by a phenomenological constitutive model integrating: (i) a yield surface, (ii) a flow rule and (iii) a hardening law (Zyczkowski, 1981). In case of the formulation implemented in DD3IMP code, an associated flow rule is adopted. The elastic behavior is described by the Hooke's generalized law. Therefore, it is necessary to define the hardening law and the yield criterion. In the following sections, some relevant hardening laws and yield criteria found in the literature are presented. Emphasis is given to the ones implemented in the DD3IMP code.

2.2. Hardening Law

As previously mentioned, during plastic deformation the yield surface evolves with the increase of plastic deformation, which is known as hardening behavior. Typically, the evolution of the yield surface can be of two types: (i) isotropic, which corresponds to the homothetic expansion of the yield surface and (ii) kinematic, corresponding to the translational movement of the surface's center. Kinematic hardening allows describing the mechanical behavior of materials presenting a decrease of the yield stress with a reverse strain path change, *i.e.* presenting Bauschinger effect. In order to better describe the material mechanical behavior, these two laws are generally combined in the so-called mixed isotropic-kinematic hardening law. The three types are schematically presented in Figure 2.3, highlighting the correspondence between the yield surfaces and stress *vs*. plastic strain curves.

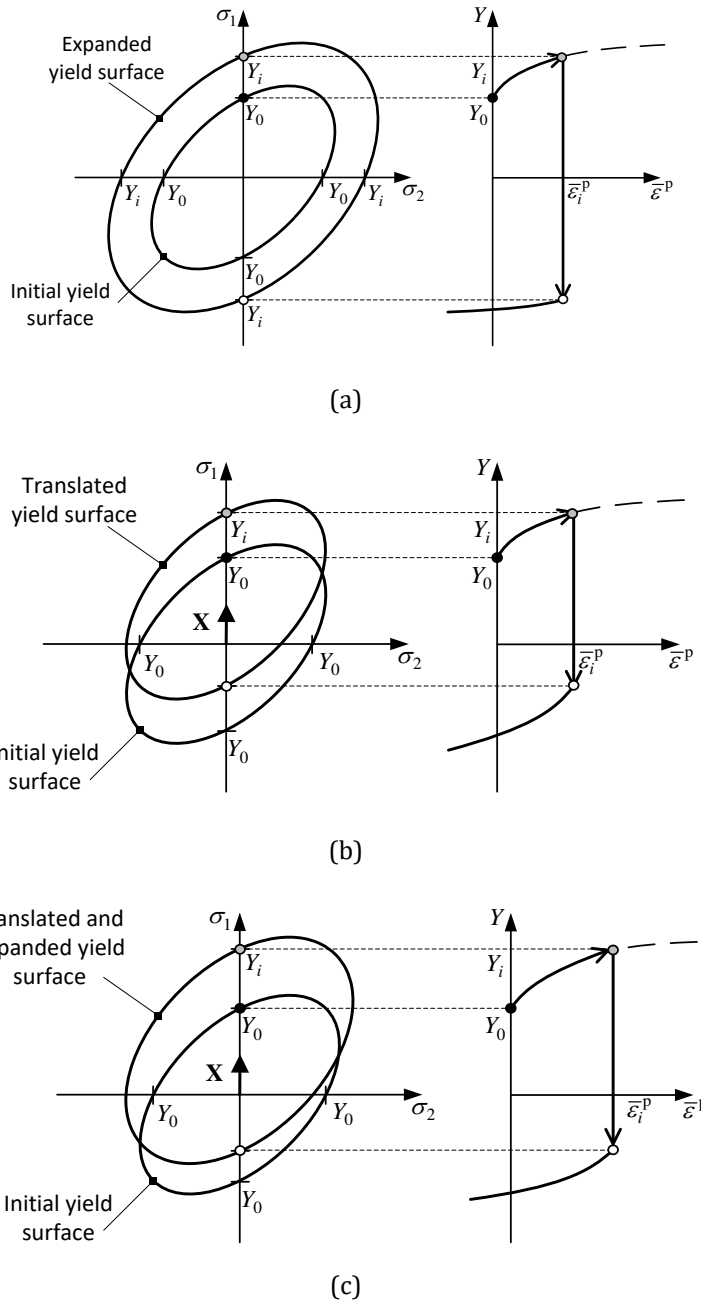

Figure 2.3. Schematic representation of the plastic behavior of materials in tension-compression on the $\sigma_1 - \sigma_2$ plane and corresponding stress *vs.* plastic strain curves. (a) Isotropic hardening; (b) Kinematic hardening; (c) Mixed isotropic-kinematic hardening (adapted from Prates (2014)).

2.2.1. Isotropic Hardening

One of the first isotropic hardening laws was proposed by Ludwik (1909), giving the evolution of the yield stress, Y, with the equivalent plastic strain, $\bar{\varepsilon}^{\mathrm{p}}$, in the form

$$Y = Y_0 + K\left(\bar{\varepsilon}^{\mathrm{p}}\right)^n, \tag{2.3}$$

where Y_0, K and n represent the initial yield stress, the hardening modulus and the hardening coefficient, respectively. Different isotropic hardening laws were proposed by several authors, to better reproduce the experimentally observed hardening behavior. The most well-known are the ones proposed by:

(Prager, 1945) $$Y = Y_S \tanh\left(\frac{H\bar{\varepsilon}^{\mathrm{p}}}{Y_S}\right), \tag{2.4}$$

(Hollomon, 1945) $$Y = K\left(\bar{\varepsilon}^{\mathrm{p}}\right)^n, \tag{2.5}$$

(Voce, 1948) $$Y = Y_0 + \left(Y_{\mathrm{sat}} - Y_0\right)\left[1 - \exp\left(-C_Y\bar{\varepsilon}^{\mathrm{p}}\right)\right], \tag{2.6}$$

(Swift, 1952) $$Y = K\left(\varepsilon_0 + \bar{\varepsilon}^{\mathrm{p}}\right)^n, \tag{2.7}$$

(Hockett and Sherby, 1975) $$Y = Y_0 + \left(Y_{\mathrm{sat}} - Y_0\right)\left[1 - \exp\left(-C_Y\left(\bar{\varepsilon}^{\mathrm{p}}\right)^a\right)\right], \tag{2.8}$$

where ε_0, a, C_Y, H, Y_{sat} and Y_S are material parameters. The most used laws are the Voce (Eq. (2.6)) and Swift (Eq. (2.7)). the Voce law is used to describe the behavior of materials exhibiting isotropic hardening with saturation, which occurs in face centered cubic metallic materials like aluminum; and the Swift law, which is the most adopted for materials exhibiting isotropic hardening without saturation, like steels. In order to increase the flexibility for fitting stress-strain curves, weighted combinations of isotropic hardening laws are used, such as

$$Y = \left(1-\alpha\right)\left[K\left(\varepsilon_0 + \bar{\varepsilon}^{\mathrm{p}}\right)^n\right] + \alpha\left[Y_0 + \left(Y_{\mathrm{sat}} - Y_0\right)\left[1 - \exp\left(-C_Y\bar{\varepsilon}^{\mathrm{p}}\right)\right]\right], \tag{2.9}$$

$$Y = \left(1-\alpha\right)\left[K\left(\varepsilon_0 + \bar{\varepsilon}^{\mathrm{p}}\right)^n\right] + \alpha\left[Y_0 + \left(Y_{\mathrm{sat}} - Y_0\right)\left[1 - \exp\left(-C_Y\left(\bar{\varepsilon}^{\mathrm{p}}\right)^a\right)\right]\right], \tag{2.10}$$

where $\alpha \in [0,1]$ corresponds to the weighting coefficient between the power and saturation laws.

2.2.2. Kinematic Hardening

An accurate kinematic hardening modeling is essential to describe materials showing one, or all, of the following phenomena upon reverse strain path: transient behavior, hardening stagnation and permanent softening. Figure 2.4 schematically shows these phenomena observed during a tension-compression test. The reloading shows three stages: (i) the transient Bauschinger effect, characterized by early re-yielding and a smooth elastoplastic transition, followed by a rapid change of the hardening rate; (ii) eventual subsequent hardening stagnation in a certain range of the reverse deformation; and (iii) the permanent softening, characterized by the offset in the stress values relatively to the ones predicted for pure isotropic hardening. These stages can be more or less noticeable, depending on the material. For example, the aluminum alloys studied in the 3DS project only show transient behavior while the steels also have a clear hardening stagnation (Banu et al., 2001). Anyhow, the Bauschinger effect is known to have a great influence on the accuracy of numerical results where springback is important, since this phenomenon corresponds to the elastic strain recovery and its magnitude depends on the through thickness stress gradients predicted (Meinders et al., 2008).

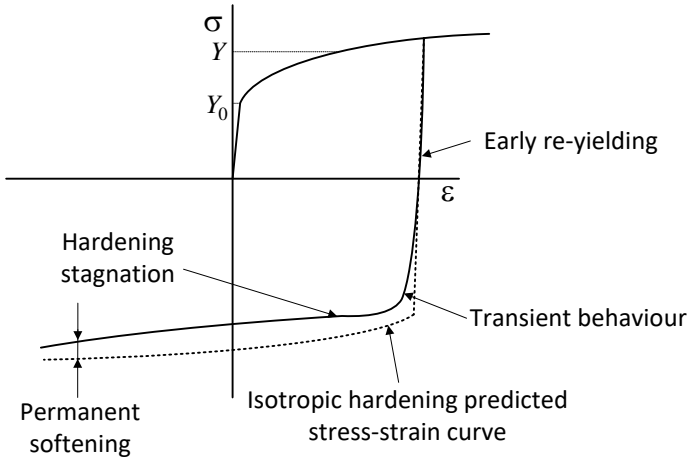

Figure 2.4. Hardening behavior during a tension-compression test, highlighting the stages associated with the Bauschinger effect (adapted from Yoshida and Uemori (2003)).

As previously stated, the evolution of the yield surface's center during deformation can be described by the kinematic component of hardening using the backstress tensor

$\mathbf{X}$ (see Figure 2.3). Prager (1949, 1956) proposed a linear kinematic hardening model in the form

$$\dot{\mathbf{X}} = k\mathbf{D}^{\mathrm{p}}, \text{ with } \mathbf{X}(0) = \mathbf{0} \tag{2.11}$$

where $\dot{\mathbf{X}}$ is the velocity of translation of the yield surfaces center. k depends on the material, meaning that the two tensorial quantities are proportional. Although the assumption of a linear kinematic hardening is advantageous in terms of numerical implementation, it fails to predict the nonlinear behavior observed for metallic materials. Thus, nonlinear kinematic models were proposed such as the one by Armstrong and Frederick (1966) given by

$$\dot{\mathbf{X}} = C_x \left[X_{\mathrm{sat}} \frac{(\boldsymbol{\sigma}' - \mathbf{X})}{\bar{\sigma}} - \mathbf{X} \right] \dot{\bar{\boldsymbol{\varepsilon}}}^{\mathrm{p}} \text{ with } \mathbf{X}(0) = \mathbf{0}, \tag{2.12}$$

where X_{sat} and C_x correspond to the saturation value of the backstress tensor and the rate of approximation to the saturation value, respectively. This model, combined with an isotropic hardening law, allows describing the progressive saturation of the kinematic hardening observed experimentally, for instance in aluminum alloys (Banu et al., 2001). However, this mixed hardening model is unable to describe the behavior of materials presenting hardening stagnation as well as permanent softening. In this context, other mixed hardening models were proposed such as the one by Teodosiu and Hu (1998, 1995). This microstructural model takes into account the influence of a pre-strain in the subsequent plastic behavior of the material, enabling also to describe the decrease of the flow stress observed after an orthogonal strain path change. Nonetheless, this increased flexibility comes with supplementary difficulties associated with its parameter identification and required set of experimental tests. In fact, in case of steels, this model has 13 parameters while its simplified version, adequate for aluminum alloys, has 8 parameters (Banu et al., 2001).

A different approach has been proposed by Barlat et al. (2011), which does not consider the evolution of the backstress tensor. This approach is based on the so-called homogeneous anisotropic hardening (HAH) concept. When loading occurs in one direction, the yield surface expands isotropically and flattens in the opposite direction, allowing for the Bauschinger effect prediction. Figure 2.5 schematically presents the

yield surface evolution when a tensile stress is imposed in σ_1, highlighting a surface expansion in this direction and the flattening in the opposite direction. This approach imposes that the yield surface's shape in lo longer constant.

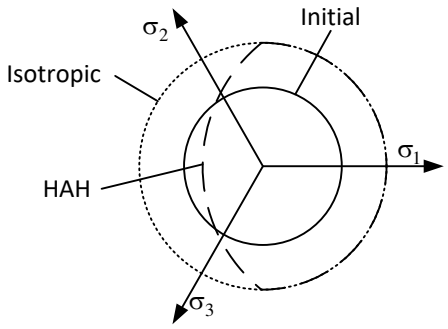

Figure 2.5. Schematic of the yield surface's shape evolution according to the HAH model.

2.3. Yield Surface

As stated before, the yield surface defines the transition between the elastic and the plastic behavior. Convexity of the yield surface and the non-existence of singular points must be guaranteed, such that there is uniqueness between the stress and the strain increment. The convexity of a function can be verified through the properties of its Hessian matrix. Lippmann, (1970) proved that it is only necessary to make proof of convexity of the function in the principal axis, such that its Hessian matrix ought to be positive semi-definite (Eggleston, 1958; Rockafellar, 1972) *i.e.*, its eigenvalues must be positive or null. The Hessian matrix, $\mathbf{H}$, is defined by

$$H_{ij} = \frac{\partial^2 \mathcal{F}}{\partial \sigma_i \partial \sigma_j}, \tag{2.13}$$

where $\mathcal{F}$ represents the yield condition (see Eq. (2.1)) and σ_i and σ_j (with $i, j = 1, 2, 3$) are the Cauchy principal stresses. It has been shown that the application of a linear transformation to the stress tensor does not change the convexity of the yield function (Eggleston, 1958; Rockafellar, 1972). This is a milestone for the development of convex anisotropic yield criteria from isotropic ones (Barlat et al., 1991a; Karafillis and Boyce, 1993).

In the following section, some yield criteria found in the literature are presented, giving emphasis on the ones implemented in the DD3IMP code. In this context, only three-dimensional (3D) yield criteria are discussed since all the numerical simulations were performed considering eight-node hexahedral solid finite elements. Nevertheless, when considering thin metallic sheets, it is not possible to evaluate the off-plane properties and, consequently, the anisotropy parameter. Therefore, the corresponding anisotropy parameters cannot be evaluated and, therefore, the corresponding isotropic values are commonly adopted.

In this work, only isotropic hardening was considered, so it is assumed in the following sections that $\mathbf{X} = \mathbf{0}$, *i.e.* $\boldsymbol{\Sigma} = \boldsymbol{\sigma}'$.

2.3.1. Isotropic yield criteria

If the material's mechanical behavior is independent of the loading orientation, then it is considered isotropic. For describing the yield surface for such materials, only one equation is needed in the form

$$f\left(\boldsymbol{\sigma}\right) = K\,, \tag{2.14}$$

where $\boldsymbol{\sigma}$ the Cauchy stress tensor and K is a constant that characterizes the material behavior, usually the yield stress obtained from a tensile test.

2.3.1.1. Tresca (1864)

The Tresca yield criterion (Tresca, 1864) considers that plastic deformation in metals occurs by dislocation movements in preferred planes and directions. Thus, the model proposed is based on the maximum shear stress definition, $\tau_{\max}$. This is a function of the σ_1 and σ_3 which are, respectively, the major and minor principal stresses. The yield criterion is expressed by

$$\tau_{\max}\left(\frac{\sigma_1 - \sigma_3}{2}\right) = \tau_0\,, \tag{2.15}$$

where τ_0 is the critical shear stress value, above which plastic deformation occurs, for the specific material. The uniaxial yield stress, Y_0, is two times the shear stress τ_0, $\left(Y = 2\tau_0\right)$. Thus, considering the material's hardening behavior, Eq. (2.15) becomes

$$\sigma_1 - \sigma_3 = Y\,. \tag{2.16}$$

2.3.1.2. von Mises (1913)

The von Mises yield criterion (von Mises, 1913) is based on the fact that only the deviatoric component of the stress promotes permanent deformation, *i.e.* yielding occurs when J_2' reaches a critical value, or, in other words, J_3' can be neglected. The von Mises criterion can be written as

$$\left(\sigma_1 - \sigma_2\right)^2 + \left(\sigma_2 - \sigma_3\right)^2 + \left(\sigma_1 - \sigma_3\right)^2 = 2Y^2 \tag{2.17}$$

where σ_1, σ_2 and σ_3 are the principal stresses. In the Oxyz axis, it can be written as

$$\left(\sigma_{yy} - \sigma_{zz}\right)^2 + \left(\sigma_{zz} - \sigma_{xx}\right)^2 + \left(\sigma_{xx} - \sigma_{yy}\right)^2 + 6\tau_{yz}^2 + 6\tau_{zx}^2 + 6\tau_{xy}^2 = 2Y^2\,, \tag{2.18}$$

where Y is the uniaxial yield stress and σ_{xx}, σ_{yy}, σ_{zz}, τ_{xy}, τ_{zx} and τ_{yz} are the components of the Cauchy stress tensor.

Hencky suggested a physical interpretation for this assumption based on the fact that yielding begins when the (recoverable) elastic energy of distortion reaches a critical value. Thus, a hydrostatic pressure does not cause yielding since it produces only elastic energy of compression in an isotropic metal. Other interpretations of this yield criterion were proposed, as discussed in (Hill, 1950).

Figure 2.6 presents a comparison between the Tresca and the von Mises yield criteria, assuming the same value for the yield stress in simple tension. It is possible to confirm that the most significant difference occurs for a state of pure shear, where the von Mises criterion gives a yield stress $2/\sqrt{3}$ times higher than that given by the Tresca yield criterion. It has been shown that the von Mises yield criterion can reproduce the experimental results for many ductile metals, although in some cases it has been reported that Tresca leads to better results (Hill, 1950). Figure 2.6 also highlights another important difference between these yield criteria: the normal vector for the

von Mises yield surface is smooth, while the normal vector to the Tresca yield surface presents singular points. This poses additional difficulties in the numerical implementation of the Tresca yield criterion.

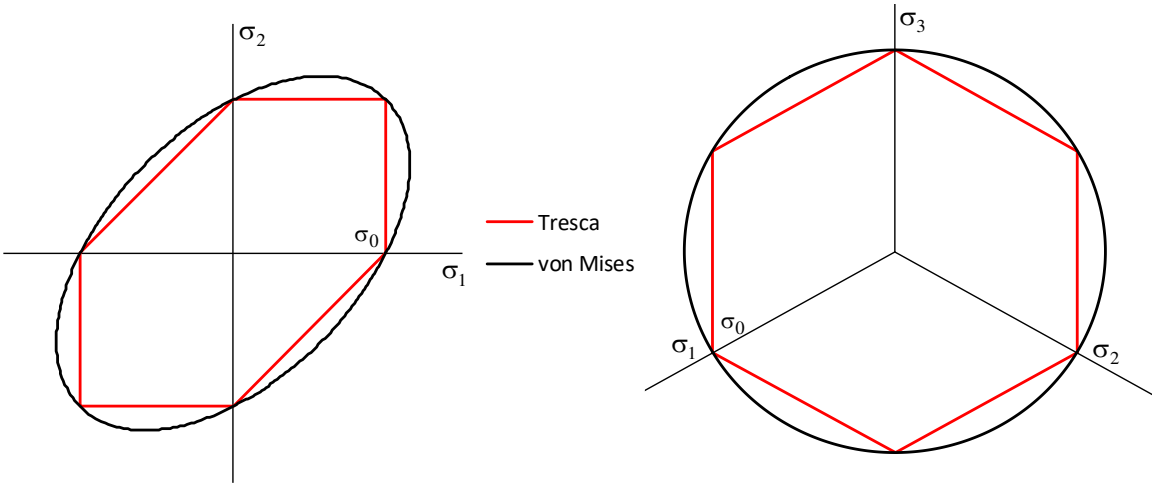

Figure 2.6. Tresca and von Mises yield surfaces in the $\sigma_1 - \sigma_2$ plane (left) and π-plane (right).

2.3.1.3. Drucker (1949)

The Drucker yield criterion (Drucker, 1949) is a function of the second and third invariant of the effective stress tensor, defined by

$$J_2^3 - cJ_3^2 = 27\left(\frac{Y}{3}\right)^6, \tag{2.19}$$

where J_2 and J_3, can be expressed as a function of the Cauchy stress tensor components, given by

$$J_2 = \frac{1}{6}\left[\left(\sigma_{xx}-\sigma_{yy}\right)^2 + \left(\sigma_{yy}-\sigma_{zz}\right)^2 + \left(\sigma_{xx}-\sigma_{zz}\right)^2\right] + \tau_{yz}^2 + \tau_{zx}^2 + \tau_{xy}^2 \text{ and} \tag{2.20}$$

$$\begin{aligned} J_3 = {} & \frac{2}{27}\left[\sigma_{xx}^3 + \sigma_{yy}^3 + \sigma_{zz}^3\right] + \frac{4}{9}\sigma_{xx}\sigma_{yy}\sigma_{zz} + 2\tau_{xy}^2\tau_{yz}^2\tau_{xz}^2 \\ & -\frac{1}{9}\left[\left(\sigma_{yy}-\sigma_{zz}\right)\sigma_{xx}^2 + \left(\sigma_{xx}-\sigma_{zz}\right)\sigma_{yy}^2 + \left(\sigma_{xx}+\sigma_{yy}\right)\sigma_{zz}^2\right] \\ & -\frac{1}{3}\left[\tau_{xz}^2\left(2\sigma_{yy}-\sigma_{zz}-\sigma_{xx}\right) + \tau_{xy}^2\left(2\sigma_{zz}-\sigma_{yy}-\sigma_{xx}\right) + \tau_{yz}^2\left(2\sigma_{xx}-\sigma_{yy}-\sigma_{zz}\right)\right] \end{aligned} . \tag{2.21}$$

c is a material constant. If c is zero, the Drucker yield criterion reduces to von Mises. In order to ensure convexity, $c \in [-3.375, 2.250]$. Figure 2.7 presents the Drucker's yield

surfaces for different values of c, showing that for increasing positive values it approaches the Tresca yield criterion. For increasing negative values it tends to a limit surface similar in shape to the Tresca one but located outside the one defined by the von Mises yield criterion.

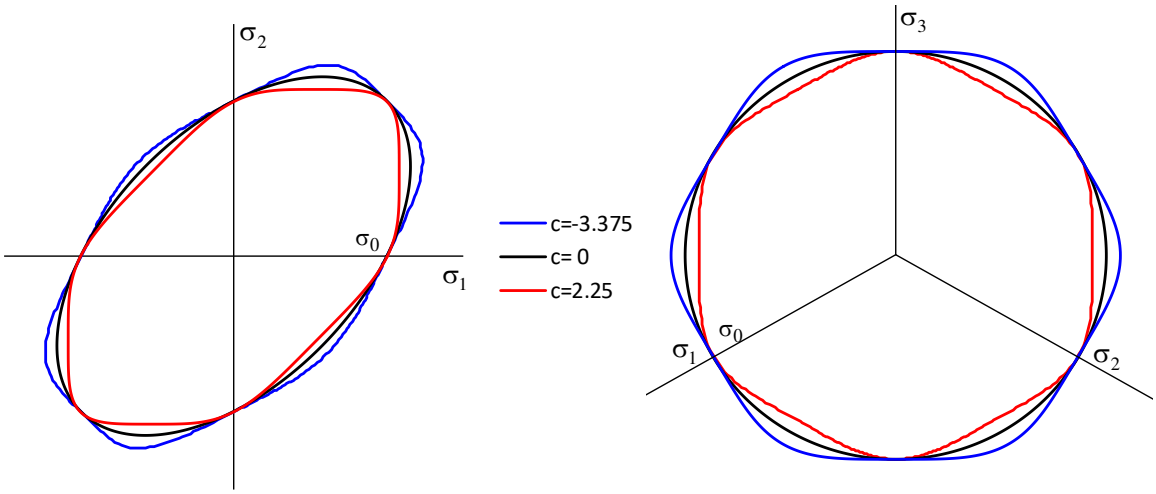

Figure 2.7. Drucker's yield surfaces in the $\sigma_1 - \sigma_2$ plane (left) and π-plane (right) for different values of c.

2.3.1.4. Hershey and Hosford (1972)

Hershey (1954) proposed a yield function based on a polycrystalline deformation auto-consistent model and Hosford (1972) generalized its application. The yield surfaces described by this model are between the ones given by Tresca and von Mises, depending on the value considered for the integer exponent m. The yield surface is defined as

$$\left(\sigma_1 - \sigma_2\right)^m + \left(\sigma_2 - \sigma_3\right)^m + \left(\sigma_1 - \sigma_3\right)^m = 2Y^m . \tag{2.22}$$

If $m = 2$, the von Mises yield criterion is recovered. On the other hand, when $m \to \infty$ the Tresca yield criterion is obtained. Thus, the yield surfaces are all located between these two limits. m can be chosen in function of the material's crystalline structure (Logan and Hosford, 1980). Usually, $m = 6$ for metals with body centered cubic (BCC) structures and $m = 8$ for face centered cubic (FCC) structures. Figure 2.8 presents the yield surfaces for different values of the exponent m.

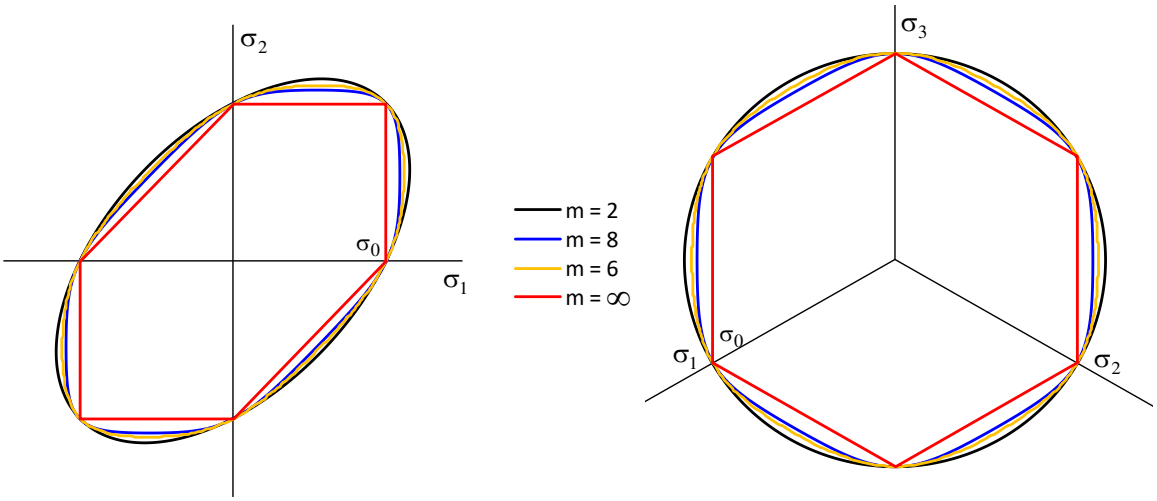

Figure 2.8. Hosford's yield surfaces in the $\sigma_1 - \sigma_2$ plane (left) and π-plane (right) for different values of the exponent m.

2.3.2. Anisotropic yield criteria

Anisotropic yield criteria allow modeling the dependency of the yield stresses on the loading direction. This is important since sheet metal forming processes are carried out under multiaxial solicitations. In the formulation of an anisotropic yield criterion, it is advisable that it has the possibility to reduce to an isotropic one, to avoid artificial anisotropic effects when applied to isotropic materials (Barlat et al., 2005). In the following sections, two materials from the literature are used in order to show the potential of each anisotropic yield criteria to capture both yield stress an *r*-values in-plane directionalities: an AKDQ steel (Dick et al., 2011) and an AA2090-T3 aluminum alloy (Barlat et al., 1991). These materials were selected since they present distinct orthotropic behavior and are further studied in Chapter 4. The parameters for each yield criterion, implemented in DD3IMP, were identified using the DD3MAT in-house code, considering all the available experimental data, but with all the weighting coefficients considered unitary, *i.e.* equal to 1.0. The results obtained under these conditions are shown in this chapter highlighting the flexibility of each yield criterion.

2.3.2.1. Hill (1948)

The Hill'48 yield criterion (Hill, 1948) is one of the most widely used for the numerical simulation of sheet metal forming processes, since it adequately describes the anisotropy of metals sheets, allied to a simple formulation and easy implementation in numerical simulation codes. It is a generalization of the quadratic isotropic von Mises criterion for orthotropic materials. Assuming that the Oxyz axis corresponds to the principal axis of anisotropy, it can be formulated as

$$\mathrm{F}\left(\sigma_{yy}-\sigma_{zz}\right)^2+\mathrm{G}\left(\sigma_{zz}-\sigma_{xx}\right)^2+\mathrm{H}\left(\sigma_{xx}-\sigma_{yy}\right)^2+2\mathrm{L}\tau_{yz}^2+2\mathrm{M}\tau_{zx}^2+2\mathrm{N}\tau_{xy}^2=Y^2, \quad (2.23)$$

where σ_{xx}, σ_{yy}, σ_{zz}, τ_{xy}, τ_{zx} and τ_{yz} are the components of the Cauchy stress tensor and F, G, H, L, M and N are the material anisotropy parameters. Note that the von Mises yield criterion is recovered when the relationship between the anisotropy parameters is $\mathrm{F}=\mathrm{G}=\mathrm{H}=\mathrm{L}/3=\mathrm{M}/3=\mathrm{N}/3=0.5$. Thus, in case of metallic sheets, it is assumed that $\mathrm{L}=\mathrm{M}=1.5$. The other four parameters can be identified using the in-plane yield stresses or the *r*-values (Hill, 1950). The most usual methodology considers the results from three uniaxial tensile tests, assuming the condition $\mathrm{G}+\mathrm{H}=1$, *i.e.* that the hardening law corresponds to the stress *vs* strain curve obtained for RD. In that case, the parameters are obtained as

$$\begin{aligned} \mathrm{F}&=\frac{\mathrm{H}}{r_{90}} & \mathrm{H}&=r_0\mathrm{G} \\ \mathrm{G}&=\frac{1}{r_0+1} & \mathrm{N}&=\frac{1}{2}\frac{\left(r_0+r_{90}\right)\left(2r_{45}+1\right)}{r_{90}\left(r_0+1\right)}, \end{aligned} \quad (2.24)$$

where r_0, r_{45} and r_{90} are the anisotropy coefficients determined from the tensile test performed with the specimen oriented 0º, 45º and 90º from RD.

This yield criterion is appropriate mainly for steels, with a good description of the orthotropic behavior when the value of the normal anisotropy coefficient, $\bar{r}$, is higher than 1.0. This coefficient is defined as

$$\bar{r}=1/4\left(r_0+2r_{45}+r_{90}\right). \quad (2.25)$$

The main drawback of this yield criterion is its low flexibility, since only three independent parameters are used to describe the planar anisotropy of metallic sheets,

not allowing a simultaneous accurate description of both the yield stresses' and *r*-values in-plane evolutions. This leads to an inability to describe the so-called "anomalous" behavior observed by Woodthorpe and Pearce, (1970), characterized by $\bar{r} < 1$ and $\sigma_b > \sigma_0$ or reciprocal. Banabic (2010) also refers that the Hill'48 yield criterion cannot describe a "second order anomalous" behavior, characterized by $r_0 > r_{90}$ and $\sigma_0 < \sigma_{90}$ (or *vice versa*). Figure 2.9 and Figure 2.10 present the Hill'48 yield surfaces and in-plane *r*-values and yield stresses directionalities, respectively, for both the AKDQ and AA2090-T3 aluminum alloy. Figure 2.10 shows that the AKDQ steel presents an $\bar{r} > 1$ while the AA2090-T3 aluminum alloy has a $\bar{r} < 1$, thus the first has a $\sigma_b > \sigma_0$ while the second presents a $\sigma_b < \sigma_0$ (see Figure 2.9). This is why it is usually stated that the Hill'48 criterion cannot accurately describe materials with $\bar{r} < 1$., such as aluminum alloys. Both materials follow the conditions $r_0 < r_{90}$ while $\sigma_0 > \sigma_{90}$. As shown in Figure 2.10, the Hill'48 describes the trend for the *r*-values but fails in the description of the yield stresses (*i.e.* $\sigma_0 < \sigma_{90}$).

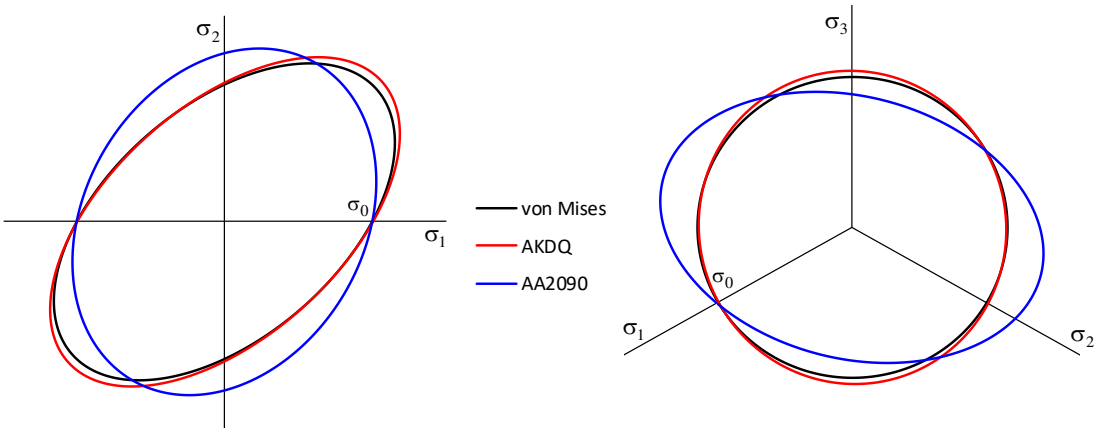

Figure 2.9. Normalized anisotropic Hill'48 yield surfaces in the $\sigma_1 - \sigma_2$ plane (left) and π-plane (right) for the AKDQ steel and the AA2090-T3 aluminum alloy.

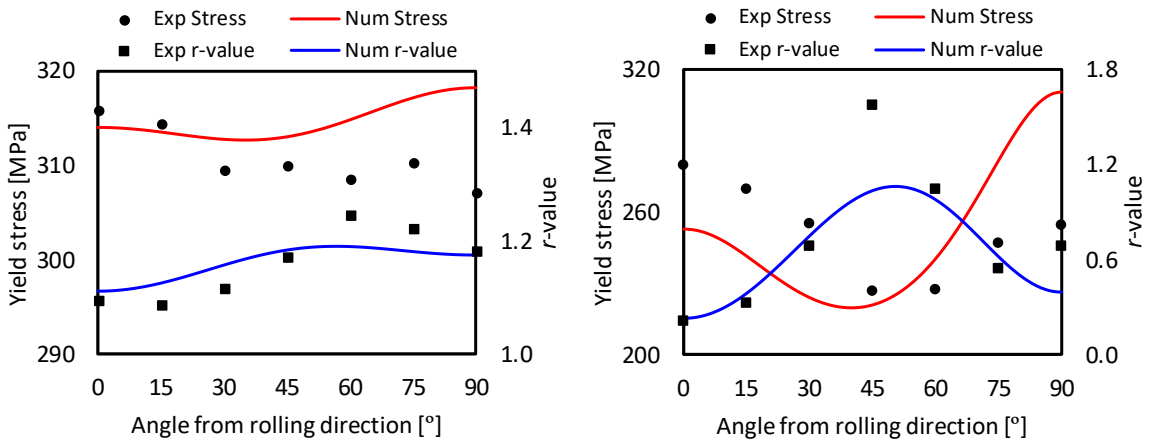

Figure 2.10. Experimental and numerically predicted yield stresses and *r*-values for the (a) AKDQ steel and (b) AA2090-T3 aluminum alloy.

2.3.2.2. Barlat's yield criteria

To better describe the orthotropic behavior of metallic sheets, particularly aluminum alloys, Barlat et al. (1991) developed a criterion which is an extension to orthotropy of the isotropic criterion proposed by Hosford (see section 2.3.1.4). This is based on the use of a linear transformation, $\mathbf{L}$, of the deviatoric stress tensor such that $\mathbf{s} = \mathbf{L} : \boldsymbol{\sigma}'$. This linear transformation concept consists in transforming the deviatoric stress tensor in an isotropic plasticity equivalent (IPE) stress state, as schematically illustrated in Figure 2.11. This linear transformation always leads to a deviatoric tensor.

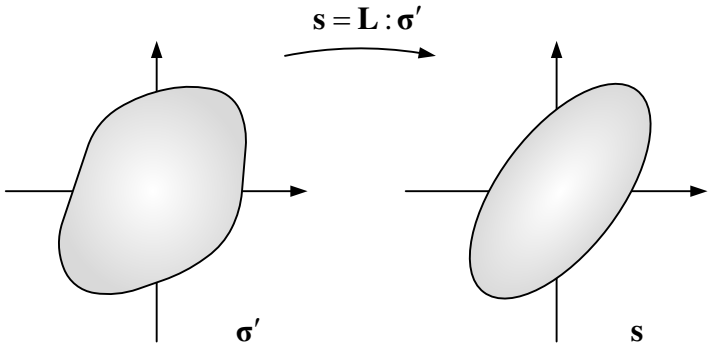

Figure 2.11. Schematic representation of the linear transformation of the yield surface of the anisotropic material to the equivalent isotropic one (adapted from Karafillis and Boyce, 1993).

The YLD91 yield criterion is then expressed by

$$\left\{\frac{1}{2}\left[\left|s_1-s_2\right|^m+\left|s_2-s_3\right|^m+\left|s_1-s_3\right|^m\right]\right\}^{\frac{1}{m}}=Y\,, \tag{2.26}$$

where s_1, s_2 and s_3 are the principal values of $\mathbf{s}$ and m is the exponent that controls the shape of the isotropic yield surface, usually taken as 6 or 8 for BCC and FCC materials, respectively (Barlat et al., 1991a). Y is the hardening law, which can be assumed as equal to the stress-strain curve in uniaxial tension, and $\mathbf{L}$ is the proposed constant 4th-order tensor. Assuming the Voigt notation for the deviatoric stress tensor

$$\begin{Bmatrix}\sigma'_{11}\\ \sigma'_{22}\\ \sigma'_{33}\\ \sigma'_{23}\\ \sigma'_{13}\\ \sigma'_{12}\end{Bmatrix}=\begin{Bmatrix}\sigma'_{1}\\ \sigma'_{2}\\ \sigma'_{3}\\ \sigma'_{4}\\ \sigma'_{5}\\ \sigma'_{6}\end{Bmatrix}, \tag{2.27}$$

the tensor $\mathbf{L}$ is expressed in the principal axis of anisotropy as

$$\mathbf{L}=\begin{bmatrix}\left(c_2+c_3\right)/3 & -c_3/3 & -c_2/3 & 0 & 0 & 0\\ -c_3/3 & \left(c_3+c_1\right)/3 & -c_1/3 & 0 & 0 & 0\\ -c_2/3 & -c_1/3 & \left(c_1+c_2\right)/3 & 0 & 0 & 0\\ 0 & 0 & 0 & c_4 & 0 & 0\\ 0 & 0 & 0 & 0 & c_5 & 0\\ 0 & 0 & 0 & 0 & 0 & c_6\end{bmatrix}, \tag{2.28}$$

which, for a 3D stress state, involves only 6 independent anisotropy coefficients c_i for $(i=1,\ldots,6)$. For thin metallic sheets $c_4=c_5=1.0$. Figure 2.12 and Figure 2.13 present the YLD91 yield surfaces and in-plane *r*-values and yield stresses directionalities, respectively, for both the AKDQ and AA2090-T3 aluminum alloy. When comparing with the Hill'48 yield criterion, the shape of the yield surfaces is sharper, particularly for the AKDQ. Nonetheless, the trends predicted for the in-plane orthotropic behavior are quite similar, for both materials, since both yield criteria share the same number of anisotropy parameter, *i.e.* four.

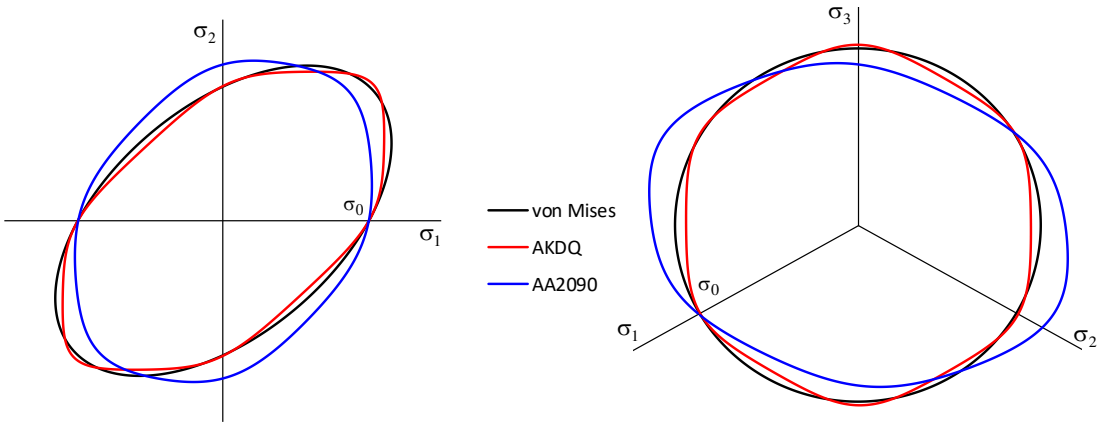

Figure 2.12. Normalized anisotropic YLD91 yield surfaces in the $\sigma_1 - \sigma_2$ plane (left) and π-plane (right) for the AKDQ steel and AA2090-T3 aluminum alloy.

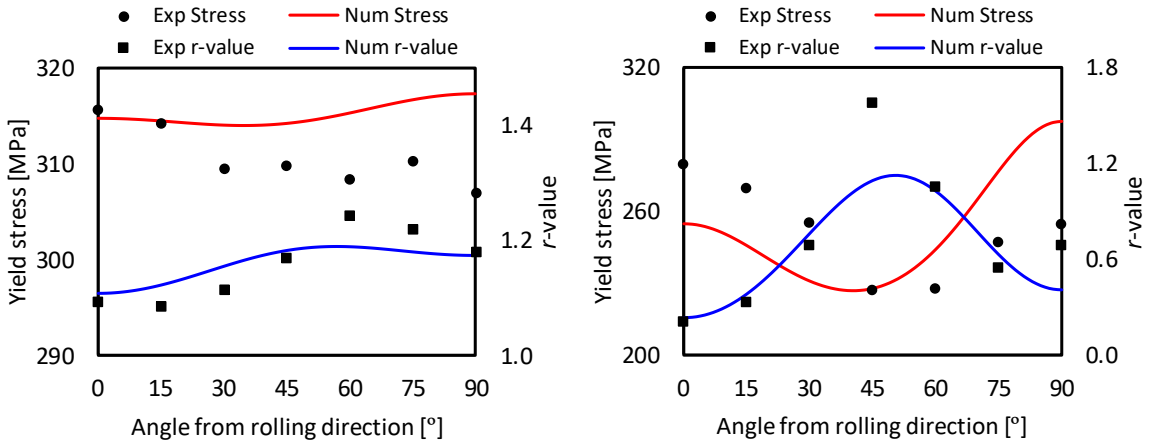

Figure 2.13. Experimental and YLD91 predicted yield stresses and *r*-values for the (a) AKDQ steel and (b) AA2090-T3 aluminum alloy.

Barlat et al. (1997) proposed the YLD94 yield criterion since it was observed that the YLD91 could not accurately describe the behavior of some materials, especially near pure shear stress state conditions $\left(\sigma_{xx}/\sigma_{yy} = -1\right)$. The YLD94 expression is given by

$$\left\{\frac{1}{2}\left[\alpha_1\left|s_1 - s_2\right|^m + \alpha_2\left|s_2 - s_3\right|^m + \alpha_3\left|s_1 - s_3\right|^m\right]\right\}^{\frac{1}{m}} = Y\,, \tag{2.29}$$

where s_1, s_2 and s_3 are the principal values of $\mathbf{s}$ and m is the exponent that controls the shape of the isotropic yield surface, as in Eq. (2.26), with the coefficients α_k (with

$k = 1, 2, 3$) obtained from the anisotropy parameters α_x, α_y and α_z considering the transformation

$$\alpha_k = \alpha_x p_{1k}^2 + \alpha_y p_{2k}^2 + \alpha_z p_{3k}^2, \tag{2.30}$$

where p_{ik} are the components of the transformation tensor $\mathbf{p}$ between the anisotropy axes and the principal directions of the tensor $\mathbf{s}$. Thus, the YLD94 has five independent parameters. For $\alpha_x = \alpha_y = \alpha_z = 1.0$, the YLD91 yield criterion is recovered.

The YLD96 yield criterion is proposed by Barlat et al. (1997b) to improve both the YLD91 and YLD94 yield criteria. According to the authors, the normal to the yield surface for tensile stress states in RD and TD is dictated by the correspondent *r*-value. Accordingly, slight variations in the yield surface can result in string changes of the *r*-values predicted. This sensibility is pointed out as a weakness as well as the inability to simultaneously capture the yield stress and *r*-value for 45° to RD (only one anisotropy parameter is available, c_6). In the YLD96, both Eq. (2.29) and Eq. (2.30) are used, but a variation of the parameter α_z with β is proposed. β is the angle defined between the RD and the direction associated with the eigenvector of $\mathbf{s}$ presenting the higher absolute value (s_1 or s_3). Therefore,

$$\alpha_z = \alpha_{z0} \cos^2(2\beta) + \alpha_{z1} \sin^2(2\beta), \tag{2.31}$$

where α_{z0} and α_{z1} are anisotropy parameters, resulting in a total of seven. The non-proven convexity, mainly when associated with multiaxial stress states, is the main drawback of this yield criterion. In addition, its numerical implementation is difficult due to the complex analytical formulation of the required derivatives (Alves, 2003).

Based on the principle that an improved description of the orthotropic behavior of the material requires a higher number of anisotropy parameters, the Yld2004-18p yield criterion was proposed by Barlat et al. (2005), considering the use of two linear transformations of the stress tensor. Assuming the Voigt notation, the use of two linear transformations leads to the tensors

$$\mathbf{s}' = \mathbf{L}'\boldsymbol{\sigma} \text{ and } \mathbf{s}'' = \mathbf{L}''\boldsymbol{\sigma}. \tag{2.32}$$

The linear transformation tensors $\mathbf{L}'$ and $\mathbf{L}''$ are then given by

$$\mathbf{L}' = \begin{bmatrix} 0 & -c'_{12} & c'_{13} & 0 & 0 & 0 \\ -c'_{21} & 0 & -c'_{23} & 0 & 0 & 0 \\ -c'_{31} & -c'_{32} & 0 & 0 & 0 & 0 \\ 0 & 0 & 0 & c'_{44} & 0 & 0 \\ 0 & 0 & 0 & 0 & c'_{55} & 0 \\ 0 & 0 & 0 & 0 & 0 & c'_{66} \end{bmatrix} \tag{2.33}$$

and

$$\mathbf{L}'' = \begin{bmatrix} 0 & -c''_{12} & c''_{13} & 0 & 0 & 0 \\ -c''_{21} & 0 & -c''_{23} & 0 & 0 & 0 \\ -c''_{31} & -c''_{32} & 0 & 0 & 0 & 0 \\ 0 & 0 & 0 & c''_{44} & 0 & 0 \\ 0 & 0 & 0 & 0 & c''_{55} & 0 \\ 0 & 0 & 0 & 0 & 0 & c''_{66} \end{bmatrix}. \tag{2.34}$$

Thus, the yield function given by this criterion depends on two sets of principal values as

$$\begin{aligned} \bar{\sigma} = &\left|s'_1 - s''_1\right|^a + \left|s'_1 - s''_2\right|^a + \left|s'_1 - s''_3\right|^a + \left|s'_2 - s''_1\right|^a + \left|s'_2 - s''_2\right|^a \\ &+ \left|s'_3 - s''_1\right|^a + \left|s'_3 - s''_2\right|^a + \left|s'_3 - s''_3\right|^a = 4Y^a \end{aligned} \tag{2.35}$$

where s'_1, s'_2 and s'_3 are the principal values of $\mathbf{s}'$ and s''_1, s''_2 and s''_3 are the principal values of $\mathbf{s}''$. a is an exponent dependent on the material's crystalline structure such that, in order to describe the behavior of BCC and FCC materials, should be considered equal to 6 or 8, respectively. When $a = 2$ (or 4) and the anisotropy parameters c'_{ij} and c''_{ij} are equal to 1.0, the von Mises yield criterion is recovered. Also, if $\mathbf{L}' = \mathbf{L}''$ only one linear transformation is considered by the formulation. The convexity of this yield function is proven in Barlat et al. (2005). Considering a fixed, according to the crystalline structure, 18 anisotropy parameters must be determined. In this context, for sheet metal forming applications, it is recommended to use the yield stresses and the anisotropy coefficients obtained from the uniaxial tensile test for 7 directions in the plane of the sheet (from rolling direction to transverse direction in 15° increments), plus the biaxial yield stress. As for the remaining data, Barlat et al. (2005) suggested

the use of polycrystal simulations to determine the yield stress for uniaxial tension at 45º between the rolling and the normal direction and between the transverse and the normal direction, and for simple shear in the RD-ND and TD-ND planes, for instance. If no crystallographic texture results are available, it is recommended to consider the isotropic values for the out-of-plane properties, being this the most used approach. In that case, the number of anisotropy parameters reduces from 18 to 14.

2.3.2.3. Karafillis and Boyce (1993)

The KB93 yield criterion (Karafillis and Boyce, 1993) was developed introducing anisotropy into the Hosford's isotropic yield criterion, using also a linear transformation of the stress tensor. It can be considered a generalization of the YLD91 and is given by

$$(1-c)\phi_1 + c\frac{3^{2k}}{2^{2k-1}+1}\phi_2 = 2Y^{2k}, \tag{2.36}$$

where $c \in [0,1]$ is a weighting parameter, $2k$ is an isotropic exponent, such that k must be a positive integer to guarantee convexity. ϕ_1 and ϕ_2 are then defined as

$$\phi_1 = (s_1 - s_2)^{2k} + (s_2 - s_3)^{2k} + (s_3 - s_1)^{2k}, \tag{2.37}$$

$$\phi_2 = |s_1|^{2k} + |s_2|^{2k} + |s_3|^{2k}, \tag{2.38}$$

where s_1, s_2 and s_3 are the principal values of $\mathbf{s}$ as in YLD91. When $k = 1$ in Eq. (2.37), it corresponds to the von Mises yield surface whereas when $k \to \infty$ it corresponds to the Tresca one. When $k = 1$ the yield surface of Eq. (2.38) also corresponds to the von Mises yield surface whereas when $k \to \infty$ it corresponds to the upper bound limit surface, similar in shape to the Tresca one, but located outside the one defined by the von Mises yield criterion. By varying the value of the mixing factor c, a family of yield surfaces is created, sweeping the space between the two bounds set by the selection of k. In this case, the number of anisotropy parameters is the same as for the YLD91 with the addition of the weighting parameter c and the exponent k.

Figure 2.14 and Figure 2.15 present the KB93 yield surfaces and in-plane *r*-values and yield stresses directionalities, respectively, for both the AKDQ and AA2090-T3

aluminum alloy. Note that the results were obtained assuming that $k = 1$. Thus, the resulting in-plane orthotropic behavior and the yield surfaces are similar to the ones obtained with the Hill'48 yield criterion (see Figure 2.9 and Figure 2.10).

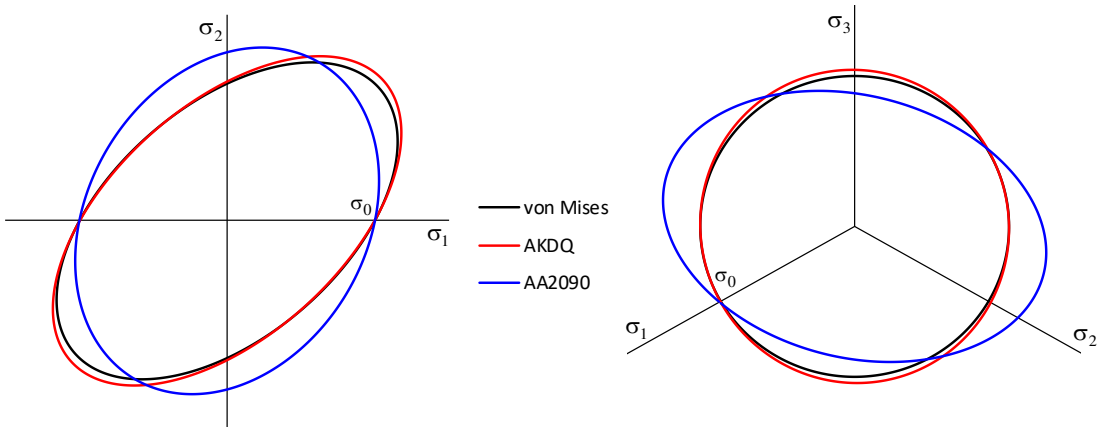

Figure 2.14. Normalized anisotropic KB93 yield surfaces in the $\sigma_1 - \sigma_2$ plane (left) and π-plane (right), for the AKDQ steel and AA2090-T3 aluminum alloy.

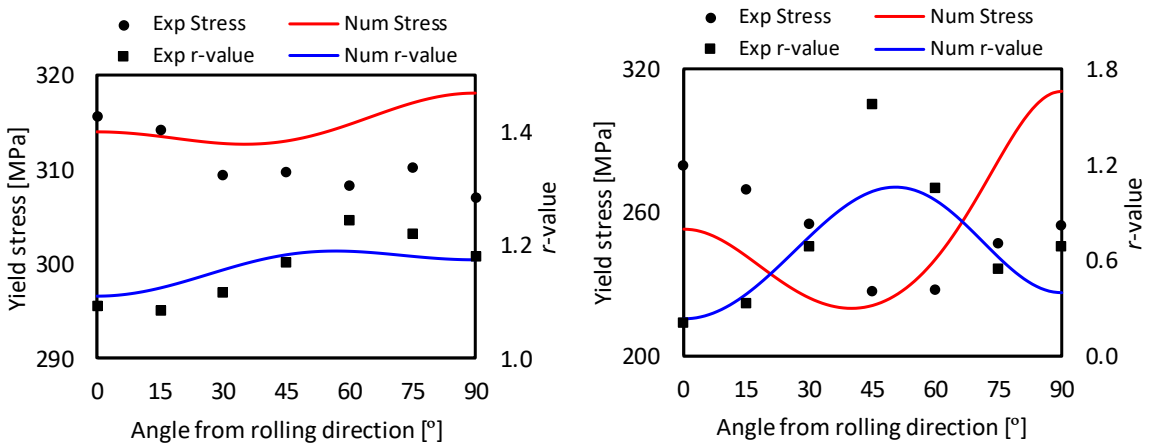

Figure 2.15. Experimental and KB93 predicted yield stresses and *r*-values for the (a) AKDQ steel and (b) AA2090-T3 aluminum alloy.

2.3.2.4. Drucker + L (2001)

This yield criterion, proposed by Cazacu and Barlat (2001), is an extension of the Drucker's isotropic criterion (see section 2.3.1.3) to anisotropy using the IPE stress state, *i.e.* using the linear transformation proposed by Karafillis and Boyce, (1993), to the deviatoric stress tensor. The corresponding expression for the potential is given by

$$\left[\frac{1}{2}tr\left(\mathbf{s}^2\right)\right]^3 - c\left[\frac{1}{3}tr\left(\mathbf{s}^3\right)\right]^2 = 27\left(\frac{Y}{3}\right)^6 \tag{2.39}$$

where $\mathbf{s} = \mathbf{L}\boldsymbol{\sigma}'$ and c is a weighting parameter. The isotropic Drucker yield criterion is recovered when considering $c_i = 1.0 \ \ (i = 1 \text{ to } 6)$. In this case, the parameters to be determined are c and those from the linear transformation (same as Eq. (2.28)). For thin metallic sheets c_1, c_2, c_3 and c_6 are the parameters to be determined, assuming $c_4 = c_5 = 1.0$. The convexity of the yield surface is assured since the linear transformation does not affect convexity. The only necessary condition is the same as for the isotropic case, *i.e.* $c \in [-3.375,\ 2.250]$.

Figure 2.16 and Figure 2.17 present the Drucker+L yield surfaces and in-plane *r*-values and yield stresses directionalities, respectively, for both the AKDQ and AA2090-T3 aluminum alloy. When comparing with the YLD91 yield criterion, for the AKDQ, the Drucker+L renders an improved description of the in-plane yield stress directionalities, resulting in a yield surface quite different from the von Mises one. For the aluminum alloy, the trend for the orthotropic in-plane behavior is very similar, although the shape of the yield surface is sharper for the Drucker+L. This highlights that the yield surface's shape is not fully constrained by the yield stress and *r*-value directionalities.

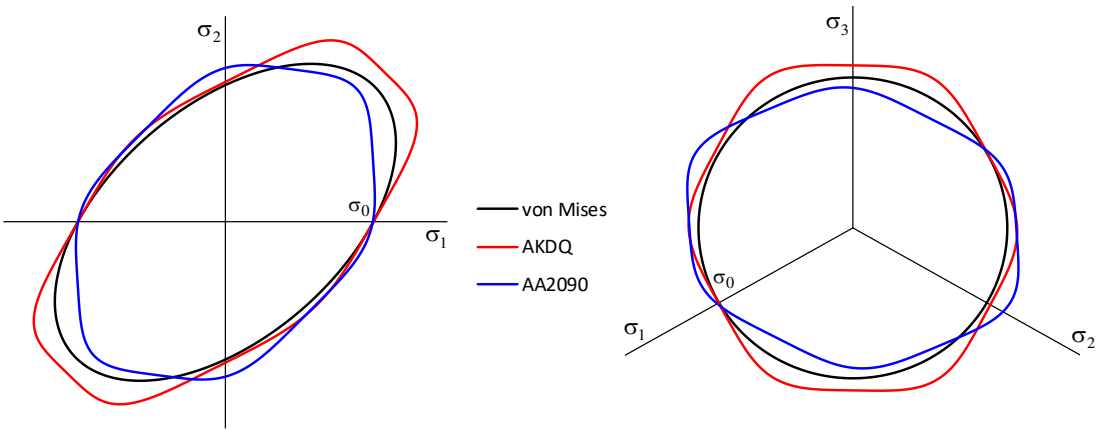

Figure 2.16. Normalized anisotropic Drucker+L yield surfaces in the $\sigma_1 - \sigma_2$ plane (left) and π-plane (right) for the AKDQ steel and AA2090-T3 aluminum alloy.

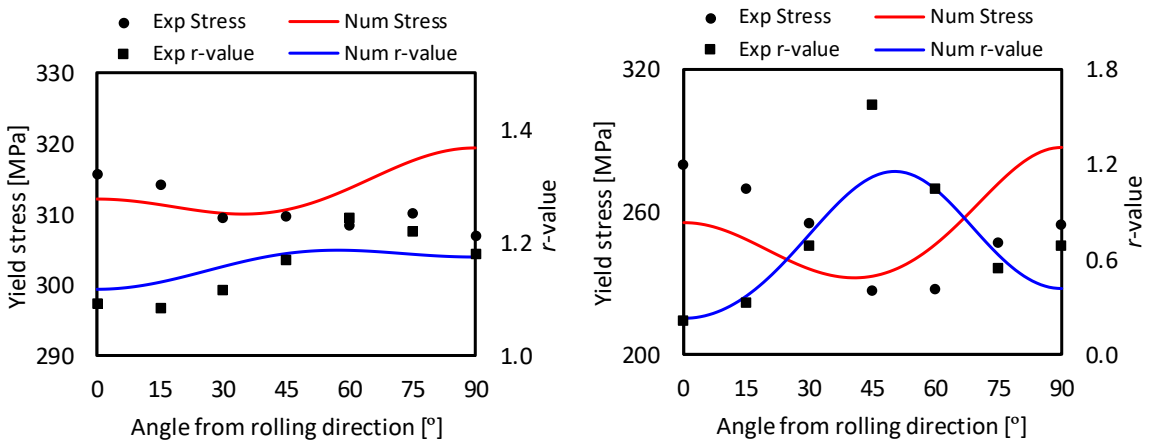

Figure 2.17. Experimental and Drucker+L predicted yield stresses and *r*-values for the (a) AKDQ steel and (b) AA2090-T3 aluminum alloy.

2.3.2.5. Cazacu & Barlat (2001)

Cazacu and Barlat (2001) proposed another yield criterion (CB2001) based on the Drucker isotropic criterion (see section 2.3.1.3). In this case, the approach adopted is the generalizing to orthotropy of the invariants of the deviatoric stress tensor, resulting in the expression

$$\left(J_2^0\right)^3 - c\left(J_3^0\right)^2 = 27\left(\frac{Y}{3}\right)^6, \tag{2.40}$$

where c is a weighting parameter and J_2^0 and J_3^0 are, respectively, the generalized to orthotropy second and third invariants of the deviatoric Cauchy stress tensor $\boldsymbol{\sigma}'$, which can be defined as

$$\begin{aligned} J_2^0 = {} & \frac{a_1}{6}(\sigma_{11}-\sigma_{22})^2 + \frac{a_2}{6}(\sigma_{11}-\sigma_{33})^2 + \frac{a_3}{6}(\sigma_{11}-\sigma_{33})^2 \\ & + a_4\sigma_{12}^2 + a_5\sigma_{13}^2 + a_6\sigma_{23}^2 \end{aligned}, \tag{2.41}$$

where a_i $(i = 1 \text{ to } 6)$ are the anisotropy parameters related to the generalized second invariant and

$$
\begin{aligned}
J_3^0 = {} & (1/27)(b_1+b_2)\sigma_{11}^3 + (1/27)(b_3+b_4)\sigma_{22}^3 \\
& + (1/27)[2(b_1+b_4)-b_2-b_3]\sigma_{33}^3 \\
& - (1/9)(b_1\sigma_{22}+b_2\sigma_{33})\sigma_{11}^2 - (1/9)(b_3\sigma_{33}+b_4\sigma_{11})\sigma_{22}^2 \\
& - (1/9)[(b_1-b_2+b_4)\sigma_{11}+(b_1-b_3+b_4)\sigma_{22}]\sigma_{33}^2 \\
& + (2/9)(b_1+b_4)\sigma_{11}\sigma_{22}\sigma_{33} \\
& - \left(\sigma_{13}^2/3\right)[2b_9\sigma_{22}-b_8\sigma_{33}-(2b_9-b_8)\sigma_{11}] \\
& - \left(\sigma_{12}^2/3\right)[2b_{10}\sigma_{33}-b_5\sigma_{22}-(2b_{10}-b_5)\sigma_{11}] \\
& - \left(\sigma_{23}^2/3\right)[(b_6-b_7)\sigma_{11}-b_6\sigma_{22}-b_7\sigma_{33}] + 2b_{11}\sigma_{12}\sigma_{23}\sigma_{13}
\end{aligned}
\quad , \qquad (2.42)
$$

where b_i $(i=1 \text{ to } 11)$ are the anisotropy parameters associated to the generalized third invariant. Thus, the proposed yield criterion involves 18 anisotropy parameters for triaxial stress states. For metal sheets, the number of parameters reduces to 11, since parameters a_5, a_6 and b_k $(k=6,7,8,9,11)$ cannot be evaluated. Thus, the corresponding isotropic values are adopted, *i.e.* 1.0. The remaining parameters can be determined based on experimental results obtained from uniaxial tensile tests (yield stresses and anisotropy coefficients) as well as from the biaxial tensile yield stress, σ_b. When considering an isotropic material behavior, the convexity is assured for $c \in [-3.375, 2.250]$, as for the Drucker yield criterion. However, for anisotropic materials, the convexity conditions are not yet established, reason for which the parameters identification strategy should contemplate surface convexity tests, in order to penalize non-convex solutions (see further details in Appendix A).

Figure 2.18 and Figure 2.19 present the CB2001 yield surfaces and in-plane *r*-values and yield stresses directionalities, respectively, for both the AKDQ and AA2090-T3 aluminum alloy. Figure 2.19 highlights the flexibility of this yield criterion, particularly for the AKDQ steel. For the aluminum alloy, the description of the in-plane orthotropic behavior can be enhanced by adjusting the weighting coefficients in the identification procedure, as it will be shown in Chapter 4.

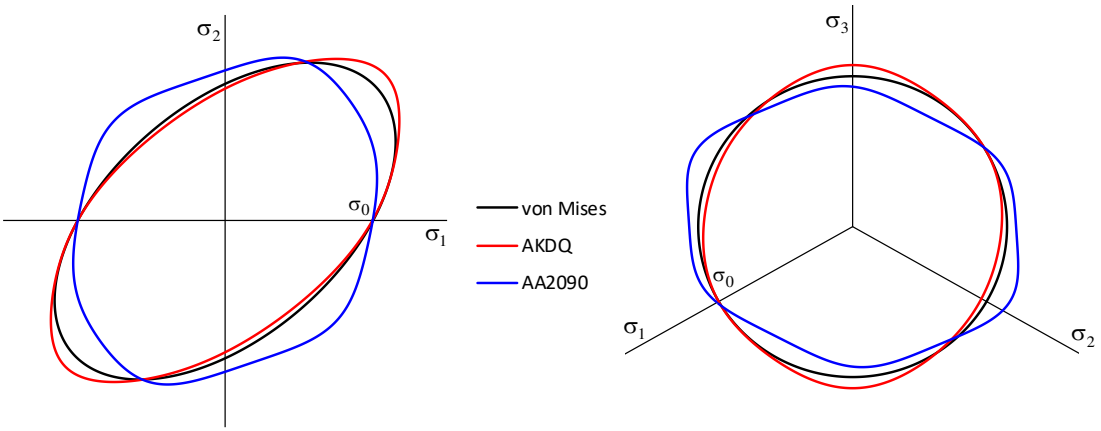

Figure 2.18. Normalized anisotropic CB2001 yield surfaces in the $\sigma_1 - \sigma_2$ plane (left) and π-plane (right) for the AKDQ steel and AA2090-T3 aluminum alloy.

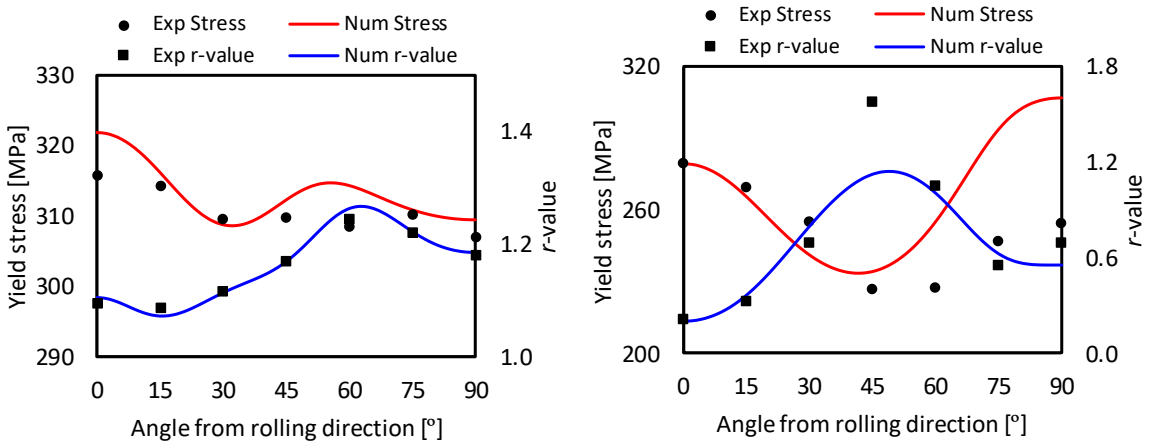

Figure 2.19. Experimental and CB2001 predicted yield stresses and *r*-values for the (a) AKDQ steel and (b) AA2090-T3 aluminum alloy.

2.3.2.6. Cazacu yield criteria accounting SD effects

Cazacu and Barlat (2004) proposed an anisotropic yield criterion enabling also the modeling of strength differential effects, in the form

$$\left(J_2^0\right)^{3/2} - cJ_3^0 = \tau_Y{}^3, \tag{2.43}$$

where J_2^0 and J_3^0 are, respectively, the generalized to orthotropy second and third invariants of the deviatoric stress tensor $\boldsymbol{\sigma}'$, defined as in Eq. (2.41) and Eq. (2.42). τ_Y

is the yield stress in pure shear and c is a material constant that can be expressed in terms of the uniaxial yield stresses in tension, σ^{T}, and compression, σ^{C}, such that

$$c = \frac{3\sqrt{3}\left[\left(\sigma^{\mathrm{T}}\right)^3 - \left(\sigma^{\mathrm{C}}\right)^3\right]}{2\left[\left(\sigma^{\mathrm{T}}\right)^2 + \left(\sigma^{\mathrm{C}}\right)^2\right]}. \tag{2.44}$$

Note that, for $c = 0$, *i.e.* equal yield stresses in tension and compression, the proposed criterion reduces to the von Mises yield criterion. Also, in order to guarantee convexity for the isotropic form of this yield criterion, $c \in \left[-3\sqrt{3}/2,\ 3\sqrt{3}/2\right]$ as proven in Cazacu and Barlat (2004).

Cazacu, Plunkett & Barlat (2006) proposed a new isotropic yield criterion able to describe the strength-differential effect, in the form

$$Y = B\left[\left(\left|s_1\right| - k\, s_1\right)^a + \left(\left|s_2\right| - k\, s_2\right)^a + \left(\left|s_3\right| - k\, s_3\right)^a\right]^{\frac{1}{a}}, \tag{2.45}$$

where s_1, s_2 and s_3 are the principal values of $\mathbf{s} = \boldsymbol{\sigma}'$. The coefficient k allows describing the strength differential effects and a is a positive integer related with the degree of homogeneity. Considering a fixed value of the parameter a, the coefficient k gives a direct measure of the ratio between tensile and compressive yield stresses, as

$$k = \frac{1-h}{1+h}, \text{ with } h = \left[\frac{2^a - 2\left(\dfrac{\sigma^{\mathrm{T}}}{\sigma^{\mathrm{C}}}\right)^a}{\left(2\dfrac{\sigma^{\mathrm{T}}}{\sigma^{\mathrm{C}}}\right)^a - 2}\right]^{1/a}, \tag{2.46}$$

with σ^{T} and σ^{C} the uniaxial yield stresses in tension and compression, respectively. For $a = 2$ and $k = 0$, the von Mises yield criterion is recovered. As for convexity, it is guaranteed for any integer $a \geq 2$ and $k \in \left[-1,1\right]$. Figure 2.20 shows the effect of the k parameter on the yield surfaces shape. For $k < 0$, the yield *locus* is interior to the von Mises one, while for $k > 0$ it is interior; both have a triangular shape with rounded corners. In fact, for $k < 0$, the yield stress in compression is always higher than the tensile one, while the opposite is observed for $k > 0$.

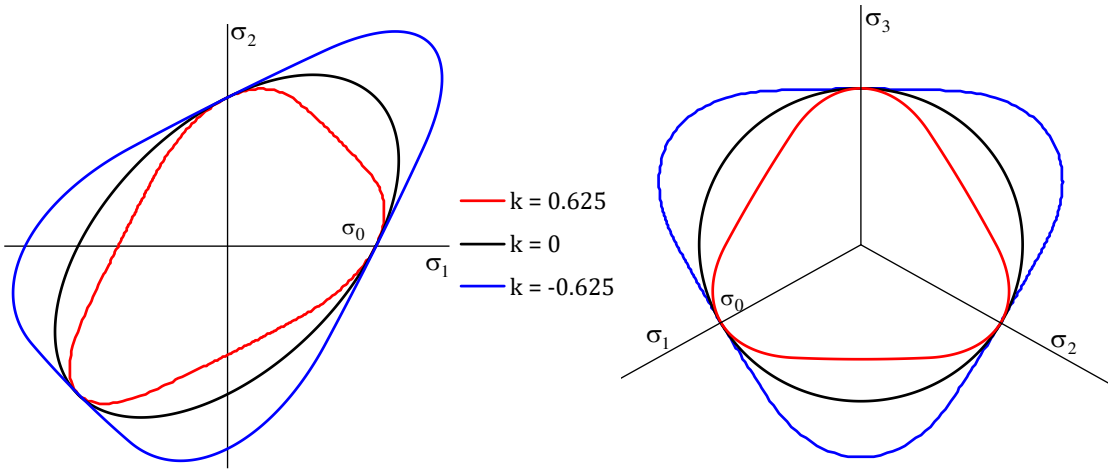

Figure 2.20. Normalized isotropic CPB06 yield surfaces in the $\sigma_1-\sigma_2$ plane (left) and π-plane (right) for different values of k.

The extension of this yield criterion to orthotropy, designated CPB06, is performed applying a linear transformation on the deviatoric stress tensor, for the function given in Eq. (2.45), where s_1, s_2 and s_3 are the principal values of $\mathbf{s}=\mathbf{C}\boldsymbol{\sigma}'$. $\mathbf{C}$ is a constant 4th-order tensor which, for 3-D stress conditions, involves 9 independent anisotropy coefficients and, assuming the Voigt notation, is given by

$$\mathbf{C}=\begin{bmatrix} C_{11} & C_{12} & C_{13} & 0 & 0 & 0 \\ C_{12} & C_{22} & C_{23} & 0 & 0 & 0 \\ C_{13} & C_{23} & C_{33} & 0 & 0 & 0 \\ 0 & 0 & 0 & C_{44} & 0 & 0 \\ 0 & 0 & 0 & 0 & C_{55} & 0 \\ 0 & 0 & 0 & 0 & 0 & C_{66} \end{bmatrix}. \tag{2.47}$$

In Eq. (2.45), B is a constant defined such that Y reduces to the tensile yield stress in the rolling direction, and is given by

$$B=\left[\frac{1}{\left(|\phi_1|-k\,\phi_1\right)^a+\left(|\phi_2|-k\,\phi_2\right)^a+\left(|\phi_3|-k\,\phi_3\right)^a}\right]^{\frac{1}{a}}, \tag{2.48}$$

with

$$\phi_i=(2/3)C_{i1}-(1/3)C_{i2}-(1/3)C_{i3} \text{ for } i=1,2,3. \tag{2.49}$$

Again, for $a = 2$, $k = 0$ and $\mathbf{C}$ equal to the 4th-order identity tensor, the von Mises yield criterion is recovered. In case of thin metallic sheets, the parameters $C_{44} = C_{55} = 1.0$, corresponding to the isotropic values. Moreover, it is recommended to consider C_{11} always equal to 1.0 due to the homogeneity of the criterion. The adoption of this condition eliminates the possibility of obtaining non-unique sets of parameters, as it will be discussed in Chapter 4. Therefore, the total number of anisotropy parameters to identify is 6 plus the k value. Note that, in case of anisotropic materials, the physical meaning of the k value is lost. Moreover, the a also needs to be selected.

Figure 2.21 and Figure 2.22 present the CPB06 yield surfaces and in-plane *r*-values and yield stresses directionalities, respectively, for both the AKDQ and AA2090-T3 aluminum alloy. It should be mentioned that the results were obtained considering that $a = 2$. For the AKDQ, there is no data available regarding uniaxial compression tests ($k = 0$). Therefore, the CPB06 leads to a yield surface and in-plane directionalities similar to the ones previously reported for less flexible yield criteria (see, *e.g.* Figure 2.9 and Figure 2.10). For the AA2090-T3, is clearly visible both in the yield stress and *r*-values in-plane directionalities. Nonetheless, the results in tension are close to the ones obtained from less flexible yield criteria.

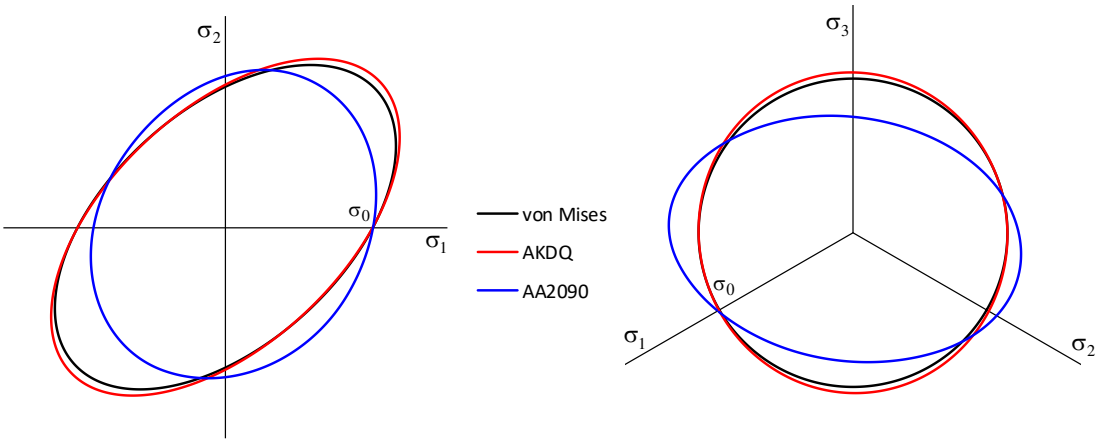

Figure 2.21. Normalized anisotropic CBP06 yield surfaces in the $\sigma_1 - \sigma_2$ plane (left) and π-plane (right) for the AKDQ steel and AA2090-T3 aluminum alloy.

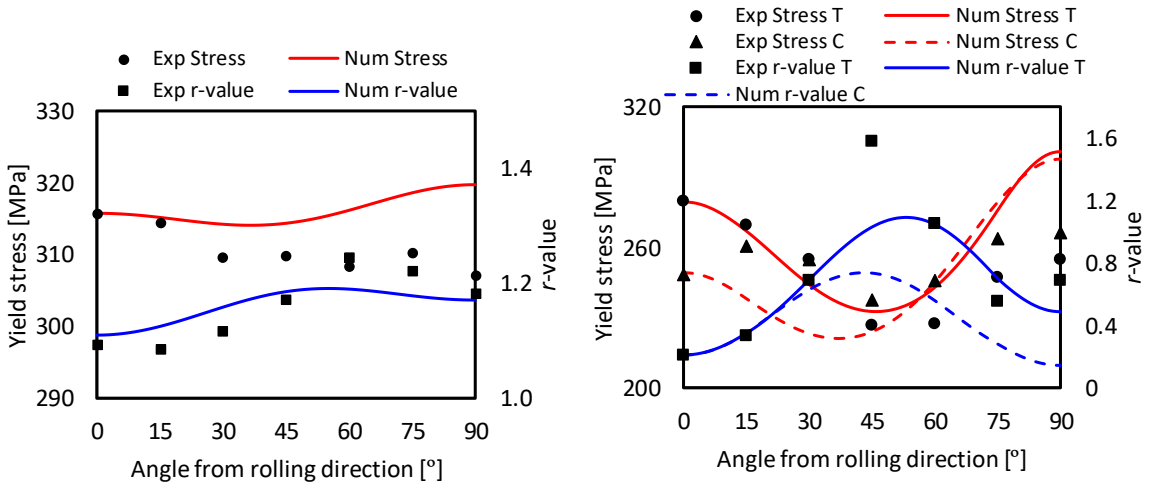

(a) (b)

Figure 2.22. Experimental and CPB06 predicted yield stresses and *r*-values for the (a) AKDQ steel and (b) AA2090-T3 aluminum alloy.

Plunkett et al. (2008) proposed an extension of the CPB06 yield criterion, denoted CPB06ex2, considering two linear transformations, thus effectively doubling the number of anisotropy parameters. The higher number of anisotropy parameters allows a better description of the experimental material's mechanical behavior. In this case, the yield criterion is given in the form

$$Y = B\left[\begin{array}{l}\left(\left|s_1\right|-k\,s_1\right)^a+\left(\left|s_2\right|-k\,s_2\right)^a+\left(\left|s_3\right|-k\,s_3\right)^a \\ +\left(\left|s'_1\right|-k'\,s'_1\right)^a+\left(\left|s'_2\right|-k'\,s'_2\right)^a+\left(\left|s'_3\right|-k'\,s'_3\right)^a\end{array}\right]^{\frac{1}{a}}, \tag{2.50}$$

where B remains a constant defined such that Y reduces to the tensile yield stress in the rolling direction and is now given by

$$B = \left[\frac{1}{\begin{array}{l}\left(\left|\phi_1\right|-k\,\phi_1\right)^a+\left(\left|\phi_2\right|-k\,\phi_2\right)^a+\left(\left|\phi_3\right|-k\,\phi_3\right)^a \\ +\left(\left|\phi'_1\right|-k'\,\phi'_1\right)^a+\left(\left|\phi'_2\right|-k'\,\phi'_2\right)^a+\left(\left|\phi'_3\right|-k'\,\phi'_3\right)^a\end{array}}\right]^{\frac{1}{a}}, \tag{2.51}$$

with the same definition for the ϕ_i, $i=1,2,3$ as in Eq. (2.49).

$$\phi'_i = (2/3)C'_{i1} - (1/3)C'_{i2} - (1/3)C'_{i3} \text{ for } i=1,2,3, \tag{2.52}$$

and the tensor $\mathbf{C}'$ is a constant 4th-order tensor given by

$$\mathbf{C}' = \begin{bmatrix} C'_{11} & C'_{12} & C'_{13} & 0 & 0 & 0 \\ C'_{12} & C'_{22} & C'_{23} & 0 & 0 & 0 \\ C'_{13} & C'_{23} & C'_{33} & 0 & 0 & 0 \\ 0 & 0 & 0 & C'_{44} & 0 & 0 \\ 0 & 0 & 0 & 0 & C'_{55} & 0 \\ 0 & 0 & 0 & 0 & 0 & C'_{66} \end{bmatrix}. \tag{2.53}$$

The convexity is still guaranteed for $a \geq 2$, $k \in [-1,1]$ and $k' \in [-1,1]$ since the use of one or several linear transformations does not affect convexity of the yield function (Eggleston, 1958; Rockafellar, 1972). For $\mathbf{C} = \mathbf{C}'$ and $k = k'$, the CPB06ex2 yield criterion reduces to the original form of the CPB06.

Figure 2.23 and Figure 2.24 present the CPB06ex2 yield surfaces and in-plane *r*-values and yield stresses directionalities, respectively, for both the AKDQ and AA2090-T3 aluminum alloy. It should be mentioned that the results were obtained considering that $a = 2$. When comparing with the CPB06, for the AKDQ, no differences are visible in both the yield *locus* and yield stress and *r*-values in-plane directionalities. For the AA2090-T3, only a slight improvement in the description of both the yield tensile yield stress and *r*-values. The adoption of $a = 2$ seems to limit this yield criterion's flexibility. Also, the selection of the weighting coefficients in the identification procedure can also help to improve the description of the material's behavior, as it will be discussed in Chapter 4.

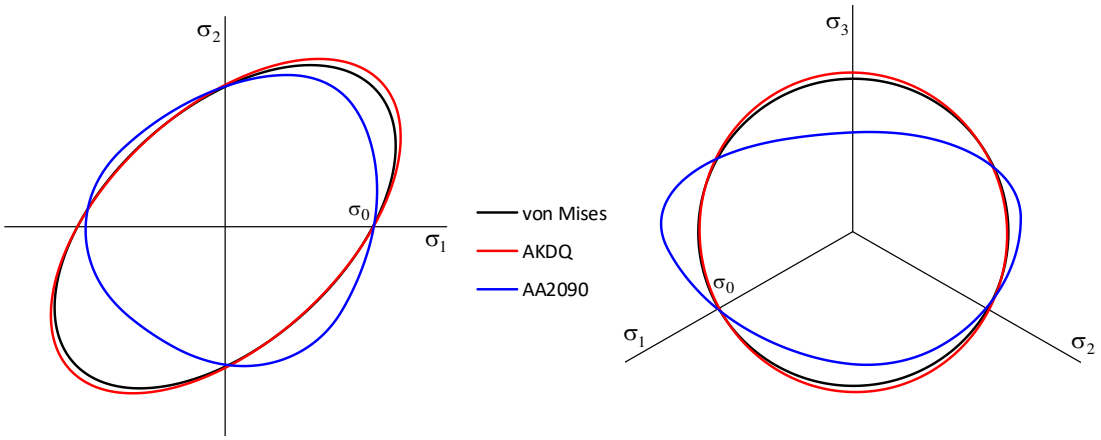

Figure 2.23. Normalized anisotropic CPB06ex2 yield surfaces in the $\sigma_1 - \sigma_2$ plane (left) and π-plane (right) for the AKDQ steel and AA2090-T3 aluminum alloy.

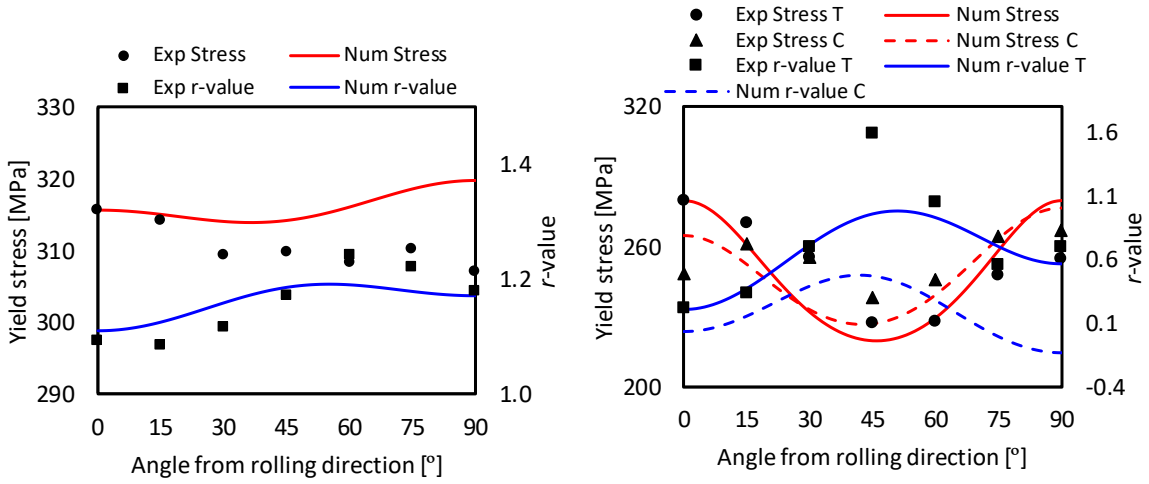

(a) (b)

Figure 2.24. Experimental and CPB06ex2 predicted yield stresses and *r*-values for the (a) AKDQ steel and (b) AA2090-T3 aluminum alloy.

2.3.2.7. Yoshida (2013)

Yoshida et al. (2013) proposed a yield criterion based on the sum of a number of components of the Drucker+L yield criterion (see section 2.3.2.4) in the form

$$\frac{27}{n}\sum_{i=1}^{n}\left\{\left(\frac{1}{2}\mathrm{tr}\left(\mathbf{s}^{(i)}\right)^2\right)^3 - c^{(i)}\left(\frac{1}{3}\mathrm{tr}\left(\mathbf{s}^{(i)}\right)^3\right)^2\right\} = Y^6, \tag{2.54}$$

where $i = 1,...,n$ are the components of the yield criterion. Each tensor $\mathbf{s}^{(i)}$ is obtained through the linear transformation $\mathbf{s}^{(i)} = \mathbf{L}^{(i)}\boldsymbol{\sigma}$ where $\mathbf{L}^{(i)}$ is the 4th-order tensor given by

$$\mathbf{L}^{(i)} = \begin{bmatrix} \left(c_2^{(i)} + c_3^{(i)}\right)/3 & -c_3^{(i)}/3 & -c_2^{(i)}/3 & 0 & 0 & 0 \\ -c_3^{(i)}/3 & \left(c_3^{(i)} + c_1^{(i)}\right)/3 & -c_1^{(i)}/3 & 0 & 0 & 0 \\ -c_2^{(i)}/3 & -c_1^{(i)}/3 & \left(c_1^{(i)} + c_2^{(i)}\right)/3 & 0 & 0 & 0 \\ 0 & 0 & 0 & c_4^{(i)} & 0 & 0 \\ 0 & 0 & 0 & 0 & c_5^{(i)} & 0 \\ 0 & 0 & 0 & 0 & 0 & c_6^{(i)} \end{bmatrix}, \quad (2.55)$$

Such as in the Drucker+L yield criterion, for thin metallic sheets, c_1, c_2, c_3 and c_6 are the parameters to be determined for each $\mathbf{L}^{(i)}$, since $c_4 = c_5 = 1.0$. However, the increased number of anisotropy parameters, which gives a higher flexibility, demands a higher number of experimental data for the identification process. The strategy adopted in the development of this yield criterion can be applied to others based on linear transformation.

2.4. Final Remarks

Some of the models used to describe the yield surface and the hardening behavior of metallic materials, when subjected to cold plastic deformation, were reviewed.

The adoption of new materials with increasingly complex behaviors, as well as the demand for higher accuracy on the numerical predicted, are the main factors for the development of models with increased flexibility, aimed to accurately and simultaneously describe the experimentally observed material behavior.

Choosing a constitutive model and, in particular, a yield criterion is closely related to the observed material behavior to be modeled, as well as the accuracy required and allowed computational time. For simple processes, a simple model may be sufficient if, for example, the material is highly isotropic or no strain path changes occur. In this

context, the Hill'48 is still frequently used for industrial applications with its general acceptance resulting from its mathematical simplicity and direct relation with the classical mechanical tests usually performed. Moreover, the availability of experimental data is a constraint when selecting a constitutive model. Table 2.1 highlights the number of parameters involved in the definition of each yield criterion implemented in the DD3IMP in-house code. Note that some of these parameters are predefined by the user, whereas the remaining need to be identified, requiring a set of experimental data, providing enough information to allow their identification (at least an equal number of mechanical and anisotropy parameters).

The following chapter comprises some classical material parameters identification procedures, including the most widely experimental tests for data acquisition and their correspondent advantages and drawbacks.

Table 2.1. Yield criteria implemented in the DD3IMP in-house code and respective parameters for the general 3D case as well as for thin metallic sheets.

	Number of parameters: designation adopted		
Author, year	General 3D case	Thin metallic sheets	SD effect
Hill, 1948	6: F, G, H, L, M and N	4: F, G, H and N	
Barlat, 1991	7: c_i $(i=1,\ldots,6)$ and m	5: c_1, c_2, c_3, c_6 and m	
Karafillis and Boyce, 1993	8: c_i $(i=1,\ldots,6)$, c and k	6: c_1, c_2, c_3, c_6, c and k	
Drucker+L, 2001	7: c_i $(i=1,\ldots,6)$, c	5: c_1, c_2, c_3, c_6, c	
Cazacu and Barlat, 2001	18: a_i $(i=1 \text{ to } 6)$, b_i $(i=1 \text{ to } 11)$, c	11: a_i $(i=1 \text{ to } 4)$, b_i $(i=1 \text{ to } 5)$, b_{10}, c	
Cazacu and Barlat, 2004	18: a_i $(i=1 \text{ to } 6)$, b_i $(i=1 \text{ to } 11)$, c	11: a_i $(i=1 \text{ to } 4)$, b_i $(i=1 \text{ to } 5)$, b_{10}, c	X
Cazacu, Plunkett and Barlat, 2006	10: C_{12}, C_{13}, C_{22}, C_{23}, C_{33}, C_{44}, C_{55}, C_{66}, k and a	8: C_{12}, C_{13}, C_{22}, C_{23}, C_{33}, C_{66}, k and a	X
Plunkett, Cazacu and Barlat, 2008	19: C_{12}, C_{13}, C_{22}, C_{23}, C_{33}, C_{44}, C_{55}, C_{66}, C'_{12}, C'_{13}, C'_{22}, C'_{23}, C'_{33}, C'_{44}, C'_{55}, C'_{66}, k, k' and a	15: C_{12}, C_{13}, C_{22}, C_{23}, C_{33}, C_{66}, C'_{12}, C'_{13}, C'_{22}, C'_{23}, C'_{33}, C'_{66}, k, k' and a	X

(Page intentionally left blank)

Chapter 3

Material Parameters Identification

This chapter presents an overview of the commonly adopted parameters identification procedures for constitutive models for metal sheets, i.e. classical and inverse identification strategies are briefly presented. Particular emphasis is given to classical identification procedures used to identify material parameters for yield criteria, since this was one of the focuses of this work. In this context, first, an overview of the objective function used is presented, proceeded by the optimization algorithm adopted to its minimization. Furthermore, the most used experimental test are presented while discussing their advantages and disadvantages in the scope of sheet metal forming applications.

(Page intentionally left blank)

3.1. Introduction

The accuracy of the numerical results of sheet metal forming processes depends on the ability of the constitutive model selected for describing the material's behavior. Thus, the model parameters should be determined such that the predicted mechanical behavior describes the observed one as close as possible. As previously mentioned, the constitutive model is a combination of a hardening law and a yield criterion, which, assuming an associated flow rule, describes both the orthotropic behavior and the plastic potential. Typically, for metallic sheets, the shape of the *yield locus* is assumed constant, *i.e.* the orthotropic behavior is constant, while its evolution is described by the hardening law. Thus, the constitutive parameters identification procedure should assure that the yield criterion enables an accurate description of all the experimental flow curves when using the adjusted hardening law. This is exemplified in Figure 3.1 (a), where several stress-strain curves are presented, for different strain paths. The use of an appropriate hardening law, combined with a yield criterion, should enable the description of all the experimental results for the different strain paths (see Figure 3.1 (b)).

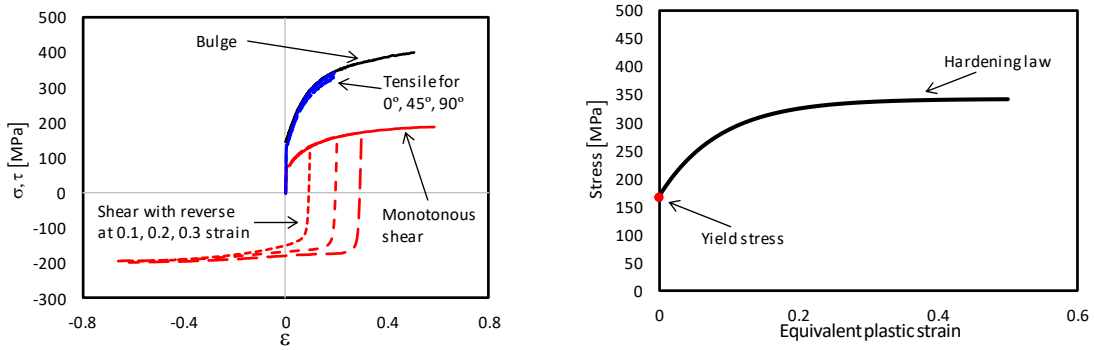

(a) (b)

Figure 3.1. (a) Experimental stress-strain curves obtained from different tests and (b) example of an adjusted hardening law, enabling the description of the experimental results when combined with an appropriate yield criterion.

To classically evaluate the material orthotropic behavior, it is necessary to perform, at least, uniaxial tensile tests at the RD, 45º and TD, enabling the experimental

evaluation of the flow curves as well as the anisotropy parameters. This information allows determining if the material presents, or not, strong in-plane directionalities of both the yield stress and *r*-values, *i.e.* if it is necessary to adopt an anisotropic yield criterion or not. When using anisotropic yield criteria, different strategies can be adopted for the parameters identification: (i) the hardening law is identified first and the yield criterion is adjusted accordingly (*e.g.* 3DS, 2004); (ii) the yield criterion is identified first and the hardening law is adjusted accordingly (*e.g.* Chaparro, 2006); and (iii) perform the simultaneous identification of the hardening law and the yield criterion (*e.g.* (Pilvin, 2003)).

In the first case, different approaches can also be adopted, for instance, considering that the hardening law should fit: (a) a pre-selected flow curve, such as the one obtained for the uniaxial tensile test at RD; (b) the average value of the flow curves collected from the same type of test; or (c) the flow curves, assuming isotropic behavior (*e.g.* 3DS, 2004). Then, the parameters of the yield criterion can be identified for the assumed hardening law, considering either the yield stress values (commonly evaluated for 0.2% of plastic strain) or flow stresses for a pre-determined plastic work value (*e.g.* Yoon and Cazacu, 2011).

In the second case, the parameters of the yield criterion are identified considering the yield stress values, commonly considering the normalized values with the yield stress at the RD (*e.g.* Chaparro, 2006). This can be a strong disadvantage when there is an initial evolution of the in-plane flow stresses, since the values considered should be coherent with the *r*-values, which are commonly determined for about 10% of equivalent plastic strain. This could be circumvented assuming the in-plane stress values normalized with a yield stress, generally at the RD, for a pre-determined plastic work value. When adopting a strategy which sequentially identifies the hardening law and yield criterion parameters, or *vice-versa*, an analytical computation of the stress state for a given strain state, and *vice-versa*, can be performed.

In the third case, when performing the simultaneous identification, the use of analytical computations is not straightforward since it is not possible to impose an equivalent plastic strain value corresponding to a certain flow stress, since it depends on the yield criterion parameters. Therefore, in this case, it is common to resort to numerical computations, normally performed considering only one finite element or a

single integration point using numerical time integration procedures (*e.g.* (Pilvin, 2003)).

Whatever the strategy adopted, the calibration of the constitutive model is usually performed solving an optimization problem regarding the minimization of an objective function, which evaluates the difference between the values estimated by the phenomenological constitutive models and the experimental ones. When considering the hardening law, the objective function corresponds to the minimization of the difference between the numerical and the experimental flow curves, obtained from a single or different mechanical tests. For the yield criterion, the objective function should consider the difference, in the stress space, between the numerical and experimental yield stresses as well as the *r*-values (*i.e.* the normal to the surface). Since there are different objectives, both minimization problems could be treated as multi-objective. Nevertheless, since these type of problems are hard to solve, the strategy typically adopted is to use a single objective function, corresponding to the weighted sum of the different objectives. Some authors also adopt sequential procedures, using distinct objective functions in each step of the sequence (see, *e.g.* Prates et al. (2015)).

The use of the weights enables the differentiated treatment of different test results or even of different parts of the flow curve. For instance, some authors always give a reduced weight for the yield stress determined from the shear test (Thuillier and Manach, 2009). Regarding the hardening law, some authors propose a weight based on the flow curve length (Andrade-Campos et al., 2012). Nevertheless, the increasing flexibility and accuracy of the constitutive models leads to an increase in both the number and complexity of the necessary material experimental tests.

For classical identification strategies, the experiments consist of mechanical test where the specimen's geometry guarantees that both the stress and strain fields are homogeneous, with the most common being the tensile, the shear and the biaxial tests. The relatively low uniform strain achieved in the tensile test, as a result of the localization, motivated the development of the shear and the biaxial tests, enabling the identification of the hardening law for higher strain values (Bouvier et al., 2006; Martins et al., 2013). All these tests can be analyzed considering homogeneous conditions, at least in a small portion of the specimen, allowing a stress state that can be directly determined from the loads applied. These experimental tests allow

obtaining the most relevant data for the yield criteria anisotropy parameters identification, *i.e.* the yield stresses and/or anisotropy coefficients. Moreover, it is possible to define the analytical expressions for the test conditions (stress/strain), avoiding the use of FE analysis. The downfall of the shear and the bulge test is the lack of consensus on a global standard, with different laboratories using different specimen's geometries, conditions and even procedures for the results analysis. In fact, difficulties arise in extracting flow curves for a plastically deforming specimen, particularly beyond uniform elongation.

The inverse identification strategies can use conventionally obtained experimental measures, like tool forces and displacements, in the objective function adopted in the identification procedure (Gelin et al., 1994; Gelin and Ghouati, 1995). Moreover, considering heterogeneous deformation and/or strain path changes, by performing tests considering a specimen with a non-standard geometry, it is possible to replicate the conditions usually found during real sheet metal forming processes. The main advantages are the higher amount of data recovered from a single mechanical test and the non-requirement of uniform stress and strain distributions. These inverse strategies can be coupled with measurements of the displacement and/or strain fields, usually performed with a full-field technique (grid methods digital image correlation (DIC) techniques,) in the surface of the sample. This allows retrieving reliable information for non-uniform stress states including post-necking for the calibration of damage models (see *e.g.* Li et al., 2011; Roux and Bouchard, 2015).

In this context, inverse identification strategies can be carried out considering a finite element model updating (FEMU) in which, for a pre-determined test, the numerical results are compared with the experimental ones and the constitutive model's parameters are iteratively updated until achieving a sufficiently accurate fit. This comparison is usually performed using a single objective function, which is a weighted function of both the loads and the full-field measurements. The disadvantages usually pointed to FEMU are the mesh-dependence and the difficulties in the definition of the boundary conditions (Avril et al., 2008).

Inverse techniques that do not require FEA numerical simulations are also used. The virtual fields method (VFM) relies on the virtual work principle expressing the global equilibrium of a solid of any shape. The set of constitutive parameters is

iteratively updated by minimizing the difference between the external work and the internal virtual work of the specimen. One of the main advantages of the VFM method over the FEMU is not requiring a FE numerical model of the test making it less time-consuming. However, the accuracy of the parameters identification depends on the adequate choice of the virtual field. Rossi and Pierron (2012) first applied the virtual fields to anisotropic plasticity and Kim et al. (2014) developed an application to planar anisotropy. VFM can also be applied to the characterization of damage laws as in Notta-Cuvier et al. (2015) in which it was used for the characterization of a fully coupled elastoplastic-damage model for under associated plasticity using the von Mises criterion and a nonlinear hardening law.

Inverse strategies can also be applied to identify crystal plasticity models parameters based on full-field measurements. At the microstructural scale, the use of Scanning Electron Microscope (SEM) imaging provides intragranular DIC measurements with high spatial resolution on the surface of polycrystals that make possible the coupling with crystal plasticity calculations (Guery et al., 2016; Héripré et al., 2007; Lim et al., 2015). Nevertheless, as previously mentioned, the use of this type of constitutive models still leads to very time-consuming numerical simulations.

In the commonly referred as classical identification methodologies, the objective function is defined based on the data acquired from experimental tests (namely tensile, bulge and shear tests) with linear strain paths and homogeneous deformation in the measuring region. Since more flexible yield functions require a higher number of material parameters, a significant number of experimental tests are required. Therefore, inverse identification methodologies have also been proposed, trying to explore the information obtained from more complex experimental tests, which involve non-homogeneous strain fields (see *e.g.* Cooreman et al., 2008; Güner et al., 2012; Pottier et al., 2012; Prates et al., 2015). The characterization of the mechanical behavior of metal sheets limited to a restricted number of tests with linear strain paths and homogeneous deformation can lead to a somewhat incomplete characterization of the overall plastic behavior of the material (Zidane et al., 2010). On the other hand, the classical identification methodologies enable a more detailed control of the error committed for the monotonic strain-paths selected, instead of a global average error. Anyhow, due to several experimental limitations, a fundamental problem with the

phenomenological approach is that most of the stress space is left unexplored when fitting the parameters of the yield function with either classical or inverse methodologies (Zhang et al., 2015). Figure 3.2 presents a schematic resume of the classification adopted in this review, highlighting the correlation between the identification strategy and the type of experimental test adopted.

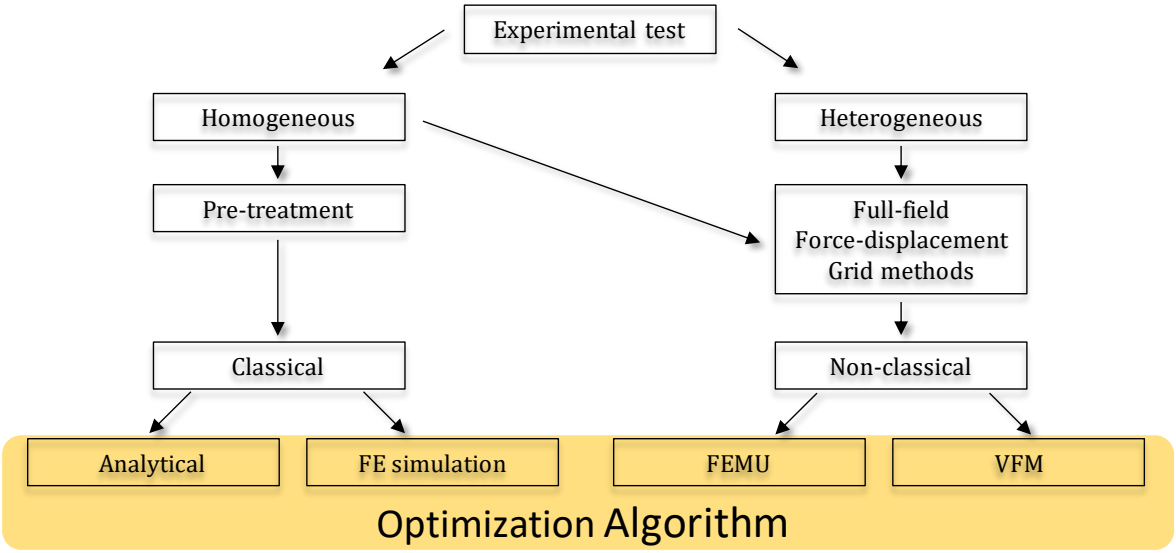

Figure 3.2. Schematic representation of the type of experimental tests and their correlation with both classical and non-classical inverse identification strategies.

In this work, a classical inverse identification methodology was adopted, assuming that the parameters of the hardening law are determined previously to the ones of the yield criterion, based on experimental results of homogeneous tests. Therefore, in the following sections, the objective function and optimization algorithm adopted are discussed, as well as some details concerning the more relevant mechanical tests.

3.2. Objective function

Several objective functions have been proposed in the literature for the identification of both the hardening law and the anisotropy parameters. An objective function should be formulated in order to offer the best fit to the experimental results and guide the process in order to guarantee the success of the optimization methodology. The purpose is to minimize the difference between computed and experimental results of

one or more experiments. This difference, expressed by the objective function, is minimized using optimization algorithms, which automatically operate on the values of the constitutive parameters. Further details concerning the objective functions developed specifically for the hardening law can be found in Andrade-Campos et al. (2012). For the yield criteria, the anisotropy parameters identification procedure is usually performed considering the values of the yield stresses and anisotropy coefficients for tests considering different orientations on the sheet's plane (Banabic et al., 2005).

In this work, the DD3MAT in-house code is used for determining the yield criterion parameters that accurately adjust a given material experimental behavior (Barros et al., 2016). This is relevant since there are several yield criteria implemented in the DD3IMP in-house code (Menezes and Teodosiu, 2000; Neto et al., 2015; Oliveira et al., 2008), some of them involving a large number of parameters (see Table 2.). The procedure adopted is based on the minimization of an objective function, which evaluates the difference between the estimated values and experimental ones, in the form

$$\begin{aligned} F(\mathbf{A}) = & w_{\sigma_\theta^{\mathrm{T}}} \sum_{\theta} \left(\sigma_\theta^{\mathrm{T}}(\mathbf{A}, \bar{\varepsilon}^{\mathrm{p}}) / \sigma_\theta^{\mathrm{T}}(\bar{\varepsilon}^{\mathrm{p}}) - 1 \right)^2 + w_{\sigma_\theta^{\mathrm{C}}} \sum_{\theta} \left(\sigma_\theta^{\mathrm{C}}(\mathbf{A}, \bar{\varepsilon}^{\mathrm{p}}) / \sigma_\theta^{\mathrm{C}}(\bar{\varepsilon}^{\mathrm{p}}) - 1 \right)^2 \\ & + w_{r_\theta^{\mathrm{T}}} \sum_{\theta} \left(r_\theta^{\mathrm{T}}(\mathbf{A}) / r_\theta^{\mathrm{T}} - 1 \right)^2 + w_{r_\theta^{\mathrm{C}}} \sum_{\theta} \left(r_\theta^{\mathrm{C}}(\mathbf{A}) / r_\theta^{\mathrm{C}} - 1 \right)^2 \\ & + w_{\tau_\theta} \sum_{\theta} \left(\tau_\theta(\mathbf{A}, \bar{\varepsilon}^{\mathrm{p}}) / \tau_\theta(\bar{\varepsilon}^{\mathrm{p}}) - 1 \right)^2 + w_{\sigma_{\mathrm{b}}} \left(\sigma_{\mathrm{b}}(\mathbf{A}, \bar{\varepsilon}^{\mathrm{p}}) / \sigma_{\mathrm{b}}(\bar{\varepsilon}^{\mathrm{p}}) - 1 \right)^2 \\ & + w_{r_{\mathrm{b}}} \left(r_{\mathrm{b}}(\mathbf{A}) / r_{\mathrm{b}} - 1 \right)^2 \end{aligned} , \quad (3.1)$$

with $\mathbf{A}$ representing the set of parameters of the respective yield criterion. $\sigma_\theta^{\mathrm{T}}(\bar{\varepsilon}^{\mathrm{p}})$ and $\sigma_\theta^{\mathrm{C}}(\bar{\varepsilon}^{\mathrm{p}})$ are the experimental yield stresses in tension and compression, and r_θ^{T} and r_θ^{C} are the anisotropy coefficients determined in uniaxial tension and compression, respectively. These are obtained from the uniaxial tests for a specific orientation (θ) with respect to the rolling direction. $\tau_\theta(\bar{\varepsilon}^{\mathrm{p}})$ is the experimental yield stress in shear, obtained for a specific orientation (θ) with respect to the rolling direction. σ_{b} is the experimental yield stress obtained from the equibiaxial tensile test

and r_b is the experimental anisotropy coefficient obtained from the disc compression test. $\sigma_\theta^T\left(\mathbf{A},\bar{\varepsilon}^p\right)$, $\sigma_\theta^C\left(\mathbf{A},\bar{\varepsilon}^p\right)$, $r_\theta^T(\mathbf{A})$, $\tau_\theta\left(\mathbf{A},\bar{\varepsilon}^p\right)$, $\sigma_b\left(\mathbf{A},\bar{\varepsilon}^p\right)$ and $r_b(\mathbf{A})$ are the correspondent values predicted from the adopted yield criterion. Such procedure can be considered a generalization of the one proposed by Banabic et al. (2005), where the weighting factors, $w_{\sigma_\theta^T}$, $w_{\sigma_\theta^C}$, $w_{r_\theta^T}$, $w_{r_\theta^C}$, w_{τ_θ}, w_{σ_b} and w_{r_b}, are used to balance the influence of the experimental data. The stress values are evaluated for a pre-determined value of equivalent plastic strain $\bar{\varepsilon}^p$, which is not necessarily null (Khalfallah et al., 2015). Moreover, this value is normally different for each stress path, since it is evaluated for a similar value of plastic work. This enables the correlation with the pre-determined hardening law (Yoon and Cazacu, 2011). In fact, although the different objectives are formulated in normalized form in the objective function, from the author's experience the optimization procedure tends to adjust more easily the *r*-values (when considering an associated flow rule). However, it is very important to capture the yield stress in-plane directionalities, which normally requires the fine-tuning of the weighting coefficients. The selection of the weighting factors is still a manual procedure strongly dependent on the users' expertise, performed based on the analysis of the global trends between the experimental and the numerical results.

3.3. Optimization algorithms

The increasing complexity of the yield criteria results in an enhanced accuracy of sheet metal forming simulation results (Bouvier et al., 2005). However, the cost associated with the parameter identification procedure also increases dramatically, since it becomes computationally more time consuming and requires a large number of costly mechanical tests (Aretz and Barlat, 2013; Cazacu et al., 2006; Grytten et al., 2008). The directional yield stresses, the *r*-values and the biaxial values are all a function of the anisotropy parameters, included in the nonlinear function that defines the yield criteria. The number of anisotropy parameters is always less than the number of experimental values, which results in an over-constrained problem. Thus, in classical

identifications procedures, the parameter identification problem is formulated as a nonlinear optimization problem.

The solving of the optimization problem can be performed considering different methods which can be divided mainly into three groups: (i) Direct search algorithms, (ii) gradient-based algorithms and (iii) nature-based metaheuristics algorithms, which can be applied to different identification methodologies. Direct search algorithms are derivative-free and easy to implement. As its name suggests, these algorithms do not use the information of the derivatives of the objective function. The new solutions are found only based on the value of the objective function on some key points. Gradient-based algorithms, on the other hand, use the information of the derivative of the objective function to update the solution until the convergence criterion is achieved. In fact, several gradient-based algorithms are available, relying only on the first derivative or on both first and second derivatives, which can be evaluated numerically. As for the nature-based metaheuristics algorithms, these are based on the change of a set of initial solutions, generally using a strategy of solutions updating based on analogies with the theory of biological systems evolution such as, *e.g.* genetic algorithm. For the case of evolutionary algorithms, the principle is that stronger individuals tend to pass their information to the next generation while weaker individuals tend to disappear through natural selection (Chaparro et al., 2008). The global idea of any of these algorithms is to update the set of constitutive parameters during the identification procedure, with the type of algorithm selected assuming an important role since it controls the efficiency and, consequently, the result of the optimization process.

The DD3MAT employs an optimization algorithm based on the Nelder–Mead (downhill simplex) algorithm, which has become one of the most widely used direct search methods for nonlinear unconstrained optimization. This type of algorithm, being independent on the gradient of the cost function, tends to be suitable for problems that are non-smooth or non-continuous. It resorts on a spatial approximation to minimize an objective function. Each iteration of a simplex-based direct search method begins with a simplex (a geometric figure in n dimensions of nonzero volume that is the convex hull of $n + 1$ vertices), specified by its $n + 1$ vertices and the associated function values. One or more test points are computed, along with their function values, and the iteration terminates with a new simplex, such that the function values at its

vertices satisfy some form of descent condition compared to the previous simplex (Lagarias et al., 1998).

The algorithm implemented in DD3MAT requires the pre-definition of the range to be considered for each anisotropy parameter. Table 3.1 presents the range considered for each set of parameters, for the respective yield criteria. Typically, the algorithm considers isotropy for the initial solution and builds the vertices for each parameter, in each iteration. The procedure stops when the difference in the objective function for two consecutive iterations reaches a threshold of 10^{-14}, or the maximum number of iterations is attained. The maximum number of iterations is a user-defined parameter given as input at the beginning of the program execution.

Table 3.1. Yield criteria implemented in the DD3MAT in-house code and respective range considered for the parameters of the yield criteria.

Author, year	Anisotropy parameters	User selected parameters
Hill, 1948	$F, G, H, N \in [0,5]$	
Barlat, 1991	$c_1, c_2, c_3, c_4 \in [0,5]$	$m \geq 2$
Karafillis and Boyce, 1993	$c_1, c_2, c_3, c_4 \in [0,5]$ $c \in [0,1]$	$k \geq 1$
Drucker+L, 2001	$c_1, c_2, c_3, c_4 \in [0,5]$ $c \in [-3.375,\ 2.250]$	
Cazacu and Barlat, 2001	$a_i \in [0,5]$ for $(i = 1 \text{ to } 4)$ $b_i \in [-10,10]$ for $(i = 1 \text{ to } 5)$ $b_{10} \in [-10,10]$ $c \in [-3.375,\ 2.250]$	
Cazacu, Plunkett and Barlat, 2006	$C_{12}, C_{13}, C_{23} \in [-5,5]$ $C_{11}, C_{22}, C_{33} \in [-4,6]$ $k \in [-1,1]$	$a \geq 2$
Plunkett, Cazacu and Barlat, 2008	$C_{12}, C_{13}, C_{23} \in [-5,5]$ $C'_{11}, C'_{22}, C'_{33} \in [-4,6]$ $C_{12}, C_{13}, C_{23} \in [-5,5]$ $C'_{11}, C'_{22}, C'_{33} \in [-4,6]$ $k \in [-1,1]$ $k' \in [-1,1]$	$a \geq 2$

3.4. Experimental Tests

To identify the yield criteria parameters, it is necessary to recover the experimentally measured material's behavior. The number and type of experimental tests depend on the constitutive model chosen for the numerical simulation of the forming process, as previously mentioned in Chapter 2. These experimental tests should allow obtaining the most relevant data concerning the anisotropic behavior of the material, *i.e.* the yield stresses and the anisotropy coefficients. Different experimental tests lead to different stress states in the $\sigma_1 - \sigma_2$ plane, as schematically presented in Figure 3.3.

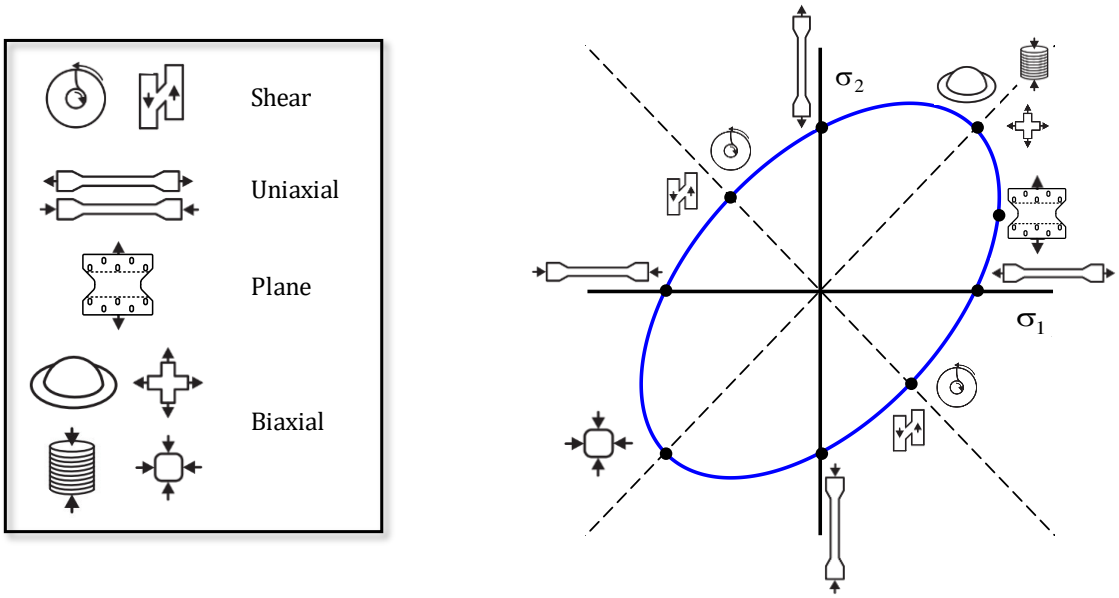

Figure 3.3. Common experimental tests used for sheet metal characterization (adapted from Yin et al., 2014).

In the following section, the most common experimental tests are presented together with the respective experimental data retrieved and some comments concerning their advantages and limitations.

3.4.1. Uniaxial Tensile Test

The most common experimental test for metal sheet's characterization is the uniaxial tensile test, since it is a normalized test, easy to perform and presents good reproducibility up to necking. This test is mainly used to determine the flow curves for

a uniaxial tensile stress state for a specific orientation, θ, with respect to the rolling direction, as schematically shown in Figure 3.4.

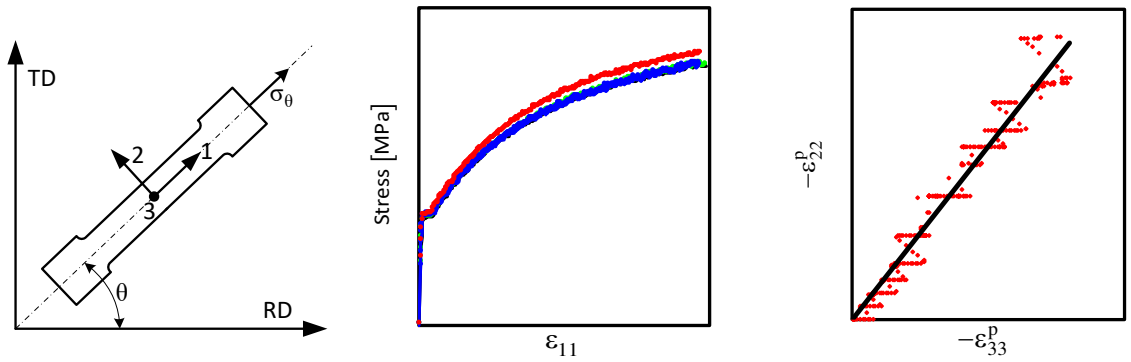

Figure 3.4. (a) Specimen for the tensile test performed for a direction θ in the plane of the metal sheet and corresponding (b) experimental stress-strain curves for three directions and (c) experimental strains for *r*-value calculation.

This test has as advantage the homogeneous deformation of the specimen's center until necking, which allows an accurate evaluation of the material behavior up to this point (maximum of about 30% strain, depending on the material). The onset of necking leads to a triaxial stress state in the specimen's center, not allowing assuming a uniaxial stress state and, consequently, the results treatment under this assumption. The necking occurrence is the main disadvantage of this test since it disables the adequate characterization of the hardening law up to large plastic deformations.

The anisotropy coefficient, r, can be calculated considering the definition

$$r = \frac{\varepsilon_{22}^{\mathrm{p}}}{\varepsilon_{33}^{\mathrm{p}}}, \tag{3.2}$$

where $\varepsilon_{22}^{\mathrm{p}}$ and $\varepsilon_{33}^{\mathrm{p}}$ correspond to the plastic strains in the specimen's width and thickness direction, respectively (as schematically shown in Figure 3.4 (c)). For sheet metals, the thickness is very small compared to the width, leading to relative errors of measurement of the two strains, which can be quite different. Thus, taking into account the volume conservation condition,

$$\varepsilon_{11}^{\mathrm{p}} + \varepsilon_{22}^{\mathrm{p}} + \varepsilon_{33}^{\mathrm{p}} = 0, \tag{3.3}$$

Eq. (3.2) becomes

$$r = -\frac{\varepsilon_{22}^{\mathrm{p}}}{\varepsilon_{11}^{\mathrm{p}} + \varepsilon_{22}^{\mathrm{p}}}. \tag{3.4}$$

For a tensile test performed for a specific orientation, θ, with respect to the rolling direction, the anisotropy coefficient is given by

$$r_\theta = \frac{\sin^2(\theta)\dfrac{d\mathcal{G}}{d\sigma_{11}} - 2\sin(\theta)\cos(\theta)\dfrac{d\mathcal{G}}{d\sigma_{12}} + \cos^2(\theta)\dfrac{d\mathcal{G}}{d\sigma_{22}}}{-\left(\dfrac{d\mathcal{G}}{d\sigma_{11}} + \dfrac{d\mathcal{G}}{d\sigma_{22}}\right)}, \tag{3.5}$$

where $\mathcal{G}$ is the plastic potential which, considering an associated flow rule, corresponds to the yield function (see section 2.1). The in-plane orthotropic behavior of metal sheets is commonly evaluated considering the anisotropy coefficients obtained for 0º, 45° and 90º, with respect to the RD, known as the normal anisotropy coefficient, $\bar{r}$, defined in Eq. (2.25). This value is related to the ability of the metal sheet on resisting elongation when subjected to tensile and, when assuming a negligible SD effect, compression forces. Typically, a high value of the normal anisotropy coefficient is desired in the deep drawing process in order to prevent excessive thinning. In this context, it is also usual to evaluate the variation of the normal anisotropy with the angle from the rolling direction, which is given by

$$\Delta r = \frac{r_0 - 2r_{45} + r_{90}}{2}. \tag{3.6}$$

This quantity, known as planar anisotropy coefficient, indicates the difference of behavior of the material in the plane of the sheet, function of the different directions considered. This quantity is related to the earing amplitude of deep-drawn cups, meaning that if the value of the anisotropy coefficient is the same along all the directions in the plane of the sheet metal $(\Delta r = 0)$, earing will not be observed. Nevertheless, it should be mentioned that nowadays it is consensual that the earing profile is also influenced by the in-plane yield stress directionalities.

3.4.2. Uniaxial Compression Test

Uniaxial in-plane compression tests are important for retrieving the material's mechanical behavior for this stress states. These properties are important for most lightweight metals since they tend to present pronounced tension-compression asymmetry. As in the uniaxial tensile test, the important information to retrieve from the test should be the yield stresses and the anisotropy coefficients, which are evaluated using the same definitions used for the uniaxial tensile test. However, this test presents some specific difficulties when considering metal sheets, mainly related with buckling effects, which prevent uniaxial deformations and consequently not allowing deformations higher than about 10%. Also, in most of the studies, this test is used to evaluate the Bauschinger effect and not the tension-compression asymmetry. Consequently, to the author's knowledge, there are only a few studies where the compression *r*-values are evaluated for metal sheets (Zhou et al. (2016)). In fact, the information concerning the compression *r*-values is crucial for the identification of the CPB06 yield criterion anisotropy parameters since, from the author's experience and also in Raemy et al. (2017), if these values are not controlled, the model may deliver unrealistic results, which can significantly deteriorate the accuracy of the numerical simulation.

To circumvent the buckling problems observed in compression testing, two major methods are generally used: (i) control of the specimen's geometry or (ii) control of the boundary conditions, both of which are schematically represented in Figure 3.5. The first method includes specimens with small length-to-thickness ratios, incorporating a short gage length (Tritschler et al., 2014), or packing multiple thin sheet specimens together, usually glued with some kind of adhesive (Barlat et al., 1997a). The second involves the use of a single thin-sheet specimen with a relatively large length-to-thickness ratio and using an anti-buckling device (Kuwabara et al., 2009). Recently, Zhou et al. (2016) proposed a simpler design for monotonic in-plane uniaxial compression for thin sheets considering only a single-sided grooved specimen supported only from the back, thus leaving the front side visible for strain analysis.

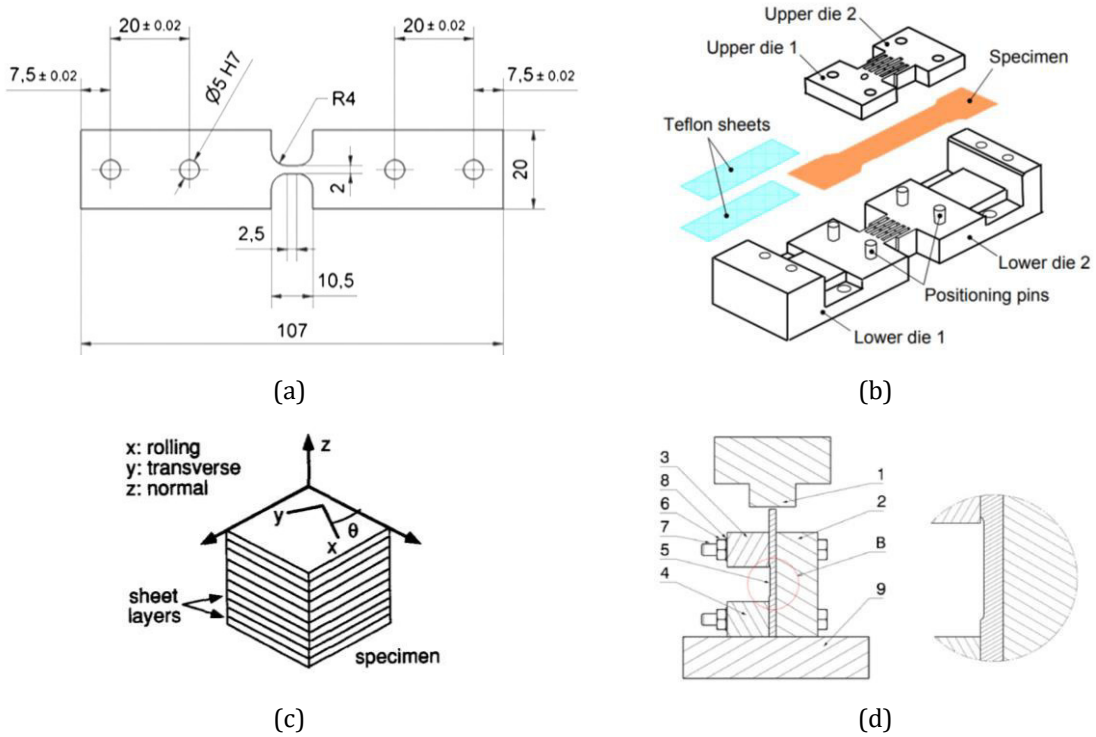

Figure 3.5. Usual uniaxial compression tests considering: (a) a specimen with small length-to-thickness ratio (Tritschler et al., 2014), (b) an anti-buckling device (Kuwabara et al., 2009), (c) pilled specimens (Barlat et al., 1997a) and (d) a single-sided grooved specimen (Zhou et al., 2016).

3.4.3. Disc Compression Test

The disc compression test was originally proposed by Bourne and Hill (1950) and consists in the compression of several piled up sheet metal discs. The discs are stacked and the strain measurement is performed on the middle disc, in order to minimize the influence of any shear stresses induced by friction. This through-thickness compression state is equivalent to the equibiaxial tensile stress state[2], since the same deviatoric stress tensor is obtained for both stress states as

$$\boldsymbol{\sigma} = \begin{bmatrix} 0 & 0 & 0 \\ 0 & 0 & 0 \\ 0 & 0 & -\sigma_{33}^{C} \end{bmatrix}, \text{ such that } \boldsymbol{\sigma}' = \begin{bmatrix} (1/3)\sigma_{33}^{C} & 0 & 0 \\ 0 & (1/3)\sigma_{33}^{C} & 0 \\ 0 & 0 & (-2/3)\sigma_{33}^{C} \end{bmatrix}, \tag{3.7}$$

and

[2] Some authors state that bulge tension test results and those from direct uniaxial compression should, theoretically, give the same stress-strain curves, disregarding friction effects during experimental testing (Vial et al., 1983). Nevertheless, other authors showed that the bulge test conditions force the material towards an equibiaxial strain state, inducing deviations of the average stress from the equibiaxial stress path (Mulder et al., 2015; Reis et al., 2015; Yoshida, 2013).

$$\boldsymbol{\sigma} = \begin{bmatrix} \sigma_{\mathrm{b}}^{\mathrm{T}} & 0 & 0 \\ 0 & \sigma_{\mathrm{b}}^{\mathrm{T}} & 0 \\ 0 & 0 & 0 \end{bmatrix}, \text{ such that } \boldsymbol{\sigma}' = \begin{bmatrix} (1/3)\sigma_{\mathrm{b}}^{\mathrm{T}} & 0 & 0 \\ 0 & (1/3)\sigma_{\mathrm{b}}^{\mathrm{T}} & 0 \\ 0 & 0 & (-2/3)\sigma_{\mathrm{b}}^{\mathrm{T}} \end{bmatrix}. \tag{3.8}$$

This enables the evaluation of the stress state as schematically shown in Figure 3.3, since, from Eq. (3.7) and Eq. (3.8), $\sigma_{\mathrm{b}}^{\mathrm{T}} = \sigma_{33}^{\mathrm{C}}$. Nonetheless, for anisotropic materials, the equibiaxial stress state is not guaranteed. More recently, Barlat et al. (2003) used this test to determine the anisotropic biaxial coefficient, r_{b}, required for the proper identification of the yield function YLD2000-2D. In fact, in the majority of sheet metal forming processes, the blank undergoes a biaxial stress state, making the flow stress determined from only uniaxial tests insufficient to describe its mechanical behavior. By measuring the deformed discs' diameter in both the rolling and transverse direction, it is possible to define the biaxial anisotropy coefficient following the expression

$$r_{\mathrm{b}} = \frac{\varepsilon_{22}^{\mathrm{p}}}{\varepsilon_{11}^{\mathrm{p}}}, \tag{3.9}$$

where $\varepsilon_{22}^{\mathrm{p}}$ and $\varepsilon_{11}^{\mathrm{p}}$ correspond to the plastic strains in the transverse and in the rolling directions, respectively. An example of the discs' geometry evolution for increasing values of deformation is presented in Figure 3.6. The trajectory obtained by this test is equivalent to that in biaxial tension.

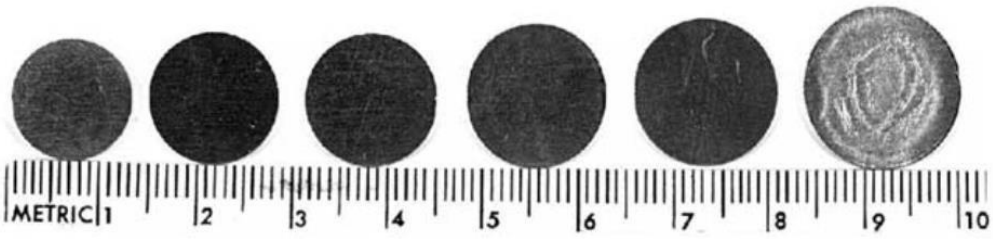

Figure 3.6. Discs' geometry, for increasing values of deformation, obtained from the disc compression test (Barlat et al., 2005).

3.4.4. Shear Test

The shear test is widely used for the mechanical characterization of metal sheets since it allows achieving larger strains, when compared with the tensile test, without plastic instability (Bouvier et al., 2006; Rauch, 1998; Thuillier and Manach, 2009; Yoon et al., 2005). Just like the tensile specimens, shear test specimens can be machined at different orientations from the rolling direction, in order to characterize the anisotropic behavior in the sheet's plane. In addition, it is possible to perform trajectories inversion, allowing the characterization and modeling of the Bauschinger effect. In fact, this test is very important for characterizing the material hardening behavior for orthogonal strain path changes, which is commonly done based on a uniaxial tensile test followed by a simple shear. Nevertheless, high shear stresses are normally associated to processes that involve ironing operations or to sheet bulk metal forming. For these reasons, some authors consider that this strain path is not particularly interesting to characterize the anisotropy of the material behavior.

Miyauchi (1984) proposed a simple shear equipment, allowing to achieve high levels of shear strain, consisting of a clamping device with two rigid parts subjected to parallel movement, which is then mounted to a tensile test machine. The specimens' geometry considers two shear zones subjected to a vertical displacement (Figure 3.7 (a)). Specimens with only a single shear zone were developed by Genevois (1992) as shown in Figure 3.7 (b), being the most widely used due to the simple geometry of the sample. In this case, the shear stress is calculated as

$$\tau = \frac{F}{Le}, \tag{3.10}$$

where F is the measured force, L is the length and e is the thickness of the gauge area considered, *i.e.* sheared areas.

Although this test seems simple, it presents some drawbacks. These are related to: (i) the difficulty in measuring the local strains due to the narrow shear zone, (ii) some heterogeneity of the strain state and buckling on the shear zone, depending on the specimen's dimensions, and (iii) possible sliding of the specimen under the grips. In this context, several improvements have been suggested for the specimen's geometry, trying to improve the test robustness (Pereira et al., 2015; Souto et al., 2016)

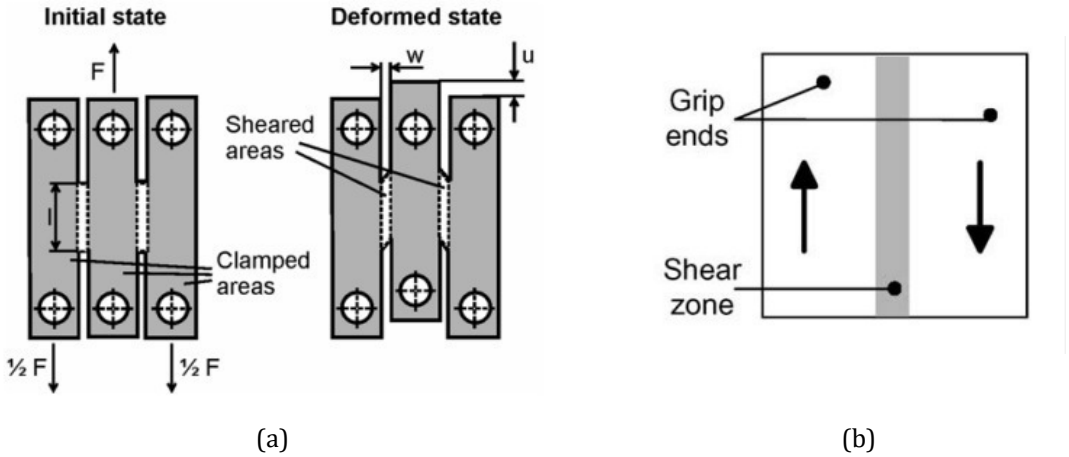

(a) (b)

Figure 3.7. Specimens' geometry developed by (a) Miyauchi (1984) (as extracted from Hußnätter and Merklein (2008)) and (b) Genevois (1992) (as extracted from Yoon et al. (2005)).

3.4.5. Plane Strain Tensile Test

Plane strain tests are also widely used to characterize the plastic behavior of sheet metals between uniaxial and equibiaxial tension. In fact, stretching failures in automotive stamping occur near the plane strain state (Ayres et al., 1978). The uniaxial tensile test can be modified using a very wide, short specimen to change the strain state from the one with large negative strain, towards the one with small or null strain. However, there is always some error because the edge is inherently in uniaxial tension. Specific plane strain specimens were proposed in the literature in order to induce stress states equivalent to plane strain in a determined area of the specimen (Bron and Besson, 2004; Kuwabara et al., 2002; Wagoner and Wang, 1979). Examples of specimens used for achieving plane strain conditions are presented in Figure 3.8.

The results analysis for this test is not straightforward because only one of the stress values is measured and the evaluation of the resistant area may not be direct. Therefore, to model the deformation behavior of sheet metals in the plane strain state it may be necessary to rely on plasticity theories based on uniaxial tensile hardening data (see *e.g.* Wagoner and Wang (1979)). In fact, this is the main advantage of the apparatus proposed by Kuwabara et al. (2002), which allows the evaluation of the strain ratio associated to different pre-defined stress ratios, including ones near the plane strain condition. Using this experimental test, it is possible to evaluate the yield stress ratio, based on the obtained stress-strain curves, as well as the normal to the

yield surface, based on the ratio between the measured in-plane strains. The strain measurement is usually performed with digital image correlation (DIC). Nevertheless, it should be mentioned that this can only be performed until relatively small strain values.

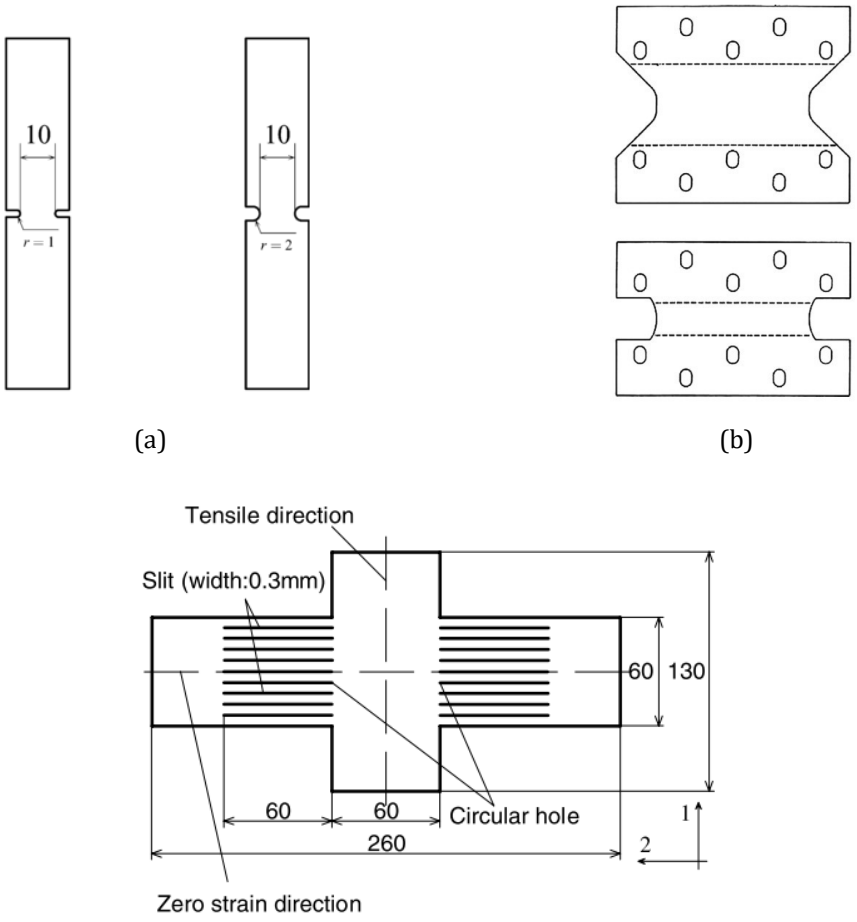

Figure 3.8. Plane strain specimens as developed by (a) Bron and Besson (2004), (b) Wagoner (1981) and (c) Kuwabara (2007).

3.4.6. Biaxial Tensile Test

The idea of testing cruciform specimens dates back to the 1960s with tests showing the potential for the parameters identification of both anisotropic yield criteria and hardening laws (Galster, 1963). The test can be performed considering displacement-driven or load controlled apparatus. The number of actuators may also influence the results. If the stroke is obtained with one actuator, and thus the geometrical configurations cannot be changed during the test, side bending of the specimens can

occur for large deformations. By using four independent actuators, the biaxial states of both stress and strains in the specimen central zone are better defined, even for highly anisotropic materials. The planar biaxial test allows obtaining multiple ratios for σ_x/σ_y, usually by stretching a cruciform shaped specimen and by applying simultaneously longitudinal and transverse loads on their arms, with the relevant deformation zone occurring in the middle of the specimen. Figure 3.9 (a) presents an experimental apparatus proposed by Kuwabara et al. (1998).

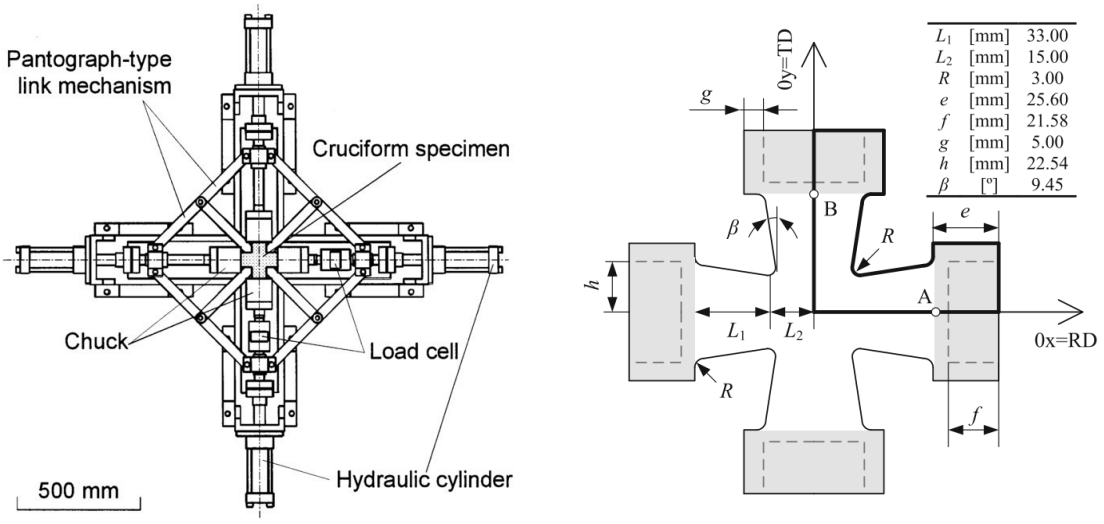

(a) (b)

Figure 3.9. (a) Biaxial testing setup (Kuwabara et al., 1998) and (b) cruciform specimen example (Prates, 2014).

One of the major issues, which leads to extensive research, is the cruciform specimen geometry. Numerical simulation allows some optimization of the geometry aiming to avoid stress concentration in areas out of the center section. An example of a cruciform specimen proposed by Prates (2014) is presented in Figure 3.9 (b). Other authors adopt specimen geometries similar to the one shown in Figure 3.8 (c), but with slits in both arms (Kuwabara, 2007). In that case, as for the plane strain test, the premature failure of the specimens at the arms still limits its application. The analysis of the test results is performed as for the plane strain, with the strain measures usually performed with digital image correlation (DIC).

3.4.7. Hydraulic Bulge Test

The bulge test allows determining the stress *vs.* strain curves up to significantly higher values of deformation (up to 70%, depending on the material), when compared to the values achieved through uniaxial tensile tests, for which homogeneous deformation is limited by the necking occurrence. This enables the determination of the hardening law parameters for high values of strain and obtaining supplementary information regarding the materials' anisotropy, specifically the equibiaxial yield stress, σ_b. Another advantage is its the reproducibility.

This test specimen consists of a circular metal sheet, which is radially clamped using a circular drawbead, preventing the sheet from moving in the radial direction. A hydraulic fluid (Montay et al., 2007), viscous material (Nasser et al., 2010; Sigvant et al., 2009) or a pneumatic gas (Banabic et al., 2005) is then used as a pressure medium and applied in the central area on one side of the sheet. The use of hydraulic pressure minimizes the problems associated with the characterization of frictional contact. During deformation, the central area of the sheet deforms into an approximately spherical or ellipsoidal shape, depending on the geometry of the die, being circular or elliptical, respectively. Figure 3.10 presents the initial (left) and instantaneous (right) geometries of the bulge test, including a detail of the pole corresponding to the measurement area.

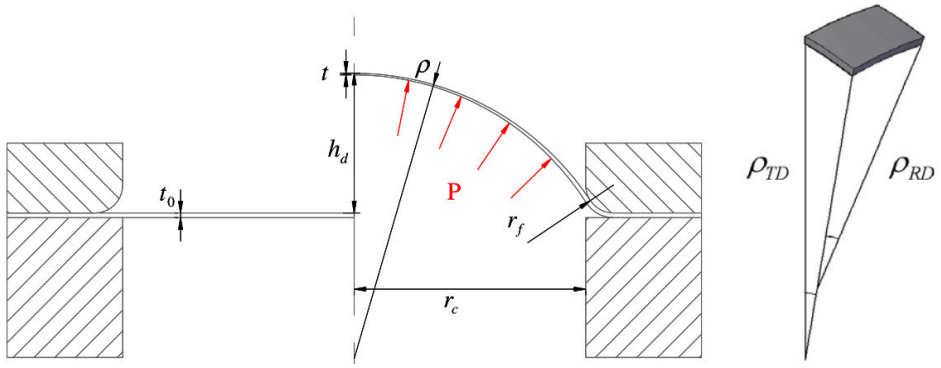

Figure 3.10. Schematic representation of the hydraulic Bulge test (Koç et al., 2011).

The evaluation of the stress-strain curve requires the recording of the evolutions of pressure, radius of curvature and strain at the pole of the cap during the test. The measurements of radius of curvature and strain can be performed by a spherometer and an extensometer, respectively (Martins et al., 2012; Young et al., 1981). An optical

system can replace these mechanical systems with advantages, since it enables the description of the geometry and strain distributions on the sheet surface during the bulge test (Bleck and Blumbach, 2005; Mulder et al., 2013). Some authors also propose the use of mathematical models to evaluate the thickness and the radius of curvature at the pole of the cap using the total height at the pole (see *e.g.* Reis et al., 2016). Whatever the measurement system adopted, it is always necessary to use the membrane theory which relates the stresses at the pole with the pressure, the radius of curvature, and sheet thickness (Lăzărescu et al., 2011).

Despite the recently recommended procedure by ISO 16808 (ISO, 2004), the analysis of the bulge test results still presents some uncertainties. In fact, the accurate evaluation of the stress *vs.* strain curves depends on assumptions and simplifications, whose assessment is still under study. For example, Mulder et al. (2015) and Yoshida (2013) examined the validity and the conditions for using the membrane theory, which includes issues related to the geometry of the cap that affects the evaluation of the equibiaxial stress state assumption in case of orthotropic materials. Although the analyzed materials present relatively low anisotropy in the sheet plane, Mulder et al. (2015) concluded that the test conditions force the material towards an equibiaxial strain state, which leads to deviations of the average stress from the equibiaxial stress lower than 3%, while Yoshida (2013) reported deviations between 1–5%. Reis et al. (2017) extended the analysis for material with higher anisotropy, showing that the geometry of the cap (radius of curvature and sheet thickness), at each moment of the test, is quite similar for both orthotropic directions in the sheet plane. However, for anisotropic materials, the ratio between both measured principal strains in the sheet plane is different from 1.0. In this case, the inability of occurrence of equibiaxial stress and strain paths is a natural consequence of the normality condition between the stress and the increment of strain. In that case, the errors associated with the approach traditionally used, which considers equibiaxial stress (and eventually strain) paths at the pole of the cap, isotropy and the simplified equation of the membrane theory, can lead to deviations in the evaluation of the stress-strain curve as high as 10%. In this context, Reis et al. (2017) proposed an empirical equation for the circular bulge test, relating the stress path with the strain path at the pole of the cap, which allows

determining the stress path based on the knowledge of the strain path, which can be assessed by digital image correlation.

Many researchers recommend the use of balanced biaxial data, whenever possible (Banabic et al., 2005a; Barlat et al., 2007), to improve the adjustment of the yield surface for the biaxial loading mode. In this context, Banabic et al. (2008) carried out a sensitivity analysis on the influence of the balanced biaxial stress σ_b and the equibiaxial strain ratio (r_b-value) based on the FE results of a cross-die test, showing that the balanced biaxial stress σ_b has a higher effect on predicted results than the r_b value. In this context, the stress-strain curve of the hydraulic bulge test has been extensively used to evaluate the equibiaxial yield stress. However, it is known that for lower equivalent plastic strain levels, the error in the estimated stress can be relatively high, due to the high value of the radius of curvature at the pole (see *e.g.* Reis et al., 2016). Thus, it is preferable to use the information concerning a pre-defined value of the plastic work. However, in any case, the assumption of an equibiaxial stress state should be carefully analyzed, considering the results reported by Reis et al. (2017). In fact, in the authors' opinion, the common use of the assumption of an equibiaxial stress state at the pole of the cap, of the hydraulic bulge test specimen, may had contributed for improper conclusions concerning the ability of classical identification methodologies to properly describe the metal sheet anisotropic behavior.

3.5. Final Remarks

The constitutive material parameters identification is a multidisciplinary subject, very dependent on both the results obtained from experimental testing and the algorithms and users' choices during the parameters identification procedure. It should be mentioned that, when adopting an associated flow rule, the modeling of the material's plastic behavior is performed considering a combination of a yield criterion and a hardening law. The identification of the corresponding parameters is mainly performed regarding two approaches: classical or non-classical. Classical approaches rely on the use of experimental tests that allow the direct estimation of both stresses and strain fields, while non-classical strategies can be applied also to other type of

experimental results involving non-homogeneous strain fields. Both approaches rely on optimization algorithms to minimize one or more functions that estimate the difference between experimental and numerical results.

Whatever the identification approach adopted, the experimental tests considered constrain the stress-strain space explored when fitting the parameters (Zhang et al., 2015). When adopting phenomenological constitutive models, the stress-strain space can be expanded combining results from crystal plasticity approaches (*e.g.* Knezevic et al., 2013). In fact, the computational efficiency of phenomenological models is still a factor contributing to its more generalized adoption, mainly for industrial applications.

Chapter 4

Contributions to the numerical simulation of the drawing of cylindrical cups

This chapter presents the contributions of this research in the framework of the analysis of the impact of the description of the orthotropic behavior of the material, including or not tension-compression asymmetry, in the numerical simulation of cylindrical cups. The subchapters correspond to the collection of publications that contain the innovative work, including the validation of the identification strategies and implementations adopted for the CPB06 yield criterion. This was performed considering a more general example, the four-point bending test, highlighting its potential application for describing the anisotropic behavior of materials presenting a strong SD effect. Partial results of the work and studies about their application in more case studies, including benchmarks examples proposed under the Numisheet conference series, were also published in international journals or conferences, as detailed in Appendix B.

(Page intentionally left blank)

4.1. DD3IMP, 3D fully implicit finite element solver: implementation of CB2001 yield criterion

This subchapter contains the paper "DD3IMP, 3D fully implicit finite element solver: implementation of CB2001 yield criterion", published in the Romanian Journal of Technical Sciences Applied Mechanics. This work shows the strategies and algorithms adopted in the fully implicit FE solver DD3IMP to model the orthotropic behavior of metallic sheets, as well the procedure for parameters' identification with a special and detailed emphasis given to the numerical implementation of the Cazacu and Barlat (2001) yield criterion. It shows that a good description of the anisotropy of both flow stresses and r-values are important to the overall accuracy of the predicted earing profile. In addition, the global process history or the process parameters may influence the earing prediction, particularly the contact interactions with the flange during the forming process.

(Page intentionally left blank)

DD3IMP, 3D FULLY IMPLICIT FINITE ELEMENT SOLVER: IMPLEMENTATION OF CB2001 YIELD CRITERION

P.D. BARROS[1], D.M. NETO[1], J.L. ALVES[2], M.C. OLIVEIRA[1], L.F. MENEZES[1]

Abstract. The strategies and algorithms adopted in the fully implicit FE solver DD3IMP to model the orthotropic behavior of metallic sheets, as well the procedure for parameters' identification, are the main focus of this work; a special and detailed emphasis will be given to the numerical implementation of the Cazacu and Barlat (2001) yield criterion. The usage and application of the aforesaid solver and yield criterion will be exemplified with the deep drawing of a cylindrical cup, an example typically adopted to study the effect of the material's orthotropy in forming operations. Two materials with distinct anisotropic behaviors are considered, namely: the AA5042 aluminum alloy and the AKDQ steel. The material parameters are identified from experimental data taking into account both flow stresses and *r*-values. The analysis of the results indicates that a good description of the anisotropy of both flow stresses and *r*-values are important to the overall accuracy of the predicted earing profile. However, either the global process history or the process parameters may influence the earing prediction, particularly the contact interactions with the flange during the forming process.

Key words: DD3IMP, implicit time integration, sheet metal forming, elastoplasticity, orthotropy, CB2001 yield criterion.

1. INTRODUCTION

Nowadays, the virtual try-out of sheet metal forming components has become an indispensable tool for the automotive industry, providing a strong reduction of development times. The process parameters optimization can be performed by a computer system in a virtual environment, replacing the expensive trial-and-error procedures by numerical ones [1]. Despite recent developments in the numerical tools, the finite element analysis of sheet metal forming processes still represents a challenge from the computational and modelling point of view; the problem is

[1] CEMUC, Department of Mechanical Engineering, University of Coimbra, Polo II, Pinhal de Marrocos, 3030-788 Coimbra, Portugal

[2] MEMS, Microelectromechanical Systems Research Unit, University of Minho, Campus de Azurém, 4800-058 Guimarães, Portugal

highly nonlinear due to the large deformations (geometry), the elastoplastic behavior (material) and the occurrence of frictional contact between the blank and the forming tools. Therefore, effective and robust finite element algorithms are required to provide accurate predictions when dealing with such complex industrial problems.

The time integration scheme used in the problem formulation dictates the efficiency and robustness of numerical simulations [2]. The dynamic explicit and the static implicit procedures are the two main formulations currently adopted [3]. Historically, the sheet metal forming analysis has been mainly carried out using explicit time integration schemes, which do not require an iterative procedure in each time increment, and thus avoiding convergence problems. Nevertheless, this method is only conditionally stable, requiring extremely small time steps (smaller than a critical time step) to guarantee the stability of the numerical solution. Thus, for *quasi*-static processes like typical sheet metal forming operations, when using dynamic explicit schemes it is necessary to resort to artificial strategies such as higher tool velocities to artificially increase the time step and achieve admissible computational times. Besides, in opposition to the static implicit schemes, the explicit procedures do not check equilibrium requirements at the end of each time increment [4]. Therefore, particularly when analyzing the influence of constitutive models in the numerical results accuracy, it is consensual that implicit time integration schemes lead to more accurate results (see e.g. [5]).

The elastoplastic behavior of the metallic sheet, namely the anisotropy and the work-hardening, are usually described by phenomenological constitutive models, which have a strong impact in the numerical solutions [6]. The material's orthotropic behavior is modelled by the yield surface, used to describe the yielding and the plastic flow of the material: this dual role of the yield surface requires a particular care and accuracy in its modeling and numerical implementation. Also, due to the increasingly advanced materials, the yield surface modeling has become more complex, relying on an increasing number of material parameters. However, some authors point out that although they are capable of a more accurate description of the in-plane directional (uniaxial) properties, they may predict sensibly different plastic properties for neighboring stress states.

The aim of this work is to present the algorithm adopted in the implementation of the non-quadratic yield criterion proposed by Cazacu and Barlat (2001) [7] in the implicit in-house code DD3IMP, and the strategies for parameters identification. The case study selected for analysis is a cylindrical cup deep drawing, since it is one of the typical forming operations in which the effect of the material's orthotropic behavior is more pronounced. Since the numerical results are also influenced by other numerical aspects, such as the finite elements adopted and the algorithm for contact with friction treatment, a brief description of the state update algorithm of DD3IMP is presented in the next section.

2. DD3IMP FINITE ELEMENT SOLVER

A brief description of the mechanical model and numerical methods currently implemented in the FE solver DD3IMP, which has been continuously developed and optimized to simulate sheet metal forming processes [8, 9], is given in this section. The evolution of the deformation process is described by an updated Lagrangian scheme. The mechanical model takes into account the large elastoplastic deformations and rotations of the deformable body (metallic sheet). Besides, the hypothesis of small elastic strains is adopted, assuming that the elastic strains are negligibly small with respect to unity. The forming tools are assumed as rigid bodies, while the frictional contact between the sheet and the tools is described by the Coulomb's classical law. The augmented Lagrangian approach proposed by Alart and Curnier [10] is used to regularize the constraints arising from the frictional contact conditions. Both nodal displacements and contact forces are involved in the resulting system of nonlinear equations, leading to a mixed formulation. A fully implicit Newton–Raphson method is adopted to solve, in a single iterative loop, all problem nonlinearities (geometry, material and contact) [8].

In order to improve the convergence rate of the numerical simulation, each time increment is divided into two steps: (i) the *Predictor* step, which determines the explicit trial solution, and (ii) the *Corrector* step, where this solution is iteratively corrected by an implicit method. Since the quality of the trial solution provided by the *Predictor* step is determinant for the convergence of the iterative process, a $r_{\min}$ strategy is employed to impose several restrictions and optimize the time step size [11]. Then, the equilibrium state of the deformable body is satisfied in each time step using the Newton-Raphson algorithm, which exhibits quadratic convergence in the vicinity of the solution (equilibrium).

The forming tools are modelled with Nagata patches [12], which result from the surface smoothing procedure applied to a coarse mesh [13]. The blank sheet is discretized with 3D solid finite elements, allowing an accurate evaluation of the contact forces and the stress gradients through the thickness [14]. Since the equilibrium conditions are checked in each time step, the use of solid elements is more CPU time consuming. Therefore, some high performance computing techniques have been incorporated, such as OpenMP directives, in the most time consuming branches of the code [15].

The elastoplastic constitutive model adopted considers isotropic elasticity and anisotropic plasticity. The elastic regime is described by the generalized Hooke law, while the plastic behavior of the material is modelled by: (i) an associated flow rule; (ii) a yield criterion and (iii) a work-hardening law. Several yield criteria are currently implemented, namely: (i) Hill'48 [16]; (ii) Barlat'91 [17]; (iii) Drucker [18]; (iv) Karafillis & Boyce'93 [19]; (v) Cazacu & Barlat'01 [7] and Cazacu, Plunkett & Barlat'06 [20]. Concerning the work-hardening law, which describes the evolution of the yield surface with the plastic work, various laws are available:

(i) pure isotropic hardening by means of a power law (Swift) or a Voce type saturation law; (ii) the combination of these two laws with a linear (Prager type) or non-linear kinematic hardening law proposed by Lemaître and Chaboche [21]; and (iii) the microstructural hardening model proposed by Teodosiu and Hu [22].

2.1. THE CONSTITUTIVE MODEL

The differential form of the elastoplastic behavior law is, in its general form,

$$\dot{\boldsymbol{\sigma}}^{\mathrm{J}} = \mathbf{C}^{\mathrm{ep}} : \mathbf{D}\,, \tag{1}$$

where $\dot{\boldsymbol{\sigma}}^{\mathrm{J}}$ is the Jaumann derivative of the Cauchy stress tensor $\boldsymbol{\sigma}$, given by

$$\dot{\boldsymbol{\sigma}}^{\mathrm{J}} = \dot{\boldsymbol{\sigma}} + \boldsymbol{\sigma}\mathbf{W} - \mathbf{W}\boldsymbol{\sigma}\,, \tag{2}$$

where $\dot{\boldsymbol{\sigma}}$ stands for the time derivative of the Cauchy stress tensor and $\mathbf{W}$ is the total spin tensor defined by

$$\mathbf{W} = \dot{\mathbf{R}}\mathbf{R}^{\mathrm{T}}\,, \tag{3}$$

with $\mathbf{R}$ being the orthogonal elastic rotation tensor. $\mathbf{D}$ is the strain rate tensor and $\mathbf{C}^{\mathrm{ep}}$ is a fourth-order tensor corresponding to the elastoplastic module. This tensor depends of the algorithms adopted in the integration of the constitutive model and the type of relation considered between the states at the beginning and at the end of the loading increment. Thus, it is possible to consider the tangent elastoplastic modulus or the consistent elastoplastic modulus. The tangent elastoplastic modulus can be defined as [23]

$$\mathbf{C}^{\mathrm{ep}}\Big|_{\mathrm{tangent}} = \mathbf{C}^{\mathrm{e}} - \alpha f_0 \mathbf{V} \otimes \mathbf{V}\,, \tag{4}$$

where $\alpha = 0$ if the material is in an elastic state, or during elastic unloading; and $\alpha = 1$ if the material is in an elastoplastic loading state. f_0 is a function of the isotropic and kinematic hardening law adopted. Although the example considered in this work does not include kinematic hardening, in order to keep the back-stress tensor in the equations, the Prager's kinematic law, $\dot{\mathbf{X}} = k\mathbf{D}^{\mathrm{p}}$, is considered, with the single parameter k. Therefore, f_0 can be written in the general form

$$f_0 = \frac{4\mu^2}{\left(k + 2\mu\right)\mathbf{V} : \mathbf{V} + H'}\,, \tag{5}$$

where μ is the Lamé parameter. $\mathbf{V}$ is one of the tensorial quantities to be determined as function of the adopted yield criterion, and it is, by definition

$$\mathbf{V} = \frac{\partial \overline{\sigma}}{\partial\left(\boldsymbol{\sigma}' - \mathbf{X}\right)}, \tag{6}$$

where $\overline{\sigma}$ is the equivalent stress given by the yield criterion, $\boldsymbol{\sigma}'$ the deviatoric Cauchy stress tensor, and $\mathbf{X}$ the deviatoric and symmetric second-order back-stress tensor.

The strain rate can be decomposed into elastic and plastic parts as

$$\mathbf{D} = \mathbf{D}^{\mathrm{e}} + \mathbf{D}^{\mathrm{p}}, \tag{7}$$

where $\mathbf{D}^{\mathrm{p}}$, the plastic strain rate tensor, is a deviatoric tensor, given by the associated inviscid flow rule as

$$\mathbf{D}^{\mathrm{p}} = \dot{\lambda}\frac{\partial \mathcal{F}}{\partial\left(\boldsymbol{\sigma}' - \mathbf{X}\right)} = \dot{\lambda}\mathbf{V}, \tag{8}$$

in which $\dot{\lambda}$ is the plastic multiplier and $\mathcal{F}$ is the plastic potential, identified as a scalar function defining the elastic limit surface, such that

$$\mathcal{F}\left(\overline{\sigma}, Y\right) = \overline{\sigma} - Y = 0, \tag{9}$$

where Y is the flow stress, modelled by the isotropic work-hardening law. From this definition, the consistency condition in rate form states that

$$\dot{\mathcal{F}}\left(\overline{\sigma}, Y\right) = \dot{\overline{\sigma}} - H'\dot{\overline{\varepsilon}}^{\mathrm{p}} = 0, \tag{10}$$

where

$$H' = \partial Y \big/ \partial \overline{\varepsilon}^{\mathrm{p}} \tag{11}$$

is the isotropic hardening modulus, and, if the yield function is a homogeneous function of degree one, one has that $\dot{\overline{\varepsilon}}^{\mathrm{p}} = \dot{\lambda}$. $\dot{\overline{\sigma}}$ and $\dot{\overline{\varepsilon}}^{\mathrm{p}}$ are, respectively, the time derivatives of the equivalent stress and of the equivalent plastic strain. The total equivalent plastic strain is defined as

$$\overline{\varepsilon}^{\mathrm{p}} = \int_0^t \frac{\left(\boldsymbol{\sigma}' - \mathbf{X}\right) : \mathbf{D}^{\mathrm{p}}}{\overline{\sigma}} \mathrm{d}t. \tag{12}$$

2.2. TIME INTEGRATION

Since the elastic behavior is considered isotropic, the hypoelastic form of the Hooke's law can be written as [23]

$$\dot{\boldsymbol{\sigma}} = \mathbf{C}^{\mathrm{e}} : \left(\mathbf{D} - \mathbf{D}^{\mathrm{p}}\right) \tag{13}$$

which, by integration, corresponds to the stress increment in $[t, t+\Delta t]$, i.e.

$$\boldsymbol{\sigma}_{\mathrm{F}} - \boldsymbol{\sigma}_0 = \mathbf{C}^{\mathrm{e}} : \Delta\boldsymbol{\varepsilon} - \mathbf{C}^{\mathrm{e}} : \Delta\boldsymbol{\varepsilon}^{\mathrm{p}} \tag{14}$$

with subscripts 0 and F denoting the quantities at the beginning and at the end of the time increment $[t, t+\Delta t]$, respectively. $\boldsymbol{\Delta\varepsilon}^{\mathrm{p}}$ and $\boldsymbol{\Delta\varepsilon}$ are the increments of the plastic and total strain tensors, respectively, determined over the time increment. Applying the generalized middle point rule to determine the $\mathbf{D}^{\mathrm{p}}$ evolution, and since $\mathbf{D}^{\mathrm{p}} = \dot{\lambda}\mathbf{V}$, it can be written

$$\Delta\boldsymbol{\varepsilon}^{\mathrm{p}} = \Delta\lambda\mathbf{V}_{\gamma}, \tag{15}$$

with

$$\mathbf{V}_{\gamma} = (1-\gamma)\mathbf{V}_0 + \gamma\mathbf{V}_{\mathrm{F}} \quad \text{and} \quad \gamma \in [0,1]. \tag{16}$$

To calculate $\Delta\lambda$ and $\mathbf{V}_{\mathrm{F}}$ it is necessary to determine $(\boldsymbol{\sigma}'_{\mathrm{F}} - \mathbf{X}_{\mathrm{F}})$. $\boldsymbol{\sigma}_{\mathrm{F}}$ is calculated from Eq. 14, leading to deviatoric and hydrostatic components given by, respectively,

$$\boldsymbol{\sigma}'_{\mathrm{F}} = \boldsymbol{\sigma}'_0 + 2G\Delta\varepsilon' - 2G\Delta\lambda\mathbf{V}_{\mathrm{F}} \quad \text{and} \tag{17}$$

$$\mathrm{tr}(\boldsymbol{\sigma}_{\mathrm{F}}) = \mathrm{tr}(\boldsymbol{\sigma}'_0) + \frac{E}{1+2\upsilon}\mathrm{tr}(\boldsymbol{\Delta\varepsilon}). \tag{18}$$

G and E are the shear and Young's modulus, while υ is the Poisson's ratio. In order to determine both $(\boldsymbol{\sigma}'_{\mathrm{F}} - \mathbf{X}_{\mathrm{F}})$ and $\Delta\bar{\varepsilon}^{\mathrm{p}} = \Delta\lambda$, the consistency condition at the end of the time step is imposed, i.e.,

$$\bar{\sigma}(\boldsymbol{\sigma}'_F - \mathbf{X}) - Y_F\left(\bar{\varepsilon}_0^p + \Delta\bar{\varepsilon}^p\right) = 0. \tag{19}$$

This allows to define the non-linear system of equations to be solved in the state update algorithm, with unknowns $(\boldsymbol{\sigma}'_{\mathrm{F}} - \mathbf{X}_{\mathrm{F}})$ and $\Delta\bar{\varepsilon}^{\mathrm{p}}$, i.e.,

$$\boldsymbol{\mathcal{Q}}\left(\boldsymbol{\sigma}'_{\mathrm{F}} - \mathbf{X}_{\mathrm{F}}, \Delta\bar{\varepsilon}^{\mathrm{p}}\right) = \begin{bmatrix} \boldsymbol{\mathcal{G}} \\ g \end{bmatrix} = \begin{bmatrix} \mathbf{0} \\ 0 \end{bmatrix}. \tag{20}$$

Assuming that the Prager's kinematic law is considered, the system of equations defined in Eq. 20 can be re-written as

$$\begin{bmatrix} (\boldsymbol{\sigma}'_{\mathrm{F}} - \mathbf{X}_{\mathrm{F}}) - (\boldsymbol{\sigma}'_0 - \mathbf{X}_0) - 2G\Delta\varepsilon' - (k+2G)\Delta\bar{\varepsilon}^{\mathrm{p}}\mathbf{V}_{\mathrm{F}} \\ \bar{\sigma}(\boldsymbol{\sigma}'_{\mathrm{F}} - \mathbf{X}_{\mathrm{F}}) - Y_{\mathrm{F}}\left(\bar{\varepsilon}_0^{\mathrm{p}} - \Delta\bar{\varepsilon}^{\mathrm{p}}\right) \end{bmatrix} = \begin{bmatrix} \mathbf{0} \\ 0 \end{bmatrix}. \tag{21}$$

The updated state variables are determined solving the non-linear system of equations Eq. 21 using the Newton-Raphson method. The calculation of $\boldsymbol{\mathcal{Q}}$ and $\partial\boldsymbol{\mathcal{Q}}/\partial\boldsymbol{\varsigma}$ (with $\boldsymbol{\varsigma}=\left[\boldsymbol{\sigma}'_{\mathrm{F}}-\mathbf{X}_{\mathrm{F}},\Delta\bar{\varepsilon}^{\mathrm{p}}\right]$) depends on the adopted yield criterion: the following matrix quantities must be analytically determined:

$$\frac{\partial\boldsymbol{\mathcal{Q}}}{\partial\boldsymbol{\varsigma}}=\begin{bmatrix}[\mathbf{A}] & [\mathbf{c}]\\ [\mathbf{b}] & d\end{bmatrix}, \tag{22}$$

where

$$\mathbf{A}=\frac{\partial\boldsymbol{\mathcal{Q}}}{\partial\left(\boldsymbol{\sigma}'_{\mathrm{F}}-\mathbf{X}_{\mathrm{F}}\right)},\quad \mathbf{b}=\frac{\partial g}{\partial\left(\boldsymbol{\sigma}'_{\mathrm{F}}-\mathbf{X}_{\mathrm{F}}\right)},\quad \mathbf{c}=\frac{\partial\boldsymbol{\mathcal{G}}}{\partial\left(\Delta\bar{\varepsilon}^{\mathrm{p}}\right)},\quad d=\frac{\partial g}{\partial\left(\Delta\bar{\varepsilon}^{\mathrm{p}}\right)}. \tag{23}$$

In the case of Prager's kinematic hardening law, these expression can be written as:

$$\mathbf{A}=\mathbf{I}_4+\left(k+2G\right)\Delta\bar{\varepsilon}^{\mathrm{p}}\mathbf{Q}_{\mathrm{F}},\quad \mathbf{c}=\mathbf{V}_{\mathrm{F}}, \tag{24}$$

$$\mathbf{b}=\mathbf{V}_{\mathrm{F}},\quad d=-H'_{\mathrm{F}},$$

where

$$\mathbf{V}_{\mathrm{F}}=\frac{\partial\bar{\sigma}}{\partial\left(\boldsymbol{\sigma}'_{\mathrm{F}}-\mathbf{X}_{\mathrm{F}}\right)},\quad \mathbf{Q}_{\mathrm{F}}=\frac{\partial^2\bar{\sigma}}{\partial\left(\boldsymbol{\sigma}'_{\mathrm{F}}-\mathbf{X}_{\mathrm{F}}\right)^2}\quad\text{and}\quad H'_{\mathrm{F}}=\partial Y\big/\partial\bar{\varepsilon}^{\mathrm{p}}. \tag{25}$$

The tensor $\mathbf{Q}$ corresponds to the second order derivative of the yield criterion with respect to the effective stress state $\boldsymbol{\Sigma}=\boldsymbol{\sigma}'-\mathbf{X}$, being used both in the state update algorithm and on the definition of the consistent elastoplastic modulus,

$$\mathbf{C}^{\mathrm{ep}}=\mathbf{C}^{\mathrm{e}}-4G^2\left(1-\beta\right)\left(\frac{\mathbf{V}_{\mathrm{F}}\otimes\mathbf{V}_{\mathrm{F}}}{H'_{\mathrm{F}}}+\Delta\bar{\varepsilon}^{\mathrm{p}}\mathbf{Q}_{\mathrm{F}}\right)\boldsymbol{\Lambda}, \tag{26}$$

where $\boldsymbol{\Lambda}$ also depends on the kinematic hardening law adopted. In case of Prager's kinematic hardening law it can be written as

$$\boldsymbol{\Lambda}^{-1}=\left[\mathbf{I}_4+\left(k+2\mu\right)\left(\frac{\mathbf{V}_{\mathrm{F}}\otimes\mathbf{V}_{\mathrm{F}}}{H'_{\mathrm{F}}}+\Delta\bar{\varepsilon}^{\mathrm{p}}\mathbf{Q}_{\mathrm{F}}\right)\right]. \tag{27}$$

Since the strain increment can be either elastic or plastic, parameter β and $\left(1-\beta\right)$ is introduced in Eq. 26 to separate, respectively, the elastic and plastic parts of the total strain increment.

2.3. CAZACU AND BARLAT YIELD CRITERION

The Cazacu and Barlat (2001) [7] yield criterion is a generalization of the Drucker's isotropic criterion to orthotropy, and, in its general form, is given by:

$$\overline{\sigma} = \left\{ 27 \left[\left(J_2^0 \right)^3 - c \left(J_3^0 \right)^2 \right] \right\}^{\frac{1}{6}}, \tag{28}$$

where J_2^0 and J_3^0 are the second and third generalized invariants of the effective stress tensor $\boldsymbol{\Sigma}$, defined as

$$\begin{aligned} J_2^0 = {} & \frac{a_1}{6}(\Sigma_{11} - \Sigma_{22})^2 + \frac{a_2}{6}(\Sigma_{11} - \Sigma_{33})^2 + \frac{a_3}{6}(\Sigma_{11} - \Sigma_{33})^2 \\ & + a_4 \Sigma_{12}^2 + a_5 \Sigma_{13}^2 + a_6 \Sigma_{23}^2 \end{aligned}, \tag{29}$$

$$\begin{aligned} J_3^0 = {} & (1/27)(b_1 + b_2)\Sigma_{11}^3 + (1/27)(b_3 + b_4)\Sigma_{22}^3 \\ & + (1/27)\left[2(b_1 + b_4) - b_2 - b_3 \right]\Sigma_{33}^3 \\ & - (1/9)(b_1 \Sigma_{22} + b_2 \Sigma_{33})\Sigma_{11}^2 - (1/9)(b_3 \Sigma_{33} + b_4 \Sigma_{11})\Sigma_{22}^2 \\ & - (1/9)\left[(b_1 - b_2 + b_4)\Sigma_{11} + (b_1 - b_3 + b_4)\Sigma_{22} \right]\Sigma_{33}^2 \\ & + (2/9)(b_1 + b_4)\Sigma_{11}\Sigma_{22}\Sigma_{33} \\ & - \left(\Sigma_{13}^2 / 3 \right)\left[2b_9 \Sigma_{22} - b_8 \Sigma_{33} - (2b_9 - b_8)\Sigma_{11} \right] \\ & - \left(\Sigma_{12}^2 / 3 \right)\left[2b_{10} \Sigma_{33} - b_5 \Sigma_{22} - (2b_{10} - b_5)\Sigma_{11} \right] \\ & - \left(\Sigma_{23}^2 / 3 \right)\left[(b_6 - b_7)\Sigma_{11} - b_6 \Sigma_{22} - b_7 \Sigma_{33} \right] + 2b_{11}\Sigma_{12}\Sigma_{23}\Sigma_{13}, \end{aligned} \tag{30}$$

where c, $a_1, ..., a_6$ and $b_1, ..., b_{11}$ are the anisotropy parameters. Σ_{ij}, $i, j = 1,2,3$ are the effective stress components defined in the material frame. For metal sheets, parameters a_5, a_6 and b_k $(k = 6,7,8,9,11)$ cannot be evaluated, thus the corresponding commonly isotropic values are adopted, i.e. 1.0. Although the anisotropy parameters reduce from 18 to 11, this yield function is flexible enough to enable the accurate description of the in-plane anisotropy of both *r*-value and flow stresses (or yield stresses).

The analytical expressions for the tensorial quantities **V** and **Q**, previously introduced in Eq. 24, are detailed in Appendix A in case of CB2001 yield criterion, along with the definition of the scalar quantity β (see Eq. 26).

3. DEEP DRAWING AND IRONING OF A CYLINDRICAL CUP

The deep-drawing of an axisymmetric cylindrical cup, benchmark proposed in the framework of Numisheet 2011 conference [24], was the example selected in this work to highlight the overall performance and capabilities of DD3IMP. This example encompasses two forming stages: (i) deep-drawing and (ii) ironing of the cylindrical cup. The geometry of the forming tools for both operations is shown in Fig. 1 (a). The specific geometry of the die allows to perform both the drawing and the ironing operations within one punch stroke. Therefore, the process is modeled considering three phases: (i) closing of the blank-holder until attain a prescribed force of 8.9 kN; (ii) punch displacement of 72.1 mm and (iii) springback. Due to geometrical and material symmetries, only one quarter of the global structure is modeled. The radius of the blank sheet is 38.062 mm for both materials (AA5042 aluminum alloy and AKDQ steel). The initial thickness of the blank is 0.208 mm for the AA5042 aluminum and 0.229 mm for the AKDQ steel. The blank sheet was discretized with 8-node hexahedral finite elements, combined with a selective reduced integration technique [25]. The use of solid finite elements is particularly important to simulate the ironing phase, due to double sided contact. Fig. 1 (b) presents the in-plane finite element mesh considered in the analysis. This mesh was built considering two layers of elements through thickness, leading to a total of 8464 finite elements [26]. The friction coefficient between the blank and the (rigid) forming tools is considered as $\mu=0.05$, according with the benchmark description [24]. All simulations were carried out in a single multi-core CPU workstation: Intel® Core™ i7-2600K (3.4 GHz) CPU and the Windows7 Professional (64-bits platform) operating system.

The materials' mechanical behavior is assumed isotropic in the elastic regime, being described by the Young's modulus, E, and the Poisson ratio, υ. The plastic behavior is described using an isotropic work hardening Voce type law,

$$Y\left(\bar{\varepsilon}^{\mathrm{p}}\right)=Y_0+(Y_{\mathrm{sat}}-Y_0)\left[1-\exp(-C_{\mathrm{Y}}\bar{\varepsilon}^{\mathrm{p}})\right], \tag{31}$$

where Y_0, Y_{sat} and C_{Y} are material parameters. The parameters assumed for the isotropic work hardening law adopted for both materials correspond to the ones identified by the benchmark committee for the tensile test performed along the rolling direction (Table 1).

Besides the CB2001 yield criterion, also the well-known Hill'48 yield criterion was considered and used as reference for comparison purposes and analysis. In this case, the equivalent stress is defined as

$$\begin{aligned}\bar{\sigma}^2 &= F(\Sigma_{22}-\Sigma_{33})^2+G(\Sigma_{33}-\Sigma_{11})^2+H(\Sigma_{11}-\Sigma_{22})^2\\ &\quad +2L\Sigma^2{}_{23}+2M\Sigma^2{}_{13}+2N\Sigma^2{}_{12},\end{aligned} \tag{32}$$

where F, G, H, L, M and N are the anisotropy parameters. For thin metallic sheets, it is not possible to determine parameters L and M. Therefore, the values considered for these parameters are the ones corresponding to the isotropic case, i.e. 1.5.

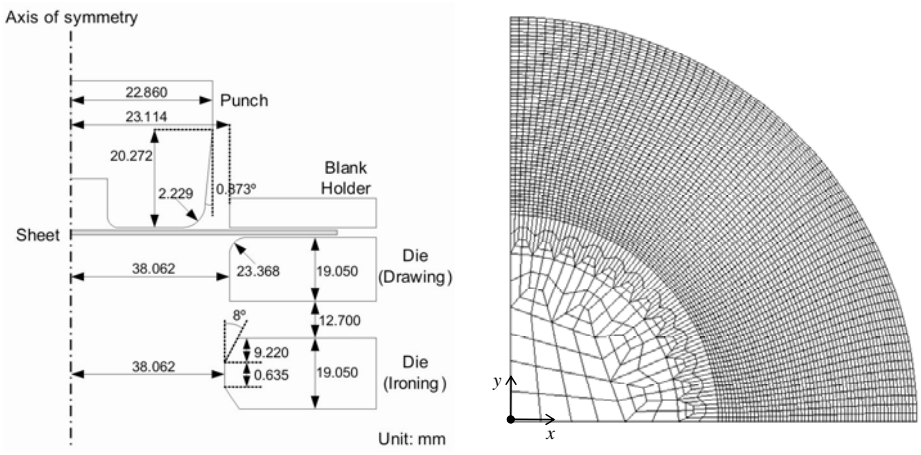

(a) (b)

Fig. 1 – Forming tools and blank geometry: a) main dimensions; b) in-plane blank sheet discretization.

Table 1

Elastic and work hardening properties for both materials

		AA5042	AKDQ
Elastic properties	E [GPa]	68.9	210.0
	υ	0.33	0.30
Voce law	Y_0 [MPa]	267.80	297.79
	Y_{sat} [MPa]	375.08	471.76
	C_Y	17.859	15.889

The anisotropy parameters for both yield criteria were determined using the DD3MAT in-house code [27], taking into account the experimental data reported by the benchmark committee for uniaxial tensile, equi-biaxial tension and the disc compression tests [24]. In DD3MAT, the identification procedure adopted is based on the minimization of an error function that evaluates the differences between the estimated values and the experimental ones, as follows

$$F(\mathbf{A}) = \sum_{\theta=0}^{90} w_{\sigma_\theta^T}\left(\sigma_\theta^T(\mathbf{A})/\sigma_\theta^T - 1\right)^2 + \sum_{\theta=0}^{90} w_{r_\theta}\left(r_\theta(\mathbf{A})/r_\theta - 1\right)^2 + w_{\sigma_b}\left(\sigma_b(\mathbf{A})/\sigma_b - 1\right)^2 + w_{r_b}\left(r_b(\mathbf{A})/r_b - 1\right)^2, \quad (33)$$

where **A** represents the set of parameters associated with the selected yield criterion, $\sigma_\theta^{\mathrm{T}}$ and r_θ are the experimental yield stresses in tension and *r*-values, respectively, obtained from the uniaxial tensile tests for a specific orientation (θ) with respect to the rolling direction (RD). σ_b is the experimental yield stress obtained from the equibiaxial tensile test, r_b is the experimental *r*-value obtained from the disc compression test, and $\sigma_\theta^{\mathrm{T}}(\mathbf{A})$, $r_\theta(\mathbf{A})$, $\sigma_b(\mathbf{A})$ and $r_b(\mathbf{A})$ are the correspondent values predicted from the adopted yield criterion. Such procedure can be considered a generalization of the one proposed by Banabic et al., 2005 [28], where the weighting factors, $w_{\sigma_\theta^{\mathrm{T}}}$, w_{r_θ}, w_{σ_b} and w_{r_b} are used to balance the influence of the experimental data. Nevertheless, the selection of the weighting factors is normally a manual procedure, strongly dependent on users' expertise and knowledge. In this study, all the weighting factors are considered equal to 1.0.

The parameters identification procedure takes into account, for both yield criteria, the yield stresses and *r*-values for 7 orientations to RD, the r_b value and the biaxial yield stress, σ_b (a total of 16 values). This results in an over constrained problem for both yield criteria, since the Hill'48 has only 4 parameters to be identified and CB2001 has 11. Nevertheless, recent studies indicate that the accurate prediction of the earing profile requires an accurate fit of the in-plane *r*-values anisotropy, but also of the yield stresses. Moreover, rather than capture values for specific orientations, it seems to be more relevant to be able to describe the trend of the anisotropy of the in-plane yield stresses [29]. For each orientation to the rolling direction $\theta_i \in]0°, 90°[$, two auxiliary vectors are defined:

$$\mathbf{v}_{\theta_i}^{\exp} = \begin{Bmatrix} \theta_{i+1} - \theta_{i-1} \\ \sigma_{\theta_{i+1}}^{\exp} - \sigma_{\theta_{i-1}}^{\exp} \end{Bmatrix} \quad \text{and} \quad \mathbf{v}_{\theta_i} = \begin{Bmatrix} \theta_{i+1} - \theta_{i-1} \\ \sigma_{\theta_{i+1}} - \sigma_{\theta_{i-1}} \end{Bmatrix}, \tag{34}$$

using the experimental and the numerical yield stress values, respectively. This enables the evaluation of the trend error for each angle θ_i, using the dot product between both vectors (i.e. the trend is the same for a value of $\mathbf{v}_{\theta_i}^{\exp} \cdot \mathbf{v}_{\theta_i}$ equal to 1.0). In order to integrate the two objectives in the optimization problem, a new objective function was added to the one defined in Eq. 33, in order to avoid the use of multi-objective optimization algorithms. The new objective function adds the difference in the yield stress trend, between two consecutive orientations, being defined as:

$$F_{\mathrm{trend}}(\mathbf{A}) = F(\mathbf{A}) + w_{\mathrm{trend}} \sum_{\theta=0}^{90} \left(1 - \left(\frac{\mathbf{v}_{\theta_i}^{\exp} \cdot \mathbf{v}_{\theta_i}}{\left\| \mathbf{v}_{\theta_i}^{\exp} \right\| \left\| \mathbf{v}_{\theta_i} \right\|} \right) \right). \tag{35}$$

w_{trend} corresponds to the weight given to the function that tries to improve the correlation between the experimental and the predicted trend for the in-plane yield stresses directionalities. As for the weight used in function $F(\mathbf{A})$, the selection of this weighting factor is also a manual procedure. Another comment should be added concerning the fact that the conditions that guarantee the convexity of CB2001 are unknown. Therefore, following Soare *et al*. [30], the minimization process adopted for this yield criterion includes testing the convexity of the yield surface, for several planes in the stress space [31]. The algorithm implemented in DD3MAT to minimize the cost function is based on a downhill simplex method.

Table 2 presents a summary of the parameters determined for both yield criteria and both materials, using the optimization procedure previously described. w_{trend} was considered null except in case of the identification of the aluminum alloy and CB2001 yield criterion. Besides, the Hill'48 yield criterion is not flexible enough to enable an accurate description of the anisotropy of both *r*-values and yield stresses. Moreover, the inclusion of the new objective functions tends to penalize the accuracy of the *r*-values anisotropy.

Table 2

Identified parameters for both materials (AA5042 and AKDQ) and yield criteria (Hill'48 and CB2001)

		AA5042	AKDQ
Hill'48	F	0.2457	0.4028
	G	0.9553	0.4261
	H	0.2704	0.4730
	N	1.6459	1.3951
	$L = M$	1.5000	1.5000
CB2001	a_1	0.9425	1.0462
	a_2	0.6986	0.9568
	a_3	1.0778	0.9681
	a_4	0.9792	1.0599
	b_1	6.0000	1.1731
	b_2	–0.3273	1.1183
	b_3	2.8941	1.1681
	b_4	–2.5143	1.0252
	b_5	–2.4348	0.8815
	b_{10}	1.2299	1.0622
	c	0.2397	1.6209

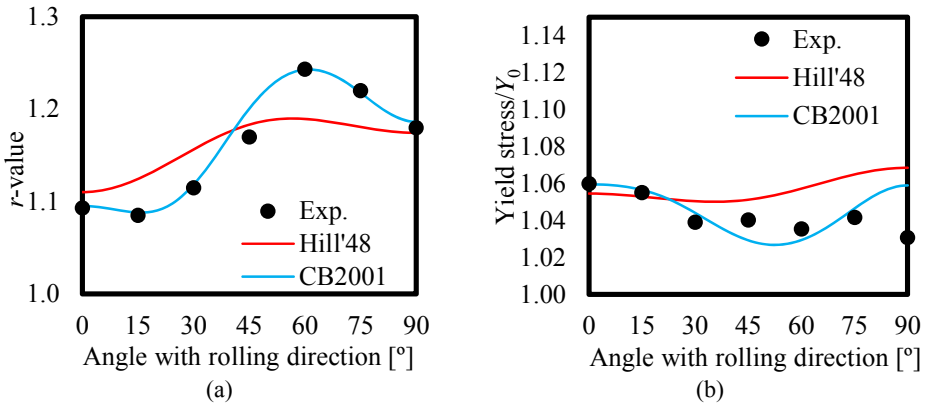

Fig. 2 – Experimental and predicted: a) *r*-values; b) yield stresses for AKDQ.

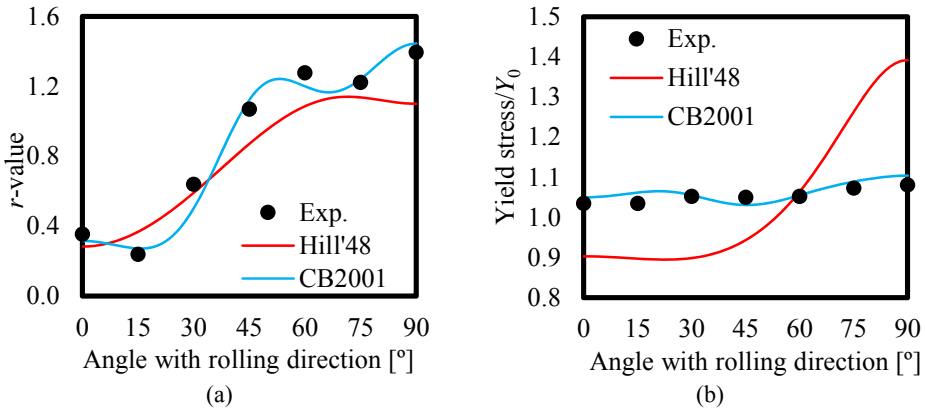

Fig. 3 – Experimental and predicted: a) *r*-values; b) yield stresses for AA5042.

Figures 2 and 3 present the comparison between the numerical and experimental *r*-values and the normalized yield stresses, for the AKDQ steel and AA5042 aluminum, respectively. The tensile yield stresses are normalized with the yield stress predicted by the hardening law, i.e. Y_0, which is different from the value reported for σ_0^T (see [24]). The AKDQ steel presents an almost isotropic distribution of the in-plane *r*-values and yield stresses. The CB2001 yield criterion, as expected, allows a better description of both yield stress directionalities and *r*-values. The AA5042 aluminum alloy presents a strong anisotropy of the *r*-values, while being almost isotropic in the tensile yield stresses. Therefore, the Hill'48 only captures the proper trend for the *r*-values. The CB2001 yield criterion allows the description of the anisotropy of both yield stresses and *r*-values.

The yield surfaces predicted for the AKDQ steel and the AA5042 aluminum for the plane σ_{11},σ_{22}, with $\sigma_{33}=0$, are presented in Fig. 4a and b, respectively.

Since the AKDQ is quite isotropic, as expected the yield surfaces are very similar, and the points related with the yield stress in RD, transverse direction (TD) and the biaxial one are very close for both yield criteria. On the contrary, for the AA5042, the yield surfaces predicted by both yield criteria are completely different. Moreover, the CB2001 yield surface exhibits sharper corners, for both materials.

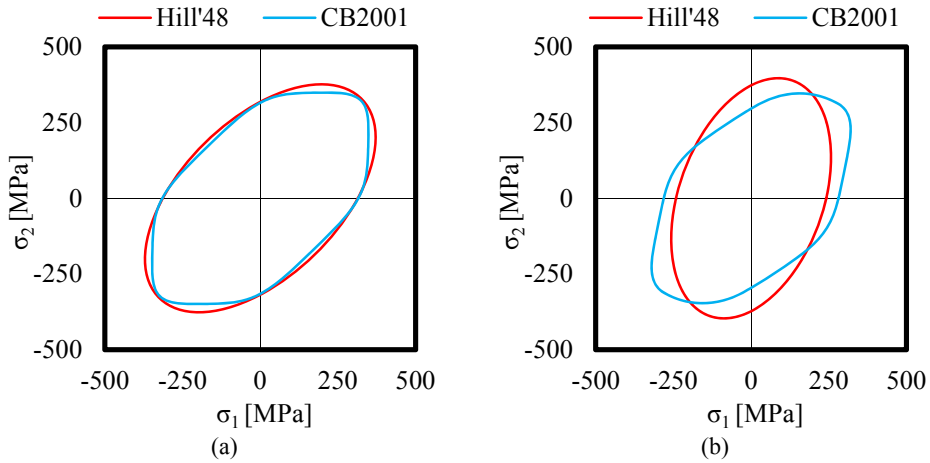

Fig. 4 – Predicted yield surfaces in the σ_{11}, σ_{22} plane for: a) AKDQ; b) AA5042.

4. RESULTS AND DISCUSSION

The *r*-values and yield stresses directionalities (the anisotropy) are the input parameters for the phenomenological constitutive models, and are directly linked with the earing phenomenon. In fact, it has been stated that a good prediction of such material directionalities controls the overall behavior of the earing profile. Based on these results, Yoon et al. 2011 [29] proposed an analytical function to estimate the cup height directionality,

$$H^{\text{cup}}(\theta) = t_0 + r_c + \frac{R_b}{A_{\theta+90}+1}\left(d^{A_{\theta+90}} - \frac{1}{d}\right) B_\theta^{A_{\theta+90}}, \tag{36}$$

where t_0 is the initial blank thickness, R_b is the blank radius and r_c is the radius of the cup defined by the punch fillet radius. The *r*-value and the yield stress directionalities influence is dictated by

$$A_{\theta+90} = \frac{r_{\theta+90}}{1+r_{\theta+90}} \quad \text{and} \quad B_\theta = \left(\frac{\sigma_{\text{ref}}}{\sigma_\theta^{\text{T}}}\right)^{\beta'}, \tag{37}$$

respectively. As shown in Fig. 5, the behavior of the rim in the direction defined by θ (to the RD) is controlled by the material compression properties in the direction defined by θ+90. Assuming that the uniaxial tension and compression lead to identical *r*-values, these can be expressed as a function of the plastic strains at the rim

$$r_{\theta+90} = \frac{\varepsilon_r}{\varepsilon_t} = -\frac{\varepsilon_r}{\varepsilon_r + \varepsilon_\theta}, \tag{38}$$

were subscripts *r*, θ and *t* correspond to the radial, circumferential and thickness directions, respectively. Based on Fig. 5, it is also assumed that the radial tensile traction can be modelled from the yield stress directionality σ_θ^T, such that

$$\sigma^{ref} = \frac{\int_0^{2\pi} \sigma_\theta^T d\theta}{2\pi} = \frac{1}{12}\left[\sigma_0^T + 2\left(\sigma_{15}^T + \sigma_{30}^T + \sigma_{45}^T + \sigma_{60}^T + \sigma_{75}^T\right) + \sigma_{90}^T\right], \tag{39}$$

for an orthotropic material, for which data is known for every 15°. The deceleration β′ factor is introduced to take into account the variation of the stress mode along the flange, as shown in Fig. 5, i.e. β′=1 corresponds to the assumption that the stress mode at the inner most flange is applied to the entire flange; β′=0.5 corresponds to a linear distribution of the radial tensile stress; the recommended value is $0.5 \le \beta' \le 1$. Finally, *d* corresponds to the ratio between the blank radius R_b and the cup radius R_c.

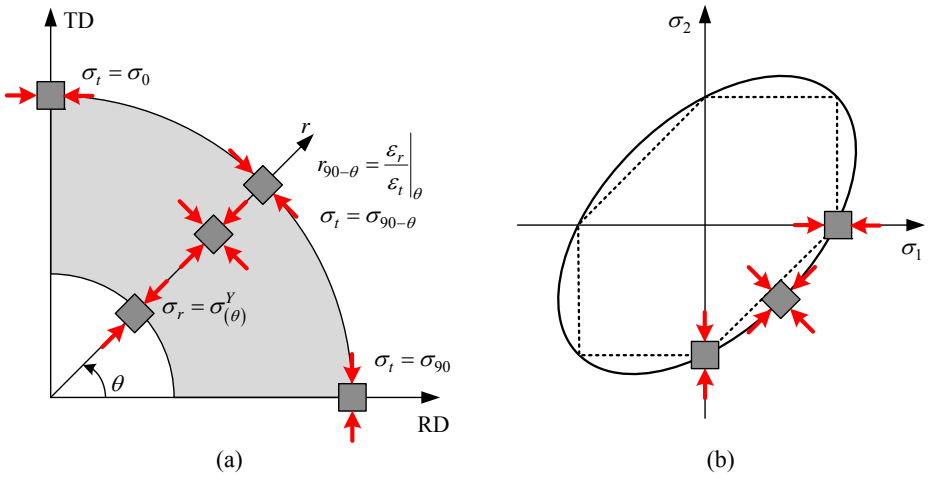

Fig. 5 – Deformation of an element on the flange: a) stress states on the flange; b) stress states on the yield surface (adapted from Yoon *et al*. 2011 [29]).

The numerical, experimental and analytical predictions of the cup height at the end of the deep drawing stage are compared in Fig. 6, for both materials. The analytical height was estimated based on the *r*-value and yield stress directionalities predicted using the CB2001 yield criterion, since it allows a better correlation with the experimental values (see Fig. 2 and Fig. 3). Globally, the cup height is relatively well predicted by either the analytical function or the numerical simulations. However, the number of ears and their peak-to-peak amplitude differs.

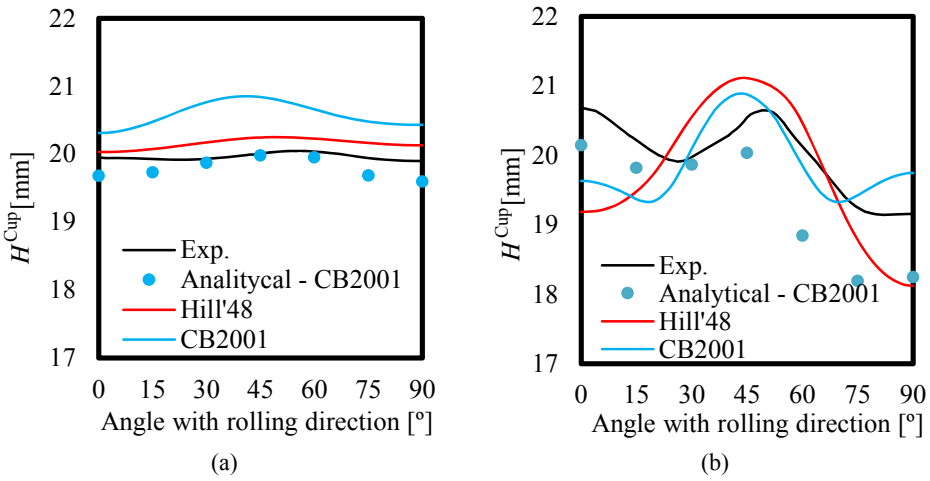

Fig. 6 – Experimental, numerical and analytical predictions of the cup height after deep drawing: a) AKDQ; b) AA5042.

In order to try to understand the differences in the predictions, the stress and strain states evolutions were analyzed for points located in the outermost flange, at every 15° with RD. Figure 7 presents the evolution of the ratio between the plastic strain along the radial and the thickness direction, estimated from the numerical results, and the *r*-values estimated with the CB2001 for each angle with RD, for both materials. The results presented correspond to the simulations performed with the CB2001, until a maximum value of the punch stroke of 20 mm, corresponding approximately to the instant at which the blank holder loses the contact with the blank. In case of AKDQ, the estimated $\varepsilon_r/\varepsilon_t$ values are always higher than the $r_{\theta+90}$ predicted by the CB2001. However, for the AA5042, there is a correlation between the $\varepsilon_r/\varepsilon_t$ and the $r_{\theta+90}$, except for $\theta=60°$ and $\theta=75°$. These different behaviors of the outer most flange can be explained based on the stress component

in the thickness direction, as shown in Fig. 8. For the AKDQ the blank-holder force is distributed more or less evenly in the entire flange, due to the almost isotropic behavior. Thus, for each in-plane direction, the stress component in the thickness direction is nonzero, and tends to increase with the punch displacement as a result of the decrease of the flange area. In case of AA5042, the blank-holder force is unevenly distributed, leading to null values except for θ=60°, θ=75° and θ=90°. These results indicate the influence of nonzero stress components in the thickness direction, modifying the shear stress state assumed by Yoon et al. [29] in their analytical formulation.

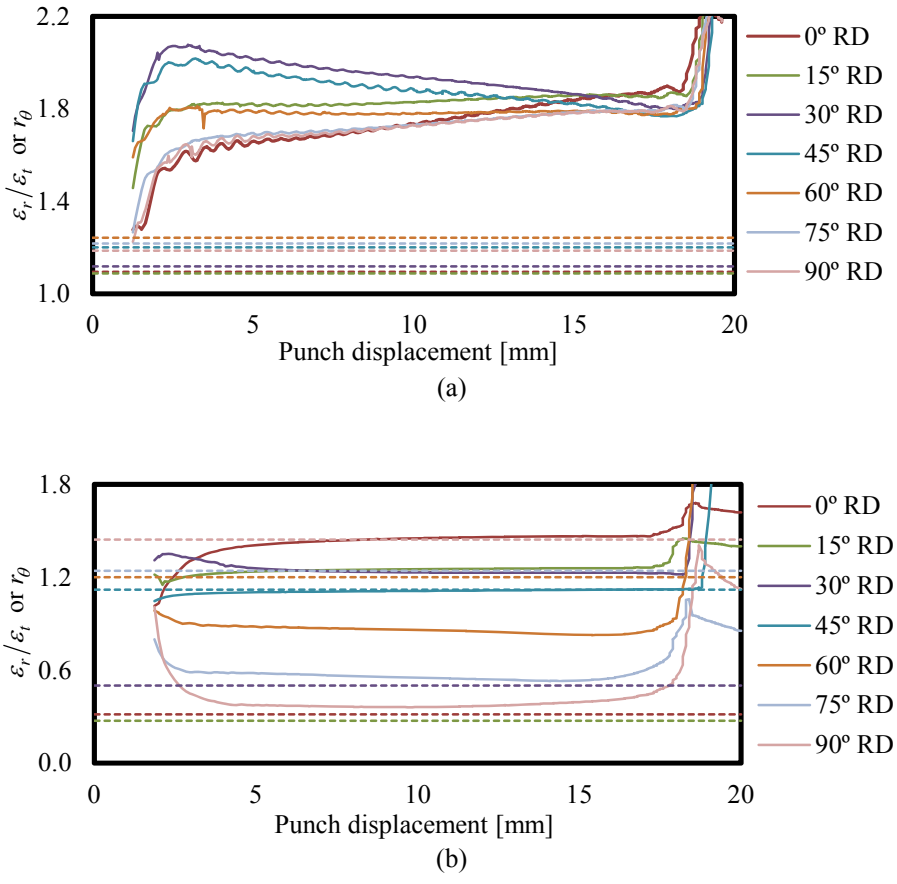

Fig. 7 – Evolution, with the punch displacement, of $\varepsilon_r/\varepsilon_t$ and r-values estimated with the CB2001, for each angle with RD: a) AKDQ; b) AA5042.

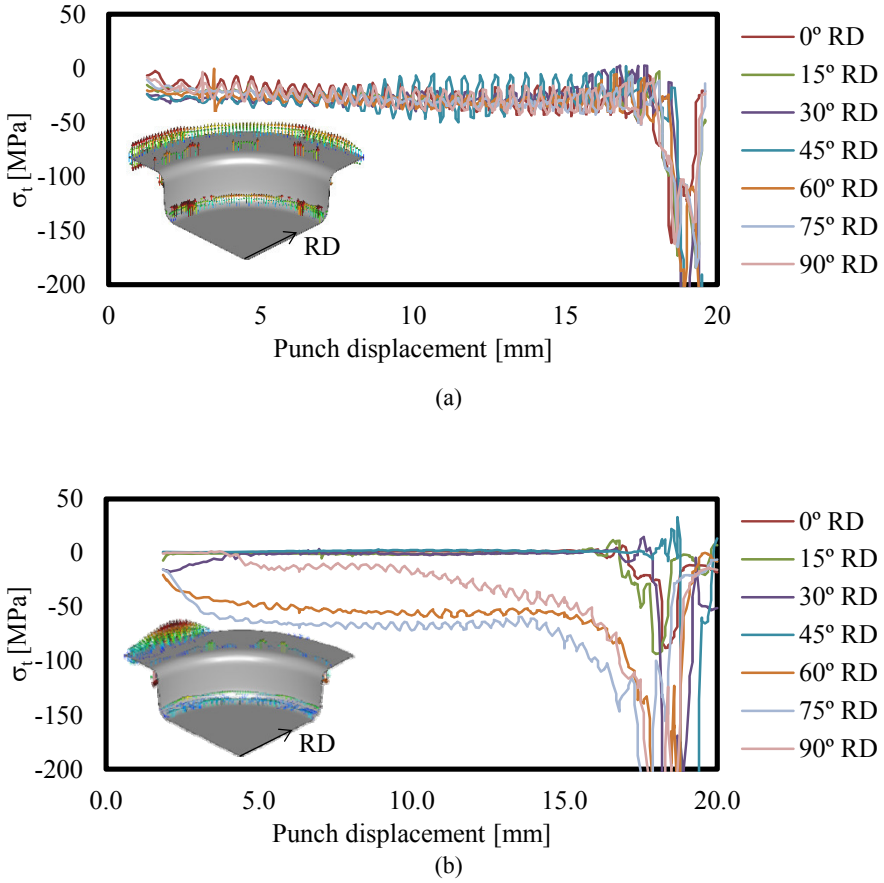

Fig. 8 – Evolution of the stress component in the thickness direction as function of the punch displacement, for several angles with RD: a) AKDQ; b) AA5042.

The numerical simulation of the deep drawing of the cylindrical cup was also performed considering a constant gap between the blank-holder and the die (0.27 mm), for the AA5042 using the CB2001. In this condition, the stress component in the thickness direction remains always close to zero for all directions, until a punch displacement of approximately 14.0 mm (see Fig. 9b). Therefore, the estimated $\varepsilon_r/\varepsilon_t$ values are always close to the $r_{\theta+90}$ values predicted by the CB2001, as shown in Fig. 9a. However, the stress directionalities can have more impact than the *r*-values in the estimative of the cup height and ears profile [29]. Therefore, Fig. 10 presents the evolution of the ratio between the circumferential stress and

the flow stress, estimated from the numerical results, and the ratio between the yield stress estimated with the CB2001 and Y_0, for each angle with RD. Also in this case the estimated σ_θ/Y values are always close to the $\sigma_{\theta+90}/Y_0$ values predicted by the CB2001, for the simulation performed with a constant gap between the blank holder and the die (see in Fig. 10b).

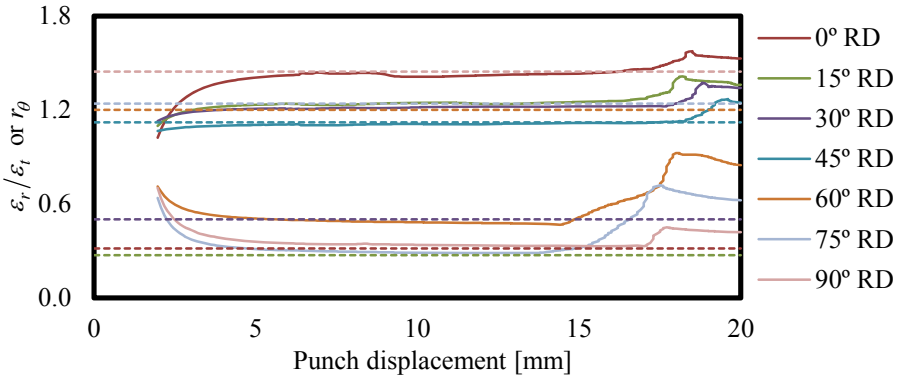

(a)

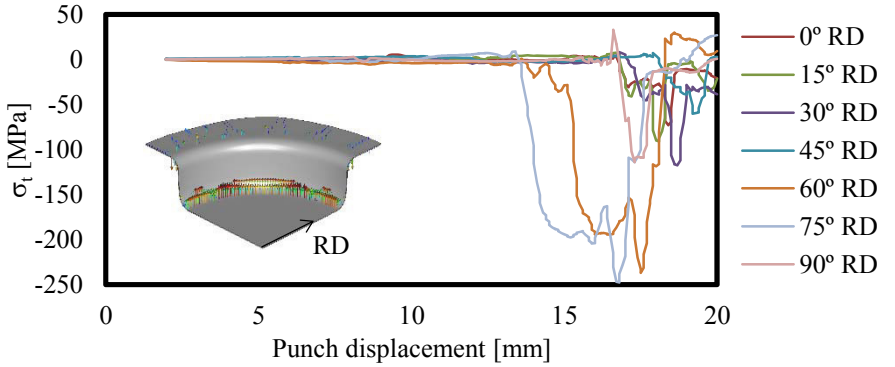

(b)

Fig. 9 – Numerical simulation of AA5042 considering a fixed position of the blank-holder: evolution with the punch displacement of: a) $\varepsilon_r/\varepsilon_t$ and r-values estimated with the CB2001, for each angle with RD; b) the stress component in the thickness direction, for each angle with RD.

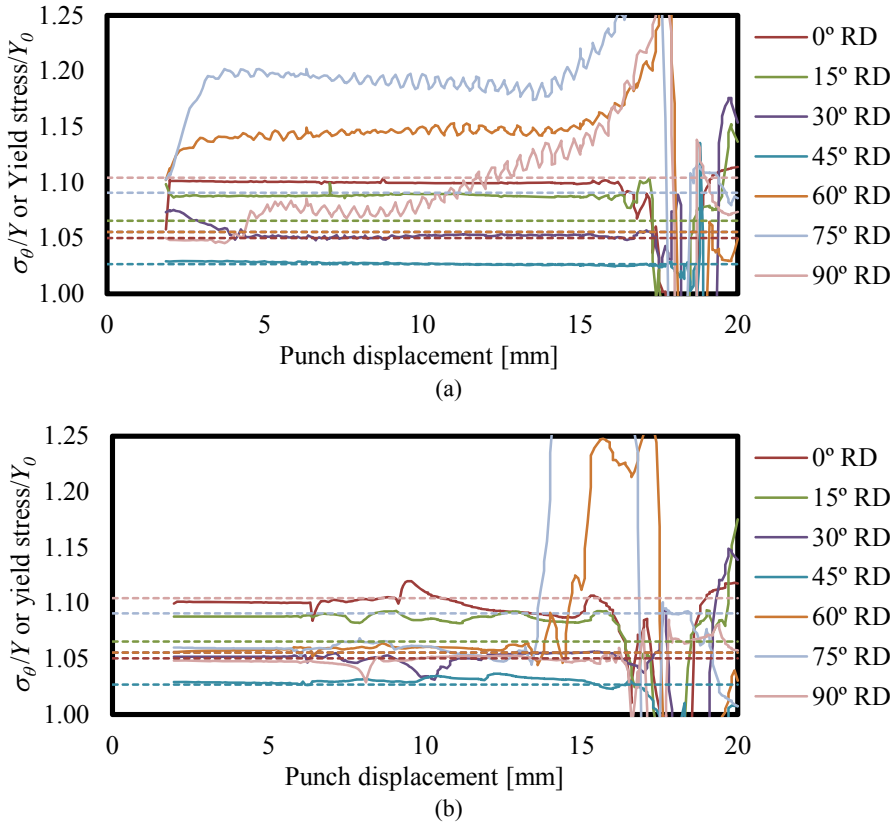

Fig. 10 – Evolution with the punch displacement of σ_θ/Y and ratio between the yield stress estimated with the CB2001 and Y_0, for each angle with RD. Numerical simulation of AA5042 considering: a) a constant blank holder force; b) a fixed position of the blank-holder.

For a constant blank holder force, there is a correlation between the σ_θ/Y and the $\sigma_{\theta+90}/Y_0$, except for $\theta \geq 60º$ (see in Fig. 10a). Consequently, the numerically predicted cup height becomes closer to the analytical one when using the fixed gap (labelled CB2001F), as shown in Fig. 11a. The comparison between both numerical results shows that the higher differences occur for $\theta \geq 60º$, which corresponds to zone of the flange with compressive stresses in the thickness direction (see Fig. 8b. Yoon and Cazacu [32] reported a similar trend with the friction coefficient change, i.e. the decrease of this value lead to a smaller cup height mainly for $\theta \geq 60º$. The same was observed for the simulation performed with a null value for the friction coefficient (labelled CB2001(f = 0), as also shown in Fig. 11a. Although not shown here, the stress component in the thickness

direction vanishes, in the must outer flange, for $\theta = 90^{o}$, when using a null friction coefficient. Both results highlight the importance of the stress state in the cup's flange for an accurate description of the cup height, number and amplitude of the ears. The analysis of Fig. 6b and Fig. 11a indicates that the value predicted for the peak-to-peak amplitude of the cup height is closer for the numerical results obtained with a constant blank-holder force with the Hill'48 yield criterion and a fixed blank-holder with the CB2001, than with both conditions using the CB2001 yield criterion. This is also related with the stress state in the flange, since the Hill'48 predicts a higher blank thickening in the flange area leading to a maximum value of the gap between the blank-holder and the die similar to the one imposed in the simulation performed with a fixed value (see Fig. 11b). For the AKDQ steel the friction coefficient does not change the earing trend and only slightly changes the cup height, as shown in Fig. 12a, for a friction coefficient of zero (labelled CB2001(f = 0)) and 0.1 (labelled CB2001(f = 0.1). This is related with the small change in the blank-holder displacement (see Fig. 12b), influenced by the small increase of the radial stress, induced by the increase of the friction coefficient. Nevertheless, this effect is similar for the entire flange, leading to a negligible effect in the earing trend. Thus, a good prediction of the material directionalities controls the overall accuracy of the earing profile, because it dictates the interaction with process parameters such as the blank holder force distribution.

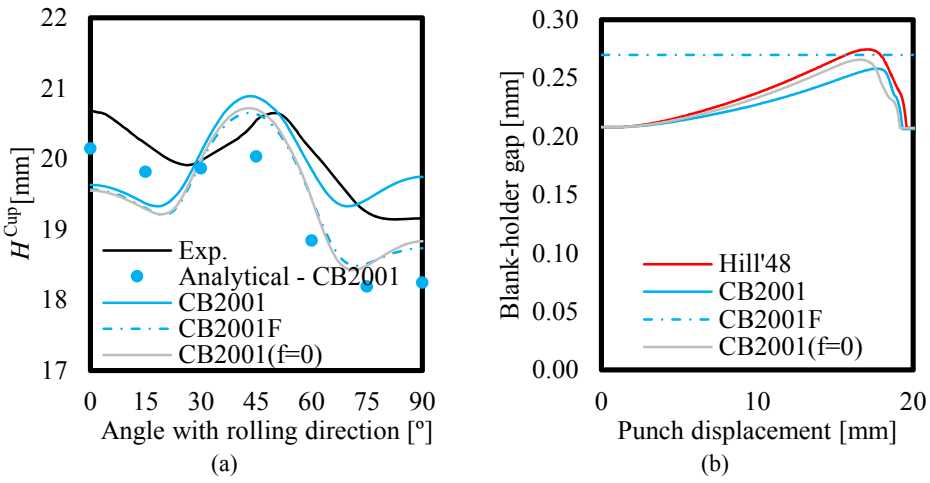

Fig. 11 – a) Experimental, numerical and analytical predictions of the AA5042 cup height after deep drawing; b) evolution with the punch displacement of the blank holder gap with the die.

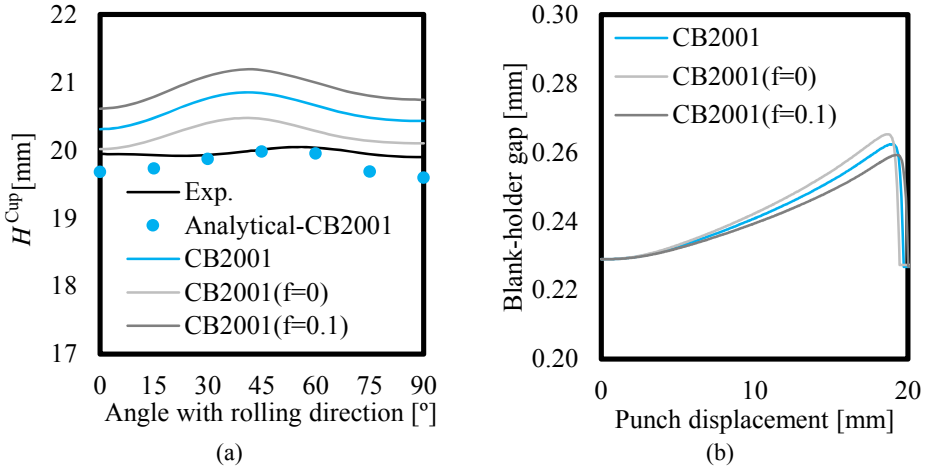

Fig. 12 – a) Experimental, numerical and analytical predictions of the AKDQ cup height after deep drawing; b) evolution with the punch displacement of the blank holder gap with the die.

The computational efficiency of the proposed integration algorithm is shown in Table 3, by means of both elapsed real time and total number of time increments to carry out the simulation of the deep drawing phase, using the two yield criteria, i.e. Hill48 and CB2001. The number of increments with its size reduced (*NTrial* Strategy), caused by convergence problems during the iterative loop, was selected in this study to indicate the robustness of the integration algorithm. Indeed, the so-called *NTrial* strategy, currently implemented in DD3IMP, allows overcoming most of convergence issues by automatically reducing the increment size, when convergence is not attained within the allowed number of iterations. The results show that the computational efficiency is not directly penalized by the selection of the CB2001 yield criterion. In fact, the numerical simulations performed with AKDQ steel, presenting a more isotropic behavior, tends to require more iterations. This is mainly related with the difficulties associated with contact status convergence for a higher number of nodes, in each iteration. This effect is more visible for AKDQ due to the alignment of the nodes along the circumferential direction, enabling the simultaneous change of the contact conditions that results in higher oscillations of the contact forces and, consequently, of the non-equilibrated forces and stress fields (see Fig. 8).

Nevertheless, during the deep drawing phase, only small differences in the punch force evolution predicted with both yield criteria can be observed. These results are shown in Fig. 13a and Fig. 14a, for the AKDQ and the AA5042, respectively. For AKDQ, the higher thickening predicted for the outermost flange, for a punch displacement of 35 mm (see Fig. 13b), results in a slightly higher value for the maximum punch force, visible also for the ironing stage. In case of

AA5042, the maximum value of the punch force is always slightly higher when using CB2001. However, it is more difficult to correlate this result with the thickening predicted for the most outer flange, for a punch displacement of 35 mm (see Fig. 14b). As expected the ironing process increases the cup height, although not changing the peak-to-peak amplitude, for both yield criteria. The results for the cup height at the end of the ironing stage are shown in Fig. 15 for both materials. They should be compared with the ones presented in Fig. 6 to confirm that also the experimental results show a similar profile before and after the ironing stage. Globally, the conditions for the ironing phase are quite different for both materials, since the blanks present distinct thickness profiles at the end of the drawing stage and similar at the end of the ironing (see Fig. 1). Moreover, conditions differ for both yield criteria, since the deep drawing stage imposes cups with different heights and maximum thickness values. Therefore, the analysis of the computational performance based on the number of increments for the ironing stage is biased.

Table 3

Computational performance of the deep drawing stage using different yield criteria

	AKDQ		AA5042	
	Hill'48	CB2001	Hill'48	CB2001
N° of increments	553	667	553	512
N° of iterations	5727	5853	5298	4075
NTrial strategy	73	226	137	78
Computational time [hours]	5.35	5.96	4.34	3.35

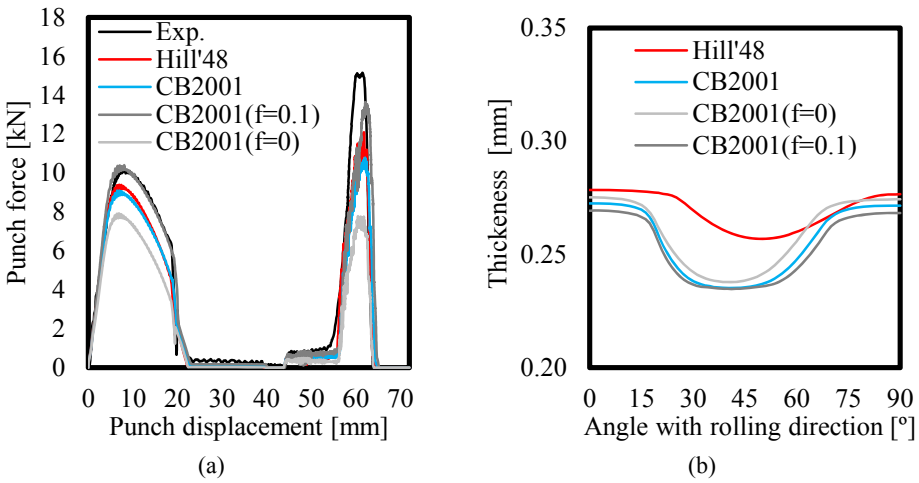

(a) (b)

Fig. 13 – AKDQ: a) punch force evolution with its displacement; b) thickness distribution on the most outer flange, for a punch displacement of 35 mm.

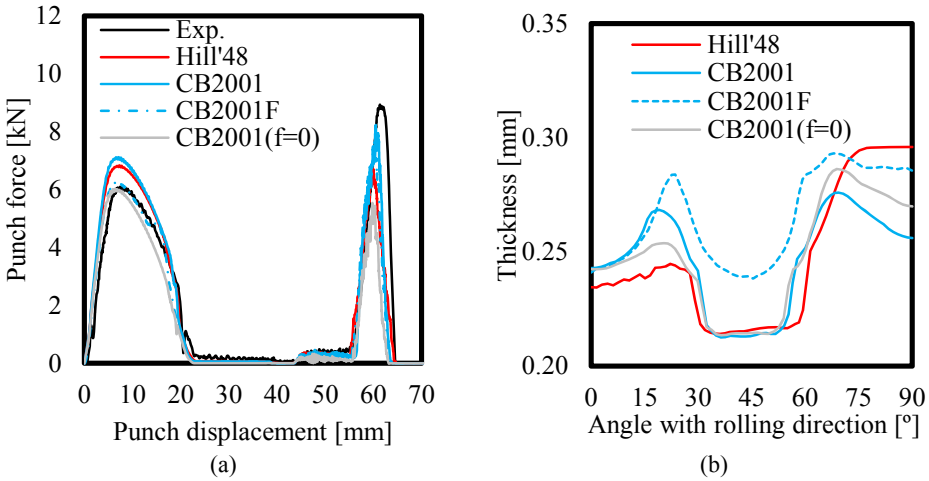

Fig. 14 – AA5042: a) Punch force evolution with its displacement; b) thickness distribution on the most outer flange, for a punch displacement of 35 mm.

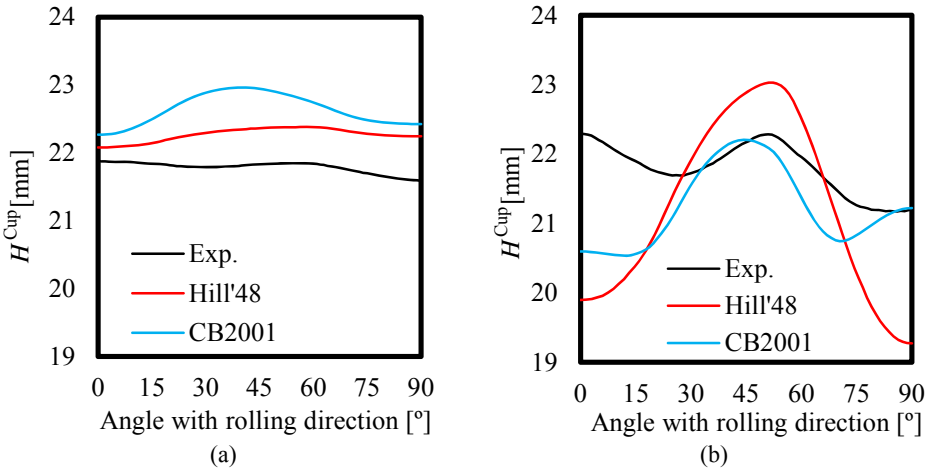

Fig. 15 – Experimental and numerical predictions of the cup height after the ironing process for: a) AKDQ; b) AA5042.

5. CONCLUDING REMARKS

The numerical simulation of the deep drawing of a cylindrical cup is performed with the implicit in-house finite element solver DD3IMP. The analysis is focused in the accurate description of the orthotropic behavior of metallic sheets

using the non-quadratic anisotropic yield criterion CB2001. Two different materials are considered for the blank: AA5042 aluminum alloy and AKDQ steel. The material parameters are identified from experimental data, by best fit to the experimental results of conventional uniaxial tensile tests, biaxial yield stress and r_b. The results shown that the accuracy of the earing profile prediction is strongly influenced by the description of the anisotropy of both *r*-values and yield stresses. Additionally, for materials with a strong anisotropic behavior of the *r*-values (e.g. AA5042 aluminum alloy), the earing profile is influenced by the global process modeling, particularly the contact conditions in the flange. This is related with the uneven thickness strain distribution in the sheet plane, which leads to a non-uniform contact force distribution, more concentrated in a limited region of the flange. Also, the computational time of the numerical simulations is mainly dictated by the contact conditions between the die and the blank-holder, with a negligible influence of the sharper curvature of the yield surface. Thus, when using analytical partial derivatives of the yield surface in the constitutive model numerical integration, the use of non-quadratic anisotropic yield criteria does not affect the computational performance efficiency.

APPENDIX A: ANALYTICAL EXPRESSIONS OF THE DERIVATIVES OF THE CB2001 YIELD CRITERION

This section is related to the calculations of the following quantities,

$$\beta, \quad \mathbf{V} = \frac{\partial \bar{\sigma}}{\partial\left(\boldsymbol{\sigma}'_{\mathrm{F}} - \mathbf{X}_{\mathrm{F}}\right)}, \quad \mathbf{Q} = \frac{\partial^2 \bar{\sigma}}{\partial\left(\boldsymbol{\sigma}'_{\mathrm{F}} - \mathbf{X}_{\mathrm{F}}\right)^2}. \tag{40}$$

specifically related with the numerical implementation of the CB2001 yield criterion in the FE solver DD3IMP.

Taking into account the isochoric character of plasticity, the implementation of the state update algorithm in DD3IMP is done in a five-dimensional deviatoric space, instead of the Cartesian space, given that any symmetric deviatoric tensor has only 5 independent components [23]. Thus, considering the effective deviatoric stress state tensor Σ_{ij}, $i, j = 1,2,3$, represented in the Cartesian space, its components in the five-dimensional deviatoric space Σ_I, $I = 1,...5$, are given by the following transformations

$$\Sigma_1 = \frac{1}{\sqrt{2}}\left(\Sigma_{11} - \Sigma_{22}\right); \quad \Sigma_2 = \sqrt{\frac{3}{2}}\left(\Sigma_{11} + \Sigma_{22}\right) = -\sqrt{\frac{3}{2}}\Sigma_{33};$$

$$\Sigma_3 = \sqrt{2}\Sigma_{23}; \quad \Sigma_4 = \sqrt{2}\Sigma_{13}; \quad \Sigma_5 = \sqrt{2}\Sigma_{12}. \tag{41}$$

This transformation from Σ_{ij} $(i, j = 1,2,3)$ to Σ_I (with $I = 1,...,5$) can also be written in matrix form using Voigt notation of the symmetric tensor Σ_{ij} $(i, j = 1,2,3)$, introducing the following transformation matrix:

$$\begin{Bmatrix} \Sigma_1 \\ \Sigma_2 \\ \Sigma_3 \\ \Sigma_4 \\ \Sigma_5 \end{Bmatrix} = \begin{bmatrix} 1/\sqrt{2} & -1/\sqrt{2} & 0 & 0 & 0 & 0 \\ \sqrt{3/2} & \sqrt{3/2} & 0 & 0 & 0 & 0 \\ 0 & 0 & 0 & \sqrt{2} & 0 & 0 \\ 0 & 0 & 0 & 0 & \sqrt{2} & 0 \\ 0 & 0 & 0 & 0 & 0 & \sqrt{2} \end{bmatrix} \begin{Bmatrix} \Sigma_{11} \\ \Sigma_{22} \\ \Sigma_{33} \\ \Sigma_{23} \\ \Sigma_{13} \\ \Sigma_{12} \end{Bmatrix}. \tag{42}$$

The inverse transformation, from the five-dimensional space to the Cartesian one, i.e. from Σ_I (with $I = 1,...,5$) to Σ_{ij} $(i, j = 1,2,3)$, can also be written as:

$$\begin{Bmatrix} \Sigma_{11} \\ \Sigma_{22} \\ \Sigma_{33} \\ \Sigma_{23} \\ \Sigma_{13} \\ \Sigma_{12} \end{Bmatrix} = \begin{bmatrix} 1/\sqrt{2} & 1/\sqrt{6} & 0 & 0 & 0 \\ -1/\sqrt{2} & 1/\sqrt{6} & 0 & 0 & 0 \\ 0 & -\sqrt{2/3} & 0 & 0 & 0 \\ 0 & 0 & 1/\sqrt{2} & 0 & 0 \\ 0 & 0 & 0 & 1/\sqrt{2} & 0 \\ 0 & 0 & 0 & 0 & 1/\sqrt{2} \end{bmatrix} \begin{Bmatrix} \Sigma_1 \\ \Sigma_2 \\ \Sigma_3 \\ \Sigma_4 \\ \Sigma_5 \end{Bmatrix}. \tag{43}$$

The same can also be applied for any fourth-order symmetric and deviatoric tensor **T**, which corresponds to T_{KL} (with $K, L = 1,...6$) using the Voigt notation. Thus, the use of the five-dimensional deviatoric space enables expressing this tensorial quantity as T_{IJ} (with $I, J = 1,...5$). This reduces the number of independent terms and simplifies the notation, as shown afterwards, for the second-order tensor **V** and particularly for the fourth-order tensor **Q**.

In the case of CB2001 yield criterion, the equivalent stress is given by Eq. 28, but the invariants J_2^0 and J_3^0 can be written as a function of the components of the effective stress tensor in the five-dimensional deviatoric space, i.e.

$$J_2^0 = A_1\Sigma_1^2 + A_2\Sigma_2^2 + A_3\Sigma_1\Sigma_2 + A_4\Sigma_5^2 + A_5\Sigma_4^2 + A_6\Sigma_3^2 \quad \text{and} \tag{44}$$

$$\begin{aligned} J_3^0 = {} & B_1\Sigma_1^3 + B_2\Sigma_1^2\Sigma_2 + B_1\Sigma_1\Sigma_2^2 + B_4\Sigma_2^3 + B_5\Sigma_1\Sigma_3^2 + B_6\Sigma_2\Sigma_3^2 \\ & + B_7\Sigma_1\Sigma_4^2 + B_8\Sigma_2\Sigma_4^2 + B_9\Sigma_1\Sigma_5^2 + B_{10}\Sigma_2\Sigma_5^2 + B_{11}\Sigma_3\Sigma_4\Sigma_5 \end{aligned}, \tag{45}$$

where

$$\begin{aligned} A_1 &= 1/12\left(4a_1 + a_2 + a_3\right) & B_1 &= 1/\left(54\sqrt{2}\right)\left(4b_1 + b_2 + b_3 - 4b_4\right) \\ A_2 &= 1/4\left(a_2 + a_3\right) & B_2 &= 3/\left(\sqrt{3}\right)/\left(54\sqrt{2}\right)\left(2b_1 + b_2 + b_3 + 2b_4\right) \\ A_3 &= 1/2\sqrt{3}\left(a_3 - a_2\right) & B_3 &= 9/\left(54\sqrt{2}\right)\left(b_2 - b_3\right) \\ A_4 &= 1/2\left(a_4\right) & B_4 &= 3/\left(\sqrt{3}\right)/\left(54\sqrt{2}\right)\left(-2b_1 + b_2 + b_3 - 2b_4\right) \\ A_5 &= 1/2\left(a_5\right) & B_5 &= -\sqrt{2}/12\left(2b_6 + b_7\right) \\ A_6 &= 1/2\left(a_6\right) & B_6 &= -\sqrt{6}/12\left(b_7\right) \\ & & B_7 &= -\sqrt{2}/12\left(b_8 - 4b_9\right) \\ & & B_8 &= -\sqrt{6}/12\left(b_8\right) \\ & & B_9 &= -\sqrt{2}/6\left(b_5 - b_{10}\right) \\ & & B_{10} &= \sqrt{6}/6\left(b_{10}\right) \\ & & B_{11} &= 1/\sqrt{2}\left(b_{11}\right) \end{aligned} \tag{46}$$

The scalar β has to be evaluated whenever the effective stress state at the beginning of the time increment is elastic. It is determined with the consistency condition, such that

$$\mathcal{F}\left(\beta\right) = \bar{\sigma}\left(\boldsymbol{\sigma}_0 - \mathbf{X}_0, \Delta\boldsymbol{\varepsilon}', \beta\right) - Y_I = \bar{\sigma}\left(\Sigma_0, \Delta\boldsymbol{\varepsilon}', \beta\right) - Y_I = 0\,, \tag{47}$$

where subscript I denotes the flow stress at the beginning of the time increment. β is the only unknown of this non-linear equation. Thus, the Newton method is used to iteratively determine β, given by the relation

$$\beta^{i+1} = \beta^{i} - \frac{\mathcal{F}^{i}}{\mathcal{F}^{i\prime}}. \tag{48}$$

The scalar quantities $\mathcal{F}^{i}$ and $\mathcal{F}^{i\prime}$ are required, being the first one given by Eq. 47 and the second one by

$$\mathcal{F}^{i\prime} = \frac{\partial\bar{\sigma}\left(\boldsymbol{\sigma}_0 - \mathbf{X}_0, \Delta\boldsymbol{\varepsilon}', \beta\right)}{\partial\beta^{i}} = \frac{\partial\bar{\sigma}}{\partial\boldsymbol{\Sigma}^{i}}\frac{\partial\boldsymbol{\Sigma}^{i}}{\partial\beta^{i}} = \mathbf{V}^{i} : \left(2\mu\Delta\boldsymbol{\varepsilon}'\right). \tag{49}$$

Taking into account the equivalent stress definition given in Eq. 28 and the two generalized invariants defined in the five-dimensional deviatoric space, after some mathematical developments the tensor **V** can be written as

$$V_I\big|_{CB2001} = \frac{\partial\bar{\sigma}}{\partial\Sigma_I} = \frac{9}{2\bar{\sigma}^5}\left[3\left(J_2^0\right)^2\frac{\partial J_2^0}{\partial\Sigma_I} - 2c\left(J_3^0\right)\frac{\partial J_3^0}{\partial\Sigma_I}\right], \text{ with } I = 1,...,5. \tag{50}$$

The tensor **Q** is given by

$$\begin{aligned} Q_{IJ}\big|_{CB2001} &= \frac{\partial^2\bar{\sigma}}{\partial\Sigma_I\partial\Sigma_J} = \frac{\partial V_I}{\partial\Sigma_J} = \\ &= -\frac{5}{\bar{\sigma}}V_I V_J + \frac{9}{2\bar{\sigma}^5}\left[6\left(J_2^0\right)\frac{\partial J_2^0}{\partial\Sigma_I}\cdot\frac{\partial J_2^0}{\partial\Sigma_J} + 3\left(J_2^0\right)^2\frac{\partial^2 J_2^0}{\partial\Sigma_I\partial\Sigma_J}\right., \\ &\left. -2c\left(J_3^0\right)\frac{\partial J_3^0}{\partial\Sigma_I}\cdot\frac{\partial J_3^0}{\partial\partial\Sigma_J} - 2c\left(J_3^0\right)\frac{\partial^2 J_3^0}{\partial\Sigma_I\partial\Sigma_J}\right] \end{aligned} \tag{51}$$

with $I, J = 1,...,5$. The terms relative to the first order derivatives $\frac{\partial J_2^0}{\partial\Sigma_I}$ and $\frac{\partial J_3^0}{\partial\Sigma_I}$ are defined as

$$\frac{\partial J_2^0}{\partial \Sigma_I} = \begin{Bmatrix} 2A_1\Sigma_1 + A_3\Sigma_2 \\ 2A_2\Sigma_2 + A_3\Sigma_1 \\ 2A_6\Sigma_3 \\ 2A_5\Sigma_4 \\ 2A_4\Sigma_5 \end{Bmatrix}, \tag{52}$$

and

$$\frac{\partial J_3^0}{\partial \Sigma_I} = \begin{Bmatrix} 3B_1\Sigma_1^2 + 2B_2\Sigma_1\Sigma_2 + B_3\Sigma_2^2 + B_5\Sigma_3^2 + B_7\Sigma_4^2 + B_9\Sigma_5^2 \\ B_2\Sigma_1^2 + 2B_3\Sigma_1\Sigma_2 + B_4\Sigma_2^2 + B_6\Sigma_3^2 + B_8\Sigma_4^2 + B_{10}\Sigma_5^2 \\ 2B_5\Sigma_1\Sigma_3 + 2B_6\Sigma_2\Sigma_3 + B_{11}\Sigma_4\Sigma_5 \\ 2B_7\Sigma_1\Sigma_4 + 2B_8\Sigma_2\Sigma_4 + B_{11}\Sigma 3\Sigma_5 \\ 2B_9\Sigma_1\Sigma_5 + 2B_{10}\Sigma_2\Sigma_5 + B_{11}\Sigma_3\Sigma_4 \end{Bmatrix}, \tag{53}$$

with $I = 1,...,5$. The terms relative to the second order derivatives, $\frac{\partial^2 J_2^0}{\partial \Sigma_I \partial \Sigma_J}$ and $\frac{\partial^2 J_3^0}{\partial \Sigma_I \partial \Sigma_J}$, are defined as

$$\frac{\partial^2 J_2^0}{\partial \Sigma_I \partial \Sigma_J} = \begin{Bmatrix} 2A_1 & A_3 & 0 & 0 & 0 \\ A_3 & 2A_2 & 0 & 0 & 0 \\ 0 & 0 & 2A_6 & 0 & 0 \\ 0 & 0 & 0 & 2A_5 & 0 \\ 0 & 0 & 0 & 0 & 2A_4 \end{Bmatrix}, \tag{54}$$

and

$$\frac{\partial^2 J_3^0}{\partial \boldsymbol{\Sigma}_I \partial \boldsymbol{\Sigma}_J} = \begin{Bmatrix} 6B_1\Sigma_1 + 2B_2\Sigma_2 & 2B_2\Sigma_1 + 2B_3\Sigma_2 & 2B_5\Sigma_3 & 2B_7\Sigma_4 & 2B_9\Sigma_5 \\ 2B_2\Sigma_1 + 2B_3\Sigma_2 & 2B_3\Sigma_1 + 2B_4\Sigma_2 & 2B_6\Sigma_3 & 2B_8\Sigma_4 & B_{10}\Sigma_5 \\ 2B_5\Sigma_3 & 2B_6\Sigma_3 & 2B_5\Sigma_1 + 2B_6\Sigma_2 & B_{11}\Sigma_5 & B_{11}\Sigma_4 \\ 2B_7\Sigma_4 & 2B_8\Sigma_4 & B_{11}\Sigma_5 & 2B_7\Sigma_1 + 2B_8\Sigma_2 & B_{11}\Sigma_3 \\ 2B_9\Sigma_5 & 2B_{10}\Sigma_5 & B_{11}\Sigma_4 & B_{11}\Sigma_3 & 2B_9\Sigma_1 + 2B_{10}\Sigma_2 \end{Bmatrix} \tag{55}$$

The initial effective stress state is then updated to the initial yield surface as

$$\left(\boldsymbol{\sigma}_0 - \mathbf{X}_0\right)^* \leftarrow \boldsymbol{\sigma}_0 - \mathbf{X}_0 + \beta\left(2\mu\Delta\boldsymbol{\varepsilon}'\right). \tag{56}$$

Acknowledgements. The authors gratefully acknowledge the financial support of the Portuguese Foundation for Science and Technology (FCT) under project PTDC/EMS-TEC/1805/2012. P.D. Barros is also grateful to the FCT for the PhD Grant SFRH/BD/98545/2013 and D.M. Neto is also grateful for the Post-Doctoral Fellowship SFRH/BPD/101334/2014.

Received on June 8, 2015

REFERENCES

1. GANTAR, G., PEPELNJAK, T., KUZMAN, K., *Optimization of sheet metal forming processes by the use of numerical simulations*, J. Mater. Process. Technol., **130–131**, pp. 54–59, 2002.
2. NOELS, L., STAINIER, L., PONTHOT, J-P., *Combined implicit/explicit time-integration algorithms for the numerical simulation of sheet metal forming*, J. Comput. Appl. Math., **168**, pp. 331–339, 2004.
3. YANG, D.Y., JUNG, D.W., SONG, I.S., YOO, D.J., LEE, J.H., *Comparative investigation into implicit, explicit, and iterative implicit/explicit schemes for the simulation of sheet-metal forming processes*, J. Mater. Process. Technol., **50**, pp. 39–53, 1995.
4. TEKKAYA, A.E., MARTINS, P.A.F., *Accuracy, reliability and validity of finite element analysis in metal forming: a user's perspective*, Engineering Computations, **26**, *8*, pp. 1026–1055, 2009.
5. SAFAEI, M., *Constitutive modelling of anisotropic sheet metals based on a non-associated flow rule*, PhD Thesis, Faculty of Engineering and Architecture, Ghent University, Belgium, 2013.
6. NETO, D.M., OLIVEIRA, M.C., ALVES, J.L., MENEZES, L.F., *Influence of the plastic anisotropy modelling in the reverse deep drawing process simulation*, Mater Des, **60**, pp. 368–379, 2014.
7. CAZACU, O., BARLAT, F., *Generalization of Drucker's Yield Criterion to Orthotropy*, Math. Mech. Solids., **6**, *6*, pp. 613–630, 2001.
8. MENEZES, L.F., TEODOSIU, C., *Three-dimensional numerical simulation of the deep-drawing process using solid finite elements*, J. Mater. Process. Technol., **97**, pp. 100–106, 2000.
9. OLIVEIRA, M.C., ALVES, J.L., MENEZES, L.F., *Algorithms and Strategies for Treatment of Large Deformation Frictional Contact in the Numerical Simulation of Deep Drawing Process*, Arch. Comput. Methods. Eng., **15**, pp. 113–162, 2008.
10. ALART, P., CURNIER, A., *A mixed formulation for frictional contact problems prone to Newton like solution methods*, Comput. Methods. Appl. Mech. Eng., **92**, *3*, pp. 353–375, 1991.

11. YAMADA, Y., YOSHIMURA, N., SAKURAI, T., *Plastic stress-strain matrix and its application for the solution of elastic-plastic problems by the finite element method*, Int J Mech Sci, **10**, *5*, pp. 343–354, 1968.
12. NETO, D.M., OLIVEIRA, M.C., MENEZES, L.F., ALVES, J.L., *Applying Nagata patches to smooth discretized surfaces used in 3D frictional contact problems*, Comput. Methods. Appl. Mech. Eng., **271**, pp. 296–320, 2014.
13. NETO, D.M., OLIVEIRA, M.C., MENEZES, L.F., ALVES, J.L., *Nagata patch interpolation using surface normal vectors evaluated from the IGES file*, Finite Elem Anal Des, **72**, pp. 35–46, 2013.
14. TEODOSIU, C., DANIEL, D., CAO, H-L., DUVAL, J-L., *Modelling and simulation of the can-making process using solid finite elements*, J. Mater. Process. Technol., **50**, pp. 133–143, 1995.
15. MENEZES, L.F., NETO, D.M., OLIVEIRA, M.C., ALVES, J.L., *Improving Computational Performance through HPC Techniques: case study using DD3IMP in-house code*, AIP Conf. Proc, **1353**, pp. 1220–1225, 2011.
16. HILL, R., *A Theory of the Yielding and Plastic Flow of Anisotropic Metals*, Proc. R. Soc. A. Math. Phys. Eng. Sci., **193**, pp. 281–297, 1948.
17. BARLAT, F., LEGE, D.J., BREM, J.C., *A six-component yield function for anisotropic materials*, Int. J. Plast., **7**, *7*, pp. 693–712, 1991.
18. DRUCKER, D.C., PRAGER, W., *Soil mechanics and plastic analysis for limit design*, Q. Appl. Math., **10**, pp. 157–165, 1952.
19. KARAFILLIS, A.P., BOYCE, M.C., *A general anisotropic yield criterion using bounds and a transformation weighting tensor*, J. Mech. Phys. Solids., **41**, *12*, pp. 1859–1886, 1993.
20. CAZACU, O., PLUNKETT, B., BARLAT, F., *Orthotropic yield criterion for hexagonal closed packed metals*, Int. J. Plast., **22**, *7*, pp. 1171–1194, 2006.
21. LEMAITRE, J., CHABOCHE, J-L., *Mechanics of Solid Materials*, Cambridge University Press, 1990.
22. TEODOSIU, C., HU, Z., *Evolution of the intergranular microstructure at moderate and large strains: Modelling and computational significance*, Numiform'95 on Simulation of Materials Processing: Theory, Methods and Applications, Balkema, pp. 173–182, 1995.
23. ALVES, J.L., *Simulação numérica do processo de estampagem de chapas metálicas: modelação mecânica e métodos numéricos*, PhD Thesis, University of Minho, Portugal, 2003.
24. DICK, R.E., YOON, J.W., HUH, H.S., BAE, G., *BM1 – Earing Evolution During Drawing and Ironing processes, Part C Benchmark Problems and Results*, Numisheet'2001 8th Int. Conf. Work. Numer. Simul. 3D Sheet Met. Form. Process, pp. 171–226, 2011.
25. HUGHES, T.J.R., *Generalization of selective integration procedures to anisotropic and nonlinear media*, Int. J. Numer. Methods. Eng., **15**, *9*, pp. 1413–1418, 1980.
26. BARROS, P.D., ALVES, J.L., OLIVEIRA, M.C., MENEZES, L.F., *Earing evolution during drawing and ironing processes*, WCCM 10th World Congr. Comput. Mech., Sao Paulo, pp. 3954–3973, 2012.
27. ALVES, J.L., OLIVEIRA, M.C., MENEZES, L.F., *An advanced constitutive model in the sheet metal forming simulation: the Teodosiu microstructural model and the Cazacu Barlat yield criterion*, AIP Conf. Proc, **712**, pp. 1645–1650, 2004.
28. BANABIC, D., ARETZ, H., COMSA, D.S., PARAIANU, L., *An improved analytical description of orthotropy in metallic sheets*, Int J Plast, **21**, *3*, pp. 493–512, 2005.

29. YOON, J.W., DICK, R.E., BARLAT, F., *A new analytical theory for earing generated from anisotropic plasticity*, Int J Plast, **27**, *8*, pp. 1165–1184, 2011.
30. SOARE, S., YOON, J.W., CAZACU, O., *On the use of homogeneous polynomials to develop anisotropic yield functions with applications to sheet forming*, Int. J. Plast., **24**, *6*, pp. 915–944, 2008.
31. BARROS, P.D., OLIVEIRA, M.C., ALVES, J.L., MENEZES, L.F., *Earing Prediction in Drawing and Ironing Processes Using an Advanced Yield Criterion*, Key Eng. Mater, **554-557**, pp. 2266–2276, 2013.
32. YOON, J.H., CAZACU, O., *Anisotropic yield function capable of predicting eight ears*, Numisheet'2001 8th Int. Conf. Work. Numer. Simul. 3D Sheet Met. Form. Process., 2011, pp. 86–91.

4.2. Modeling of tension–compression asymmetry and orthotropy on metallic materials: Numerical implementation and validation

This subchapter presents the paper "Modeling of tension–compression asymmetry and orthotropy on metallic materials: Numerical implementation and validation", published in the International Journal of Mechanical Sciences. This work presents the details concerning the implementation of the yield criterion developed by Cazacu et al. 2006 (CPB06), which accounts for both tension–compression asymmetry and orthotropy of the plastic flow, in DD3IMP. Further, a set of anisotropy parameters describing the mechanical behavior of two metallic materials at room temperature, namely Zirconium and AZ31-Mg alloy, are identified using strategies developed and implemented in DD3MAT. The numerical simulation of a four-point bending test is performed, validating the implementation and the parameters identification procedure. For the specific case of the CPB06 yield criterion, the identification is performed without the r-values in compression. The results show that, when the material behavior is well described by the CPB06, the trend for the compression r-values can be recovered. The results comparing the numerical simulation between the CPB06 and CB2001 yield criteria show that the strength differential effect affects the final deformed shape of the beam, particularly for materials exhibiting strong tension–compression asymmetry.

(Page intentionally left blank)

International Journal of Mechanical Sciences 114 (2016) 217–232

Contents lists available at ScienceDirect

International Journal of Mechanical Sciences

journal homepage: www.elsevier.com/locate/ijmecsci

Modeling of tension–compression asymmetry and orthotropy on metallic materials: Numerical implementation and validation

P.D. Barros [a,*], J.L. Alves [b], M.C. Oliveira [a], L.F. Menezes [a]

[a] CEMUC, Department of Mechanical Engineering, University of Coimbra, Pólo II, Rua Luís Reis Santos, Pinhal de Marrocos, 3030-788 Coimbra, Portugal
[b] CMEMS, Microelectromechanical Systems Research Unit, University of Minho, Campus de Azurém, 4800-058 Guimarães, Portugal

ARTICLE INFO

Article history:
Received 22 January 2016
Received in revised form
9 May 2016
Accepted 23 May 2016
Available online 24 May 2016

Keywords:
Tension–compression asymmetry
Yield criterion
Sheet metal forming
Finite element implementation
CPB06
DD3IMP

ABSTRACT

The details concerning the implementation of the yield criterion developed by Cazacu et al. 2006 (CPB06) [1], which accounts for both tension–compression asymmetry and orthotropy of the plastic flow, in the fully implicit FE solver DD3IMP (contraction of 'Deep Drawing 3-D IMPlicit') are presented in this work. The implemented constitutive model is extensively described, including the analytical first and second order derivatives required to the stress update algorithm. A set of anisotropy parameters describing the mechanical behavior of two metallic materials at room temperature, namely Zirconium and AZ31-Mg alloy, are identified with the DD3MAT (contraction for 'Deep Drawing 3-D MATerial') in-house code (Alves, 2004) [2]. The anisotropy parameters are identified for both the CPB06 and the Cazacu and Barlat (2001) (CB2001) [3] yield criteria, in order to emphasize the importance and role of the strength differential effect. The results clearly show that the CPB06 yield criterion is able to accurately describe both the in-plane anisotropy and tension–compression asymmetry, as well a different anisotropic behavior in uniaxial tension and uniaxial compression. The numerical simulation of a four-point bending test is performed, considering different orientations of the beam, i.e. of the hard/soft to deform direction relatively to the load direction, allowing to validate the implementation. The results obtained with the CPB06 show its ability to describe with accuracy the strain fields in the beam's central cross-section, the distribution of the tensile and compressive layers and, consequently, the shift of the neutral layer. The comparison with the results obtained with CB2001 indicates that the strength differential effect affects the final deformed shape of the beam, particularly for materials exhibiting strong tension–compression asymmetry.

© 2016 Elsevier Ltd. All rights reserved.

1. Introduction

Currently, plastic forming of metals with hexagonal closed packed (HCP) structure poses tremendous challenges due to their low ductility at room temperature and their unusual deformation characteristics, i.e. very pronounced anisotropy with strong asymmetry between tensile and compressive behavior. Unlike cubic metals (both face centered cubic (FCC) and body centered cubic (BCC)), hexagonal metals deform due to the activation of mechanical twinning or non-Schmid type slip at single crystal level. In contrast to slip, twinning is a directional shear mechanism: in general, shear in one direction can produce twinning while shear in the opposite direction cannot [1,3–6]. This causes the strength differential (SD) effect, or tension–compression asymmetry. However, although less pronounced, the SD effect is also present in materials with cubic structure [7].

Until recent years, the SD effect has been neglected with the major developments being made in macroscopic plasticity models for materials with cubic structure. In fact, in most numerical analysis of metal forming processes, the yield surface is assumed to possess a point-symmetry with respect to the center, such that a stress state and its reverse state have the same absolute value [3,8–11].

Cazacu et al. (2004) extended an isotropic yield function to the anisotropic case through invariants generalizing, able to describe both the materials anisotropy and tension–compression asymmetry [4]. Later, Cazacu et al. presented another yield function (CPB06) that enables describing the asymmetric yielding between tension and compression due to twining as well as in-plane anisotropy through a linear transformation, with a fourth-order tensor, of the deviatoric stress tensor [1]. Some authors have later adopted several linear transformations in order to more accurately capture in-plane anisotropy [6,12]. Tuninetti et al. characterized the mechanical behavior of a Ti-6Al-4V alloy using uniaxial tension, uniaxial compression, simple shear and plane strain tests in three orthogonal material directions, identifying the CPB06 yield criterion parameters by inverse modeling of the axial strain field of

* Corresponding author.
E-mail address: pedro.barros@dem.uc.pt (P.D. Barros).

http://dx.doi.org/10.1016/j.ijmecsci.2016.05.020
0020-7403/© 2016 Elsevier Ltd. All rights reserved.

Nomenclature

$\mathbf{A}$	set of parameters used in the objective function according to the selected yield criterion
$\mathbf{C}$	anisotropy parameters tensor for the CPB06 yield criterion
$\mathbf{C}^{e}$	Elastic modulus
$\mathbf{C}^{ep}$	Elastoplastic modulus
$c, a_1, \ldots, a_6, b_1, \ldots, b_{11}$	CB2001 yield criterion anisotropy parameters
$C_{11}, C_{22}, C_{33}, C_{44}, C_{55}, C_{66}, C_{23}, C_{13}, C_{12}, k, a$	CPB06 yield criterion parameters
$\mathbf{D}$	Strain rate tensor
$\mathbf{D}^{e}$	elastic strain rate tensor
$\mathbf{D}^{p}$	plastic strain rate tensor
E	Young's modulus
$\mathbf{E}$	Green-Lagrange strain tensor
$\mathbf{F}$	Deformation gradient tensor
G	Shear modulus
H'	isotropic hardening modulus
$\mathbf{I}_4$	forth-order identity tensor
J_2^0, J_3^0	second and third generalized invariants of $\boldsymbol{\Sigma}$
$\mathbf{Q}$	second derivative of the equivalent stress $\bar{\sigma}$ in order to the effective stress tensor, $\boldsymbol{\Sigma}$
$\mathbf{R}$	orthogonal plastic rotation tensor
r_θ	anisotropy coefficient for direction θ with the rolling direction
s_1, s_2, s_3	principal values of $\mathbf{s} = C\boldsymbol{\sigma}'$
$\mathbf{V}$	first derivative of the equivalent stress $\bar{\sigma}$ in order to the effective stress tensor, $\boldsymbol{\Sigma}$
$\mathbf{W}$	total spin tensor
$w_{\sigma_\theta^T}, w_{\sigma_\theta^C}, w_{r_\theta}, w_{\sigma_b}, w_{r_b}$	weighting factors used in the objective function
Y	flow stress
α	material state parameter
β	material state parameter
γ	generalized middle point rule parameter
$\boldsymbol{\Delta\varepsilon}$	total strain increment tensor
$\boldsymbol{\Delta\varepsilon}^{p}$	plastic strain increment tensor
$\bar{\varepsilon}^{p}$	equivalent plastic strain
θ	angle with the rolling direction
$\dot{\lambda}$	plastic multiplier
μ	Lamé parameter
υ	Poisson ratio
$\boldsymbol{\Sigma}$	effective stress tensor
$\boldsymbol{\sigma}$	Cauchy stress tensor
$\boldsymbol{\sigma}'$	Deviatoric Cauchy stress tensor
$\overset{\nabla J}{\boldsymbol{\sigma}}$	Jaumann derivative of the Cauchy stress tensor
$\bar{\sigma}$	equivalent stress
σ_θ^T	tensile yield stress for direction θ with the rolling direction
σ_θ^C	compression yield stress for direction θ with the rolling direction
σ_b^T	equibiaxial yield stress in tension
σ_b^C	equibiaxial yield stress in compression
Φ	Yield surface and plastic potential

compression specimens in the three orthogonal directions of the material [13]. In fact, several works have been made for the characterization of both titanium [14,15] and magnesium alloys [16,17], both presenting a HCP crystal structure.

The modeling of the SD effects allowed to point a new interpretation of Swift effects. Considering the isotropic form of the CPB06 yield criterion, Cazacu et al. showed that a slight difference between the uniaxial yield stresses in tension and compression leads to irreversible length changes under monotonic free-end testing conditions [18]. Revil-Baudard et al. show that there is a correlation between the Swift phenomenon in torsion and the stress–strain behavior in uniaxial tension and compression [17]. Chandola et al. showed that to explain and accurately predict the room-temperature torsional response of a strongly textured AZ31 Mg material it is necessary to account for the combined effects of anisotropy and tension–compression asymmetry at polycrystalline level [16].

Revil-Baudard and Cazacu numerically assessed the influence of the tension–compression asymmetry of the plastic flow in the matrix on void evolution and the location of the zone corresponding to maximum damage, in round tensile specimens subject to uniaxial tension [19]. Alves and Cazacu [20] used a detailed micromechanical finite-element analyses of three-dimensional unit cells, considering a spherical void at its center, with the plastic flow of the matrix described by the isotropic form of the CPB06 yield criterion. It was shown that there is a strong correlation between SD effects in the plastic flow of the matrix, arising from its dependence on the third stress invariant, with void evolution, and ultimately the ductility of porous metallic polycrystals. The combined effect of both the tension–compression asymmetry and anisotropic behavior of the material was also studied [17]. Also, due to non-negligible twinning activity accompanied by grain reorientation and highly directional grain interactions, the influence of the texture evolution on the hardening behavior of HCP materials cannot be neglected, even for the simplest monotonic loading paths [21]. In fact, Plunkett et al. shows a way of describing distortional hardening based on the evolution, with plastic strain, of the CPB06 yield *locus* [5].

The aim of this work is to evaluate the importance of taking into account the tension–compression asymmetry in the constitutive model. In this context, an associated flow rule is considered, neglecting the evolution of the shape of the yield surface with plastic work. The manuscript starts by presenting the details concerning the constitutive model, including the non-quadratic yield criterion proposed by Cazacu, Plunkett and Barlat and its implementation into the implicit in-house FE code DD3IMP, which has been continuously developed and optimized to simulate sheet metal forming processes [22,23]. In this context, the main aspects of the implementation of the CPB06 yield criterion in an implicit finite element code are presented, including the general aspects of the linear transformation operating in the deviatoric stress space. The validation of the implemented model is performed with the numerical simulation of a beam subjected to a four-point-bending test, along two different directions. The results obtained with the CPB06 yield criterion are compared with the ones of the Cazacu and Barlat (CB2001) [3] yield criterion, since the later enables an accurate description of the in-plane anisotropy while neglecting the SD effect. This allows analyzing the strain fields evolution in the beam's cross section, as well as the final shape of the beam when considering, or not, the SD effect.

2. Constitutive model

The constitutive equation that models the materials' mechanical behavior establishes the relationship between the most relevant state variables characterizing the continuum medium. In the following, it is assumed that constitutive modeling is

formulated in the objective frame, and thus all tensorial quantities are invariant. The differential form of the elastoplastic behavior law is, in its general form,

$$\dot{\boldsymbol{\sigma}}^{\mathrm{J}} = \mathbf{C}^{\mathrm{ep}}\colon \mathbf{D}, \tag{1}$$

where $\dot{\boldsymbol{\sigma}}^{\mathrm{J}}$ is the Jaumann derivative of the Cauchy stress tensor $\boldsymbol{\sigma}$, given by

$$\dot{\boldsymbol{\sigma}}^{\mathrm{J}} = \dot{\boldsymbol{\sigma}} + \boldsymbol{\sigma}\mathbf{W} - \mathbf{W}\boldsymbol{\sigma}, \tag{2}$$

where $\dot{\boldsymbol{\sigma}}$ stands for the time derivative of the Cauchy stress tensor and $\mathbf{W}$ is the total spin tensor defined by

$$\mathbf{W} = \dot{\mathbf{R}}\mathbf{R}^{\mathrm{T}}, \tag{3}$$

with $\mathbf{R}$ being the orthogonal rotation tensor (it is assumed that the plastic spin tensor is negligibly small [24]). The global and objective frames are related through the rotation tensor $\mathbf{R}$, which is derived from the polar decomposition of the deformation gradient. $\mathbf{D}$ is the strain rate tensor and $\mathbf{C}^{\mathrm{ep}}$ is a fourth-order tensor corresponding to the elastoplastic modulus. The expression for this tensor depends of the algorithms adopted in the integration of the constitutive model and the type of relation considered between the states at the beginning and at the end of the loading increment. Therefore, it is possible to consider the tangent elastoplastic or the consistent elastoplastic moduli. The implicit algorithm adopted in DD3IMP relies on the Newton–Raphson method to determine the incremental displacements that guarantee the static equilibrium of the deformable body, in each increment. This method assures quadratic convergence only when the consistent elastoplastic modulus is used, i.e. when the same approximations used to calculate the incremental strains and rotations and the updated state variables are also applied to linearize the principle of virtual power [25]. The trial solution for the Newton–Raphson method is obtained using an explicit approach, relying on the tangent elastoplastic modulus, defined as [26]

$$\mathbf{C}^{\mathrm{ep}}|_{\mathrm{tangent}} = \mathbf{C}^{\mathrm{e}} - \alpha f_0 \mathbf{V} \otimes \mathbf{V}, \tag{4}$$

where $\alpha = 0$ if the material is in an elastic state, or during elastic unloading, and $\alpha = 1$ if the material is in an elastoplastic loading state. f_0 is a function of the hardening law adopted which, considering only the isotropic hardening, can be written in the general form as

$$f_0 = \frac{4\mu^2}{2\mu\mathbf{V}\colon \mathbf{V} + H'}, \tag{5}$$

where μ is the Lamé parameter. $\mathbf{V}$ is one of the tensorial quantities to be determined as function of the adopted yield criterion, and it is, by definition

$$\mathbf{V} = \frac{\partial \Phi}{\partial \boldsymbol{\sigma}'}, \tag{6}$$

where $\boldsymbol{\sigma}'$ is the deviatoric Cauchy stress tensor and Φ is the plastic potential, identified as a scalar potential defining the elastic limit surface, such that

$$\Phi\left(\boldsymbol{\sigma}', \bar{\varepsilon}^{\mathrm{p}}\right) = \bar{\sigma} - Y = 0, \tag{7}$$

where $\bar{\sigma}$ is the equivalent stress given by the yield criterion and Y is the flow stress, modeled by the isotropic work-hardening law.

The strain rate can be decomposed into elastic and plastic parts as

$$\mathbf{D} = \mathbf{D}^{\mathrm{e}} + \mathbf{D}^{\mathrm{p}} \tag{8}$$

where $\mathbf{D}^{\mathrm{p}}$, the plastic strain rate tensor, is a deviatoric tensor, given by the associated inviscid flow rule as

$$\mathbf{D}^{\mathrm{p}} = \dot{\lambda}\frac{\partial \Phi}{\partial \boldsymbol{\sigma}'} = \dot{\lambda}\mathbf{V}, \tag{9}$$

in which $\dot{\lambda}$ is the plastic multiplier. From the plastic potential definition (see (7)), the consistency condition in the rate form states that

$$\dot{\Phi}\left(\bar{\sigma}, Y\right) = \dot{\bar{\sigma}} - H'\dot{\bar{\varepsilon}}^{\mathrm{p}} = 0, \tag{10}$$

where

$$H' = \partial Y/\partial \bar{\varepsilon}^{\mathrm{p}} \tag{11}$$

is the isotropic hardening modulus. If Φ is a homogeneous function of degree one, then $\dot{\bar{\varepsilon}}^{\mathrm{p}} = \dot{\lambda}$. $\dot{\bar{\sigma}}$ and $\dot{\bar{\varepsilon}}^{\mathrm{p}}$ are, respectively, the time derivatives of the equivalent stress and of the equivalent plastic strain. The total equivalent plastic strain is defined as

$$\bar{\varepsilon}^{\mathrm{p}} = \int_0^t \frac{\boldsymbol{\sigma}'\colon \mathbf{D}^{\mathrm{p}}}{\bar{\sigma}}\mathrm{d}t. \tag{12}$$

2.1. Time integration

Since the elastic behavior is considered isotropic, the hypoelastic form of the Hooke's law can be written as [26]

$$\dot{\boldsymbol{\sigma}} = \mathbf{C}^{\mathrm{e}}\colon \left(\mathbf{D} - \mathbf{D}^{\mathrm{p}}\right), \tag{13}$$

which, by integration, corresponds to the stress increment in the time interval $[t, t + \Delta t]$, i.e.

$$\boldsymbol{\sigma}_{\mathrm{F}} - \boldsymbol{\sigma}_0 = \mathbf{C}^{\mathrm{e}}\colon \Delta\boldsymbol{\epsilon} - \mathbf{C}^{\mathrm{e}}\colon \Delta\boldsymbol{\epsilon}^{\mathrm{p}}, \tag{14}$$

with subscripts 0 and F denoting the quantities at the beginning and at the end of the time increment $[t, t + \Delta t]$, respectively. $\Delta\boldsymbol{\epsilon}^{\mathrm{p}}$ and $\Delta\boldsymbol{\epsilon}$ are the increments of the plastic and total strain tensors, respectively, determined over the time increment. Applying the generalized middle point rule to determine the $\mathbf{D}^{\mathrm{p}}$ evolution, and since $\mathbf{D}^{\mathrm{p}} = \dot{\lambda}\mathbf{V}$, it can be written that

$$\Delta\boldsymbol{\epsilon}^{\mathrm{p}} = \Delta\lambda\mathbf{V}_{\gamma}, \tag{15}$$

with

$$\mathbf{V}_{\gamma} = \left(1 - \gamma\right)\mathbf{V}_0 + \gamma\mathbf{V}_{\mathrm{F}} \text{ and } \gamma \in [0, 1]. \tag{16}$$

To calculate $\Delta\lambda$ and $\mathbf{V}_{\mathrm{F}}$ it is necessary to determine $\boldsymbol{\sigma}'_{\mathrm{F}}$. $\boldsymbol{\sigma}_{\mathrm{F}}$ is calculated from Eq. (14), leading to deviatoric and hydrostatic components given by, respectively,

$$\boldsymbol{\sigma}'_{\mathrm{F}} = \boldsymbol{\sigma}'_0 + 2G\Delta\epsilon' - 2G\Delta\lambda\mathbf{V}_{\mathrm{F}} \text{ and} \tag{17}$$

$$\mathrm{tr}(\boldsymbol{\sigma}_{\mathrm{F}}) = \mathrm{tr}\left(\boldsymbol{\sigma}'_0\right) + \frac{E}{1 + 2\upsilon}\mathrm{tr}\left(\Delta\boldsymbol{\epsilon}\right). \tag{18}$$

G and E are the shear and Young's modulus, while υ is the Poisson's ratio. In order to determine both $\boldsymbol{\sigma}'_{\mathrm{F}}$ and $\Delta\bar{\epsilon}^{\mathrm{p}} = \Delta\lambda$, the consistency condition at the end of the time step is imposed, i.e.

$$\bar{\sigma}\left(\boldsymbol{\sigma}'_F\right) - Y_F\left(\bar{\epsilon}^{p}_0 + \Delta\bar{\epsilon}^{p}\right) = 0. \tag{19}$$

Together, Eqs. (17) and (19) define a non-linear system of equations, which needs to be solved in the state update algorithm, with unknowns $\boldsymbol{\sigma}'_{\mathrm{F}}$ and $\Delta\bar{\epsilon}^{\mathrm{p}}$, i.e.,

$$\mathbf{Q}\left(\boldsymbol{\sigma}'_{\mathrm{F}}, \Delta\bar{\epsilon}^{\mathrm{p}}\right) = \begin{bmatrix}\mathbf{G}\\ g\end{bmatrix} = \begin{bmatrix}\mathbf{0}\\ 0\end{bmatrix}, \tag{20}$$

or

$$\begin{bmatrix}\mathbf{G}\\ g\end{bmatrix} = \begin{bmatrix}\boldsymbol{\sigma}'_{\mathrm{F}} - \boldsymbol{\sigma}'_0 - 2G\Delta\epsilon' - 2G\Delta\bar{\epsilon}^{\mathrm{p}}\mathbf{V}_{\mathrm{F}}\\ \bar{\sigma}\left(\boldsymbol{\sigma}'_{\mathrm{F}}\right) - Y_{\mathrm{F}}\left(\bar{\epsilon}^{\mathrm{p}}_0 + \Delta\bar{\epsilon}^{\mathrm{p}}\right)\end{bmatrix} = \begin{bmatrix}\mathbf{0}\\ 0\end{bmatrix}. \tag{21}$$

So, the updated state variables are determined solving the non-linear system of equations Eq. (21) using the Newton–Raphson method. The calculation of $\mathbf{Q}$ and $\partial\mathbf{Q}/\partial\boldsymbol{\varsigma}$ (with $\boldsymbol{\varsigma} = \left[\boldsymbol{\sigma}'_{\mathrm{F}}, \Delta\bar{\varepsilon}^{\mathrm{p}}\right]$) depends on the adopted yield criterion, with $\mathbf{Q}$ calculated considering Eq. (21) and $\partial\mathbf{Q}/\partial\boldsymbol{\varsigma}$ calculated considering partial derivatives, such that:

$$\frac{\partial \mathbf{Q}}{\partial \boldsymbol{\varsigma}} = \begin{bmatrix} [\mathbf{A}] & [\mathbf{c}] \\ [\mathbf{b}] & d \end{bmatrix}, \tag{22}$$

where

$$\mathbf{A} = \frac{\partial \mathbf{Q}}{\partial \boldsymbol{\sigma}'_{\mathrm{F}}},\ \mathbf{b} = \frac{\partial g}{\partial \boldsymbol{\sigma}'_{\mathrm{F}}},\ \mathbf{c} = \frac{\partial \mathbf{G}}{\partial \Delta\bar{\varepsilon}^{\mathrm{p}}},\ d = \frac{\partial g}{\partial \Delta\bar{\varepsilon}^{\mathrm{p}}}. \tag{23}$$

After some mathematical developments, the above expressions can be written as:

$$\begin{aligned} &\mathbf{A} = \mathbf{I}_4 + 2G\Delta\bar{\varepsilon}^{\mathrm{p}}\mathbf{Q}_{\mathrm{F}}, \quad \mathbf{c} = \mathbf{V}_{\mathrm{F}}, \\ &\mathbf{b} = \mathbf{V}_{\mathrm{F}}, \qquad\qquad d = -\boldsymbol{H}'_{\mathrm{F}}, \end{aligned} \tag{24}$$

where

$$\mathbf{V}_{\mathrm{F}} = \frac{\partial \bar{\sigma}}{\partial \boldsymbol{\sigma}'_{\mathrm{F}}},\ \mathbf{Q}_{\mathrm{F}} = \frac{\partial^2 \bar{\sigma}}{\partial \boldsymbol{\sigma}'^2_{\mathrm{F}}} \text{ and } H'_{\mathrm{F}} = \partial Y/\partial\bar{\varepsilon}^{\mathrm{p}}. \tag{25}$$

The details concerning the previously mentioned analytical derivatives are presented in Appendix A for the CPB06 yield criterion, as implemented in DD3IMP [22]. The tensor $\mathbf{Q}$ corresponds to the second order derivative of the yield criterion with respect to the effective stress state $\boldsymbol{\Sigma} = \boldsymbol{\sigma}'$, and it is used both in the state update algorithm and on the definition of the consistent elasto-plastic modulus,

$$\mathbf{C}^{\mathrm{ep}} = \mathbf{C}^{\mathrm{e}} - 4G^2(1-\beta)\left(\frac{\mathbf{V}_{\mathrm{F}} \otimes \mathbf{V}_{\mathrm{F}}}{H'_{\mathrm{F}}} + \Delta\bar{\varepsilon}^{\mathrm{p}}\mathbf{Q}_{\mathrm{F}}\right)\boldsymbol{\Lambda}. \tag{26}$$

$\boldsymbol{\Lambda}$ depends on the hardening law adopted, given in general terms as

$$\boldsymbol{\Lambda}^{-1} = \left[\mathbf{I}_4 + 2\mu\left(\frac{\mathbf{V}_{\mathrm{F}} \otimes \mathbf{V}_{\mathrm{F}}}{H'_{\mathrm{F}}} + \Delta\bar{\varepsilon}^{\mathrm{p}}\mathbf{Q}_{\mathrm{F}}\right)\right], \tag{27}$$

where $\mathbf{I}_4$ corresponds to the forth order unit symmetric tensor, defined as $I_{ijkl} = 1/2\left(\delta_{ik}\delta_{jl} + \delta_{il}\delta_{jk}\right)$. Since the strain increment can be either elastic or plastic, parameter β and $(1-\beta)$ is introduced in Eq. (26) to separate, respectively, the elastic and elastoplastic parts of the total strain increment. Further details about the calculus of the parameter β are given in Appendix A.

2.2. Cazacu, Plunkett and Barlat yield criterion

In order to describe both anisotropy and tension–compression asymmetry, Cazacu, Plunkett and Barlat proposed a macroscopic elastoplastic yield criterion for textured metals. The equivalent stress $\bar{\sigma}$ associated with the orthotropic form of the CPB06 yield criterion is given as

$$\bar{\sigma} = B\left[\left(|s_1| - k\,s_1\right)^a + \left(|s_2| - k\,s_2\right)^a + \left(|s_3| - k\,s_3\right)^a\right]^{\frac{1}{a}}, \tag{28}$$

where a and k are material parameters and s_1, s_2, s_3 are the principal values of $\mathbf{s} = \mathbf{C}\boldsymbol{\sigma}'$, determined following Barlat et al. [27] (see Appendix A for further details). $\boldsymbol{\sigma}'$ is the deviatoric stress tensor and $\mathbf{C}$ is the constant 4th-order linear transformation tensor, given by

$$\mathbf{C} = \begin{bmatrix} C_{11} & C_{12} & C_{13} & 0 & 0 & 0 \\ C_{12} & C_{22} & C_{23} & 0 & 0 & 0 \\ C_{13} & C_{23} & C_{33} & 0 & 0 & 0 \\ 0 & 0 & 0 & C_{44} & 0 & 0 \\ 0 & 0 & 0 & 0 & C_{55} & 0 \\ 0 & 0 & 0 & 0 & 0 & C_{66} \end{bmatrix}. \tag{29}$$

For a 3-D stress state, $\mathbf{C}$ involves 9 independent anisotropy coefficients. a is a positive integer usually taken as 2. As taken from Cazacu et al. the only restrictions imposed on the tensor $\mathbf{C}$ are that it satisfies the major and minor symmetries and to be invariant with respect to the orthotropy group [6]. Considering isotropic conditions, the coefficient k alone allows for the description of the SD effect, giving a direct measure of the ratio between tensile and compressive yield stresses, as

$$k = \frac{1-h}{1+h}, \text{ With } h = \left[\frac{2^a - 2\left(\frac{\sigma^{\mathrm{T}}}{\sigma^{\mathrm{C}}}\right)^a}{\left(2\frac{\sigma^{\mathrm{T}}}{\sigma^{\mathrm{C}}}\right)^a - 2}\right]^{1/a}. \tag{30}$$

This means that the $\sigma^{\mathrm{T}}/\sigma^{\mathrm{C}}$ ratio, i.e. the ratio between the yield stress in uniaxial tension and the yield stress in uniaxial compression, for the three principal axes is the same, in isotropic conditions. However, for an anisotropic material it is not possible to define a single $\sigma^{\mathrm{T}}/\sigma^{\mathrm{C}}$ ratio and, consequently, the physical significance of the k parameter is lost [28]. B is a constant defined such that $\bar{\sigma}$ reduces to the tensile yield stress along the rolling direction, and is simply defined as

$$B = \left[\frac{1}{\left(|\phi_1| - k\,\phi_1\right)^a + \left(|\phi_2| - k\,\phi_2\right)^a + \left(|\phi_3| - k\,\phi_3\right)^a}\right]^{\frac{1}{a}}, \tag{31}$$

with

$$\begin{Bmatrix} \phi_1 \\ \phi_2 \\ \phi_3 \end{Bmatrix} = \begin{Bmatrix} (2/3)C_{11} - (1/3)C_{12} - (1/3)C_{13} \\ (2/3)C_{21} - (1/3)C_{22} - (1/3)C_{23} \\ (2/3)C_{31} - (1/3)C_{32} - (1/3)C_{33} \end{Bmatrix}. \tag{32}$$

For $a = 2$, $k = 0$ and $\mathbf{C}$ equal to the 4th-order identity tensor, the von Mises yield criterion is recovered. Convexity is guaranteed for any integer $a \geq 2$ and $k \in [-1, 1]$ [1].

3. Application to zirconium and AZ31-Mg alloy

The CPB06 yield criterion is used in this section to describe the anisotropic behavior of two metallic materials, known for exhibiting strong tension–compression asymmetry: Zirconium [6] and the AZ31-Mg alloy [16]. These materials were selected since the anisotropy parameters for the CPB06 yield criterion were previously determined [6,16].

The CB2001 yield criterion is also used to evaluate the impact in the numerical results of neglecting the strength differential effect, although taking into account the orthotropic behavior. In this context, a four-point beam bending test is used in order to analyze both the strain components distributions in the beam central cross-section, as well the punch force evolution. This test was selected because experimental results are available for the Zirconium [6].

In brief, the CB2001 yield criterion is a generalization of the Drucker's isotropic criterion to orthotropy [3] and, in its general form, is given by

$$\bar{\sigma} = \left\{ 27\left[\left(J_2^0\right)^3 - c\left(J_3^0\right)^2 \right] \right\}^{\frac{1}{6}}, \tag{33}$$

where J_2^0 and J_3^0 are the second and third generalized invariants of the effective stress tensor $\boldsymbol{\Sigma}$, defined as

$$\begin{aligned} J_2^0 = {} & \frac{a_1}{6}(\Sigma_{11} - \Sigma_{22})^2 + \frac{a_2}{6}(\Sigma_{11} - \Sigma_{33})^2 + \frac{a_3}{6}(\Sigma_{11} - \Sigma_{33})^2, \\ & + a_4\Sigma_{12}^2 + a_5\Sigma_{13}^2 + a_6\Sigma_{23}^2 \end{aligned} \tag{34}$$

$$\begin{aligned} J_3^0 = {} & (1/27)(b_1 + b_2)\Sigma_{11}^3 + (1/27)(b_3 + b_4)\Sigma_{22}^3 \\ & + (1/27)\left[2(b_1 + b_4) - b_2 - b_3\right]\Sigma_{33}^3 \\ & - (1/9)(b_1\Sigma_{22} + b_2\Sigma_{33})\Sigma_{11}^2 - (1/9)(b_3\Sigma_{33} + b_4\Sigma_{11})\Sigma_{22}^2 \\ & - (1/9)\left[(b_1 - b_2 + b_4)\Sigma_{11} + (b_1 - b_3 + b_4)\Sigma_{22}\right]\Sigma_{33}^2 \\ & + (2/9)(b_1 + b_4)\Sigma_{11}\Sigma_{22}\Sigma_{33} \\ & - \left(\Sigma_{13}^2/3\right)\left[2b_9\Sigma_{22} - b_8\Sigma_{33} - (2b_9 - b_8)\Sigma_{11}\right] \\ & - \left(\Sigma_{12}^2/3\right)\left[2b_{10}\Sigma_{33} - b_5\Sigma_{22} - (2b_{10} - b_5)\Sigma_{11}\right] \\ & - \left(\Sigma_{23}^2/3\right)\left[(b_6 - b_7)\Sigma_{11} - b_6\Sigma_{22} - b_7\Sigma_{33}\right] + 2b_{11}\Sigma_{12}\Sigma_{23}\Sigma_{13}, \end{aligned} \tag{35}$$

where c, $a_1, \ldots, a_6$ and $b_1, \ldots, b_{11}$ are the anisotropy parameters. Σ_{ij}, $i, j = 1, 2, 3$ are the effective stress components defined in the material frame. When considering metal sheets, the off-plane parameters cannot be experimentally evaluated. Thus, a_5, a_6 and b_k $(k = 6, 7, 8, 9, 11)$ are assumed as equal to the isotropic values, i.e. 1.0. For further details about the implementation and parameters identification procedure please refer to [29].

3.1. Parameters identification for the zirconium and AZ31Mg alloy

For the Zirconium and the AZ31-Mg alloy under study, the anisotropy parameters of the CPB06 yield criterion were previously identified in [6] and [16], respectively. In those studies, different sets of anisotropy parameters were identified for different levels of the plastic work. However, in order to keep the focus of the present work, such evolution of the anisotropy is not taken into account. Based on [6] and [16], the Zirconium presents the higher strength differential effect for a plastic strain value of 15%, while the AZ31-Mg shows higher strength differential effect for about 3% of plastic strain. Thus, the anisotropy parameters selected from [6] and [16] are the ones corresponding to these values of plastic strain, in order to highlight the strength differential effect. These anisotropy parameters were used to estimate virtual experimental data for both materials. The use of this virtual data, instead of the experimental one, guarantees that the material is perfectly described by the CPB06 yield criterion. Therefore, the parameters identified using the current implementation of the CPB06 yield criterion, should accurately describe the generated virtual data. Moreover, since the off-plane parameters cannot be experimentally evaluated, in this work a new set of constitutive CPB06 parameters was identified, for each material, imposing the corresponding isotropic values, i.e. $C_{44} = C_{55} = 1.0$.

Based on the sets of parameters from [6] and [16], the virtual data generated for the previously mentioned values of plastic strain is presented in Tables 1 and 2, for the Zirconium and the AZ31-Mg alloy, respectively. The virtual data includes uniaxial tensile and compression tests, equibiaxial tension and disc compression tests. Note that under this conditions it is assumed that both materials' plastic behavior is perfectly described by the CPB2006 yield criterion.

A set of anisotropy parameters, for each yield criteria, was then determined using the DD3MAT in-house code [2], taking into account the abovementioned virtual set of experimental data and $a = 2$. The anisotropy coefficients should be determined such that the yield criterion reproduces the materials' mechanical behavior as close as possible. In DD3MAT, the identification procedure is based on the minimization of an error function, using a downhill simplex method, which evaluates and weights the differences between the values determined from the constitutive equations and the experimental ones, as follow

$$\begin{aligned} F(\mathbf{A}) = {} & \sum_{\theta=0}^{90} w_{\sigma_\theta^T}\left(\sigma_\theta^T(\mathbf{A})/\sigma_\theta^T - 1\right)^2 + \sum_{\theta=0}^{90} w_{\sigma_\theta^C}\left(\sigma_\theta^C(\mathbf{A})/\sigma_\theta^C - 1\right)^2 \\ & + \sum_{\theta=0}^{90} w_{r_\theta}\left(r_\theta(\mathbf{A})/r_\theta - 1\right)^2 + w_{\sigma_b}\left(\sigma_b^T(\mathbf{A})/\sigma_b^T - 1\right)^2 \\ & + w_{r_b}\left(r_b(\mathbf{A})/r_b - 1\right)^2, \end{aligned} \tag{36}$$

where $\mathbf{A}$ represents the set of parameters associated with the selected yield criterion. σ_θ^T, σ_θ^C and r_θ are the experimental yield stresses in tension, compression and r-values determined in uniaxial tension, respectively, obtained from the uniaxial tests for a specific orientation (θ) with respect to the rolling direction (RD). σ_b^T is the experimental yield stress obtained from the equibiaxial tensile test, r_b the experimental r-value obtained from the disc compression test. $\sigma_\theta^T(\mathbf{A})$, $\sigma_\theta^C(\mathbf{A})$ $r_\theta(\mathbf{A})$, $\sigma_b^T(\mathbf{A})$ and $r_b(\mathbf{A})$ are the correspondent values predicted from the adopted yield criterion. Such procedure can be considered a generalization of the one proposed by Banabic et al. [30], where the weighting factors, $w_{\sigma_\theta^T}$, $w_{\sigma_\theta^C}$, w_{r_θ}, w_{σ_b} and w_{r_b} are used to balance the influence of the experimental data. Nevertheless, the selection of the weighting factors is normally a manual procedure, strongly dependent on users' expertise and knowledge. In this work, all the weighting factors are considered equal to 1.0.

The yield stress values presented in Tables 1 and 2 correspond to the initial yield surface, such that the yield stress Y_0 is always equal to the one obtained for the uniaxial tensile test performed along the RD, σ_{RD}^T. Previous results indicate that, for the CPB06, the value proposed for the yield stress, Y_0, defined by the hardening

Table 1
Virtual data for the Zirconium, reproduced considering the anisotropy parameters of the CPB06 yield criterion given in [6] for 15% of equivalent plastic strain.

Test direction	r-value (tension)	r-value (compression)	σ_θ^T [MPa]	σ_θ^C [MPa]
0°	6.825	−26.292	175.00	199.37
15°	7.627	−24.961	164.03	184.45
30°	9.191	−23.612	147.65	161.55
45°	10.126	−22.421	142.12	152.19
60°	9.761	−20.500	150.81	159.17
75°	8.510	−18.278	171.05	179.12
90°	7.773	−17.220	184.45	192.70
σ_b^T[MPa]	550.87			
r_b	0.532			

Table 2
Virtual data for the AZ31-Mg alloy, reproduced considering the anisotropy parameters of the CPB06 yield criterion given in [16] for 3% of equivalent plastic strain.

Test direction	r-value (tension)	r-value (compression)	σ_θ^T [MPa]	σ_θ^C [MPa]
0°	1.082	−0.304	157.12	92.68
15°	0.913	−0.337	167.68	95.17
30°	0.541	−0.403	198.95	101.30
45°	0.364	−0.445	226.10	107.16
60°	0.792	−0.445	202.00	109.07
75°	1.386	−0.406	169.15	107.50
90°	1.681	−0.384	157.74	106.32
σ_b^T[MPa]	213.31			
r_b	0.579			

Table 3
Literature and identified parameters for the Zirconium for both yield criteria. ($C_{44} = C_{55} = 1.0$ and a_5, a_6 and b_k with ($k = 6, 7, 8, 9, 11$) also considered 1.0).

CPB06 [6]	C_{11}	C_{22}	C_{33}	C_{66}	C_{23}	C_{13}	C_{12}	k
	1.0000	***0.7201***	***1.1806***	***2.9195***	***1.5212***	***1.6353***	***3.1351***	***−0.1828***
CPB06	C_{11}	C_{22}	C_{33}	C_{66}	C_{23}	C_{13}	C_{12}	k
	−1.1201	−0.9378	0.0712	−1.7037	−0.0347	−0.1507	0.2943	0.1646
CB2001	c	a_1	a_2	a_3	a_4			
	−0.6880	1.7462	0.1003	0.0084	1.926703			
	b_1	b_2	b_3	b_4	b_5	b_{10}		
	1.3207	1.5103	1.4147	0.0496	1.2485	1.6950		

Table 4
Literature and identified parameters for the AZ31-Mg for both yield criteria ($C_{44} = C_{55} = 1.0$ and a_5, a_6 and b_k with ($k = 6, 7, 8, 9, 11$) also considered 1.0).

CPB06 [16]	C_{11}	C_{22}	C_{33}	C_{66}	C_{23}	C_{13}	C_{12}	k
	1.0000	***1.0900***	***3.3420***	***0.7300***	***0.2430***	***0.0980***	***−0.1680***	***−0.625***
CPB06	C_{11}	C_{22}	C_{33}	C_{66}	C_{23}	C_{13}	C_{12}	k
	1.0526	1.1556	3.5000	0.7591	0.2527	0.0955	−0.1663	−0.6344
CB2001	c	a_1	a_2	a_3	a_4			
	1.1369	1.4620	0.7157	0.7464	0.3996			
	b_1	b_2	b_3	b_4	b_5	b_{10}		
	3.0707	−0.1938	−0.5420	−2.2672	−0.3057	0.0531		

law, should be in accordance with the σ_{RD}^{T} to enable an accurate description of the in-plane yield stresses [28]. For both yield criteria the minimization problem associated to Eq. (33) is over constrained, since that a total of 23 experimental values are used to identify only 8 parameters in case of CPB06, and 11 parameters in case of CB2001. Considering that the problem is over constrained, the r-values in uniaxial compression are not used, to check if it is possible to captured them using the remaining data, for a material that follows the CPB06 yield criterion. A summary of the sets of parameters determined for both yield criteria is presented in Tables 3 and 4 . The yield criterion parameters used to generate the virtual experimental data are also depicted (first line).

Figs. 1 and 2 and present the comparison between numerical and experimental r-values and normalized yield stresses in tension and compression for both yield criteria and both materials, respectively. The figures also present the r-values determined in uniaxial compression, although not used in the identification procedure. Note that for the CB2001 the r-values and yield stress in-plane evolution in tension and compression is the same. Regarding the Zirconium, the r-values are accurately described by both yield criteria with negligible differences between them. For the AZ31-Mg alloy the same accurate description is observed.

For the Zirconium, the yield stresses are accurately predicted with the CPB06 yield criterion, while the CB2001 presents a less accurate fit with the increase of the angle relative to the rolling direction. As for the AZ31-Mg, both yield criteria show an accurate description of the yield stresses directionalities.

The yield surfaces predicted with both yield criteria are presented in Figs. 3 and 4, for the plane σ_1, σ_2 (with $\sigma_3 = 0$) and the π-plane, for the Zirconium and the AZ31-Mg alloy, respectively. The rolling (RD), transverse (TD) and normal (ND) directions correspond to 1, 2 and 3, respectively. Note that the equibiaxial stress state is equivalent to the through-thickness uniaxial compression, i.e. there is an equivalence between the stress ratio in ND and equibiaxial $\left(\sigma_3^T/\sigma_3^C\right) = \left(\sigma_b^C/\sigma_b^T\right)$ [28], as shown in the figures.

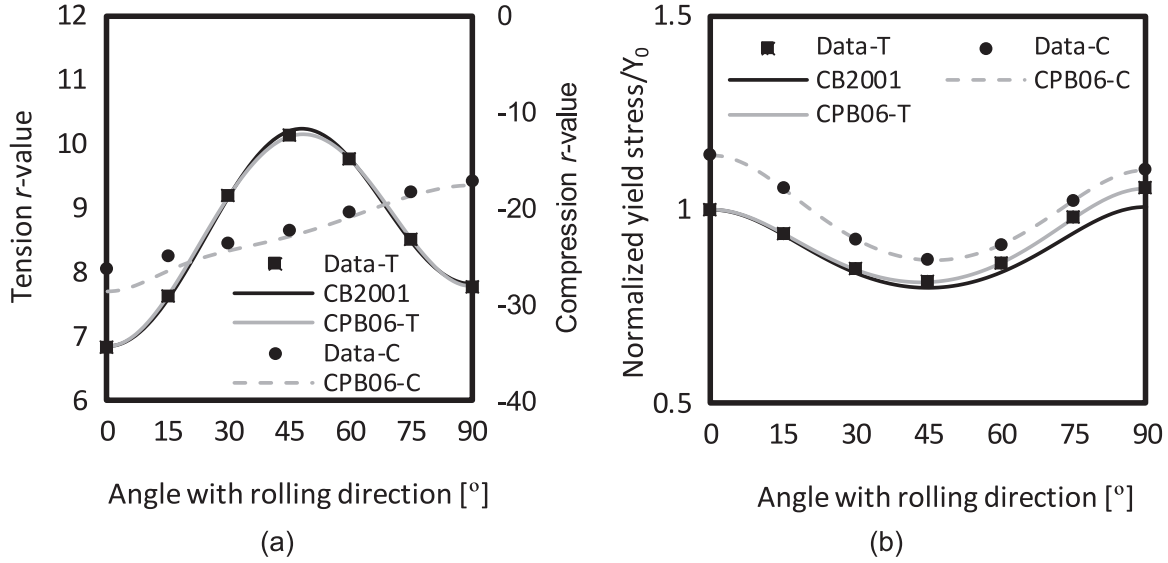

Fig. 1. Virtual and predicted (a) r-values and (b) normalized yield stresses for the Zirconium.

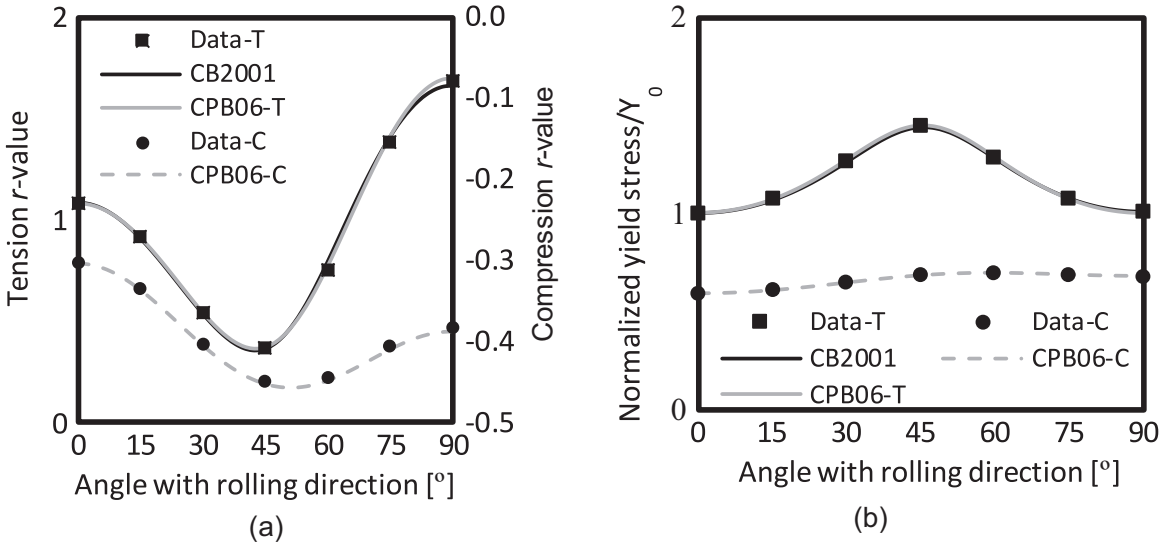

Fig. 2. Virtual and predicted (a) r-values and (b) normalized yield stresses for the AZ31-Mg alloy.

Fig. 3 shows that the yield surface for the Zirconium is well described by the CPB06 yield criterion for all stress states. Note the fact that there is a slight difference between numerical and virtual data for the point relative to equibiaxial compression, σ_b^C. Moreover, as expected, the CB2001 cannot predict the tension–compression asymmetry, falling short mainly in the point relative to equibiaxial compression, σ_b^C.

Fig. 4 shows that both the CPB06 and CB2001 accurately predict the material behavior in the first quadrant of the plane σ_1, σ_2, where tension–compression asymmetry has no influence. However, in the other quadrants, the CB2001 cannot accurately predict the material behavior, due to the point-symmetry of the criterion, while the CPB06 reproduces closely the experimental material behavior. Although CPB06 has a reduced set of anisotropy parameters, both yield criteria are flexible enough to enable the accurate description of the in-plane anisotropy of both r-values and flow stresses (yield stresses).

Comparing the CPB06 anisotropy parameters proposed in the literature with the ones identified with DD3MAT (see Table 3) for Zirconium, it should be mentioned that the parameter k changes from negative to positive, without affecting the predicted tension–compression ratios obtained for the orthotropy axes (see Table 5), highlighting that both sets of parameters are robust. Although not shown here, it should be mentioned that it is also possible to obtain a set of anisotropy parameters for the CPB06 yield criterion with a negative value for the parameter k. In that case the anisotropy parameters become symmetrical to the ones presented in Table 3, for the CPB06 yield criterion.

For the AZ31-Mg alloy, the obtained anisotropy parameters are very similar to the ones proposed on the literature (see Table 4), leading to similar stress ratios for the orthotropy axes (see Table 6). In this case, it is not possible to obtain a set of parameters with a positive value for k that accurately describes the material behavior, which seems to result from the "triangular" shape with rounded corners of the yield surface, in opposition to the elliptical shape of the Zirconium yield *locus*.

Regarding the tension–compression ratios for the orthotropy axes, for the Zirconium (see Table 5), the values obtained for the σ_1 and σ_2 directions are relatively close and lower than 1.0.

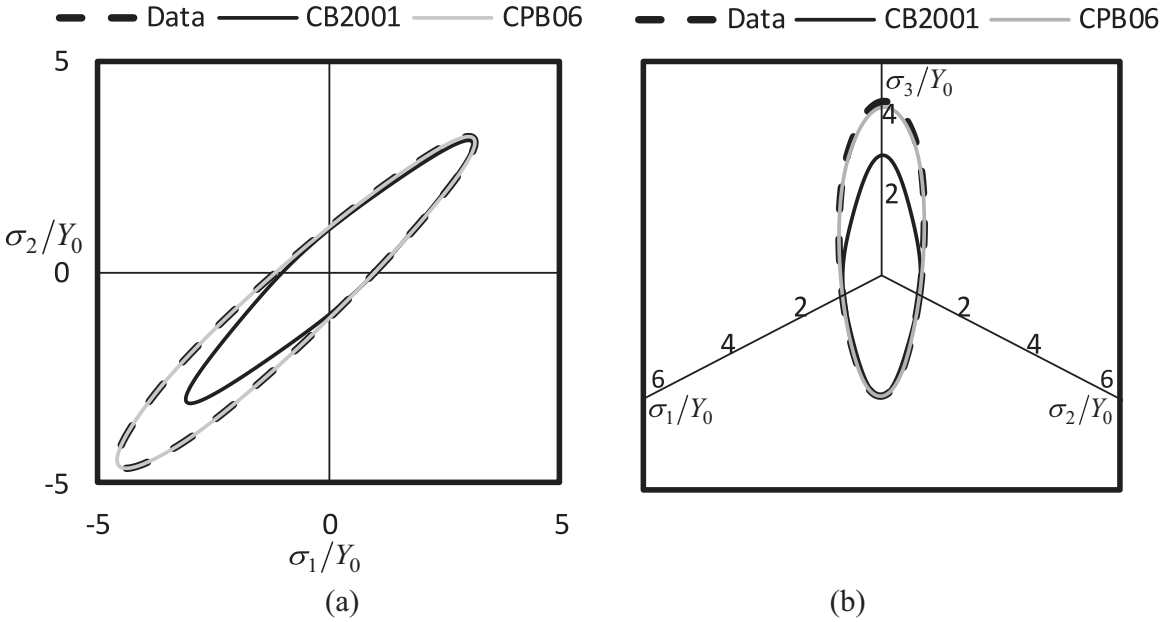

Fig. 3. Predicted yield surfaces in the (a) σ_1/Y_0, σ_2/Y_0 plane and (b) π-plane for the Zirconium.

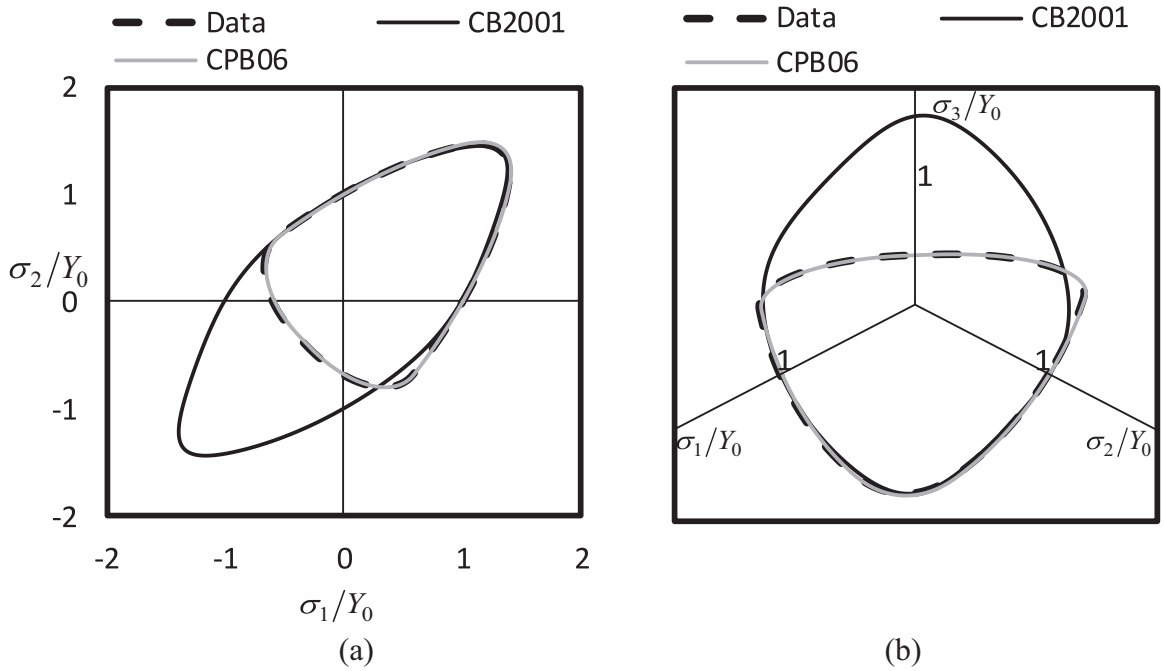

Fig. 4. Predicted yield surfaces in the (a) σ_1/Y_0, σ_2/Y_0 plane and (b) π-plane for the AZ31-Mg alloy.

Table 5
Ratios obtained for the three principal axes for the Zirconium.

	(σ_1^T/σ_1^C)	(σ_2^T/σ_2^C)	(σ_3^T/σ_3^C)
Experimental	0.8778	0.9572	1.4474
CPB06	0.8767	0.9569	1.3940

Table 6
Ratios obtained for the three principal axes for the AZ31-Mg alloy.

	(σ_1^T/σ_1^C)	(σ_2^T/σ_2^C)	(σ_3^T/σ_3^C)
Experimental	1.6953	1.4837	0.2607
CPB06	1.6998	1.4715	0.2573

Considering the σ_3 direction, the ratio is higher than 1.0 with a slight difference between numerical and experimental values, as supported by Fig. 3(b). Regarding the AZ31-Mg alloy (see Table 6), the ratios obtained for the σ_1 and σ_2 directions are relatively close and higher than 1.0, meaning that the yield stresses in tension are higher than in compression. On the other hand, the ratio in σ_3 is of about 0.26, meaning that the yield stress in compression is four times higher than the yield stress in tension. Note that, as shown in Fig. 4(b), the ratio in σ_3 is the inverse of the ratio in the equi-biaxial direction.

3.2 Four-point bending test

The beam bending example considered is based on the original work of Kaschner [31]. The simulation of the four-point bending

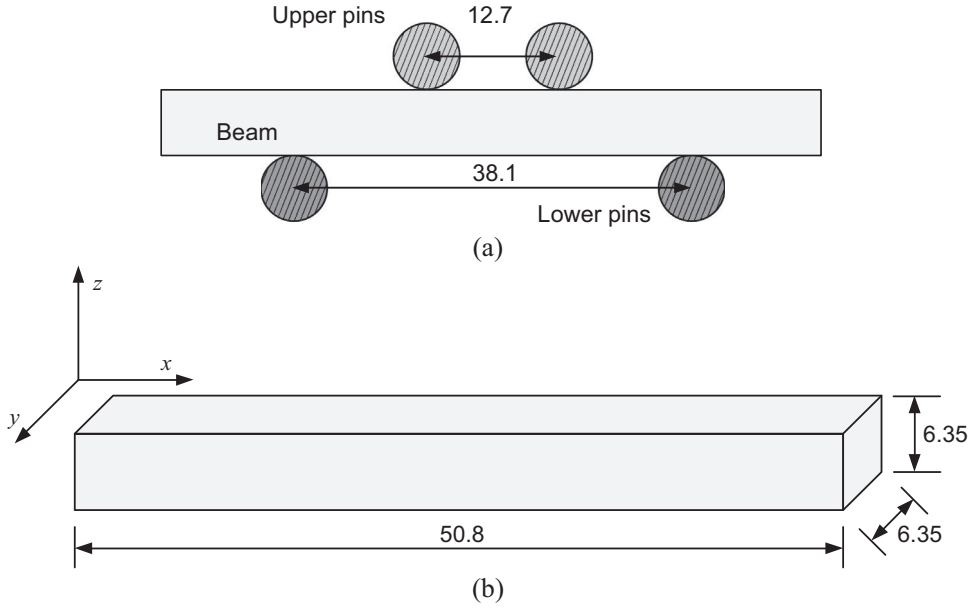

Fig. 5. Schematic of the (a) four-point bending test and (b) beam geometry and dimensions (dimensions in mm).

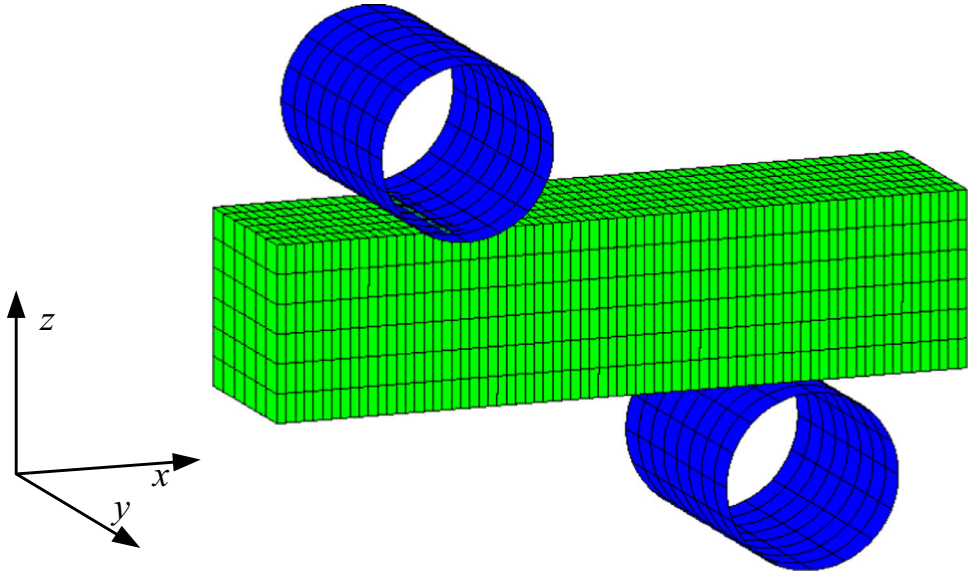

Fig. 6. Numerical model of the four-point bending test (half model).

tests is performed with both the CPB06 and CB2001 yield criteria. This test is used in order to highlight the strain distribution and shift of the neutral layer in materials which exhibit tension–compression asymmetry, and the importance of accurately modeling this phenomenon. The four-point bending fixture is composed by two upper pin dowels, having a downwards displacement of 6 mm, and two lower pins which are held stopped. The center distance between the upper pins is 12.7 mm and for the lower pins is 38.1 mm (Fig. 5). Fig. 6 presents the numerical model of the four-point bending test. The dimensions of the beam are 6.35 mm × 6.35 mm × 50.8 mm.

The beam is discretized with 8-node hexahedral finite elements, combined with a selective reduced integration technique [32]. Due to geometrical and material symmetries, only half of the global structure is modeled with the beam composed by 6×6 elements and 75 elements along the beam axes, yielding a total of 2700 finite elements.

For each material, two different beam orientations are considered, both taken with the RD aligned with the *x*-axis: (i) case TD, the TD is coincident with the global *y*-axis, i.e. the material axes are coincident with the global ones; and (ii) case ND, the ND is aligned with the global *y*, i.e. the beam is rotated 90° around the *x*-axis. This rotation allows the change in orientation of the hard/soft to deform direction relatively to the load direction. In this work, an isotropic work hardening law is considered, assuming that the initial shape of the yield surface expands only isotropically with plastic deformation.

4. Results and discussion

Fig. 7(a) presents a comparison of the predicted normalized punch force evolution obtained for Zirconium, with both yield criteria, showing that the differences observed with the change of orientation are negligible. Nonetheless, the force predicted by the CPB06 is higher, when compared with the CB2001. This can be related to the fact that yielding in compression is lower for the CB2001.

Fig. 7(b) presents the same comparison regarding the AZ31-Mg alloy. When using the CB2001 yield criterion, the difference between orientations are, again, negligible. When using the CPB06, however, the differences are evident, with the TD case presenting

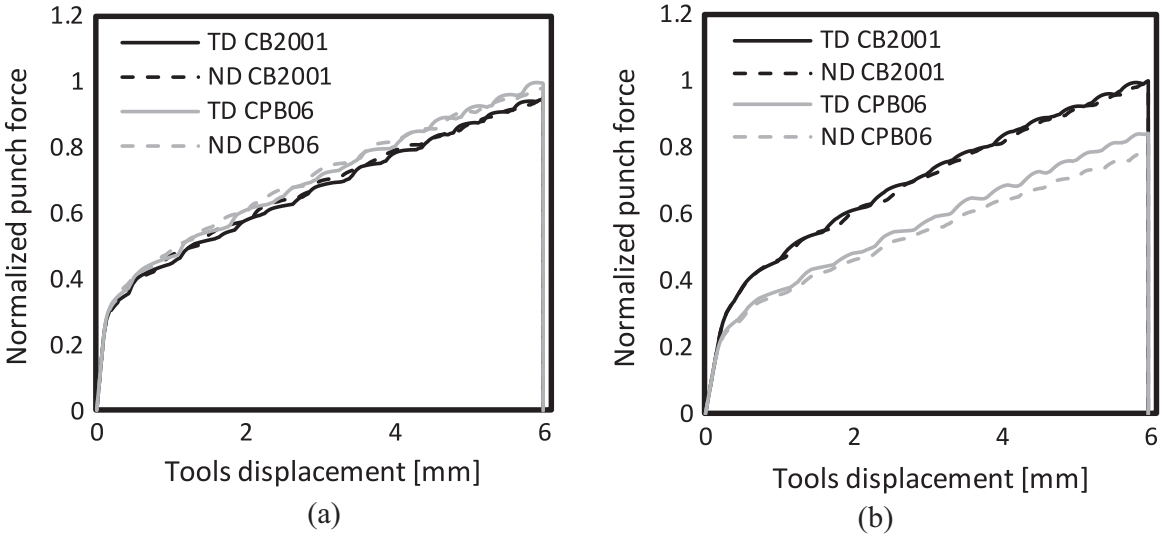

Fig. 7. Predicted punch force evolution for both CPB06 and CB2001 yield criteria, for (a) Zirconium and (b) AZ31-Mg alloy.

higher values than the ND case. For this material, the CB2001 predicts higher yield stresses in compression when compared with the CPB06, thus resulting in a higher punch force evolution for CB2001.

Regarding the predicted deformed bar central cross-section, the results for the Zirconium are presented in Fig. 8, for both orientations. Note that for the Zirconium, the experimentally measured strain distributions are available, as well as the y–z cross-sections of the deformed bars [6]. Considering the TD case, the final shapes obtained for both yield criteria are in good agreement with the experimental ones, with negligible differences between both. As for the ND case, the final shape is very close to the initial one, for both yield criteria. This means that both yield criteria correctly model the rigidity of the bar in the hard to deform $\langle c\rangle$-axis direction. This is coherent with the fact that the Zirconium presents a strong basal structure, i.e. $\langle c\rangle$-axis of the crystals predominantly oriented along the plate normal direction. Hence, in the TD case, the $\langle c\rangle$-axis, are mostly aligned with the z-axis while for the ND case, the $\langle c\rangle$-axis are mostly aligned with the y-axis. In fact, even though the CB2001 does not allow describing the compression yield stresses evolution, that evolution is very close in shape to the experimental one, with only slightly lower values (see Fig. 1(b)). Moreover, as shown in Fig. 1(a) the in-plane r-values present high absolute values in order to describe the lack of ability to deform of the ND direction. The fact that the CPB06 presents negative uniaxial compression r-values does not seems to affect the final geometry of the beam central cross-section.

Fig. 9 shows the deformed bars central cross-section for the AZ31-Mg alloy. For this material, when considering the TD case, the CB2001 yield criterion predicts a wedge shape, similar to the one obtained for the Zirconium. The CPB06, predicts a barrel-like shape. In fact, for the beam section bellow the neutral layer, the shape predicted for both yield criteria is very similar. Above that, the CB2001 predicted section dilates in the y direction, with the z one almost constant. For the CPB06, the section narrows in the y direction and dilates in the z direction. Also note that the curvature on the top surface has different directions for both yield criteria. Regarding the ND case, the CB2001 is not sensitive to the change in orientation. For the CPB06, however, the shape becomes closer to the one obtained with the CB2001 yield criterion but with more pronounced features, mainly in the upper part of the beam. For both cases, note that the major differences appear in the layer which is subjected to compression states, for which the CPB06 reproduces the virtual compression yield stresses in-plane evolution. The CB2001 presents a compression yield stresses in-plane evolution that is neither similar in shape or values to the virtual, i.e. shows a more anisotropic behavior with overestimated values (see Fig. 2(b)). Moreover, as shown in Fig. 2(a), the CPB06 predicts negative in-plane uniaxial compression r-values. In particular the r_0 is close to the one in tension, for both yield criteria, while it is close to -0.304 for the compression predicted by the CPB06. These may explain the fact that the deformation in the ND direction is always higher than the one along TD direction for the layers submitted to compression when using the CPB06 yield criterion. Also, it can explain why, in the TD case, the beam increases height while it narrows in the y direction, i.e, the strains in both direction are symmetric, being coherent with the fact that the r-value is negative.

In order to better understand the differences between both yield criteria and material orientations, the strain distributions are compared, along the z-axis of the central cross-section (for $y = 0$, according to Figs. 8 and 9). Again, experimental data is available only for the Zirconium, obtained through digitally processed local strain measurements determined by a dot-matrix deposition and mapping (DMDM) technique [31]. Fig. 10 presents the comparison between experimental and numerically predicted Green-Lagrange strain components, for the Zirconium. The Green-Lagrange strain tensor is defined by $\mathbf{E} = 1/2(\mathbf{C} - \mathbf{I}) = 1/2(\mathbf{F}\mathbf{F}^{\mathrm{T}} - \mathbf{I})$, where $\mathbf{F}$ is the deformation gradient. Regarding the TD case (see Fig. 10(a)), both yield criteria present a good prediction of the strain components distribution when compared with the experimental ones. However, the CPB06 predicts closer results as well as the shift of the neutral layer. For the ND case, the trend is the same – both yield criteria show a good agreement with the experimental data, with the CPB06 able to have a more accurate prediction, including the shift of the neutral layer. Also, this analysis allows to confirm the consistency of results between the predicted deformed shapes presented in Fig. 8, with the predictions of both yield criteria relatively close. In fact, the negative values predicted by the CPB06 for the uniaxial compression r-values only seem to affect the Green-Lagrange strain distribution for the hard to deform direction which, in the compression layer, are closer to zero when comparing with the ones obtained by the CB2001. As previously mentioned, in the TD case the hard to deform direction is mostly aligned with the z-axis, while for the ND case is mostly aligned with the y-axis. It should also be mentioned that the test leads to a strain of about 20% in the outmost fibers of the beam [6], which is close to the plastic strain value of 15% selected to determine the yield *locus* for the Zirconium.

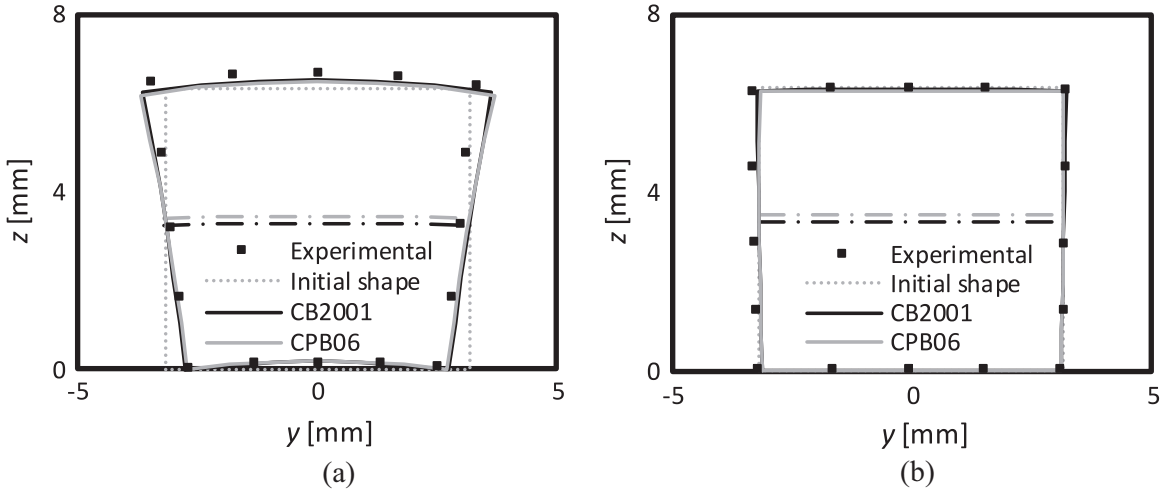

Fig. 8. Experimental and predicted y–z central cross-section of the bent bar considering (a) TD case and (b) ND case, for the Zirconium (dash-dot series indicate neutral layer for both yield criteria).

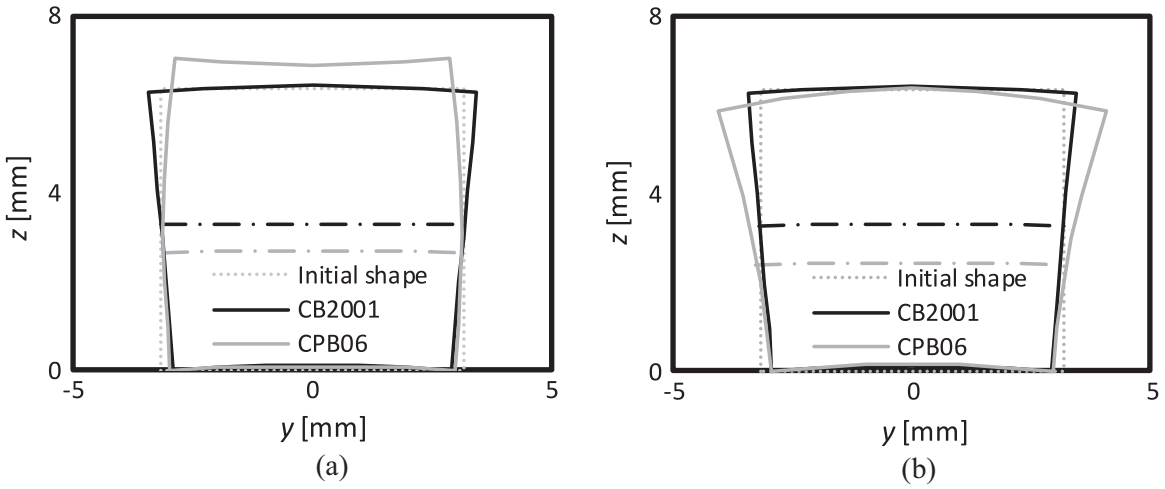

Fig. 9. Predicted y–z central cross-section of the bent bar considering (a) TD case and (b) ND case, for the AZ31-Mg alloy (dash-dot series indicate neutral layer for both yield criteria).

For the AZ31-Mg alloy, the results comparing only the numerically predicted strain components obtained along the z-axis of the beam central cross-section are presented in Fig. 11. Regarding the TD case, the CB2001 predicts strains in agreement with the final deformed shape obtained (see Fig. 9). Also note that components E_{zz} and E_{yy} have a very close evolution. As for the CPB06, there are major differences when comparing with the CB2001. The E_{yy} component is always negative with an inversion in the zone relative to the neutral layer. This evolution explains the final deformed barrel-like shape (see Fig. 9). The E_{zz} component starts at the beam bottom layer at about -0.7 and at the upper layer with a value of about 0.38. This evolution is in agreement with the fact that the beam central cross-section suffers a considerable increase in height. For the ND case, E_{zz} is almost constant and negative, thus explaining the minor change in height of the central cross-section. The E_{yy} component, however, shows a variation similar with the E_{zz} one for the TD case. This evolution is responsible for the more pronounced wedge-like shape, mainly for the area above the neutral layer. Nonetheless, it is not expected that the shape of the beam for the case of the AZ31-Mg alloy is so pronounced, since the tension–compression ratio decreases with the increase of plastic deformation (see [16]). In this case, the strain value attained in the outmost fibers of the beam is quite distinct from the plastic strain value of 3% selected to determine the yield *locus*.

5. Conclusion

The main features of the implementation of the Cazacu, Plunkett and Barlat yield criterion in the implicit in-house finite element solver DD3IMP were described. The analytical expressions for the first and second derivatives of the CPB06 yield criterion, necessary for an improved solution of the stress update algorithm, were derived and shown in detail in Appendix A, enabling its implementation in other finite element codes. The anisotropy parameters for Zirconium and AZ31-Mg alloy, both known for exhibiting strong tension–compression asymmetry as well as in-plane anisotropy, were identified for both CPB06 and CB2001 yield

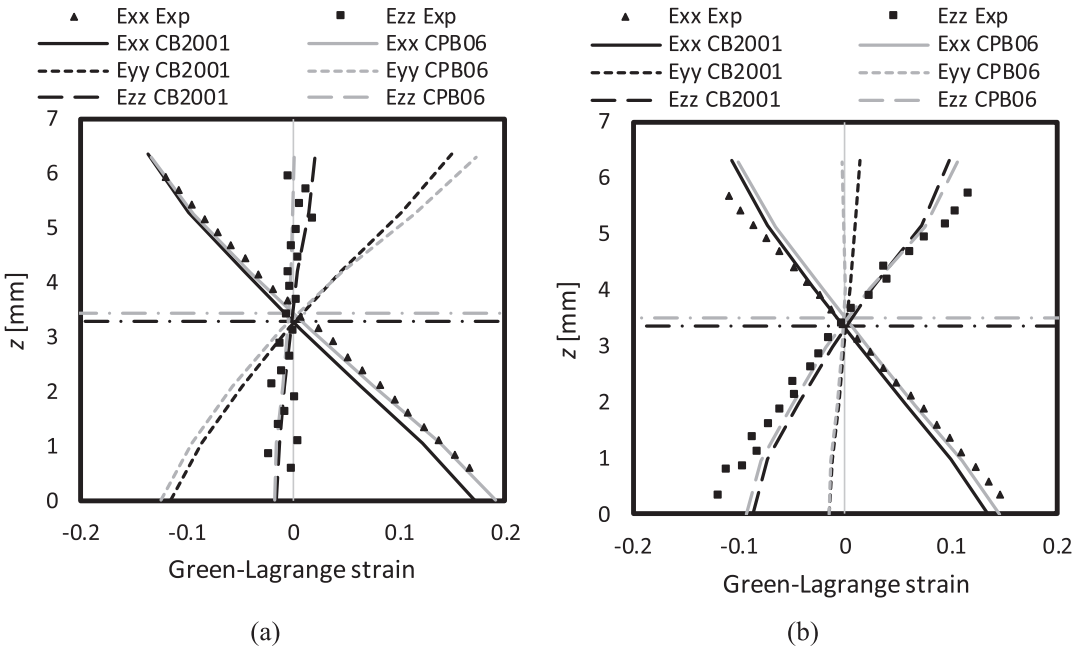

Fig. 10. Experimental and predicted Green-Lagrange strain distributions, considering (a) TD case and (b) ND case, for the Zirconium (dash-dot series indicate neutral layer for both yield criteria).

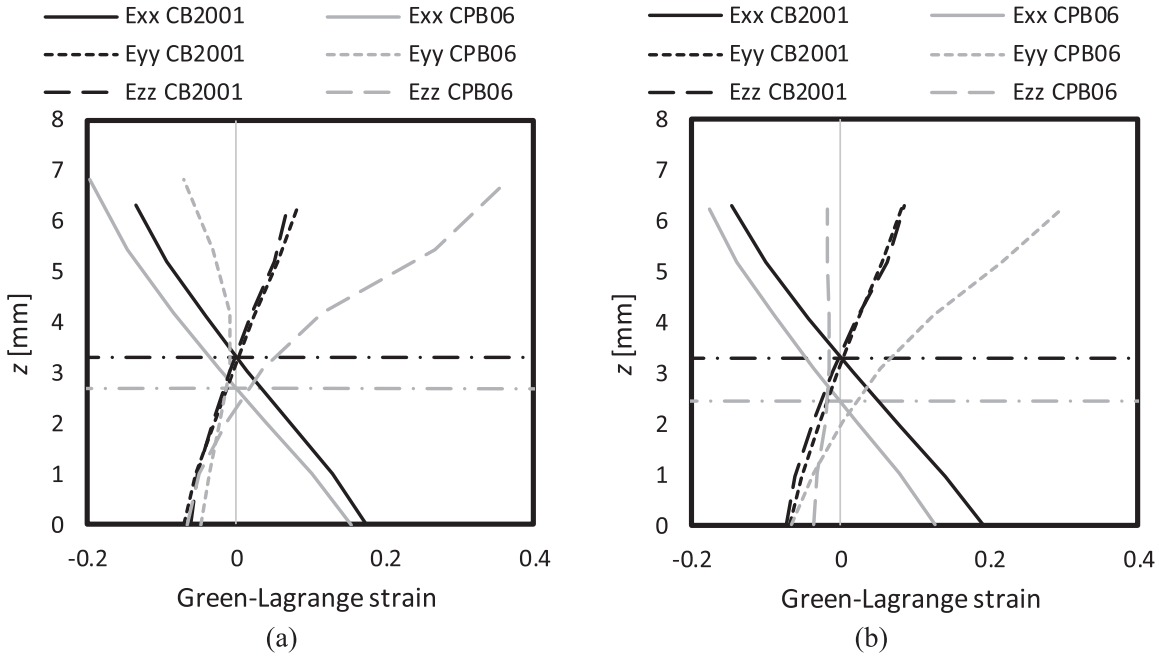

Fig. 11. Predicted Green-Lagrange strain distributions, considering (a) TD case and (b) ND case, for the AZ31-Mg alloy (dash-dot series indicate neutral layer for both yield criteria).

criteria. The results show that the yield criteria adopted can accurately describe both the yield stresses and r-values for tensile stress states, with CPB06 yield criterion also allowing an accurately prediction of the mechanical behavior for compression stress states, for both materials.

The numerical simulation of a four-point bending test was performed, considering the beam aligned along two different orientations. The results show that an accurate description of the tension–compression asymmetry influences the punch force evolution, for both materials. This effect is more relevant for the AZ31-Mg which shows a higher tension–compression asymmetry. In what concerns Zirconium and regarding the shape of the central cross-sections, both yield criteria describe well the final deformed shape with minimal differences between them, for both beam orientations, meaning that the tension–compression asymmetry is not the predominant phenomenon contributing to the almost squared shape for the ND case. In fact, the strain distribution analysis shows that both yield criteria have a good approximation to the experimental values, with the CPB06 showing better accuracy, particularly in what concerns the prediction of the shift of the neutral layer.

For the AZ31-Mg alloy and analyzing the deformed shape for the TD orientation, the difference between both yield criteria is clearly visible. The strain distributions predicted by the CPB06 show a very different trend from the CB2001, converging on a strong shift of the neutral layer. When considering the ND orientation, the CB2001 shows negligible differences in both shape and strain distributions on the central cross-section, when compared with the ones obtained for the TD case. In the ND case, the CPB06 predicts a shape similar to the one predicted by the CB2001, but more pronounced, supported by the strain distribution predicted. Thus, highlighting the sensitivity to the orientation of the CPB06 yield criterion. In summary, the global results shown and discussed, put in evidence the importance of modeling and taking into account the tension–compression asymmetry when analyzing the deformation of HCP materials.

Acknowledgment

The authors gratefully acknowledge the financial support of the Portuguese Foundation for Science and Technology (FCT), Portugal via the projects PTDC/EME-TME/118420/2010, UID/EMS/00285/2013 and by FEDER, Portugal funds through the program COMPETE – Programa Operacional Factores de Competitividade, under the project CENTRO-07-0224-FEDER-002001 (MT4MOBI). The first author is also grateful to the FCT for the Ph.D. Grant SFRH/BD/98545/2013.

Appendix A. Analytical expressions of the derivatives of the CPB2006 yield criterion

A.1. This section presents the details concerning the calculation of the following quantities

$$\beta,\ \mathbf{V}=\frac{\partial\bar{\sigma}}{\partial\boldsymbol{\sigma}},\ \mathbf{Q}=\frac{\partial^2\bar{\sigma}}{\partial\boldsymbol{\sigma}^2}, \tag{37}$$

specifically related with the numerical implementation of the CPB06 yield criterion in the FE solver DD3IMP.

The scalar β has to be evaluated whenever the effective stress state at the beginning of the time increment is elastic. It is determined with the consistency condition, such that

$$\Phi(\beta)=\bar{\sigma}\left(\boldsymbol{\sigma}'_0,\ \Delta\boldsymbol{\epsilon}',\ \beta\right)-Y_I=0, \tag{38}$$

where subscript I denotes the flow stress at the beginning of the time increment. β is the only unknown of this non-linear equation. Thus, the Newton–Raphson method is used to iteratively determine β, given by the relation

$$\beta^{i+1}=\beta^i-\frac{\Phi^i}{\Phi^{i'}}. \tag{39}$$

A schematic representation of the stress update algorithm is shown in Fig. 12, where $\boldsymbol{\sigma}'^{trial}$ corresponds to the one obtained from Eq. (17), and subscripts 0 and F denote the deviatoric stress tensor at the beginning and at the end of the time increment

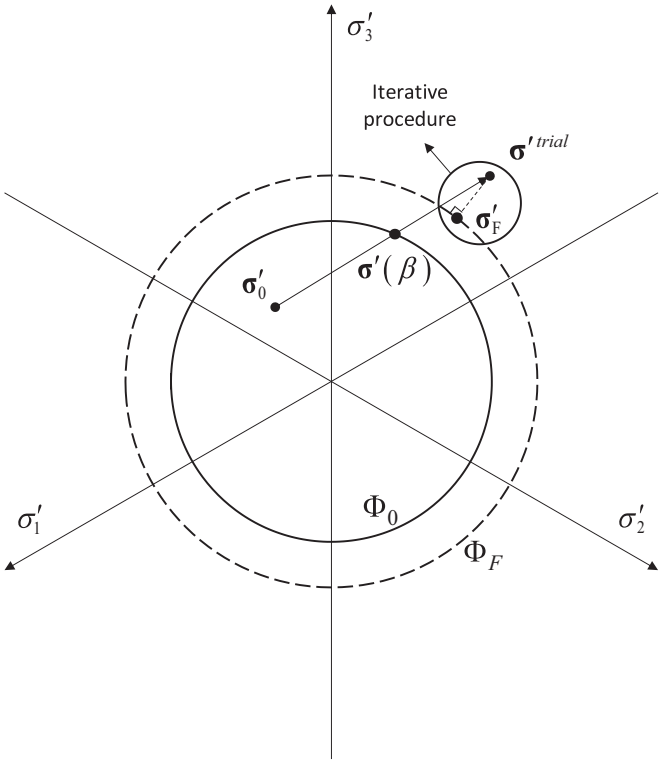

Fig. 12. Schematic representation of the stress update algorithm, with subscripts 0 and F denoting the quantities at the beginning and at the end of the time increment $[t, t+\Delta t]$.

$[t, t+\Delta t]$, respectively.

The scalar quantities Φ^i and $\Phi^{i'}$ are required, being the first one given by Eq. (38) and the second one by

$$\Phi^{i'} = \frac{\partial \bar{\sigma}(\boldsymbol{\sigma}_0', \Delta\boldsymbol{\epsilon}', \beta)}{\partial \beta^i} = \frac{\partial \bar{\sigma}}{\partial \boldsymbol{\sigma}^i}\frac{\partial \boldsymbol{\sigma}^i}{\partial \beta^i} = \mathbf{V}^i : (2\mu\Delta\boldsymbol{\epsilon}'). \tag{40}$$

The tensor $\mathbf{V}$ is given by

$$\mathbf{V}_{ij} = \frac{1}{2}\left(\frac{\partial}{\partial \boldsymbol{\sigma}_{ij}} + \frac{\partial}{\partial \boldsymbol{\sigma}_{ji}}\right)F = \frac{\partial \bar{\sigma}}{\partial s_p}\frac{\partial s_p}{\partial H_m}\frac{\partial H_m}{\partial s_{rs}}\Big|^{sym}\frac{\partial s_{rs}}{\partial \boldsymbol{\sigma}_{ij}}\Big|^{sym}, \tag{41}$$

while the tensor $\mathbf{Q}$ is given by,

$$\begin{aligned}
\mathbf{Q}_{ijkl} &= \frac{1}{2}\left(\frac{\partial}{\partial \boldsymbol{\sigma}_{kl}} + \frac{\partial}{\partial \boldsymbol{\sigma}_{lk}}\right)\mathbf{V}_{ij} \\
&= \frac{1}{2}\left(\frac{\partial}{\partial \boldsymbol{\sigma}_{kl}} + \frac{\partial}{\partial \boldsymbol{\sigma}_{lk}}\right)\left(\frac{\partial \bar{\sigma}}{\partial s_p}\frac{\partial s_p}{\partial H_m}\frac{\partial H_m}{\partial s_{rs}}\Big|^{sym}\frac{\partial s_{rs}}{\partial \boldsymbol{\sigma}_{ij}}\Big|^{sym}\right) \\
&= \frac{\partial^2 \bar{\sigma}}{\partial s_p \partial s_q}\left(\frac{\partial s_q}{\partial H_n}\frac{\partial H_n}{\partial s_{uv}}\Big|^{sym}\frac{\partial s_{uv}}{\partial \boldsymbol{\sigma}_{kl}}\Big|^{sym}\right)\left(\frac{\partial s_p}{\partial H_m}\frac{\partial H_m}{\partial s_{rs}}\Big|^{sym}\frac{\partial s_{rs}}{\partial \boldsymbol{\sigma}_{ij}}\Big|^{sym}\right) \\
&\quad + \frac{\partial \bar{\sigma}}{\partial s_p}\frac{\partial^2 s_p}{\partial H_m \partial H_n}\left(\frac{\partial H_n}{\partial s_{uv}}\Big|^{sym}\frac{\partial s_{uv}}{\partial \boldsymbol{\sigma}_{kl}}\Big|^{sym}\right)\left(\frac{\partial H_m}{\partial s_{rs}}\Big|^{sym}\frac{\partial s_{rs}}{\partial \boldsymbol{\sigma}_{ij}}\Big|^{sym}\right) \\
&\quad + \frac{\partial \bar{\sigma}}{\partial s_p}\frac{\partial s_p}{\partial H_m}\frac{\partial^2 H_m}{\partial s_{rs}\partial s_{uv}}\Big|^{sym}\frac{\partial s_{uv}}{\partial \boldsymbol{\sigma}_{kl}}\Big|^{sym}\frac{\partial s_{rs}}{\partial \boldsymbol{\sigma}_{ij}}\Big|^{sym}
\end{aligned} \tag{42}$$

The initial effective stress state is then updated to the initial yield surface as

$$(\boldsymbol{\sigma}_0')^* \leftarrow \boldsymbol{\sigma}_0' + \beta(2\mu\Delta\boldsymbol{\epsilon}') \tag{43}$$

The terms relative to the first and second order derivatives are defined bellow.

A.2. First derivatives

a) Expressions for $\partial\bar{\sigma}/\partial s_p$

$$\begin{aligned}
\frac{\partial \bar{\sigma}}{\partial s_p} &= \frac{\partial}{\partial s_p}\Big[B\cdot\big((|s_1| - k\,s_1)^a + (|s_2| - k\,s_2)^a + (|s_3| - k\,s_3)^a\big)\Big] \\
&= \frac{B}{a}\Big[(|s_1| - k\,s_1)^a + (|s_2| - k\,s_2)^a + (|s_3| - k\,s_3)^a\Big]^{\frac{1}{a}-1}\cdot \\
&\quad \left[a\big(|s_p| - k\,s_p\big)^{a-1}\left(\frac{|s_p|}{s_p} - k\right)\right], = R\cdot D(s_p)
\end{aligned} \tag{44}$$

with

$$R = \frac{B}{a}(A)^{\frac{1}{a}-1}, \tag{45}$$

and

$$A = \Big[(|s_1| - k\,s_1)^a + (|s_2| - k\,s_2)^a + (|s_3| - k\,s_3)^a\Big]. \tag{46}$$

Also,

$$D(s_p) = \left[a\big(|s_p| - k\,s_p\big)^{a-1}\left(\frac{|s_p|}{s_p} - k\right)\right]. \tag{47}$$

b) Expressions for $\partial s_p/\partial H_m$

$$\frac{\partial s_i}{\partial H_m} = \frac{\partial}{\partial H_m}\left[H_1 + 2\sqrt{H_1^2 + H_2}\cdot\cos\left(\frac{\theta}{3} + \beta_i\right)\right], \tag{48}$$

$$\frac{\partial s_i}{\partial H_1} = 1 + \frac{2H_1}{\sqrt{H_1^2 + H_2}}\cdot\cos\left(\frac{\theta}{3} + \beta_i\right) - \frac{2}{3}\sqrt{H_1^2 + H_2}\cdot \sin\left(\frac{\theta}{3} + \beta_i\right)\frac{\partial\theta}{\partial H_1}, \tag{49}$$

$$\frac{\partial s_i}{\partial H_2} = \frac{2H_1}{\sqrt{H_1^2 + H_2}}\cdot\cos\left(\frac{\theta}{3} + \beta_i\right) - \frac{2}{3}\sqrt{H_1^2 + H_2}\cdot \sin\left(\frac{\theta}{3} + \beta_i\right)\frac{\partial\theta}{\partial H_2}, \tag{50}$$

$$\frac{\partial s_i}{\partial H_3} = -\frac{2}{3}\sqrt{H_1^2 + H_2}\cdot\sin\left(\frac{\theta}{3} + \beta_i\right)\frac{\partial\theta}{\partial H_3}, \tag{51}$$

with $\beta_1 = 0$, $\beta_2 = \frac{4}{3}\pi$ and $\beta_3 = \frac{2}{3}\pi$.

$$\frac{\partial\theta}{\partial H_1} = -\frac{3}{2}\frac{\big(2H_1^2 + H_2\big)H_p - 2H_qH_1}{H_p\sqrt{H_p^3 + H_q^2}} \tag{52}$$

$$\frac{\partial\theta}{\partial H_2} = -\frac{3}{2}\frac{H_1H_p - 2H_q}{H_p\sqrt{H_p^3 + H_q^2}} \tag{53}$$

$$\frac{\partial\theta}{\partial H_3} = -\frac{H_p}{H_p\sqrt{H_p^3 + H_q^2}} \tag{54}$$

c) Expressions for $\partial H_m/\partial s_{rs}$

$$\frac{\partial H_1}{\partial s_{kl}} = \frac{1}{2}\left(\frac{\partial}{\partial s_{kl}} + \frac{\partial}{\partial s_{lk}}\right)H_1 = \frac{1}{3}\delta_{kl} \tag{55}$$

$$\frac{\partial H_2}{\partial s_{kl}} = \frac{1}{2}\left(\frac{\partial}{\partial s_{kl}} + \frac{\partial}{\partial s_{lk}}\right)H_1 = \frac{1}{3}\begin{bmatrix} -s_{yy} - s_{zz} \\ -s_{xx} - s_{zz} \\ -s_{xx} - s_{yy} \\ \frac{1}{2}(s_{zy} + s_{yz}) \\ \frac{1}{2}(s_{zx} + s_{xz}) \\ \frac{1}{2}(s_{yx} + s_{xy}) \end{bmatrix} \tag{56}$$

$$\frac{\partial H_3}{\partial s_{kl}} = \frac{1}{2}\left(\frac{\partial}{\partial s_{kl}} + \frac{\partial}{\partial s_{lk}}\right)H_1 = \frac{1}{3}\begin{bmatrix} s_{yy}s_{zz} - s_{yz}s_{zy} \\ s_{xx}s_{zz} - s_{xz}s_{zx} \\ s_{xx}s_{yy} - s_{xy}s_{yx} \\ \frac{1}{2}\left(s_{xy}s_{zx} + s_{yx}s_{xz} - s_{xx}(s_{yz} + s_{zy})\right) \\ \frac{1}{2}\left(s_{yx}s_{zy} + s_{xy}s_{yz} - s_{yy}(s_{xz} + s_{zx})\right) \\ \frac{1}{2}\left(s_{yz}s_{zx} + s_{zy}s_{xz} - s_{zz}(s_{xy} + s_{yx})\right) \end{bmatrix} \tag{57}$$

d) Expression for $\partial s_{kl}/\partial \boldsymbol{\sigma}_{ij}$

$$\frac{\partial s_{kl}}{\partial \boldsymbol{\sigma}_{ij}} = \frac{\partial}{\partial \boldsymbol{\sigma}_{ij}}\left[\mathbf{L}_{ijkl} : \boldsymbol{\sigma}_{kl}\right] = \mathbf{L}_{ijkl}\frac{\partial \boldsymbol{\sigma}_{kl}}{\partial \boldsymbol{\sigma}_{ij}} = \mathbf{L}_{ijkl}\delta_{ki}\delta_{lj} \tag{58}$$

A.3. Second derivatives

The second order derivatives have a role in the state variables update (see Eq. (56)) and in the definition of the consistent elastoplastic modulus.

a) Expression for $\partial^2\bar{\sigma}/\partial s_p \partial s_q$

$$\frac{\partial^2 \bar{\sigma}}{\partial s_p \partial s_q} = \frac{1}{A}\cdot\left(\frac{1}{a} - 1\right)\cdot\left[\frac{\partial \bar{\sigma}}{\partial s_p}\right]\cdot D(s_q) + R\cdot\frac{\partial}{\partial s_q}\left[\ D(s_p)\right] \tag{59}$$

with

$$D(s_q) = \left[a\left(\ |s_q| - k\ s_q\right)^{a-1}\left(\frac{|s_q|}{s_q} - k\right)\right] \tag{60}$$

b) Expressions for $\partial^2 s_p/\partial H_m H_n$

$$\frac{\partial^2 s_p}{\partial H_m H_n} = \frac{\partial}{H_n}\left(\frac{\partial s_p}{\partial H_m}\right) \tag{61}$$

$$\begin{aligned}\frac{\partial}{\partial H_n}\left(\frac{\partial s_i}{\partial H_1}\right) = {} & \cos\left(\frac{\theta}{3} + \beta_i\right)\cdot \mathrm{dA1}(n) - \frac{2}{3}\ \sin\left(\frac{\theta}{3} + \beta_i\right)\frac{\partial \theta}{\partial H_1}\mathrm{dA2}(n) \\ & - \frac{1}{3}\sqrt{H_1^2 + H_2}\left[\frac{2H_1}{H_1^2 + H_2}\ \sin\left(\frac{\theta}{3} + \beta_i\right) + \frac{2}{3}\cdot\cos\left(\frac{\theta}{3} + \beta_i\right)\frac{\partial \theta}{\partial H_1}\right]\frac{\partial \theta}{\partial H_n} \\ & - \frac{2}{3}\sqrt{H_1^2 + H_2}\cdot\sin\left(\frac{\theta}{3} + \beta_i\right)\frac{\partial^2 \theta}{\partial H_1 \partial H_n}\end{aligned} \tag{62}$$

$$\begin{aligned}\frac{\partial}{\partial H_n}\left(\frac{\partial s_i}{\partial H_2}\right) = {} & \cos\left(\frac{\theta}{3} + \beta_i\right)\cdot \\ & \mathrm{dA3}(n) - \frac{2}{3}\ \sin\left(\frac{\theta}{3} + \beta_i\right)\frac{\partial \theta}{\partial H_2}\mathrm{dA2}(n) \\ & - \frac{1}{3}\sqrt{H_1^2 + H_2}\left[\frac{1}{H_1^2 + H_2}\cdot\right. \\ & \left.\sin\left(\frac{\theta}{3} + \beta_i\right) + \frac{2}{3}\ \cos\left(\frac{\theta}{3} + \beta_i\right)\frac{\partial \theta}{\partial H_2}\right]\frac{\partial \theta}{\partial H_n} \\ & - \frac{2}{3}\sqrt{H_1^2 + H_2}\cdot\sin\left(\frac{\theta}{3} + \beta_i\right)\frac{\partial^2 \theta}{\partial H_2 \partial H_n}\end{aligned} \tag{63}$$

$$\begin{aligned}\frac{\partial}{\partial H_n}\left(\frac{\partial s_i}{\partial H_3}\right) = {} & -\frac{2}{3}\ \sin\left(\frac{\theta}{3} + \beta_i\right)\frac{\partial \theta}{\partial H_3}\mathrm{dA2}(n) \\ & - \frac{1}{3}\sqrt{H_1^2 + H_2}\left[\frac{2}{3}\ \cos\left(\frac{\theta}{3} + \beta_i\right)\frac{\partial \theta}{\partial H_3}\right]\frac{\partial \theta}{\partial H_n} \\ & - \frac{2}{3}\sqrt{H_1^2 + H_2}\cdot\sin\left(\frac{\theta}{3} + \beta_i\right)\frac{\partial^2 \theta}{\partial H_3 \partial H_n}\end{aligned} \tag{64}$$

with

$$\mathrm{dA1}(n) = \frac{\partial}{\partial H_n}\left(\frac{2H_1}{\sqrt{H_1^2 + H_2}}\right) = \begin{bmatrix}\frac{2H_2}{\left(\sqrt{H_1^2 + H_2}\right)^3} & -\frac{H_1}{\left(\sqrt{H_1^2 + H_2}\right)^3} & 0\end{bmatrix} \tag{65}$$

$$\mathrm{dA2}(n) = \frac{\partial}{\partial H_n}\left(\sqrt{H_1^2 + H_2}\right) = \begin{bmatrix}\frac{H_1}{\sqrt{H_1^2 + H_2}} & \frac{1}{2\sqrt{H_1^2 + H_2}} & 0\end{bmatrix} \tag{66}$$

$$\mathrm{dA3}(n) = \frac{\partial}{\partial H_n}\left(\frac{1}{\sqrt{H_1^2 + H_2}}\right) = \begin{bmatrix}-\frac{H_1}{\left(\sqrt{H_1^2 + H_2}\right)^3} & -\frac{1}{2\left(\sqrt{H_1^2 + H_2}\right)^3} & 0\end{bmatrix} \tag{67}$$

$$\frac{\partial}{\partial H_n}\left(\cos\left(\frac{\theta}{3} + \beta_i\right)\right) = -\frac{1}{3}\ \sin\left(\frac{\theta}{3} + \beta_i\right)\frac{\partial \theta}{\partial H_n} \tag{68}$$

$$\frac{\partial}{\partial H_n}\left(\sin\left(\frac{\theta}{3} + \beta_i\right)\right) = \frac{1}{3}\ \cos\left(\frac{\theta}{3} + \beta_i\right)\frac{\partial \theta}{\partial H_n}. \tag{69}$$

Also,

$$\begin{aligned}\frac{\partial}{H_n}\left(\frac{\partial \theta}{\partial H_m}\right) = {} & -\frac{H_p\frac{\partial^2 H_q}{\partial H_m \partial H_n} + \frac{\partial H_q}{\partial H_m}\frac{\partial H_p}{\partial H_n} - \frac{3}{2}\left(\frac{\partial H_q}{\partial H_n}\frac{\partial H_p}{\partial H_m} + H_q\frac{\partial^2 H_p}{\partial H_m \partial H_n}\right)}{H_p\sqrt{H_p^3 - H^2{}_q}} \\ & + \frac{\left(H_p\frac{\partial H_q}{\partial H_m} - \frac{3}{2}H_q\frac{\partial H_p}{\partial H_m}\right)}{2\left(H_p\sqrt{H_p^3 - H^2{}_q}\right)^2\sqrt{H_p^3 - H^2{}_q}}\left(\left(5H_p^3 - 2H_q^2\right)\frac{\partial H_p}{\partial H_n}\right. \\ & \left. - 2H_pH_q\frac{\partial H_q}{\partial H_n}\right),\end{aligned} \tag{70}$$

with

$$\frac{\partial H_p}{\partial H_m} = \frac{\partial}{\partial H_m}\left(H_1^2 + H_2\right) = \begin{bmatrix}2H_1 \\ 1 \\ 0\end{bmatrix}, \tag{71}$$

$$\frac{\partial H_q}{\partial H_m} = \frac{\partial}{\partial H_m}\left[\frac{1}{2}\left(2H_1^3 + 3H_1H_2 + 2H_3\right)\right] = \frac{1}{2}\begin{bmatrix}6H_1^2 + 3H_2 \\ 3H_1 \\ 2\end{bmatrix}, \tag{72}$$

$$\frac{\partial^2 H_p}{\partial H_m \partial H_n} = \frac{\partial}{\partial H_n}\left(\begin{bmatrix}2H_1 \\ 1 \\ 0\end{bmatrix}\right) = \begin{bmatrix}2 & 0 & 0 \\ 0 & 0 & 0 \\ 0 & 0 & 0\end{bmatrix}, \tag{73}$$

$$\frac{\partial^2 H_q}{\partial H_m \partial H_n} = \frac{\partial}{\partial H_n}\left[\frac{1}{2}\begin{bmatrix}6H_1^2 + 3H_2 \\ 3H_1 \\ 2\end{bmatrix}\right] = \frac{1}{2}\begin{bmatrix}12H_1 & 0 & 0 \\ 3 & 0 & 0 \\ 0 & 0 & 0\end{bmatrix}. \tag{74}$$

c) Expressions for $\partial^2 H_m/\partial s_{rs}\partial s_{uv}$

$$\frac{\partial^2 H_1}{\partial s_{kl}\partial s_{mn}} = \frac{1}{2}\left(\frac{\partial}{\partial s_{mn}} + \frac{\partial}{\partial s_{nm}}\right)\left[\frac{1}{3}\delta_{kl}\right] = \mathbf{0} \tag{75}$$

$$\frac{\partial^2 H_2}{\partial s_{kl}\partial s_{mn}} = \frac{1}{2}\left(\frac{\partial}{\partial s_{mn}} + \frac{\partial}{\partial s_{nm}}\right)\frac{\partial H_2}{\partial s_{kl}} = \frac{1}{3}\begin{bmatrix} 0 & -1 & -1 & 0 & 0 & 0 \\ -1 & 0 & -1 & 0 & 0 & 0 \\ -1 & -1 & 0 & 0 & 0 & 0 \\ 0 & 0 & 0 & \frac{1}{2} & 0 & 0 \\ 0 & 0 & 0 & 0 & \frac{1}{2} & 0 \\ 0 & 0 & 0 & 0 & 0 & \frac{1}{2} \end{bmatrix} \tag{76}$$

$$\frac{\partial^2 H_3}{\partial s_{kl}\partial s_{mn}} = \frac{1}{2}\begin{bmatrix} 0 & s_{zz} & s_{yy} & -s_{yz} & 0 & 0 \\ s_{zz} & 0 & s_{xx} & 0 & -s_{xz} & 0 \\ s_{yy} & s_{xx} & 0 & 0 & 0 & -s_{xy} \\ -s_{yz} & 0 & 0 & -\frac{1}{2}s_{xx} & \frac{1}{2}s_{xy} & \frac{1}{2}s_{xz} \\ 0 & -s_{xz} & 0 & \frac{1}{2}s_{xy} & -\frac{1}{2}s_{yy} & \frac{1}{2}s_{yz} \\ 0 & 0 & -s_{xy} & \frac{1}{2}s_{xz} & \frac{1}{2}s_{yz} & -\frac{1}{2}s_{zz} \end{bmatrix} \tag{77}$$

d) Expressions for $\partial\theta/\partial H_a$

For sake of simplicity, the following is considered

$$\theta = \arccos\left[\frac{H_q}{H_p^{3/2}}\right] = \arccos[C], \text{ with } C = \frac{H_q}{H_p^{3/2}} \tag{78}$$

Thus, the derivative for $\partial\theta/\partial H_a$

$$\frac{\partial\theta}{\partial H_a} = \frac{\partial\theta}{\partial H_p}\frac{\partial H_p}{\partial H_a} + \frac{\partial\theta}{\partial H_q}\frac{\partial H_q}{\partial H_a} \tag{79}$$

The terms for the above expression are given by

$$\frac{\partial\theta}{\partial H_q} = -\frac{1}{\sqrt{1-C^2}}\cdot\frac{1}{H_p^{3/2}} = K\cdot\frac{1}{H_p^{3/2}}, \tag{80}$$

$$\frac{\partial\theta}{\partial H_p} = -\frac{1}{\sqrt{1-C^2}}\cdot C\cdot\left(-\frac{3}{2}\frac{1}{H_p}\right) = K\cdot C\cdot\left(-\frac{3}{2}\frac{1}{H_p}\right), \tag{81}$$

$$\frac{\partial H_q}{\partial H_a} = \begin{bmatrix} 3H_1^2 + \frac{3}{2}H_2 \\ \frac{3}{2}H_1 \\ 1 \end{bmatrix}, \tag{82}$$

$$\frac{\partial H_p}{\partial H_a} = \begin{bmatrix} 2H_1 \\ 1 \\ 0 \end{bmatrix}, \tag{83}$$

with

$$K = -\frac{1}{\sqrt{1-C^2}} \tag{84}$$

e) Expressions for $\partial^2\theta/\partial H_a\partial H_b$

$$\frac{\partial^2\theta}{\partial H_a\partial H_b} = \frac{\partial}{\partial H_b}\left(\frac{\partial\theta}{\partial H_p}\frac{\partial H_p}{\partial H_a} + \frac{\partial\theta}{\partial H_q}\frac{\partial H_q}{\partial H_a}\right) = \left(\frac{\partial^2\theta}{\partial H_p\partial H_p}\frac{\partial H_p}{\partial H_b} + \frac{\partial^2\theta}{\partial H_p\partial H_q}\frac{\partial H_q}{\partial H_b}\right)\frac{\partial H_p}{\partial H_a} + \frac{\partial\theta}{\partial H_p}\left(\frac{\partial^2 H_p}{\partial H_a\partial H_b}\right), + \left(\frac{\partial^2\theta}{\partial H_q\partial H_q}\frac{\partial H_q}{\partial H_b} + \frac{\partial^2\theta}{\partial H_q\partial H_p}\frac{\partial H_p}{\partial H_b}\right)\frac{\partial H_q}{\partial H_a} + \frac{\partial\theta}{\partial H_q}\left(\frac{\partial^2 H_q}{\partial H_a\partial H_b}\right) \tag{85}$$

with

$$\frac{\partial^2 H_q}{\partial H_a\partial H_b} = \begin{bmatrix} 6H_1 & \frac{3}{2} & 0 \\ \frac{3}{2} & 0 & 0 \\ 0 & 0 & 0 \end{bmatrix} \text{ and } \frac{\partial^2 H_p}{\partial H_a\partial H_b} = \begin{bmatrix} 2 & 0 & 0 \\ 0 & 0 & 0 \\ 0 & 0 & 0 \end{bmatrix}, \tag{86}$$

$$\frac{\partial^2\theta}{\partial H_q\partial H_q} = \frac{\partial K}{\partial H_q}\cdot\left(\frac{1}{H_p^{3/2}}\right) \tag{87}$$

$$\frac{\partial^2\theta}{\partial H_q\partial H_p} = \frac{\partial K}{\partial H_p}\cdot\left(\frac{1}{H_p^{3/2}}\right) + K\cdot\left(\frac{1}{H_p^{3/2}}\right)\cdot\left(-\frac{3}{2}\frac{1}{H_p}\right) \tag{88}$$

$$\frac{\partial^2\theta}{\partial H_p\partial H_q} = \frac{\partial K}{\partial H_q}\cdot C\cdot\left(-\frac{3}{2}\frac{1}{H_p}\right) + K\cdot\frac{\partial C}{\partial H_q}\cdot\left(-\frac{3}{2}\frac{1}{H_p}\right) \tag{89}$$

$$\frac{\partial^2\theta}{\partial H_p\partial H_p} = \frac{\partial K}{\partial H_p}\cdot C\cdot\left(-\frac{3}{2}\frac{1}{H_p}\right) + K\cdot\frac{\partial C}{\partial H_p}\cdot\left(-\frac{3}{2}\frac{1}{H_p}\right) - K\cdot C\cdot\left(-\frac{3}{2}\frac{1}{H_p}\right)\frac{1}{H_p} \tag{90}$$

A.4. Principal values

The principal values are calculated by solving the characteristic equation

$$\det(\mathbf{s} - s\mathbf{I}) = 0 \tag{91}$$

where s represents the principal values of $\mathbf{s}$ and $\mathbf{s}$ is a tensor whose trace is zero,

$$\mathbf{s} = \begin{bmatrix} s_{xx} & s_{xy} & s_{xz} \\ s_{xy} & s_{yy} & s_{yz} \\ s_{xz} & s_{yz} & s_{zz} \end{bmatrix}. \tag{92}$$

x, y and z denote an orthogonal frame attached to the material (i.e. sheet rolling, transverse and normal directions, respectively).

This equation reduces to

$$s^3 - H_1 s^2 - 3H_2 s - 2H_3 = 0, \tag{93}$$

with

$$H_1 = \frac{1}{3}I_1 = \frac{1}{3}(s_{xx} + s_{yy} + s_{zz}), \tag{94}$$

$$H_2 = \frac{1}{3}I_2 = \frac{1}{3}\left(s_{yz}^2 + s_{zx}^2 + s_{xy}^2 - s_{yy}s_{zz} - s_{zz}s_{xx} - s_{xx}s_{yy}\right), \tag{95}$$

$$H_3 = \frac{1}{2}I_3 = \frac{1}{2}\left(2s_{yz}s_{zx}s_{xy} + s_{xx}s_{yy}s_{zz} - s_{xx}s_{yz}^2 - s_{yy}s_{zx}^2 - s_{zz}s_{xy}^2\right). \tag{96}$$

Through a change of variables [8],

$$s = s + H_1, \tag{97}$$

the characteristic equation becomes

$$\bar{s}^3 - 3H_p\bar{s} - 2H_q = 0, \tag{98}$$

with

$$a)\ H_p = H_1^2 + H_2, \tag{99}$$

$$b)\ H_q = \frac{1}{2}\left(2H_1^3 + 3H_1H_2 + 2H_3\right), \tag{100}$$

$$c)\ \theta = \arccos\left[\frac{H_q}{H_p^{3/2}}\right], \tag{101}$$

Cardan's solutions to the characteristic equation are

$$a)\ \bar{s}_1 = z^{1/3} + \bar{z}^{1/3}, \tag{102}$$

$$b)\ \bar{s}_2 = \omega z^{1/3} + \bar{\omega}\bar{z}^{1/3}, \tag{103}$$

$$c)\ \bar{s}_3 = \bar{\omega}z^{1/3} + \omega\bar{z}^{1/3}, \tag{104}$$

where z is a complex number. ω is a complex constant ($e^{-2i\pi/3}$), and $\bar{z}$ and $\bar{\omega}$ are their conjugate quantities.

$$z = H_q + \mathrm{i}\sqrt{H_p^3 - H_q^2}, \tag{105}$$

The principal values of s can be written as

$$\begin{cases} s_1 = H_1 + 2\sqrt{H_1^2 + H_2}\ \cos(\theta/3) \\ s_2 = H_1 + 2\sqrt{H_1^2 + H_2}\ \cos\left(\dfrac{\theta + 4\pi}{3}\right), \\ s_3 = H_1 + 2\sqrt{H_1^2 + H_2}\ \cos\left(\dfrac{\theta + 2\pi}{3}\right) \end{cases} \tag{106}$$

These values are ordered as [8]

$$s_1 \geq s_2 \geq s_3, \quad s_1 > s_3. \tag{107}$$

References

[1] Cazacu O, Plunkett B, Barlat F. Orthotropic yield criterion for hexagonal closed packed metals. Int J Plast 2006;22(7):1171–94.
[2] Alves JL. An advanced constitutive model in the sheet metal forming simulation: the Teodosiu microstructural model and the Cazacu Barlat yield criterion. AIP Conf Proc 2004;712:1645–50.
[3] Cazacu O, Barlat F. Generalization of Drucker's yield criterion to orthotropy. Math Mech Solids 2001;6(6):613–30.
[4] Cazacu O. A criterion for description of anisotropy and yield differential effects in pressure-insensitive metals. Int J Plast 2004;20(11):2027–45.
[5] Plunkett B, Cazacu O, Barlat F. Orthotropic yield criteria for description of the anisotropy in tension and compression of sheet metals. Int J Plast 2008;24 (5):847–66.
[6] Plunkett B, Lebensohn RA, Cazacu O, Barlat F. Anisotropic yield function of hexagonal materials taking into account texture development and anisotropic hardening. Acta Mater 2006;54(16):4159–69.
[7] Yoon JW, Barlat F, Chung K, Pourboghrat F, Yang DY. Earing predictions based on asymmetric nonquadratic yield function. Int J Plast 2000;16(9):1075–104.
[8] Barlat F, Aretz H, Yoon JW, Karabin ME, Brem JC, Dick RE. Linear transfomation-based anisotropic yield functions. Int J Plast 2005;21(5):1009–39.
[9] Moayyedian F, Kadkhodayan M. Combination of modified Yld2000-2d and Yld2000-2d in anisotropic pressure dependent sheet metals, 1984; 2014. p. 2804–26.
[10] Banabic D. Sheet metal forming processes.Berlin Heidelberg: Springer-Verlag; 2010.
[11] Yoon J, Barlat F, Dick R, Karabin M. Prediction of six or eight ears in a drawn cup based on a new anisotropic yield function. Int J Plast 2006;22(1):174–93.
[12] Tritschler M, Butz A, Helm D, Falkinger G, Kiese J. Experimental analysis and modeling of the anisotropic response of titanium alloy Ti-X for quasi-static loading at room temperature. Int J Mater Form 2014;7(3):259–73.
[13] Tuninetti V, Gilles G, Milis O, Pardoen T, Habraken AM. Anisotropy and tension–compression asymmetry modeling of the room temperature plastic response of Ti–6Al–4V. Int J Plast 2015;67:53–68.
[14] Gilles G, Cazacu O, Hammami W, Habraken a M, Duchêne L. Experimental and numerical study of TA-6V mechanical behavior in different monotonic loading conditions at room temperature. Procedia IUTAM 2012;3:100–14.
[15] Revil-Baudard B, Cazacu O, Flater P, Kleiser G. Plastic deformation of high-purity α-titanium: model development and validation using the Taylor cylinder impact test. Mech Mater 2014;80:264–75.
[16] Chandola N, Lebensohn RA, Cazacu O, Revil-Baudard B, Mishra RK, Barlat F. Combined effects of anisotropy and tension–compression asymmetry on the torsional response of AZ31 Mg. Int J Solids Struct 2015;58:190–200.
[17] Revil-Baudard B, Chandola N, Cazacu O, Barlat F. Correlation between swift effects and tension–compression asymmetry in various polycrystalline materials. J Mech Phys Solids 2014;70:104–15.
[18] Cazacu O, Revil-Baudard B, Barlat F. New interpretation of monotonic Swift effects: role of tension–compression asymmetry. Mech Mater 2013;57:42–52.
[19] Revil-Baudard B, Cazacu O. On the effect of the matrix tension-compression asymmetry on damage evolution in porous plastic solids. Eur J Mech A/Solids 2013;37:35–44.
[20] Alves JL, Cazacu O. Correlation between strength differential effects in the plastic flow of the matrix and the rate of damage growth in porous polycrystals. C. R. Méc. 2015;343(2):107–20.
[21] Cazacu O, Ionescu IR, Yoon JW. Orthotropic strain rate potential for the description of anisotropy in tension and compression of metals. Int J Plast 2010;26(6):887–904.
[22] Menezes LF, Teodosiu C. Three-dimensional numerical simulation of the deep-drawing process using solid finite elements. J Mater Process Technol 2000;97 (1–3):100–6.
[23] Oliveira MC, Alves JL, Menezes LF. Algorithms and strategies for treatment of large deformation frictional contact in the numerical simulation of deep drawing process. Arch Comput Methods Eng 2008;15(2):113–62.
[24] Teodosiu C. The plastic spin: microstructural origin and computational significance; 1989. p. 163–74.
[25] Simo JC, Taylor RL. Consistent tangent operators for rate-independent elastoplasticity. Comput Methods Appl Mech Eng 1985;48(1):101–18.
[26] Alves JL. Simulação numérica do processo de estampagem de chapas metálicas: modelação mecânica e métodos numéricos. University of Minho; 2003.
[27] Barlat F, Maeda Y, Chung K, Yanagawa M, Brem JC, Hayashida Y, Lege DJ, Matsui K, Murtha SJ, Hattori S, Becker RC, Makosey S. Yield function development for aluminum alloy sheets. J Mech Phys Solids 1997;45(11–12):1727–63.
[28] Barros PD, Oliveira MC, Alves JL, Andrade-Campos A, Menezes LF. Modelling of tension-compression asymmetry and orthotropic anisotropy in case of thin metallic sheets: identification procedure and case studies; 2015. p. 149–54.
[29] Barros PD, Neto DM, Alves JL, Oliveira MC, Menezes LF. DD3IMP, 3D fully implicit finite element solver: implementation of CB2001 yield criterion. Rom J Tech Sci – Appl Mech 2015;60(1–2):105–36.
[30] Banabic D, Aretz H, Comsa DS, Paraianu L. An improved analytical description of orthotropy in metallic sheets. Int J Plast . 2005;21(3):493–512.
[31] Kaschner G. Mechanical response of zirconium—II. Experimental and finite element analysis of bent beams. Acta Mater 2001;49(15):3097–108.
[32] Hughes TJR. Generalization of selective integration procedures to anisotropic and nonlinear media. Int J Numer Methods Eng 1980;15(9):1413–8.

4.3. Study on the effect of tension-compression asymmetry on the cylindrical cup forming of an AA2090-T3 alloy

This subchapter contains the paper "Study on the effect of tension-compression asymmetry on the cylindrical cup forming of an AA2090-T3 alloy", in press in the International Journal of Solids and Structures. This work shows the effect of the asymmetry between the tensile and the compressive plastic behavior in sheet metal forming, considering a cylindrical cup drawing. In this context, different sets of parameters are identified for the CPB06, taking or not into account the strength differential (SD) effect. The results show that the adoption of a yield criterion that takes into account the SD effect, combined with an associated flow rule, enables the simultaneous prediction of both compression yield stress and r-values directionalities. For the example under analysis, the earing profile is mainly dictated by the compression r-values in-plane directionalities, since the yield stresses present and small variation in the sheet plane. On the other hand, the compression yield stresses directionalities seem to play a major role in the thickness prediction. The adoption of a flexible yield criterion, such as the CB2001, allows a proper prediction of the earing profile but fails to capture the trend for the thickness distribution, since it imposes the same trend for the tensile and compression yield stresses directionalities. Following these conclusions, it is recommended the use of a yield criterion that is flexible enough to describe both the yield stresses and r-values directionalities, including the ones in compression, even for materials presenting a small SD effect.

(Page intentionally left blank)

International Journal of Solids and Structures 000 (2017) 1–10

Contents lists available at ScienceDirect

International Journal of Solids and Structures

journal homepage: www.elsevier.com/locate/ijsolstr

Study on the effect of tension-compression asymmetry on the cylindrical cup forming of an AA2090-T3 alloy

P.D. Barros[a,*], J.L. Alves[b], M.C. Oliveira[a], L.F. Menezes[a]

[a] CEMMPRE, Department of Mechanical Engineering, University of Coimbra, Polo II, Rua Luís Reis Santos, Pinhal de Marrocos, 3030-788 Coimbra, Portugal
[b] CMEMS, Center for Microelectromechanical Systems Research Unit, University of Minho, Campus de Azurém, 4800-058 Guimarães, Portugal

ARTICLE INFO

Article history:
Revised 1 May 2017
Available online xxx

Keywords:
Sheet metal forming
Finite element method
CPB06 yield criterion
Tension-compression asymmetry
Anisotropy parameters identification

ABSTRACT

In this work, the Cazacu et al. (2006) is adopted to study the effect of the asymmetry between the tensile and the compressive plastic behavior in sheet metal forming. The example selected for this analysis is a cylindrical cup drawing, since it involves tensile and compressive stress states (Yoon et al., 2000). The material selected is the 2090-T3 aluminum alloy, since the experimental data available includes both tension and compression yield stress in-plane distributions (Barlat et al., 1991b), which allows the use of a classical strategy for the anisotropy parameters identification. Different sets of parameters are identified for the CPB06, taking or not into account the strength differential (SD) effect and, consequently, considering different sets of experimental data. All numerical simulations are performed with the DD3IMP fully implicit in-house code.

The results show that the earing profile is mainly dictated by the compression *r*-values in-plane directionalities, which are commonly unavailable for thin metallic sheets. The adoption of the CPB06 taking into account the tension-compression asymmetry, with an associated flow rule, enables the simultaneous prediction of both compression yield stress and *r*-values directionalities. The compression yield stresses directionalities seem to play a major role in the thickness prediction. Therefore, it is recommended the use of a yield criterion that is flexible enough to describe both the yield stresses and *r*-values directionalities, including the ones in compression, even for materials that present a small SD effect.

© 2017 Elsevier Ltd. All rights reserved.

1. Introduction

Sheet metal forming processes are nowadays designed and optimized virtually using finite element analysis (FEA). Such virtual try-out approach is consensually accepted as the main reason for the huge decrease in the time-to-market life cycle and for the notable savings in terms of money, time and effort in the design, production and process set-up of new formed parts. The deep drawing process, which consists in giving to a thin metal sheet, initially flat, the desired shape, allows high volume production of sheet metal parts of different complexities. Thus, one of the most important industries exploring the advantages of this kind of process is the automotive, due to the high production rates. However, the success of finite elements solvers on the design and optimization of sheet metal formed parts is strongly dependent on their ability to accurately describe the material's mechanical behavior.

Sheet metals, due to their crystallographic structure and the way they are obtained, generally exhibit anisotropy of their mechanical properties. In fact, the rolling process induces a particular type of anisotropic behavior, characterized by the symmetry of the mechanical properties with respect to the three orthogonal planes, i.e. orthotropy (Banabic, 2010). As this process makes the metal sheets orthotropic, different mechanical behaviors are expected for different loading directions and conditions. Moreover, sheet metal forming processes are carried out with inhomogeneous deformation and under multiaxial strain paths.

Phenomenological models are the most widely used to describe the elastoplastic response of metallic sheets, since they are computationally efficient when compared with microscopic based models. Also, it is common to adopt an associated flow rule, meaning that the material's orthotropic behavior is modeled by a yield surface, which describes the yielding and the plastic flow of the material. This dual role of the yield surface requires a particular care and accuracy in its modeling and numerical implementation.

For isotropic materials, the Tresca (1864) and von Mises (1913) are the most widely used yield criteria. As for yield criteria for materials with orthotropic behavior, the Hill (1948) quadratic function was the first proposed for anisotropic materials and it is still the most widely used. Nevertheless, other formulations have

* Corresponding author.
E-mail address: pedro.barros@dem.uc.pt (P.D. Barros).

http://dx.doi.org/10.1016/j.ijsolstr.2017.06.034
0020-7683/© 2017 Elsevier Ltd. All rights reserved.

Please cite this article as: P.D. Barros et al., Study on the effect of tension-compression asymmetry on the cylindrical cup forming of an AA2090-T3 alloy, International Journal of Solids and Structures (2017), http://dx.doi.org/10.1016/j.ijsolstr.2017.06.034

been proposed to improve the description of the mechanical behavior of orthotropic metallic materials, in particular aluminum and its alloys (e.g. Barlat et al., (2005, 2003, 1997b, 1991a), Banabic et al., (2000), Cazacu and Barlat (2003, 2001), Comsa and Banabic, (2007) Yoshida et al., (2013)). In fact, several authors refer that an improved modeling of both the materials yield stresses and *r*-values in-plane directionalities improves the accuracy of the earing profile prediction on the deep drawing of cylindrical cups (Barros et al., 2016a, 2015a; Chung et al., 2011; Mulder and Vegter, 2011; Yoon et al., 2011).

In most numerical analysis of metal forming processes, the yield surface is assumed to possess a point-symmetry with respect to its center, such that a stress state and its reverse state have the same absolute value (Banabic, 2010). However, it has been shown that this can be an unrealistic approximation, even for cubic metals (both face centered cubic (FCC) and body centered cubic (BCC)) (Barlat et al., 1991b). Therefore, Cazacu and Barlat (2004) extended the Drucker (1949) isotropic yield function to the anisotropic case through invariants generalizing, to enable the description of both the materials anisotropy and the tension-compression asymmetry, also known as strength differential effect. Later, Cazacu et al. (2006) presented another yield criterion that enables describing also both effects using a linear transformation, with a fourth-order tensor, of the deviatoric stress tensor. This formulation has the advantage of enabling the adoption of several linear transformations in order to more accurately capture the material's anisotropic behavior (Plunkett et al., 2006; Tritschler et al., 2014). However, the adoption of several linear transformations means that the yield surface modeling becomes more complex due to the higher number of material anisotropy parameters involved, also requiring more experimental data to enable its identification.

The material anisotropy parameters identification must be performed such that a given yield criterion reproduces the materials mechanical behavior as close as possible. This procedure is typically based in an optimization problem regarding the minimization of an error function, which evaluates the difference between the estimated values and the experimental ones. The key idea is to identify the material parameters in order to numerically obtain the same results as the experimental ones.

In this work, the DD3IMP in-house code (Menezes and Teodosiu, 2000; Neto et al., 2015; Oliveira et al., 2008) is used to perform the numerical simulation of a circular cup drawing, which was chosen since it involves tensile and compressive stress states (Yoon et al., 2000). The numerical simulations are performed with two yield criteria: (i) the CPB06 yield criterion, which accounts for both tension-compression asymmetry and orthotropic plastic behavior; and (ii) the Cazacu and Barlat (2001) yield criterion, which is known for its flexibility in describing highly anisotropy in-plane behavior, due to the high number of anisotropy parameters, but it does not allows the description of the SD effect. These yield criteria are described in the following section. The identification strategy is discussed in section three, assuming that only one linear transformation of the deviatoric stress tensor is applied in the CPB06 yield criterion and the homogeneity parameter $a=2$. In section four, the numerical model adopted for the cup drawing is presented and the anisotropy parameters identification procedures are applied for a 2090-T3 aluminum alloy. For the CPB06, different sets of parameters are identified, taking or not into account the SD effect and, consequently, using different sets of experimental data. The results obtained for the punch force evolution, the earing profile and the thickness distribution are discussed. For the earing profile, the numerical results are also compared with the ones obtained with an analytical function (Yoon et al., 2011), trying to separate the effect of the compression yield stress and *r*-value directionalities. Finally, in section five, the main conclusions are summarized.

2. Anisotropic yield criteria

The Cazacu et al. (2006) yield criterion (CPB06) is adopted in this work since it allows the description of both the orthotropic behavior and the SD effect, i.e. tension-compression asymmetry. The equivalent stress $\bar{\sigma}$ associated with the orthotropic form of the CPB06 yield criterion is defined as

$$\bar{\sigma} = B\left[\left(|s_1| - k\,s_1\right)^a + \left(|s_2| - k\,s_2\right)^a + \left(|s_3| - k\,s_3\right)^a\right]^{\frac{1}{a}}, \tag{1}$$

where the exponent a, considered to be a positive integer, and k are material parameters and s_1, s_2 and s_3 are the principal values of the tensor $\mathbf{s}$. This tensor is determined following the linear transformation proposed by Barlat et al. (1997b), such that $\mathbf{s}=\mathbf{C}:\boldsymbol{\sigma}'$, where $\boldsymbol{\sigma}'$ is the deviatoric stress tensor and $\mathbf{C}$ is the constant 4th-order transformation tensor. Using the Voigt notation, such as

$$\begin{Bmatrix} \sigma'_{11} \\ \sigma'_{22} \\ \sigma'_{33} \\ \sigma'_{23} \\ \sigma'_{13} \\ \sigma'_{12} \end{Bmatrix} = \begin{Bmatrix} \sigma'_{1} \\ \sigma'_{2} \\ \sigma'_{3} \\ \sigma'_{4} \\ \sigma'_{5} \\ \sigma'_{6} \end{Bmatrix}, \tag{2}$$

the tensor $\mathbf{C}$, which for 3-D stress conditions involves 9 independent anisotropy coefficients, is expressed in the principal axis of anisotropy as

$$\mathbf{C} = \begin{bmatrix} C_{11} & C_{12} & C_{13} & 0 & 0 & 0 \\ C_{12} & C_{22} & C_{23} & 0 & 0 & 0 \\ C_{13} & C_{23} & C_{33} & 0 & 0 & 0 \\ 0 & 0 & 0 & C_{44} & 0 & 0 \\ 0 & 0 & 0 & 0 & C_{55} & 0 \\ 0 & 0 & 0 & 0 & 0 & C_{66} \end{bmatrix}. \tag{3}$$

B is a constant defined such that $\bar{\sigma}$ reduces to the tensile yield stress in the rolling direction and is given by

$$B = \left[\frac{1}{\left(|\phi_1| - k\,\phi_1\right)^a + \left(|\phi_2| - k\,\phi_2\right)^a + \left(|\phi_3| - k\,\phi_3\right)^a}\right]^{\frac{1}{a}}, \tag{4}$$

with

$$\begin{Bmatrix} \phi_1 \\ \phi_2 \\ \phi_3 \end{Bmatrix} = \begin{Bmatrix} (2/3)C_{11} - (1/3)C_{12} - (1/3)C_{13} \\ (2/3)C_{21} - (1/3)C_{22} - (1/3)C_{23} \\ (2/3)C_{31} - (1/3)C_{32} - (1/3)C_{33} \end{Bmatrix}. \tag{5}$$

The convexity is guaranteed for any integer $a \geq 2$ and $k \in [-1, 1]$ (Cazacu et al., 2006).

The equivalent stress $\bar{\sigma}$ associated with the isotropic form of the CPB06 yield criterion is defined as in Eq. (1) and, in this case, the constant 4th-order transformation tensor becomes the 4th-order identity tensor, such as $\mathbf{C}=\mathbf{I}$. Considering these conditions and $a=2$, Eq. (4) becomes

$$B = \sqrt{\frac{9/2}{3k^2 - 2k + 3}}. \tag{6}$$

Therefore, if $a=2$ and $k=0$, then $B=\sqrt{3/2}$ and $\bar{\sigma}$ becomes the von Mises equivalent stress. Moreover, for a material presenting isotropic behavior, the coefficient k alone allows for the description of the SD effect, giving a direct measure of the ratio between tensile (σ^{T}) and compressive (σ^{C}) yield stresses (Cazacu et al., 2006). However, for a material presenting orthotropic behavior it is not possible to define a single $\sigma^{\mathrm{T}}/\sigma^{\mathrm{C}}$ ratio. In case of metal sheets, the three principal axis correspond to the rolling direction (RD), the transverse direction (TD) and the normal to the sheet plane direction (ND). Therefore, it is possible to define a ratio between tensile and compressive yield stresses for each axis, which will be labeled $\sigma^{\mathrm{T}}_{\mathrm{RD}}/\sigma^{\mathrm{C}}_{\mathrm{RD}}$, $\sigma^{\mathrm{T}}_{\mathrm{TD}}/\sigma^{\mathrm{C}}_{\mathrm{TD}}$ and $\sigma^{\mathrm{T}}_{\mathrm{ND}}/\sigma^{\mathrm{C}}_{\mathrm{ND}}$, respectively. In this case, the stress ratios depend on both the anisotropy parameters and the k value.

Please cite this article as: P.D. Barros et al., Study on the effect of tension-compression asymmetry on the cylindrical cup forming of an AA2090-T3 alloy, International Journal of Solids and Structures (2017), http://dx.doi.org/10.1016/j.ijsolstr.2017.06.034

The Cazacu and Barlat (2001) yield criterion (CB2001) is a generalization of the Drucker's isotropic criterion to orthotropy and, in its general form, is given by

$$\bar{\sigma} = \left\{ 27\left[\left(J_2^0\right)^3 - c\left(J_3^0\right)^2 \right] \right\}^{\frac{1}{6}}, \tag{7}$$

where J_2^0 and J_3^0 are the second and third generalized invariants of the deviatoric stress tensor $\boldsymbol{\sigma}'$, defined as

$$\begin{aligned} J_2^0 = {} & \frac{a_1}{6}(\sigma'_{11}-\sigma'_{22})^2 + \frac{a_2}{6}(\sigma'_{11}-\sigma'_{33})^2 \\ & + \frac{a_3}{6}(\sigma'_{11}-\sigma'_{33})^2 + a_4\sigma'^2_{12} + a_5\sigma'^2_{13} + a_6\sigma'^2_{23}, \end{aligned} \tag{8}$$

$$\begin{aligned} J_3^0 = {} & (1/27)(b_1+b_2)\sigma'^3_{11} + (1/27)(b_3+b_4)\sigma'^3_{22} \\ & + (1/27)[2(b_1+b_4) - b_2 - b_3]\sigma'^3_{33} \\ & - (1/9)\left(b_1\sigma'_{22} + b_2\sigma'_{33}\right)\sigma'^2_{11} - (1/9)\left(b_3\sigma'_{33} + b_4\sigma'_{11}\right)\sigma'^2_{22} \\ & - (1/9)\left[(b_1 - b_2 + b_4)\sigma'_{11} + (b_1 - b_3 + b_4)\sigma'_{22}\right]\sigma'^2_{33} \\ & + (2/9)(b_1+b_4)\sigma'_{11}\sigma'_{22}\sigma'_{33} \\ & - \left(\sigma'^2_{13}/3\right)\left[2b_9\sigma'_{22} - b_8\sigma'_{33} - (2b_9 - b_8)\sigma'_{11}\right] \\ & - \left(\sigma'^2_{12}/3\right)\left[2b_{10}\sigma'_{33} - b_5\sigma'_{22} - (2b_{10} - b_5)\sigma'_{11}\right] \\ & - \left(\sigma'^2_{23}/3\right)\left[(b_6 - b_7)\sigma'_{11} - b_6\sigma'_{22} - b_7\sigma'_{33}\right] \\ & + 2b_{11}\sigma'_{12}\sigma'_{23}\sigma'_{13}, \end{aligned} \tag{9}$$

where c, a_1,..., a_6 and b_1,..., b_{11} are the anisotropy parameters. σ'_{ij}, $i, j = 1, 2, 3$ are the deviatoric stress tensor components defined in the material frame. The conditions that guarantee the convexity of CB2001 are unknown, except when assuming in-plane isotropic behavior, for which $c \in [-3.75, 2.25]$ (Cazacu and Barlat, 2001). For further details concerning the constitutive model and the its implementation, please refer to (Barros et al., 2016b, 2015a).

3. Material parameters identification

The anisotropy parameters should be determined such that the yield criterion reproduces the material's mechanical behavior as close as possible. The most commonly used experimental results for the identification of anisotropy parameters are the yield stresses and r-values obtained from in-plane tension for different angles (θ) with the rolling direction. When adopting classical methodologies, usually these tests are performed for several directions in the sheets plane (generally, 0°, 15°, 30°, 45°, 60°, 75° and 90° from the rolling direction). For some criteria, it is also recommended to know the experimental results for other trajectories, like the biaxial yield stress, σ_b, and the biaxial anisotropy coefficient r_b (Barlat et al., 2003; Lege et al., 1989; Pöhlandt et al., 2002). In case of yield criteria capable of describing SD effects, uniaxial compression experimental results are also necessary for describing the materials mechanical behavior for these stress states, ideally for the three axis of orthotropy. However, in order to characterize thin metallic sheets mechanical behavior for compression stress states, the use of small size specimens is necessary to avoid buckling effects. This leads to supplementary difficulties in the acquisition and analysis of the experimental results, particularly for high strain values (see e.g. Barlat et al., 1991b; Lege et al., 1989; Tritschler et al., 2014; Yoon et al., 2000).

The DD3MAT in-house code allows determining yield criterion parameters that accurately adjust a given material's experimental behavior (Barros et al., 2016c). Those parameters can then be used in the numerical simulation of forming processes, using the in-house code DD3IMP, where the yield are criteria implemented (Menezes and Teodosiu, 2000; Neto et al., 2015; Oliveira et al., 2008). The procedure adopted in DD3MAT is based on the minimization of an error function, which evaluates the difference between the estimated values and experimental ones, in the form

$$\begin{aligned} F(\mathbf{A}) = {} & w_{\sigma_\theta^T}\sum_{\theta=0}^{90}\left(\sigma_\theta^T(\mathbf{A})/\sigma_\theta^T - 1\right)^2 + w_{\sigma_\theta^C}\sum_{\theta=0}^{90}\left(\sigma_\theta^C(\mathbf{A})/\sigma_\theta^C - 1\right)^2 \\ & + w_{r_\theta}\sum_{\theta=0}^{90}\left(r_\theta(\mathbf{A})/r_\theta - 1\right)^2 + w_{\tau_\theta}\sum_{\theta=0}^{90}\left(\tau_\theta(\mathbf{A})/\tau_\theta - 1\right)^2 \\ & + w_{\sigma_b}(\sigma_b(\mathbf{A})/\sigma_b - 1)^2 + w_{r_b}(r_b(\mathbf{A})/r_b - 1)^2 \end{aligned} \tag{10}$$

where $\mathbf{A}$ represents the set of parameters associated with the selected yield criterion. σ_θ^T, σ_θ^C and r_θ are the experimental yield stresses in tension, compression and anisotropy coefficients determined in uniaxial tension, respectively, obtained from the uniaxial tests for a specific orientation (θ) with respect to the rolling direction. τ_θ is the experimental yield stress in shear, obtained for a specific orientation (θ) with respect to the rolling direction. σ_b is the experimental yield stress obtained from the equibiaxial tensile test and r_b is the experimental anisotropy coefficient obtained from the disc compression test. $\sigma_\theta^T(\mathbf{A})$, $\sigma_\theta^C(\mathbf{A})$ $r_\theta(\mathbf{A})$, $\tau_\theta(\mathbf{A})$, $\sigma_b(\mathbf{A})$ and $r_b(\mathbf{A})$ are the correspondent values predicted from the adopted yield criterion. Such procedure can be considered a generalization of the one proposed by Banabic et al. (2005), where the weighting factors, $w_{\sigma_\theta^T}$, $w_{\sigma_\theta^C}$, w_{r_θ}, w_{τ_θ}, w_{σ_b} and w_{r_b} are used to balance the influence of the experimental data. Nevertheless, the selection of the weighting factors is normally a manual procedure, strongly dependent on users' expertise and knowledge. In practice, this means that a first identification is always performed, considering unitary weights, to evaluate which experimental values are being reasonably well capture or not. Afterwards, the user can manually adjust each weighting factor, balancing the improvement in the fit of a specific experimental value, with the inevitable loss in the accuracy for the others. Since the identification procedure is sensitive to the weights considered for each experimental value, the adoption of this procedure introduces subjectivity in the definition of the best fit.

The experimental yield stress values can be used normalized with the yield stress given by the hardening law adopted. Nevertheless, the approach adopted in DD3MAT also allows considering that they correspond to the flow stress given by the hardening law for a certain equivalent plastic strain value, as long as the hardening law has been previously defined. This strategy enables the adoption of flow stress values determined for the same level of accumulated plastic work, in order to minimize inaccuracies related with the evaluation of the transition between the elastic and plastic behavior as well as some small changes in the yield surface shape (Barlat et al., 1997a).

The yield criteria parameters identification problem can be as simple as a resolution of a system of equations, when the number of experimental data is equal to the minimum necessary input data, or an optimization problem, when the number of experimental data is higher than the minimum necessary. The optimization algorithm adopted in DD3MAT is based on a downhill-simplex derivative free method, allowing to find the minimum of the objective function in a multidimensional space, with a low computational cost.

4. Cup drawing of a circular blank

The numerical simulation of the drawing of a circular cup is performed in order to analyze the influence of considering the SD effect in the final cup's geometry. This test is based on the work of Yoon et al. (2000) and was chosen since it involves tensile and compressive stress states. In fact, as long as the stress component

Please cite this article as: P.D. Barros et al., Study on the effect of tension-compression asymmetry on the cylindrical cup forming of an AA2090-T3 alloy, International Journal of Solids and Structures (2017), http://dx.doi.org/10.1016/j.ijsolstr.2017.06.034

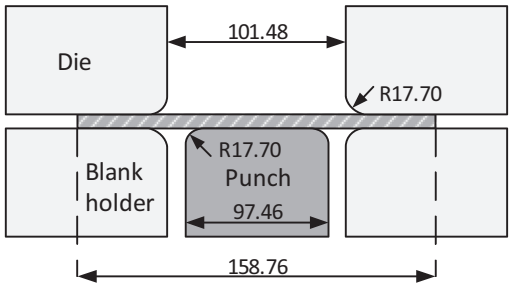

Fig. 1. Schematic of the cup drawing and main dimensions.

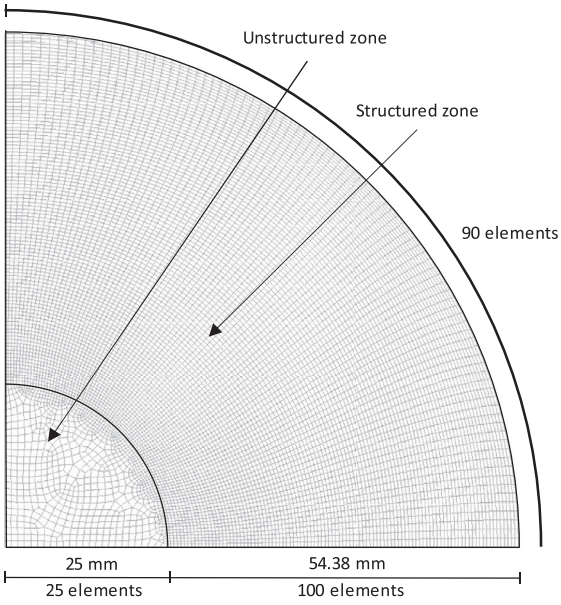

Fig. 2. In-plane blank sheet discretization.

in the thickness direction is small, the outer flange will be submitted to a compression stress state and the earing profile will be mainly dictated by the in-plane distribution of the yield stress and r-value (Yoon et al., 2011). For a material presenting SD effect, the in-plane distribution of the yield stresses in tension and compression can be quite different, meaning that it is expected to be able to evaluate the impact of taking into account the tension-compression asymmetry in the earing profile prediction.

4.1. Problem description

The schematic of the cup drawing process, together with the main dimensions, is shown in Fig. 1. Due to geometrical and material symmetries, only a quarter of the global structure is modeled. The contact with friction conditions is described by Coulomb's law, with a constant friction coefficient, μ, of 0.1. The blank sheet is circular in shape with a radius of 158.76 mm and thickness of 1.6 mm. The blank-holder force has a value of 22.2 kN, corresponding to the minimum value predicted to avoid wrinkling. Although not shown here, for this blank-holder force it is observed that the stress state component in the thickness direction is small, until a punch displacement of approximately 25 mm, thus not altering the compression stress state in the circumferential direction, for the material points located in the outer flange (Barros et al., 2016a).

The sheet is discretized with 8-node hexahedral finite elements, combined with a selective reduced integration technique (Hughes, 1980). Fig. 2 shows the in-plane sheet discretization used, highlighting the refined mesh adopted in the structured zone. Two elements are used in the thickness direction, leading to a total of 19,648 elements.

Table 1
Experimental uniaxial tension and compression yield stresses and r-values for the 2090-T3 aluminum alloy (Barlat et al., 1991b).

Test direction [°]	r-value	$\sigma_\theta^{Y_T}$ [MPa]	$\sigma_\theta^{Y_C}$ [MPa]	Stress ratio
0°	0.210	279.62	248.02	$\sigma_{RD}^{T}/\sigma_{RD}^{C}=1.127$
15°	0.330	269.72	260.75	
30°	0.690	255.00	255.00	
45°	1.580	226.77	237.75	
60°	1.050	227.50	245.75	
75°	0.550	247.20	263.75	
90°	0.690	254.45	266.48	$\sigma_{TD}^{T}/\sigma_{TD}^{C}=0.955$
σ_b		289.40		
r_b	0.670			

4.2. Material mechanical behavior

The yield criteria parameters are identified considering the experimental data for the 2090-T3 aluminum alloy presented in Table 1, which considers experimental uniaxial tension and compression yield stresses, as well as the anisotropy coefficients for different orientations with the rolling direction. The experimental yield stress and r-value obtained from the balance biaxial test and disk compression test are also presented (Barlat et al., 1991b).

This work considers a fixed value of $a=2$ for the CPB06 yield criterion. Assuming this condition, three different sets of anisotropy parameters were identified, considering: (i) $k \neq 0$ and all the experimental data available, allowing for the modeling of tension-compression asymmetry (labeled "CPB06"); (ii) $k=0$ and neglecting the experimental compression yield stresses (labeled "CPB06 $k=0$ T"); and (iii) $k=0$ and neglecting the experimental tensile yield stresses (labeled "CPB06 $k=0$ C"). For the particular case of the CPB06 with one linear transformation, adopted in this work, the yield criterion presents 9 anisotropy parameters and the k value. When considering thin metallic sheets, the off-plane properties are difficult to obtain. Thus, the corresponding anisotropy parameters, C_{44} and C_{55}, cannot be evaluated and, therefore, the corresponding isotropic values are commonly adopted, i.e. 1.0. Moreover, the C_{11} parameter is also considered equal to 1.0 due to the homogeneity of the criterion. The adoption of this condition eliminates the possibility of obtaining non-unique sets of parameters, i.e. sets with symmetrical values for k and the C_{ij} parameters that lead to the same value for the objective function, as previously reported in (Barros et al., 2016b). In brief, it is necessary to identify a total of 6 anisotropy parameters and the k value. The identification procedure assumes that $k \in [-1, 1]$ and $C_{ij} \in [-4, 6]$.

For the CB2001 yield criterion, only one set of anisotropy parameters was identified, considering all the experimental data available, except the compression yield stresses (labeled "CB2001"). For this yield criterion, the parameters a_5,a_6 and b_k ($k=6, 7, 8, 9, 11$) correspond to the off-plane properties, which cannot be evaluated and, consequently, are assumed as equal to the isotropic values, i.e. 1.0. It is also assumed that $a_i \in [-10, 10]$, $b_i \in [-10, 10]$ and $c \in [-3.75, 2.25]$. The minimization process adopted for this yield criterion includes testing the convexity of the yield surface, for several planes in the stress space (Barros et al., 2015a).

For both yield criteria the minimization problem associated to Eq. (10) is over constrained, since a total of 23 experimental values are used to identify only 7 parameters in case of CPB06, and 11 parameters in case of CB2001. In case of CPB06, when neglecting the SD effect, a total of 16 experimental values were considered.

The plastic behavior is described using an isotropic work hardening Swift type law, given by

$$Y(\bar{\varepsilon}^p) = K(\varepsilon_0 + \bar{\varepsilon}^p)^n, \tag{11}$$

Please cite this article as: P.D. Barros et al., Study on the effect of tension-compression asymmetry on the cylindrical cup forming of an AA2090-T3 alloy, International Journal of Solids and Structures (2017), http://dx.doi.org/10.1016/j.ijsolstr.2017.06.034

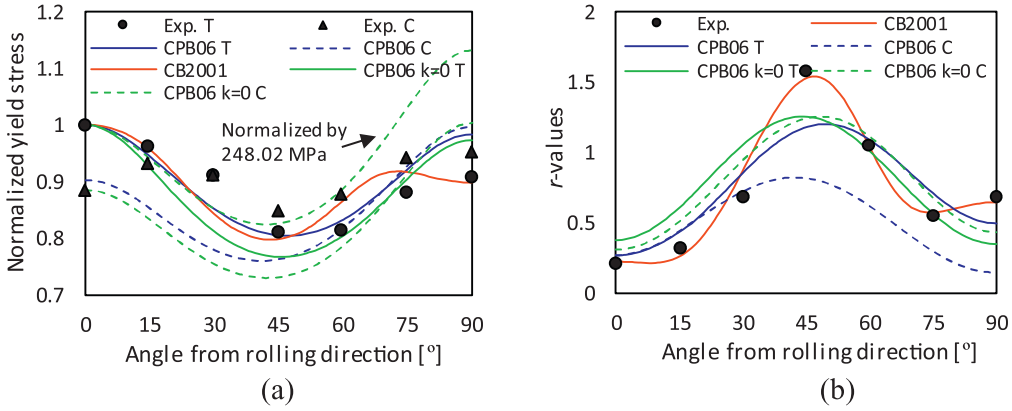

Fig. 3. Experimental and predicted in-plane evolution of the: (a) yield stress (normalized with Y_0) and (b) r-value, for the 2090-T3 aluminum alloy. (For interpretation of the references to color in this figure legend, the reader is referred to the web version of this article.)

Table 2
Elastic properties and material parameters of the work hardening law Yoon et al., (2000).

Elastic properties	Isotropic hardening (Swift law)	
	CPB06 $k=0$ C	All other cases
$E=74$ [GPa]	$K=670$ [MPa]	$K=646$ [MPa]
$\upsilon=0.34$	$\varepsilon_0=0.0183$	$\varepsilon_0=0.0250$
	$n=0.2485$	$n=0.2270$
	$Y_0=248.02$ [MPa]	$Y_0=279.62$ [MPa]

where Y is the flow stress and $\bar{\varepsilon}^p$ is the equivalent plastic strain. The material's mechanical behavior is assumed to be isotropic in the elastic regime, being described by the Young's modulus, E, and the Poisson ratio, υ.

Note that the CPB06 criterion guarantees that the yield stress Y_0 considered is always equal to the one obtained for the uniaxial tensile test performed along the rolling direction, σ^T_{RD}. Previous results indicate that the value proposed for the yield stress, Y_0, defined by the hardening law, should be in accordance with σ^T_{RD}, to enable an accurate description of the in-plane yield stress directionalities (Barros et al., 2015b). Following this recommendation, the parameters adopted for the Swift hardening law consider a yield stress value $Y_0=279.62$ MPa, for anisotropy coefficients identified considering the tensile yield stress in-plane distribution. For the same reason, for the case "CPB06 $k=0$ C" it is necessary to assume $Y_0=248.02$ MPa. Therefore, a new set of parameters for the hardening law were determined by minimizing the difference in the plastic work attained by the two hardening laws, for an equivalent plastic strain value of 0.5. A summary of the elastic properties and the hardening law parameters is presented in Table 2.

The considered weighting coefficients for each criterion are presented in Table 3, while the identified anisotropy parameters are the ones presented in Table 4. Fig. 3 presents the experimental and numerically predicted yield stresses and anisotropy coefficients for the four cases. The "CPB06" identification is able of simultaneously predict the evolution of the yield stresses in tension and in compression. The evolution of the tension yield stress is globally well predicted, with the minimum occurring for 45° while from this angle forward the values are over predicted. As for the evolution of the compression yield stresses, the main shape of the evolution is captured. For this identification, since $k\neq 0$, the r-values evolution is also different for tension and compression. The tensile r-values show the same trend as the experimental ones with the lowest value at 0° and maximum at about 45°. Regarding the compression r-values no analysis can be performed, since the experimental values are not known. Nonetheless, the results are shown to highlight the difference in the predicted values. The stress ratios predicted are $\sigma^T_{RD}/\sigma^C_{RD}=1.106$ and $\sigma^T_{TD}/\sigma^C_{TD}=0.985$, which means that they are, respectively, slightly under and overestimated, with a relative difference inferior to 5% (see Table 1). Finally, it should be mentioned that since one linear transformation was adopted, the yield criterion is not flexible enough to describe the highly orthotropic in-plane behavior of this aluminum alloy.

The CB2001 allows an excellent description of both tensile yield stresses and r-values directionalities but, since it is unable to describe the SD effect, the stress ratio in the three principal axis is always equal to 1.0. The same stress ratios are valid for the identifications performed with $k=0$. Regarding the "CPB06 $k=0$ T" identification, the evolution of the tensile yield stresses and r-values is relatively well captured. For the "CPB06 $k=0$ C" identification, since the input yield stresses were the compression ones, in Fig. 3(a) a second green dashed curve is used to present a normalization with the yield stress value $Y_0=279.62$ MPa, enabling its comparison with the experimental ones. This way it is possible to confirm that the evolution is globally well predicted. The predicted r-values are very close to the previous case, "CPB06 $k=0$ T", enabling the analysis of the influence of the compression yield stress directionalities.

The values predicted for the biaxial yield stress and biaxial anisotropy coefficient are presented in Table 5. These results are highlighted in Fig. 4, which presents the corresponding yield surfaces in both the σ_1,σ_2 plane ($\sigma_3,\sigma_{12}=0$) and the π-plane. All three CPB06 cases fail to recover the biaxial yield stress value, underestimating it. The CB2001, however, presents a good fit. As for the biaxial anisotropy coefficient, all the CPB06 cases overestimate this value, with the "CPB06 $k=0$ T" presenting the worst prediction. The CB2001 presents a very accurate fit for this value.

4.3. Results and discussion

The numerically predicted punch force and blank-holder displacement with the punch displacement are presented in Fig. 5. Even though no experimental results are available for comparison purposes, these results are shown to highlight the importance of the material mechanical behavior in the process conditions. Regarding the four cases, the results show that the punch force increases until attaining a maximum value for a punch displacement of about 31 mm, corresponding approximately to the instant where the blank-holder displacement is maximum. From this instant, the punch force decreases and, in some cases, presents a stepped decrease when the blank-holder loses contact with the blank, as seen from the dashed curves corresponding to the blank-holder displacement. Afterwards, an increase in the punch force is observed,

Please cite this article as: P.D. Barros et al., Study on the effect of tension-compression asymmetry on the cylindrical cup forming of an AA2090-T3 alloy, International Journal of Solids and Structures (2017), http://dx.doi.org/10.1016/j.ijsolstr.2017.06.034

Table 3
Weighting coefficients used in the identification procedure (if not presented, assume as 1.0).

CB2001	$w_{r_{45}} = 5\ w_{r_{75}} = 5\ w_{r_{90}} = 5\ w_{\sigma_b} = 20\ w_{\sigma_{60}^T} = 10\ w_{\sigma_{75}^T} = 10\ w_{\sigma_{90}^T} = 10$
CPB06	$w_{r_{45}} = 7\ w_{\sigma_b} = 20\ w_{\sigma_{90}^T} = 30\ w_{\sigma_{15}^C} = 40\ w_{\sigma_{30}^C} = 5\ w_{\sigma_{45}^C} = 5\ w_{\sigma_{60}^C} = 5\ w_{\sigma_{75}^C} = 5\ w_{\sigma_{90}^C} = 40$
CPB06 $k=0$ T	$w_{r_0} = w_{r_{15}} = w_{r_{30}} = w_{r_{60}} = w_{r_{75}} = w_{r_{90}} = 0.1 w_{\sigma_b} = 10 w_{\sigma_{60}^T} = 10 w_{\sigma_{75}^T} = 20 w_{\sigma_{90}^T} = 50$
CPB06 $k=0$ C	$w_{r_0} = 0.7 w_{r_{15}} = 0.2 w_{r_{30}} = w_{r_{60}} = 0.5 w_{r_{45}} = 5 w_{\sigma_b} = 10 w_{\sigma_{60}^T} = 10 w_{\sigma_{75}^T} = 20 w_{\sigma_{90}^T} = 50$

Table 4
Identified parameters for the 2090-T3 aluminum alloy for the considered yield criteria.

CB2001	a_1		a_2		a_3		a_4	
	1.358		1.848		1.075		1.709	
	b_1	b_2	b_3	b_4		b_5	b_{10}	c
	5.357	−0.623	−4.386	−3.654		−6.046	−0.882	0.857
	C_{11}	C_{22}	C_{33}	C_{66}	C_{23}	C_{13}	C_{12}	k
CPB06	1.000	−0.473	−1.381	1.421	0.151	0.119	0.999	0.050
CPB06 $k=0$ T	1.000	0.987	1.019	1.134	0.006	0.036	0.195	0.000
CPB06 $k=0$ C	1.000	1.013	1.007	−1.162	0.057	−0.059	0.196	0.000

Table 5
Experimental and numerically predicted biaxial yield stress and anisotropy coefficient for the 2090-T3 aluminum alloy.

	Experimental	CB2001	CPB06	CPB06 $k=0$ T	CPB06 $k=0$ C
σ_b [MPa]	287.48	285.89	229.48	228.13	216.63
r_b	0.67	0.660	0.893	1.078	0.710

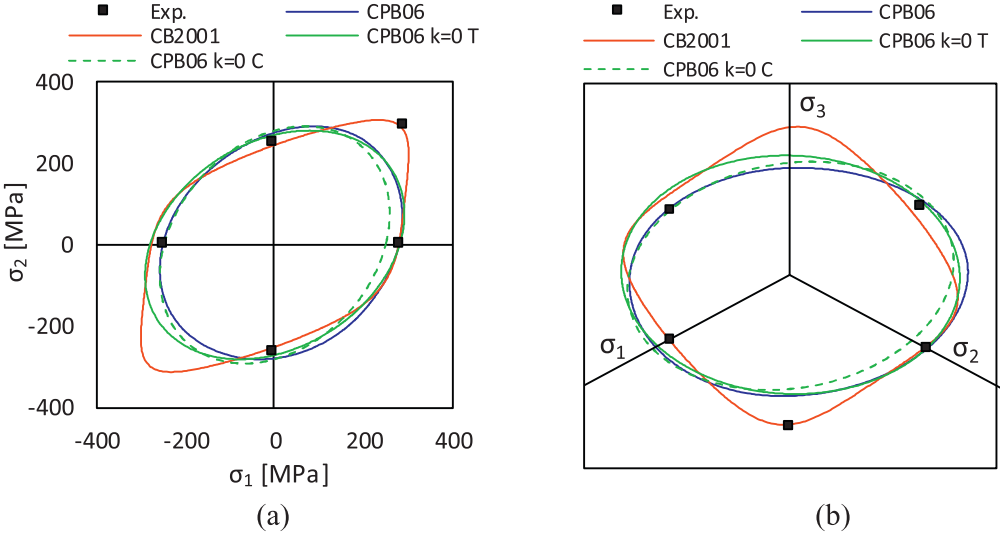

Fig. 4. Predicted yield surfaces in the (a) σ_{11},σ_{22} plane (with $\sigma_{33}=0$) and (b) π-plane (normalized with the yield stress value of $Y_0=279.62$ MPa).

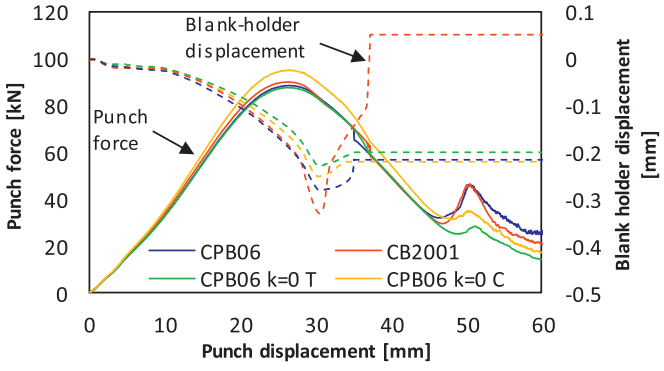

Fig. 5. Numerically predicted punch force and blank-holder displacement evolutions with punch displacement. Solid lines represent the punch force and dashed lines represent the blank-holder displacement.

between 47 mm and 52 mm of punch displacement, corresponding to the ironing of the cup's flange between the punch and the die. The lower punch force values for the ironing stage, occur for both cases of the CPB06 with $k=0$, since they present a lower value for the flange thickening, as shown in Fig. 6. Fig. 6 also shows that the "CPB06 $k=0$ T" presents a thickness strain distribution in the flange which is more uniform than the other cases. Since both CPB06 cases with $k=0$ describe the in-plane r-values similarly, the observed differences can be related with the in-plane yield stress distribution. For the "CPB06 $k=0$ T", the thickness strain distribution in the flange is more uniform than in the "CPB06 $k=0$ C" because, although the in-plane yield stress distribution presents a similar trend, the amplitude of variation is smaller for the "CPB06 $k=0$ T" (see Fig. 3(a)). The "CPB06 $k=0$ C" presents a higher thickening of the flange mainly for angles closer to the transverse direction, as shown in Fig. 6(d), which is a direct result of the fact that the yield stresses are higher for angles closer to this direction. In

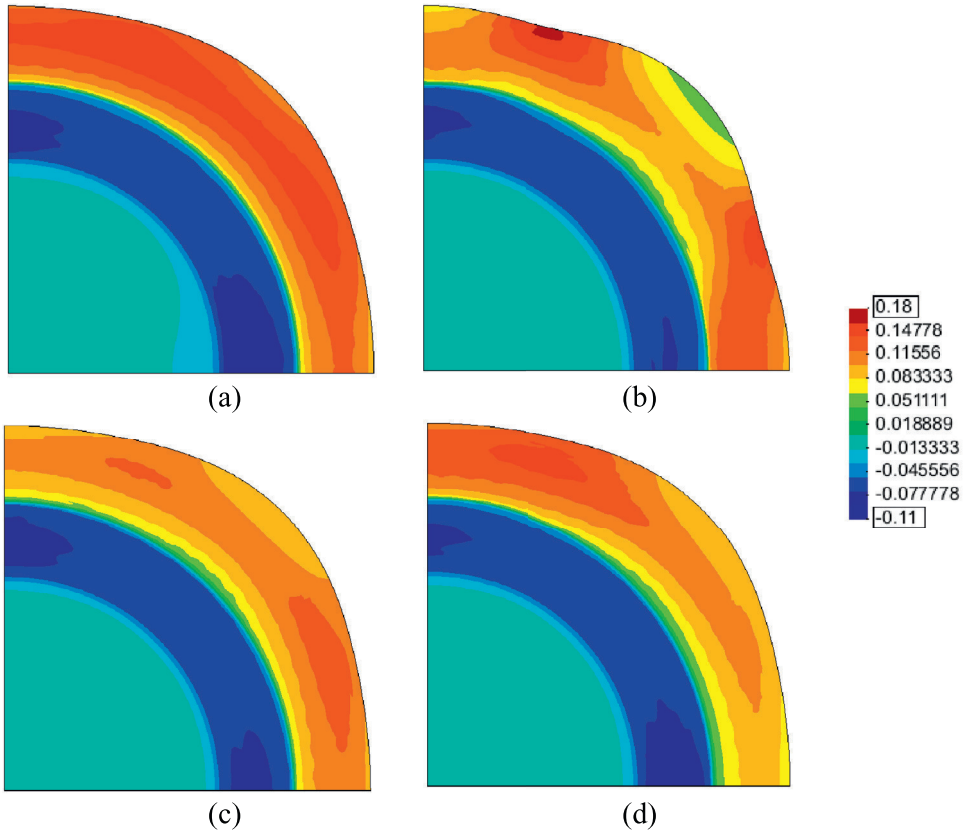

Fig. 6. Through-thickness strain distribution, for a punch displacement of 30 mm for the: (a) CPB06; (b) CB2001; (c) CPB06 $k=0$ T and (d) CPB06 $k=0$ C.

fact, the ratio between the yield stresses in RD and TD, $\sigma^{T}_{RD}/\sigma^{T}_{TD}$ are 1.028 and 0.882 for the "CPB06 $k=0$ T" and the "CPB06 $k=0$ C", respectively.

The analysis of the influence of the predicted yield stresses and anisotropy coefficients evolution in the predicted cup height, must take into account the ones corresponding to compression, since the in-plane compression stress state is the one predominant in the flange area (Yoon et al., 2011). Also, other authors have shown, considering the present example of the drawing of a circular cup, that both the compression yield stresses and the anisotropy coefficients in the rolling direction will have a direct impact on the material behavior at the transverse direction and *vice-versa*. In fact, the behavior of the rim in the direction defined by θ with the rolling direction is controlled by the material compression properties in the direction defined by $90-\theta$ (Chung et al., 2011; Mulder and Vegter, 2011; Yoon et al., 2011). Based on these results, Yoon et al. (2011) proposed an analytical function to estimate the cup height directionality,

$$H^{cup}(\theta) = t_0 + r_c + \frac{R_b}{A_{\theta+90}+1}\left(d^{A_{\theta+90}} - \frac{1}{d}\right)B_\theta{}^{A_{\theta+90}}, \tag{12}$$

where t_0 is the initial blank thickness, R_b is the blank radius and r_c is the radius of the cup defined by the punch fillet radius. The r-value and the yield stress directionalities influence is dictated by

$$A_{\theta+90} = \frac{r_{\theta+90}}{1+r_{\theta+90}} \text{ and } B_\theta = \left(\frac{\sigma_{ref}}{\sigma^{T}_{\theta}}\right)^{\beta'} \tag{13}$$

respectively. Assuming that the uniaxial tension and compression lead to identical r-values, these can be expressed as a function of the plastic strains at the rim

$$r_{\theta+90} = \frac{\varepsilon_r}{\varepsilon_t} = -\frac{\varepsilon_r}{\varepsilon_r+\varepsilon_\theta}, \tag{14}$$

were subscripts r, θ and t correspond to the radial, circumferential and thickness directions, respectively. It is also assumed that the radial tension can be modelled from the yield stress directionality σ^{T}_{θ}, such that

$$\sigma^{ref} = \frac{\int_0^{2\pi}\sigma^{T}_{\theta}d\theta}{2\pi} = \frac{1}{12}\left[\sigma^{T}_{0}+2\left(\sigma^{T}_{15}+\sigma^{T}_{30}+\sigma^{T}_{45}+\sigma^{T}_{60}+\sigma^{T}_{75}\right)+\sigma^{T}_{90}\right], \tag{15}$$

for an orthotropic material, for which data is known for every 15°. The deceleration β' factor is introduced to take into account the variation of the stress mode along the flange, i.e. $\beta'=1$ corresponds to the assumption that the stress mode at the inner most flange is applied to the entire flange; $\beta'=0.5$ corresponds to a linear distribution of the radial tensile stress; the recommended value is $0.5 \le \beta' \le 1$. Finally, d corresponds to the ratio between the blank radius R_b and the cup radius R_c.

This analytical function shows that a lower value of the anisotropy coefficient leads to lower cup height whereas lower values of the yield stresses lead to a higher cup height (Yoon et al., 2011). The cup height was estimated for all cases under analysis using Eq. (12), considering $\beta'=0.5$ and the predicted in-plane yield stress and r-value distribution. Note that, for the "CPB06" two cases where considered: (i) using the tensile yield stress and r-values (labeled "CPB06 T") and (ii) using the compression yield stresses and r-values (labelled "CPB06 C"). The results obtained for the cup height, normalized by the experimental cup height at RD, are shown in Fig. 7(a). For this particular case, the earing profile is mainly dictated by the r-value in-plane distribution, which is supported by the comparison of its trend with the one shown in Fig. 3(b). Moreover, it is possible to confirm that for the "CPB06 $k=0$ C" the cup height attains the higher values, while the "CPB06 C" leads to the lowest ones, has a consequence of the similar yield

Please cite this article as: P.D. Barros et al., Study on the effect of tension-compression asymmetry on the cylindrical cup forming of an AA2090-T3 alloy, International Journal of Solids and Structures (2017), http://dx.doi.org/10.1016/j.ijsolstr.2017.06.034

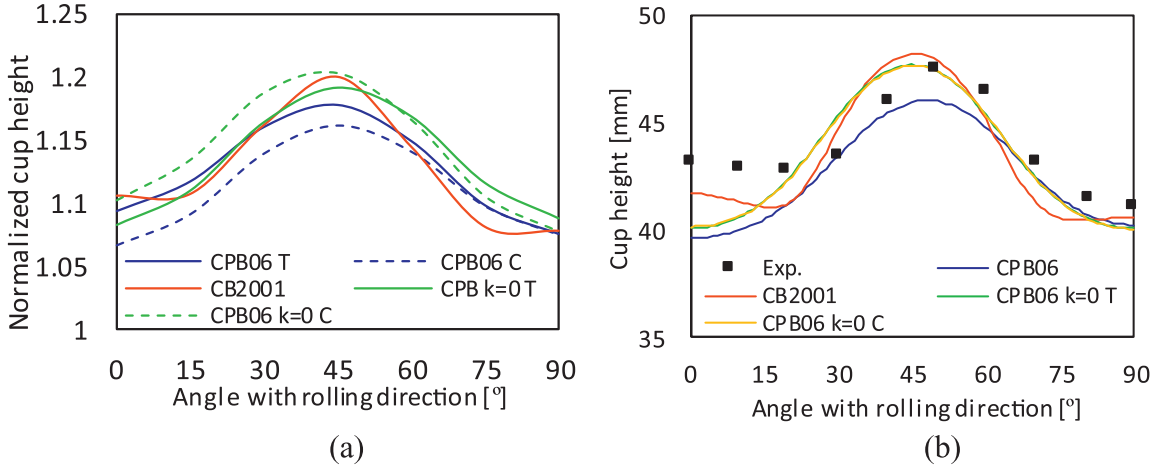

Fig. 7. (a) Analytically predicted normalized cup height; and (b) experimental and numerically predicted cup height, vs. angle from rolling direction.

stress distribution and the lower compression *r*-values. The comparison of the results obtained with both CPB06 cases with $k=0$, which present a similar in-plane distribution for the *r*-values, confirms that the yield stress in-plane distribution presents a small effect, which can be related with its small amplitude of variation.

Fig. 7(b) presents the comparison between experimental and numerically predicted cup height vs. angle from rolling direction, after the drawing operation. Regarding the earing profile, globally the shape is well predicted by for cases, with the maximum height at about 45°. Also, the average height is within the experimental values. However, the increased experimental height at 0° is not predicted by any of the CPB06 identifications, which can be attributed to the fact that this yield criterion, considering only one linear transformation, is not flexible enough to predict more than 4 ears. In fact, the CB2001 can predict the higher height for 0° as a direct consequence of the good prediction of both yield stresses and *r*-values directionalities (Fig. 3). The differences in height between the "CPB06" and both cases of the CPB06 with $k=0$ can be attributed to the difference in the predicted *r*-values for the compression state, with both "CPB06 $k=0$ T" and "CPB06 $k=0$ C" predicting similar values, which are higher than the ones predicted by the "CPB06" for approximately 30° and forward. The differences between "CPB06 $k=0$ T" and "CPB06 $k=0$ C" are negligible. These results follow the trend observed in the analytical prediction (see Fig. 7(b)), although numerically the effect of the in-plane yield stress distribution becomes even more irrelevant. In this context it should be mentioned that, although not shown here, for a punch displacement of approximately 25 mm, the contact conditions change in the flange area and the stress state component in the thickness direction alters the compression stress state in the circumferential direction, for the material points located in the outer flange (Barros et al., 2016a). This stress state change is slightly more evident for the "CPB06 $k=0$ C" than for the "CPB06" and the "CPB06 $k=0$ T", due to the higher difference in the thickness distribution in the flange area (see Fig. 6(d)). The contact conditions in the flange area influence the earing profile predicted, particularly for materials with a strong anisotropic behavior of the *r*-values (Barros et al., 2015a). This influence of the contact conditions also justifies the differences between the predictions obtained with the analytical function and the numerical simulation. For this particular case, the analytical function overestimates the cup height, but enables an analysis of the effect of the yield stress and *r*-value in-plane distribution in the earing profile.

Fig. 8 presents the thickness strains evolution along the cup, measured experimentally and the ones predicted numerically. Globally, the thickness strain is well predicted in all cases, with a reduction for an initial material position of about 40 mm, corresponding to the punch radius. From about 60 mm forward, a thickening is observed both experimentally and numerically. Globally the thickening is overestimated, whichever case considered, which can be related to the lower average height estimated for the cup (see Fig. 7(b)). Regarding the experimental trend, the thickness strain in the rolling direction is lower than the one in the transverse direction. The "CPB06" globally captures this trend, while the "CB2001" presents the opposite behavior (see Fig. 8(a)). The "CPB06 $k=0$ T" presents the same behavior as the "CB2001", while "CPB06 $k=0$ C" is able to describe the differences between the rolling and the transverse direction (see Fig. 8(b)). In fact, the "CPB06 $k=0$ C" presents a higher difference between the RD and the TD thickness strains than the "CPB06" case. This can be related with the ratio between the compression yield stress in RD and TD, $\sigma^{C}_{RD}/\sigma^{C}_{TD}$, with an experimental value of 0.931. The "CPB06 $k=0$ C" and the "CPB06" present values of 0.882 and 0.905, respectively. Thus, a higher value for the compression yield stress along TD, when compared with the one for RD (see Fig. 3), leads to a higher thickening in the transverse direction, as shown in Fig. 6. This also explains why the "CB2001" and the "CPB06 $k=0$ T" cannot capture this effect, since they impose the same trend for the tensile and compressive yield stress, with the $\sigma^{C}_{RD}/\sigma^{C}_{TD}$ ratios equal to 1.113 and 1.028, respectively. Thus, the yield stress at RD is higher than for TD. These results indicate that it is important to capture the ratio $\sigma^{C}_{RD}/\sigma^{C}_{TD}$ in order to improve the thickness prediction. Moreover, it is known that the *r*-value dictates the thickness strain, which as previously mentioned, should be the one for the compression state, but its experimental values unfortunately are unavailable.

5. Conclusions

The numerical simulation of the drawing of a cylindrical cup was performed considering a 2090-T3 aluminum alloy, with two yield criteria. The results highlight the importance of an accurate description of the material yield stresses and *r*-values in-plane directionalities, for compression stress states, in order to have more accurate predictions of both the earing profile and the thickness distributions. In fact, for the example under analysis, the results show that the earing profile is mainly dictated by the compression *r*-values in-plane directionalities, which are commonly unavailable for thin metallic sheets. The adoption of a yield criterion that takes into account the SD effect, combined with an associated flow rule, enables the simultaneous prediction of both compression yield stress and *r*-values directionalities. The compression yield

Please cite this article as: P.D. Barros et al., Study on the effect of tension-compression asymmetry on the cylindrical cup forming of an AA2090-T3 alloy, International Journal of Solids and Structures (2017), http://dx.doi.org/10.1016/j.ijsolstr.2017.06.034

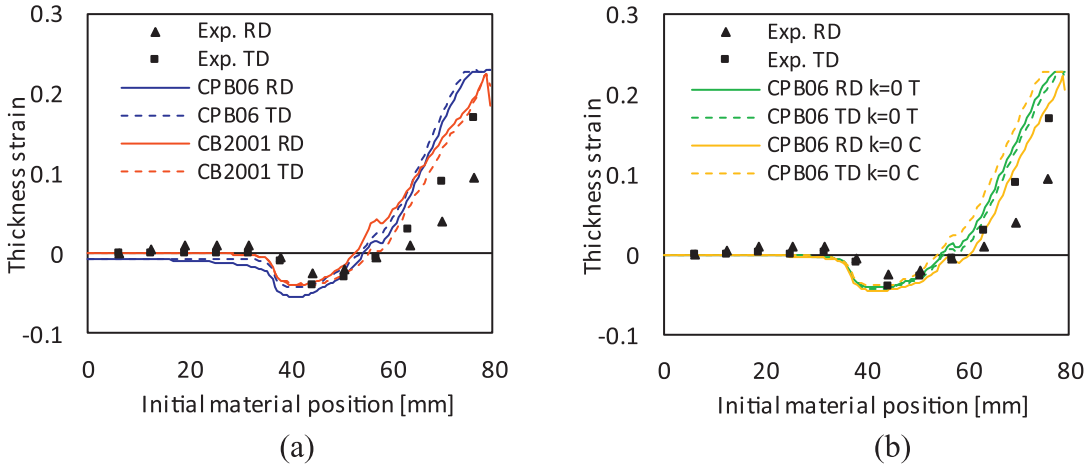

Fig. 8. Experimental and numerically predicted thickness strain for the rolling and transverse directions for the (a) CPB06 and CB2001 and (b) CPB06 $k = 0$ T and CPB06 $k = 0$ C. Solid lines used for the RD while dashed lines are used for the TD.

stresses directionalities seem to play a major role in the thickness prediction. The adoption of a flexible yield criterion, such as the CB2001, allows a proper prediction of the earing profile, but fails to capture the trend for the thickness distribution, since it imposes the same trend for the tensile and compression yield stresses directionalities. Following these conclusions, it is recommended the use of a yield criterion that is flexible enough to describe both the yield stresses and *r*-values directionalities, including the ones in compression, even for materials presenting a small SD effect. In this context, the use of the CPB06 with two linear transformations will be analyzed in a future work.

Acknowledgment

The authors gratefully acknowledge the financial support of the Portuguese Foundation for Science and Technology (FCT) under projects with reference PTDC/EMS-TEC/0702/2014 (POCI-01- 0145-FEDER-016779) and PTDC/EMS-TEC/6400/2014 (POCI-01-0145-FEDER-016876) by UE/FEDER through the program COMPETE 2020. The first author is also grateful to the FCT for the PhD grant SFRH/BD/98545/2013.

References

Banabic, D., 2010. Sheet Metal Forming Processes. Springer. Springer-Verlag, Berlin Heidelberg doi:10.1007/978-3-540-88113-1.

Banabic, D., Aretz, H., Comsa, D.S., Paraianu, L., 2005. An improved analytical description of orthotropy in metallic sheets. Int. J. Plast. 21, 493–512. doi:10.1016/j.ijplas.2004.04.003.

Banabic, D., Balan, T., Comsa, D.S., 2000. A new yield criterion for orthotropic sheet metals under plane stress conditions. In: 7th Cold Met. Form. Conf., pp. 217–224. doi:10.1016/S0020-7403(03)00139-5.

Barlat, F., Aretz, H., Yoon, J.W., Karabin, M.E., Brem, J.C., Dick, R.E., 2005. Linear transfomation-based anisotropic yield functions. Int. J. Plast. 21, 1009–1039. doi:10.1016/j.ijplas.2004.06.004.

Barlat, F., Becker, R.C., Hayashida, Y., Maeda, Y., Yanagawa, M., Chung, K., Brem, J.C., Lege, D.J., Matsui, K., Murtha, S.J., Hattori, S., 1997a. Yielding description for solution strengthened aluminum alloys. Int. J. Plast. 13, 385–401. http://dx.doi.org/10.1016/S0749-6419(97)80005-8.

Barlat, F., Brem, J.C., Yoon, J.W., Chung, K., Dick, R.E., Lege, D.J., Pourboghrat, F., Choi, S.H., Chu, E., 2003. Plane stress yield function for aluminum alloy sheets - part 1: theory. Int. J. Plast. 19, 1297–1319. doi:10.1016/S0749-6419(02)00019-0.

Barlat, F., Lege, D.J., Brem, J.C., 1991a. A six-component yield function for anisotropic materials. Int. J. Plast. 7, 693–712. doi:10.1016/0749-6419(91)90052-Z.

Barlat, F., Lege, D.J., Brem, J.C., Warren, C.J., 1991b. Constitutive behavior for anisotropic materials and application to a 2090 Al±Li alloy. In: Lowe, T., Rollett, A., Follansbee, P., Daehn, G. (Eds.), TMS Annual Meeting. TMS, New Orleans, LA, pp. 189–203.

Barlat, F., Maeda, Y., Chung, K., Yanagawa, M., Brem, J.C., Hayashida, Y., Lege, D.J., Matsui, K., Murtha, S.J., Hattori, S., Becker, R.C., Makosey, S., 1997b. Yield function development for aluminum alloy sheets. J. Mech. Phys. Solids 45, 1727–1763. doi:10.1016/S0022-5096(97)00034-3.

Barros, P.D., Alves, J.L., Oliveira, M., Menezes, L.F., 2016a. Tension-compression asymmetry modelling: strategies for anisotropy parameters identification. NUMIFORM 2016: The 12th International Conference on Numerical Methods in Industrial Forming Processes. MATEC Web of Conferences doi:10.1051/matecconf/20168005002.

Barros, P.D., Alves, J.L., Oliveira, M.C., Menezes, L.F., 2016b. Modeling of tension-compression asymmetry and orthotropy on metallic materials: numerical implementation and validation. Int. J. Mech. Sci. 114, 217–232. doi:10.1016/j.ijmecsci.2016.05.020.

Barros, P.D., Carvalho, P.D., Alves, J.L., Oliveira, M.C., Menezes, L.F., 2016c. DD3MAT - a code for yield criteria anisotropy parameters identification. J. Phys. doi:10.1088/1742-6596/734/3/032053.

Barros, P.D., Neto, D.M., Alves, J.L., Oliveira, M., Menezes, L.F., 2015a. DD3IMP, 3D fully implicit finite element solver: implementation of CB2001 yield criterion. Rom. J. Tech. Sci. Appl. Mech. 60, 105–136.

Barros, P.D., Oliveira, M.C., Alves, J.L., Andrade-Campos, A., Menezes, L.F., 2015b. Modelling of tension-compression asymmetry and orthotropic anisotropy in case of thin metallic sheets: identification procedure and case studies. In: Hora, P. (Ed.), Institute of Virtual Manufacturing. ETH Zurich, Zurich, pp. 149–154.

Cazacu, O., Barlat, F., 2004. A criterion for description of anisotropy and yield differential effects in pressure-insensitive metals. Int. J. Plast. 20, 2027–2045. doi:10.1016/j.ijplas.2003.11.021.

Cazacu, O., Barlat, F., 2003. Application of the theory of representation to describe yielding of anisotropic aluminum alloys. Int. J. Eng. Sci. 41, 1367–1385. doi:10.1016/S0020-7225(03)00037-5.

Cazacu, O., Barlat, F., 2001. Generalization of Drucker's yield criterion to orthotropy. Math. Mech. Solids 6, 613–630. doi:10.1177/108128650100600603.

Cazacu, O., Plunkett, B., Barlat, F., 2006. Orthotropic yield criterion for hexagonal closed packed metals. Int. J. Plast. 22, 1171–1194. doi:10.1016/j.ijplas.2005.06.001.

Chung, K., Kim, D., Park, T., 2011. Analytical derivation of earing in circular cup drawing based on simple tension properties. Eur. J. Mech. A Solids 30, 275–280. doi:10.1016/j.euromechsol.2011.01.006.

Comsa, D.S., Banabic, D., 2007. Numerical simulation of sheet metal forming processes using a new yield criterion. Key Eng. Mater. 344, 833–840. doi:10.4028/www.scientific.net/KEM.344.833.

Drucker, D.C., 1949. Relation of experiments to mathematical theories of plasticity. J. Appl. Mech. ASME 16, A349–A357.

Hill, R., 1948. A theory of the yielding and plastic flow of anisotropic metals. Proc. R. Soc. A Math. Phys. Eng. Sci. 193, 281–297. doi:10.1098/rspa.1948.0045.

Hughes, T.J.R., 1980. Generalization of selective integration procedures to anisotropic and nonlinear media. Int. J. Numer. Methods Eng. 15, 1413–1418. doi:10.1002/nme.1620150914.

Lege, D.J., Barlat, F., Brem, J.C., 1989. Characterization and modeling of the mechanical behavior and formability of a 2008-T4 sheet sample. Int. J. Mech. Sci. 31, 549–563.

Menezes, L.F., Teodosiu, C., 2000. Three-dimensional numerical simulation of the deep-drawing process using solid finite elements. J. Mater. Process. Technol. 97, 100–106. doi:10.1016/S0924-0136(99)00345-3.

Mulder, J., Vegter, H., 2011. An analytical approach for earing in cylindrical deep drawing based on uniaxial tensile test results 1447, 1447–1452. doi:10.1063/1.3589720.

Neto, D.M., Oliveira, M.C., Menezes, L.F., 2015. Surface smoothing procedures in computational contact mechanics. Arch. Comput. Methods Eng. doi:10.1007/s11831-015-9159-7.

Oliveira, M.C., Alves, J.L., Menezes, L.F., 2008. Algorithms and strategies for treatment of large deformation frictional contact in the numerical simulation of deep drawing process. Arch. Comput. Methods Eng. 15, 113–162.

Plunkett, B., Lebensohn, R.a., Cazacu, O., Barlat, F., 2006. Anisotropic yield function of hexagonal materials taking into account texture development and anisotropic hardening. Acta Mater. 54, 4159–4169. doi:10.1016/j.actamat.2006.05.009.

Pöhlandt, K., Banabic, D., Lange, K., 2002. Equi-biaxial anisotropy coefficient used to describe the plastic behavior of sheet metal. In: ESAFORM 2002. Krakow, Poland, pp. 723–727.

Tresca, H.-É., 1864. Mémoire sur l'écoulement des corps solides soumis à de fortes pressions. Comptes Rendus l'Académie des Sci. Paris 59, 754–758.

Tritschler, M., Butz, A., Helm, D., Falkinger, G., Kiese, J., 2014. Experimental analysis and modeling of the anisotropic response of titanium alloy Ti-X for quasi-static loading at room temperature. Int. J. Mater. Form. 7, 259–273. doi:10.1007/s12289-013-1125-z.

von Mises, R., 1913. Mechanik der festen korper im plastic-deformablen zustand. Nachrichten vos der K. gellesschaft des winssenschaften zu Gottingen 582–592.

Yoon, J.W., Barlat, F., Chung, K., Pourboghrat, F., Yang, D.Y., 2000. Earing predictions based on asymmetric nonquadratic yield function. Int. J. Plast. 16, 1075–1104. doi:10.1016/S0749-6419(99)00086-8.

Yoon, J.W., Dick, R.E., Barlat, F., 2011. A new analytical theory for earing generated from anisotropic plasticity. Int. J. Plast. 27, 1165–1184. doi:10.1016/j.ijplas.2011.01.002.

Yoshida, F., Hamasaki, H., Uemori, T., 2013. A user-friendly 3D yield function to describe anisotropy of steel sheets. Int. J. Plast. 45, 119–139. doi:10.1016/j.ijplas.2013.01.010.

Please cite this article as: P.D. Barros et al., Study on the effect of tension-compression asymmetry on the cylindrical cup forming of an AA2090-T3 alloy, International Journal of Solids and Structures (2017), http://dx.doi.org/10.1016/j.ijsolstr.2017.06.034

4.4. Numerical prediction of the earing in the cup drawing of an AA3104 aluminum alloy: process conditions *versus* yield criterion

This subchapter contains the paper "Numerical prediction of the earing in the cup drawing of an AA3104 aluminum alloy: process conditions versus yield criterion", in preparation for publication in an international scientific journal. This work presents the details concerning the strategy for the CPB06ex2 yield criterion anisotropy parameters identification implemented in DD3MAT. Also, some details about its implementation in the DD3IMP code are discussed. The material's mechanical behavior is described using both the CPB06ex2 and the CB2001 yield criteria, both of which can accurately reproduce the in-plane directionalities. No tension-compression asymmetry was considered for the CPB06ex2 since no experimental results are available. The numerical simulation results show that both the CPB06ex2 and CB2001 can accurately describe the earing behavior of the cup, which depends on the contact with friction conditions, attesting the influence of the blank holder force on the flange stress state. This stress state defines the directions of the plastic strain rates predicted by both yield criteria, which are shown to be distinct.

(Page intentionally left blank)

NUMERICAL PREDICTION OF THE EARING IN THE CUP DRAWING OF AN AA3104 ALUMINUM ALLOY: PROCESS CONDITIONS *VERSUS* YIELD CRITERION

P.D. Barros [1, a]

[a] *CEMMPRE, Department of Mechanical Engineering, University of Coimbra, Polo II, Rua Luís Reis Santos, Pinhal de Marrocos, 3030-788 Coimbra, Portugal*

D.M. Neto [a]

[a] *CEMMPRE, Department of Mechanical Engineering, University of Coimbra, Polo II, Rua Luís Reis Santos, Pinhal de Marrocos, 3030-788 Coimbra, Portugal*

R.E. Dick [b]

[b] *Rigid Packaging Technology Division, Alcoa Technical Center,*

100 Technical Drive, Alcoa Center, PA 15069, USA

M.C. Oliveira [a]

[a] *CEMMPRE, Department of Mechanical Engineering, University of Coimbra, Polo II, Rua Luís Reis Santos, Pinhal de Marrocos, 3030-788 Coimbra, Portugal*

J.L. Alves [c]

[c] *CMEMS, Center for Microelectromechanical Systems Research Unit, University of Minho, Campus de Azurém, 4800-058 Guimarães, Portugal*

A. Andrade-Campos [d]

[d] *Department of Mechanical Engineering, Centre for Mechanical Technology and Automation, GRIDS research group, University of Aveiro, Campus Universitário de Santiago, 3810-193 Aveiro, Portugal*

L.F. Menezes [a]

[a] *CEMMPRE, Department of Mechanical Engineering, University of Coimbra, Polo II, Rua Luís Reis Santos, Pinhal de Marrocos, 3030-788 Coimbra, Portugal*

[1] Corresponding author: pedro.barros@dem.uc.pt
Tel.: +351 239790700
Fax: +351 239790701

Abstract

This work concerns the numerical deep drawing of a circular cup, analyzing the influence of the yield criterion and the friction coefficient in the earing profile. An Alcoa AA3104 commercial bodystock alloy sheet was characterized using tensile, bulge and disk compression tests. The material mechanical behavior was modeled considering the Cazacu and Barlat, 2001 (CB2001) and Cazacu et al., 2006, with two linear transformations (CPB06ex2), yield criteria. The anisotropy parameters for both yield criteria were identified using the in-house code DD3MAT, allowing an accurate modeling of the experimental material behavior. Details regarding the implementation of the CPB06ex2 yield criteria in the implicit finite element code DD3IMP are given as well as the procedure specifically developed to identify the anisotropy parameters for this yield criterion. The results confirm that the trend of the earing profile is mainly dictated by the in-plane yield stresses and r-values directionalities. However, the thickness predicted for the cup wall is always lower in the results obtained with the CB2001 and, accordingly, a higher height is also predicted. Moreover, the influence of the friction coefficient is more remarked for the CB2001. The comparison of the directions of the plastic strain rates, in function of the loading direction, predicted by both yield criteria highlights that the yield locus defined by the CPB06ex2 presents a sharper shape than the one defined by the CB2001, meaning that there are more regions in the stress space with a constant slope. This explains the lower sensitivity of the CPB06ex2 yield criterion to small changes in the stress state and, accordingly, of the friction coefficient. The evaluation of the directions of the plastic strain rates also helps to analyze the influence of small changes in stress state in the strain ratio between the radial and the thickness direction. In this example, the increase of this strain ratio predicted by the CB2001 explains why the average cup height predicted is always higher than the one obtained with the CPB06ex2, which presents a more constant value for this strain ratio. This example highlights the importance of an accurate prediction of the directions of the plastic strain rates in the tension-compression stress state to predict the cup height.

Keywords: Finite element method; Yield criterion; Anisotropy parameters identification; Direction of the plastic strain rate; Cup drawing; Earing.

1 Introduction

Currently, the can-making industry produces about 370 billion units/year of aluminum beverage cans. The process from which they are produced consists of a mechanical cold forming, which considers both drawing and ironing stages (Hosford and Duncan, 1994), due to the high production rates and high quality of the components obtained with these processes. Aluminum alloys are among the most used materials for can production using sheet metal forming processes since they present good formability, a high strength to weight ratio and excellent corrosion resistance. However, cup-drawing operations lead to the formation of a number of undulations on the top of the cups, which are typically referred as earing. This phenomenon is generated by the orthotropic plastic behavior of the metal, deriving from preferred crystallographic orientation, or texture, acquired during the thermomechanical production of the thin sheets. This undesired phenomenon leads to problems in the production of aluminum cans and waste of material due to the requirement of trimming the top of the can.

Some studies have been performed to predict the earing profile, using analytical approaches, for a single step cup drawing. Barlat et al. (1991) attempted to correlate the yield stresses directionalities to the earing trends by applying the stress condition at the rim. On the other hand, Yoon et al. (2006) derived an analytical approach considering only the *r*-values directionality as the main contributor to the earing profile. Later, (Yoon et al., 2008) combined both effects, the *r*-values and yield stresses directionalities, to improve the earing profile prediction. Further improvements were made by (Mulder and Nagy, 2009), considering a non-uniform strain in the flange, as well as process conditions. An analytical approach to determine the earing profile in the drawing and ironing processes was proposed by Yoon et al. (2011), which allows to quantify the separate contribution of both the *r*-values and yield stress directionalities. The analytical approach proposed by Chung et al. (2011) also enables the evaluation of the earing profile, after a single step cup drawing, based only in the *r*-values and yield stress directionalities. These analytical studies are based on the stress conditions observed in the rim, which indicate that the outer flange will be submitted mainly to a circumferential compression stress state. Therefore, the material behavior will be dictated by the stress and *r*-values predicted for this stress state. In addition, both the compression yield stresses and the compression anisotropy coefficients in the rolling direction will have a direct impact on the material behavior at the transverse direction and *vice-versa*. In fact, the behavior of the rim in the

direction defined by θ with the rolling direction is controlled by the material compression properties in the direction defined by $90-\theta$. Thus, the analytical models that contemplate both the in-plane *r*-values and yield stress directionalities indicate that a lower value of the anisotropy coefficient leads to a lower cup height, whereas lower values of the yield stresses lead to a higher cup height (Chung et al., 2011; Mulder and Nagy, 2009; Yoon et al., 2011). This trend correlates with the experimental one, but the process conditions can alter the earing profile (Barros et al., 2015a).

Some studies have been also performed considering crystal plasticity models to describe the texture developed during the rolling and annealing processes, resulting in planar anisotropy. The studies on earing prediction were mainly performed considering a mixture of the continuum and crystal plasticity approaches, to reduce the computational effort. In this context, the visco-plastic self-consistent (VPSC) polycrystal plasticity scheme was used to describe the polycrystal structure that is embedded in and interacts with a homogeneous effective medium having average properties and to predict the earing patterns for magnesium alloys (Walde and Riedel, 2007). Engler and Kalz (2004) developed a polycrystal plasticity model that derives the boundary conditions for the VPSC computations from detailed finite element method (FEM) analysis of the stresses and strains, during cup deep drawing, enabling the prediction of the radial strain for different in-plane angles and, consequently, the resulting earing profile. The texture component crystal plasticity finite element method (TCCP-FEM) was also developed enabling the analysis of the earing profile for different (Raabe et al., 2005; Tikhovskiy et al., 2008, 2007; Zhao et al., 2004).

The most widely used method to virtually design and optimize sheet metal forming processes is the FEM, in which the mechanical behavior of the material is described using continuum plasticity models. These phenomenological models are computationally efficient when compared with crystal plasticity models. They are based on the definition of: (i) a yield criterion, which describes the yield surface of the material in a multidimensional stress space; (ii) a hardening laws, which express the evolution of the yield surface during plastic deformation; and (iii) a flow rule, to establish a relationship between the stress state and the plastic strain increment. Typically, an associated flow rule is adopted, meaning that the plastic flow and the material's orthotropic behavior is modeled by the yield surface. This dual role of the yield surface requires a particular care and accuracy in its modeling, numerical implementation and in the procedure adopted to perform the parameters identification. The Hill'48 (Hill, 1948) quadratic function was the

first proposed for describing the anisotropic behavior of metal sheets and it is still the most widely used. However, aluminum alloys are prone to present an anisotropic behavior which cannot be accurately described by quadratic yield criteria (Banabic, 2010; Pearce, 1968; Woodthorpe and Pearce, 1970). Thus, other formulations have been proposed to improve the description of the mechanical behavior of orthotropic metallic materials, in particular of aluminum and its alloys (*e.g.* (Banabic et al., 2000; Barlat et al., 2005, 2003, 1997, 1991a, Cazacu and Barlat, 2003, 2001; Comsa and Banabic, 2007; Yoshida et al., 2013)). These yield criteria have been used to describe the orthotropic behavior during sheet metal forming processes, showing that they play a fundamental role in the accurate description of the material flow. In this context, the deep drawing of a cylindrical cup can help to evaluate the impact of both the *r*-values and yield stress directionalities. In fact, some studies infer that improved modeling of both the material's yield stresses and *r*-values in-plane directionalities improves the accuracy of the earing profile prediction on the deep drawing of cylindrical cups (Barros et al., 2015a; Barros et al., 2016a; Yoon et al., 2011). However, in the numerical simulation of cylindrical cup drawing, the material flow is also influenced by the contact with friction conditions, making the analysis of the impact of both the *r*-values and yield stress directionalities very difficult. In fact, for materials with a strong anisotropic behavior of the *r*-values (AA5042 aluminum alloy), the earing profile is influenced by the contact conditions in the flange, which are related with the uneven thickness strain distribution in the sheet plane. This leads to a non-uniform contact force distribution, more concentrated in a limited region of the flange. In fact, the study performed by Barros et al. (2015a) also shows that the analytical models proposed by Yoon et al. (2011) and Chung et al. (2011) enable an accurate prediction of the trend for the earing profile, as long as the stress component in the thickness direction of the rim is small. Otherwise, even for a material with a small anisotropic behavior (AKDQ steel) the average height predicted by the numerical model differs from the one estimated by the analytical one.

In order to capture both the *r*-values and yield stress directionalities, it is important to select a yield criterion with enough flexibility. That is the case of the one proposed by Cazacu and Barlat (2001) (hereafter denoted as CB2001), which was used by (Barros et al., 2015a). However, the convexity conditions for this yield criterion are not defined, which renders supplementary difficulties in its application in FEM. On the other hand, most yield criteria possess a point-symmetry with respect to its center, meaning that a stress state and its reverse state have the same absolute value (Banabic, 2010). However,

this can be an unrealistic approximation, even for cubic metals (both face centered cubic (FCC) and body centered cubic (BCC)) (Barlat et al., 1991a). Taking into account the stress conditions observed in the rim, it was shown that this tension-compression asymmetry influences mainly the thickness prediction (Barros et al., 2016). This study was performed using the yield criterion proposed by Cazacu et al. (2006) that enables describing the materials anisotropy and the tension-compression asymmetry using a linear transformation, with a fourth-order tensor, of the deviatoric stress tensor. In order to more accurately capture the material's anisotropic behavior, several linear transformations can be adopted (Plunkett et al., 2006; Tritschler et al., 2014). However, the yield surface modeling becomes more complex due to the higher number of material anisotropy parameters involved, thus requiring a larger set of experimental data. Thus, in the current work two linear transformations will be adopted (hereafter denoted as CPB06ex2).

The anisotropy parameters must be identified such that the yield criterion reproduces the material's mechanical behavior as closely as possible. This procedure is typically based on solving an optimization problem, considering the minimization of an error function, which evaluates the difference between the estimated and the experimentally evaluated values. For the calibration of the yield criterion parameters, classical methodologies consider the experimental data acquired from experimental tests characterized for presenting linear strain paths, namely uniaxial tensile, bulge and shear tests. These tests present homogeneous deformation in the measuring region, allowing to estimate the yield stress. Uniaxial tensile and shear test can also be performed using specimens cut in several directions of the sheet's plane (generally, 0º, 15º, 30º, 45º, 60º, 75º and 90º from the rolling direction (RD)). More flexible yield functions are commonly characterized for considering a higher number of anisotropy parameters and, consequently, yield functions require a significant number of experimental tests to enable their identification. Full-field identification methodologies have also been proposed, trying to explore the information obtained from a fewer number of more complex experimental tests involving non-homogeneous strain fields (Cooreman et al., 2008; Güner et al., 2012; Pottier et al., 2012; Prates et al., 2015). This approach is also advocated by authors that state that limiting the characterization of the mechanical behavior of metal sheets to a restricted number of tests with linear strain paths and homogeneous deformation can lead to a somewhat incomplete characterization of the overall plastic behavior of the material (Zidane et al., 2010). However, whichever the methodology adopted, when using a phenomenological approach most of the stress space is left

unexplored when fitting the parameters of the yield function (Zhang et al., 2015). Therefore, it is important to improve the knowledge concerning the more relevant stress and strain states, particularly for the analysis of cylindrical cups.

In this work, the cup drawing of an Alcoa AA3104 aluminum alloy is studied using the FEM. The earing profile, thickness and punch forces evolutions as well as stress and strain states are analyzed. The following section describes the experimental procedure adopted to characterize the material mechanical behavior and to perform the cylindrical cup deep drawing. The numerical simulations are performed considering the CB2001 and CPB06ex2 yield criteria, both implemented in DD3IMP in-house code. Thus, Section 3 presents the main details concerning the constitutive model adopted. The anisotropy parameters for both yield criteria were identified using the DD3MAT in-house code. The classical procedure adopted in this code is described in Section 4, as well as some details specific for the CPB06ex2 yield criterion. The details concerning the numerical model adopted are given in Section 5. Section 6 comprises the comparison between numerical and experimental results, highlighting the correlation between the shape of the yield *locus* and the influence of the process conditions. The main conclusions of this study are discussed in Section 7.

2 Material and experiments

In this work, the Alcoa AA3104 commercial bodystock alloy delivered in sheets with 0.268 mm of thickness is adopted to perform the circular cup deep drawing tests. The experimental mechanical characterization of this aluminum alloy, as well as the cup drawing process operation, is described in this section.

2.1 Mechanical characterization

Uniaxial tensile tests were performed considering ASTM standard specimens with gage dimension of 50×12.5 mm, which were CNC machined from the AA3104 as-rolled sheet material. In order to determine the yield stress, hardening behavior, and *r*-values, the tensile specimens were cut along different orientations, namely along 0º, 15º, 30º, 45º, 60º 75º and 90º from the rolling direction (RD). A Shimadzu AG-X Plus testing machine with maximum load capacity of 10 kN was used to perform the tensile tests, considering 1×10^{-3} s^{-1} engineering strain rate. The strain measurements were performed with Digital Image Correlation (DIC) using ARAMIS v6.3 software.

Considering the uniaxial strain path, the true stress−true strain curves were computed from the load-displacement curves, assuming plastic incompressibility. On the other hand, the biaxial stress−strain behavior was determined by means of the hydraulic bulge test. The strains and curvature at the pole of the bulge were measured with a mechanical device (Lee et al., 2013) and the membrane theory was used to calculate the biaxial yield stress (Martins et al., 2013). The disk compression test was conducted to determine the biaxial *r*-value, r_b, using circular specimens with 12.7 mm of diameter. In order to reduce the friction forces, thin Teflon sheets were used between the specimen and the load platens of the test device. The diameters in the RD and transverse direction (TD) were measured before and after deformation, allowing to obtain the r_b value. Table 1 presents the Young's modulus, Poisson's ratio, yield stresses and *r*-values considered for the present work.

Table 1. Mechanical properties for the Alcoa AA3104 commercial bodystock alloy.

Test direction	*r*-value	$\sigma_\theta^{Y_T}$ [MPa]
0º	0.411	268.6
15º	0.419	269.4
30º	0.635	272.6
45º	0.968	272.9
60º	1.098	277.0
75º	1.150	280.2
90º	1.304	282.5
σ_b	-	310.0
r_b	0.620	-
Elastic properties	E [MPa]	υ
	68950	0.33

2.2 Deep drawing of a circular cup

The cylindrical cup drawing operation is carried out considering three axisymmetric forming tools (punch, die and blank holder), as schematically illustrated in Figure 1 together with the main dimensions in millimeters (Dick and Yoon, 2018). The adopted blank is circular with 76.12 mm of diameter and 0.268 mm of nominal thickness.

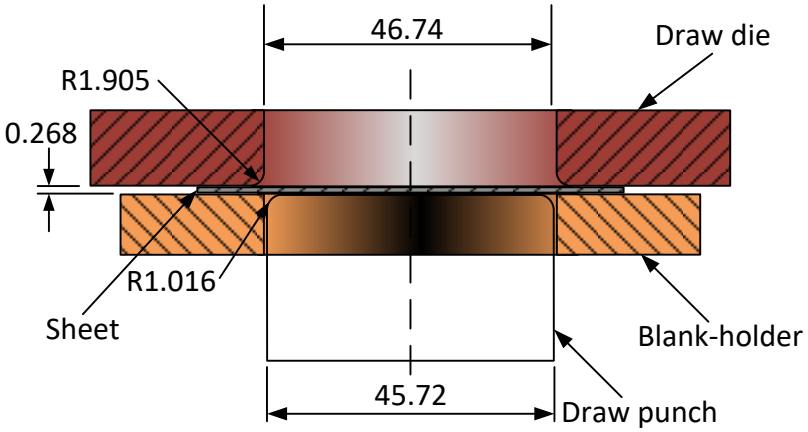

Figure 1. Schematic of the forming tools used for the cup drawing, including the main dimensions (in millimeters).

The deep drawing of the cylindrical aluminum cups is carried out at room temperature in a hydraulic press with maximum capacity of 50 kN. The press is equipped with a monitoring system (Keithley), enabling the acquisition of the punch force evolution as a function of its stroke. The drawing process is performed with a constant punch travel speed of 140 mm/s and a constant blank-holder force of 7.5 kN, which is maintained through a pressure cylinder. The cup is fully drawn considering a punch travel of 25 mm, while the gap between the blank-holder and the die is not restricted by any rigid stop or standoff during the drawing process. The experimental tests are run in triplicate for each process condition in order to investigate its reproducibility. Figure 2 presents the final geometry of the cup, highlighting the development of ears on the drawn cup (Dick and Yoon, 2018).

Figure 2. Developed earing profile in the experimental drawing of an aluminum cylindrical cup. Note for the wrinkling pattern in the vertical wall.

All forming tools are made of AISI A2 steel with 58–60 of Rockwell C hardness and surface roughness about 2–4 μm (finish working surfaces). A controlled level of oil lubricant is applied to both sides of the blank to reduce the frictional forces between the forming tools and the blank sheet during the forming. The earing profile is measured considering the distance between the cup's bottom and the height of the wall at the considered angle.

3 Constitutive model

In order to describe accurately the strong orthotropic behavior of this aluminum alloy, two advanced yield criteria are adopted in the present study, namely the Cazacu and Barlat (2001) and the Cazacu et al. (2006) yield criteria with two linear transformations. The yield criterion developed by Cazacu and Barlat (2001) is based on the generalization to orthotropy of the invariants of the deviatoric stress tensor, which are used to extend the Drucker's (1949) isotropic yield criterion. On the other hand, the yield criterion proposed by Cazacu et al. (2006), which allows the modeling of tension-compression asymmetry, is based in linear transformations applied to the deviatoric stress tensor.

A Voce type hardening law is used in this work, given by

$$Y = Y_{\text{sat}} - \left(Y_{\text{sat}} - Y_0\right)\exp\left(-C\bar{\varepsilon}^{\text{p}}\right), \tag{1}$$

where Y is the flow stress, $\bar{\varepsilon}^{\text{p}}$ is the equivalent plastic strain, and Y_{sat}, Y_0 and C are material parameters. In this work, no kinematic hardening was taken into account.

The yield condition is defined as

$$\mathcal{F}\left(\bar{\sigma}, Y\right) = \bar{\sigma} - Y = 0, \tag{2}$$

where $\bar{\sigma}$ is the equivalent stress. The flow stress Y depends of the hardening law selected, such that the yield stress is Y_0. The adopted constitutive model considers an associated flow rule, meaning that the yield function is also used to define the plastic potential ($\mathcal{F}$) and, accordingly, to determine the plastic strain increment. The plastic strain rate tensor, $\mathbf{D}^{\text{p}}$, is determined according to

$$\mathbf{D}^{\text{p}} = \dot{\lambda}\frac{\partial \mathcal{F}\left(\bar{\sigma}, Y\right)}{\partial \boldsymbol{\sigma}}. \tag{3}$$

$\dot{\lambda}$ is a scalar value designated by plastic multiplier that can be demonstrated to be equal to the equivalent plastic strain rate, $\dot{\bar{\varepsilon}}^{\mathrm{p}}$. The equivalent plastic strain is defined as

$$\bar{\varepsilon}^{\mathrm{p}} = \int_0^t \dot{\bar{\varepsilon}}^{\mathrm{p}} \mathrm{d}t = \int_0^t \frac{\boldsymbol{\sigma}'}{\bar{\sigma}} : \mathbf{D}^{\mathrm{p}} \mathrm{d}t \,. \tag{4}$$

The equivalent stress is given by the yield criterion adopted, as described in the following sections. For further details concerning the constitutive model and the its implementation, please refer to (Barros et al., 2015a; Barros et al., 2016b).

3.1 Cazacu and Barlat (2001) yield criterion

The Cazacu and Barlat (2001) yield criterion is a generalization of the Drucker's isotropic criterion to orthotropy and, in its general form, is given by

$$\bar{\sigma} = \left\{ 27 \left[\left(J_2^0 \right)^3 - c \left(J_3^0 \right)^2 \right] \right\}^{\frac{1}{6}}, \tag{5}$$

where J_2^0 and J_3^0 are the second and third generalized invariants of the deviatoric Cauchy stress tensor $\boldsymbol{\sigma}'$, defined as

$$\begin{aligned} J_2^0 = {} & \frac{a_1}{6}(\sigma_{11} - \sigma_{22})^2 + \frac{a_2}{6}(\sigma_{11} - \sigma_{33})^2 + \frac{a_3}{6}(\sigma_{11} - \sigma_{33})^2 \\ & + a_4 \sigma_{12}^2 + a_5 \sigma_{13}^2 + a_6 \sigma_{23}^2 \end{aligned}, \tag{6}$$

and

$$\begin{aligned} J_3^0 = {} & (1/27)(b_1 + b_2)\sigma_{11}^3 + (1/27)(b_3 + b_4)\sigma_{22}^3 \\ & + (1/27)[2(b_1 + b_4) - b_2 - b_3]\sigma_{33}^3 \\ & - (1/9)(b_1\sigma_{22} + b_2\sigma_{33})\sigma_{11}^2 - (1/9)(b_3\sigma_{33} + b_4\sigma_{11})\sigma_{22}^2 \\ & - (1/9)[(b_1 - b_2 + b_4)\sigma_{11} + (b_1 - b_3 + b_4)\sigma_{22}]\sigma_{33}^2 \\ & + (2/9)(b_1 + b_4)\sigma_{11}\sigma_{22}\sigma_{33} \\ & - \left(\sigma_{13}^2/3\right)[2b_9\sigma_{22} - b_8\sigma_{33} - (2b_9 - b_8)\sigma_{11}] \\ & - \left(\sigma_{12}^2/3\right)[2b_{10}\sigma_{33} - b_5\sigma_{22} - (2b_{10} - b_5)\sigma_{11}] \\ & - \left(\sigma_{23}^2/3\right)[(b_6 - b_7)\sigma_{11} - b_6\sigma_{22} - b_7\sigma_{33}] + 2b_{11}\sigma_{12}\sigma_{23}\sigma_{13} \end{aligned}, \tag{7}$$

where $a_1, ..., a_6$ and $b_1, ..., b_{11}$ are the anisotropy parameters and c is a weighting parameter. σ_{ij}, $i, j = 1, 2, 3$ are the stress components of the Cauchy stress tensor $\boldsymbol{\sigma}$. The conditions that guarantee the convexity of CB2001 are unknown, excepted when

assuming in-plane isotropic behavior, for which $c \in [-3.75, 2.25]$ (Cazacu and Barlat, 2001).

3.2 Cazacu et al. (2006) yield criterion

The Cazacu et al. (2006) yield criterion allows the description of both the orthotropic behavior and the strength-differential (SD) effect, *i.e.* tension-compression asymmetry. The orthotropic form of this yield criterion is defined as

$$\bar{\sigma} = B\left[\left(|s_1| - k\, s_1\right)^a + \left(|s_2| - k\, s_2\right)^a + \left(|s_3| - k\, s_3\right)^a\right]^{\frac{1}{a}}, \tag{8}$$

where the exponent a is a positive integer and k is a material parameter that enables the description of the SD effect when the material presents isotropic behavior. In fact, for an isotropic material, the k parameter defines the tension-compression ratio, which is the same for any orthotropy axis. However, as shown in Barros et al. (2015b), when anisotropy is taken into account, this parameter loses this meaning, since the material can present different tension-compression ratios for the three orthotropic axis. The eigenvalues components of the tensor $\mathbf{s}$ are denoted by s_1, s_2 and s_3 in Eq. (8). This tensor is determined following the linear transformation proposed by Barlat et al. (1997), such that $\mathbf{s} = \mathbf{C} : \boldsymbol{\sigma}'$, where $\boldsymbol{\sigma}'$ is the deviatoric stress tensor and $\mathbf{C}$ is the constant 4th-order transformation tensor. For 3D stress conditions, assuming the Voigt notation, this tensor involves 9 independent anisotropy coefficients and can be expressed in the principal axis of anisotropy as

$$\mathbf{C} = \begin{bmatrix} C_{11} & C_{12} & C_{13} & 0 & 0 & 0 \\ C_{12} & C_{22} & C_{23} & 0 & 0 & 0 \\ C_{13} & C_{23} & C_{33} & 0 & 0 & 0 \\ 0 & 0 & 0 & C_{44} & 0 & 0 \\ 0 & 0 & 0 & 0 & C_{55} & 0 \\ 0 & 0 & 0 & 0 & 0 & C_{66} \end{bmatrix}. \tag{9}$$

B is a constant defined such that Y reduces to the tensile yield stress in the rolling direction, and is given by

$$B = \left[\frac{1}{\left(|\phi_1| - k\,\phi_1\right)^a + \left(|\phi_2| - k\,\phi_2\right)^a + \left(|\phi_3| - k\,\phi_3\right)^a}\right]^{\frac{1}{a}}, \tag{10}$$

with

$$\phi_i = (2/3)C_{i1} - (1/3)C_{i2} - (1/3)C_{i3} \text{ for } i = 1,2,3. \tag{11}$$

The convexity of the yield function is guaranteed for $a \geq 2$ and $k \in [-1,1]$ (Cazacu et al., 2006). Note that, in terms of formulation, for the yield criteria based on the linear transformation of the deviatoric stress tensor, the number of transformations is unlimited with the only constraint being the available experimental data (Barlat et al., 2005). In fact, nine anisotropy parameters may fall short when describing the behavior of materials showing pronounced in-plane anisotropy. Therefore, Plunkett et al. (2008) extended the CPB06 to consider two linear transformations, thus doubling the number of anisotropy coefficients from 9 to 18. In the case of the CPB06ex2, the equivalent stress $\bar{\sigma}$ associated with its orthotropic form is defined as

$$\bar{\sigma} = B\left[\begin{array}{l}\left(|s_1| - k\,s_1\right)^a + \left(|s_2| - k\,s_2\right)^a + \left(|s_3| - k\,s_3\right)^a \\ + \left(|s'_1| - k'\,s'_1\right)^a + \left(|s'_2| - k'\,s'_2\right)^a + \left(|s'_3| - k'\,s'_3\right)^a\end{array}\right]^{\frac{1}{a}}. \tag{12}$$

B remains a constant defined such that Y reduces to the tensile yield stress in the rolling direction and is now given by

$$B = \left[\frac{1}{\begin{array}{l}\left(|\phi_1| - k\,\phi_1\right)^a + \left(|\phi_2| - k\,\phi_2\right)^a + \left(|\phi_3| - k\,\phi_3\right)^a \\ + \left(|\phi'_1| - k'\,\phi'_1\right)^a + \left(|\phi'_2| - k'\,\phi'_2\right)^a + \left(|\phi'_3| - k'\,\phi'_3\right)^a\end{array}}\right]^{\frac{1}{a}}, \tag{13}$$

with the same definition for the ϕ_i, $i = 1,2,3$ as in Eq. (11) and

$$\phi'_i = (2/3)C'_{i1} - (1/3)C'_{i2} - (1/3)C'_{i3} \text{ for } i = 1,2,3. \tag{14}$$

The convexity is still guaranteed for $a \geq 2$, $k \in [-1,1]$ and $k' \in [-1,1]$ since the use of one or several linear transformation does not affect convexity of the yield function (Eggleston, 1958; Rockafellar, 1972). For $\mathbf{C} = \mathbf{C}'$ and $k = k'$, the CPB06ex2 yield criterion reduces to the original form of the CPB06. Further details about the derivatives necessary for the implementation of the CPB06ex2 yield criterion in the DD3IMP code are given in Appendix A.

4 Material parameters identification

The anisotropy parameters should be determined such that the yield criterion reproduces the material's mechanical behavior as close as possible. The most commonly used experimental results for the identification of anisotropy parameters are the yield stresses and *r*-values obtained from in-plane uniaxial tension for different angles (θ) with the rolling direction (RD). When adopting classical methodologies, usually these tests are performed for several directions in the sheet's plane (generally, 0, 15, 30, 45, 60, 75 and 90 from the rolling direction). For some criteria, it is also recommended to use the experimental results for other trajectories, like the biaxial yield stress σ_{b}, and the biaxial anisotropy coefficient r_{b} (Barlat et al., 2003; Lege et al., 1989; Pöhlandt et al., 2002). In case of yield criteria capable of describing SD effects, uniaxial compression experimental results are also necessary for describing the materials mechanical behavior for these stress states, ideally for the three axis of orthotropy.

4.1 DD3MAT material parameters identification code

The DD3MAT in–house code (Barros et al., 2016c) allows determining yield criteria parameters that adjust a given material's experimental behavior. The procedure adopted is based on the minimization of an error function, evaluating the difference between estimated and experimental values, in the form

$$\begin{aligned} F(\mathbf{A}) = {} & w_{\sigma_\theta^{\mathrm{T}}} \sum_{\theta} \left(\sigma_\theta^{\mathrm{T}}(\mathbf{A}) / \sigma_\theta^{\mathrm{T}} - 1 \right)^2 + w_{\sigma_\theta^{\mathrm{C}}} \sum_{\theta} \left(\sigma_\theta^{\mathrm{C}}(\mathbf{A}) / \sigma_\theta^{\mathrm{C}} - 1 \right)^2 \\ & + w_{r_\theta^{\mathrm{T}}} \sum_{\theta} \left(r_\theta^{\mathrm{T}}(\mathbf{A}) / r_\theta^{\mathrm{T}} - 1 \right)^2 + w_{r_\theta^{\mathrm{C}}} \sum_{\theta} \left(r_\theta^{\mathrm{C}}(\mathbf{A}) / r_\theta^{\mathrm{C}} - 1 \right)^2 \\ & + w_{\tau_\theta} \sum_{\theta} \left(\tau_\theta(\mathbf{A}) / \tau_\theta - 1 \right)^2 + w_{\sigma_{\mathrm{b}}} \left(\sigma_{\mathrm{b}}(\mathbf{A}) / \sigma_{\mathrm{b}} - 1 \right)^2 + w_{r_{\mathrm{b}}} \left(r_{\mathrm{b}}(\mathbf{A}) / r_{\mathrm{b}} - 1 \right)^2 \end{aligned} \tag{15}$$

,

with $\mathbf{A}$ representing the set of parameters of the respective yield criterion. $\sigma_\theta^{\mathrm{T}}$, $\sigma_\theta^{\mathrm{C}}$ are the experimental yield stresses determined in tension and compression, and r_θ^{T}, r_θ^{C} are the experimental anisotropy coefficients determined in tension and compression. These are obtained from the uniaxial tests for a specific orientation (θ) with respect to the rolling direction. τ_θ is the experimental yield stress in shear, obtained for a specific orientation (θ) with respect to the rolling direction. σ_{b} is the experimental yield stress obtained from the equibiaxial tensile test and r_{b} is the experimental anisotropy coefficient obtained from

the disc compression test. $\sigma_\theta^{\mathrm{T}}(\mathbf{A})$, $\sigma_\theta^{\mathrm{C}}(\mathbf{A})$, $r_\theta^{\mathrm{T}}(\mathbf{A})$, $r_\theta^{\mathrm{C}}(\mathbf{A})$, $\tau_\theta(\mathbf{A})$, $\sigma_{\mathrm{b}}(\mathbf{A})$ and $r_{\mathrm{b}}(\mathbf{A})$ are the correspondent values predicted from the adopted yield criterion. In DD3MAT, these values are evaluated using the implemented analytical expression. Such procedure can be considered a generalization of the one proposed by Banabic et al. (2005), where the weighting factors, $w_{\sigma_\theta^{\mathrm{T}}}$, $w_{\sigma_\theta^{\mathrm{C}}}$, $w_{r_\theta^{\mathrm{T}}}$, $w_{r_\theta^{\mathrm{C}}}$, w_{τ_θ}, $w_{\sigma_{\mathrm{b}}}$ and $w_{r_{\mathrm{b}}}$, are used to balance the influence of the experimental data. The selection of these weighting factors is a manual procedure strongly dependent on the users' expertise and performed based on the analysis of the global trends between the experimental and the numerical results.

For the particular case of the CPB06, the yield criterion presents 9 anisotropy parameters and the k value. However, when considering metallic sheets, the anisotropy parameters C_{44} and C_{55}, cannot be evaluated. Thus, the corresponding isotropic values are usually adopted, *i.e.* 1.0. Moreover, the C_{11} parameter is also considered equal to 1.0 to avoid equivalent sets of parameters, as discussed in (Barros et al., 2016b). Therefore, it is necessary to identify a total of 6 anisotropy parameters and the k value. As for the CPB06ex2 case, the same premises are considered. In this case, $C'_{44} = C'_{55} = 1.0$ as well as $C'_{11} = 1.0$, totaling 12 anisotropy parameters and both k and k' values. For the case of the CB2001 yield criterion, a_5, a_6 and b_k $(k = 6, 7, 8, 9, 11)$ are the anisotropy parameters corresponding to the off-plane properties that cannot be evaluated for metallic sheets. Thus, they are assumed as equal to the isotropic values, *i.e.* 1.0. In this case, it is necessary to identify a total of 10 anisotropy parameters and the c value. For the CB2001, it is assumed that $a_i \in [-10,10]$, $b_i \in [-10,10]$ and $c \in [-3.75, 2.25]$.The minimization process adopted for the CB2001 yield criterion includes testing the convexity of the yield surface for several planes in the stress space (Barros et al., 2015a). The optimization algorithm adopted in DD3MAT is based on a downhill-simplex derivative-free method, which allows finding the minimum of the objective function in a multidimensional space with a low computational cost.

Regarding the CPB06ex2, the general procedure assumes that $k \in [-1,1]$, $k' \in [-1,1]$, $C_{ij} \in [-4,6]$ and $C'_{ij} \in [-4,6]$ for $i = j$, and $C_{ij} \in [-5,5]$ and $C'_{ij} \in [-5,5]$ for the remaining parameters. When no experimental data is available for compression stress states, such as in the example under analysis, $k = k' = 0$. In either

case, the identification procedure is repeated for each integer value $a \in [2,20]$ in order to select the one that gives the best fit based on the comparison of the value obtained for the objective function (see Eq. (15)), but also for the in-plane evolutions of both stresses and *r*-values. This step is particularly important when stress values from compression experimental test are used, but no compression *r*-values are available (*i.e.* $k \neq 0$ and $k' \neq 0$). In this case, it is known that the values predicted for the compression *r*-values may have odd evolutions or even no physical meaning (*e.g.* $r < 0$ (Raemy et al., 2017)). Thus, their in-plane evolution must also be carefully monitored and taken into account when selecting the a value. The following section presents a brief description of the general algorithm adopted for this yield criterion.

4.2 Algorithm implemented for the CPB06ex2 yield criterion parameters identification

The algorithm for the identification of the CPB06ex2 anisotropy parameters considers a vector for the set of anisotropy parameters $\mathbf{A} = \{k, \mathbf{C}, k', \mathbf{C}'\}$ of the objective function given in Eq. (15). The exponent a is included in the identification procedure due to the increased flexibility of the yield criterion for increasing values of this parameter. Thus, the algorithm considers integer values of $a \in [2,20]$. For each value of a, the Nelder–Mead (downhill simplex) method is applied sequentially for k, $\mathbf{C}$, k' and $\mathbf{C}'$ in order to generate, in each iteration I, a set of parameters $\mathbf{A}^{\mathrm{I}}$ to be evaluated by the objective function. The general structure of the strategy developed is presented in Table 2, highlighting this sequential approach which to be more efficient than when considering all the parameters at the same time.

Table 2. Strategy implemented in the DD3MAT code for the CPB06ex2 yield criterion parameters identification.

Begin

- Define the maximum number of iterations, *ItnMAX*
- Read experimental values

For $a = 2$ to 20

Initialize $\mathbf{C}$ and $\mathbf{C}'$ to the isotropic solution

Initialize $k = 0$ and $k' = 0$

Do While $\left| F\left(\mathbf{A}^{\mathrm{I}}\right) - F\left(\mathbf{A}^{\mathrm{I-1}}\right) \right| > 10^{-14}$ or $\mathrm{I} \leq ItnMAX$

Varying only k *in* $\mathbf{A}^{\mathrm{I}}$

Apply the downhill simplex method to generate a new set of vertices, $\mathbf{A}^{\mathrm{I}}$

Select the $\min F\left(\mathbf{A}^{\mathrm{I}}\right)$

Varying only $\mathbf{C}$ *in* $\mathbf{A}^{\mathrm{I}}$

Apply the downhill simplex method to generate a new set of vertices, $\mathbf{A}^{\mathrm{I}}$

Select the $\min F\left(\mathbf{A}^{\mathrm{I}}\right)$

Varying only k' *in* $\mathbf{A}^{\mathrm{I}}$

Apply the downhill simplex method to generate a new set of vertices, $\mathbf{A}^{\mathrm{I}}$

Select the $\min F\left(\mathbf{A}^{\mathrm{I}}\right)$

Varying only $\mathbf{C}'$ *in* $\mathbf{A}^{\mathrm{I}}$

Apply the downhill simplex method to generate a new set of vertices, $\mathbf{A}^{\mathrm{I}}$

Select the $\min F\left(\mathbf{A}^{\mathrm{I}}\right)$

End Do

Write $\mathbf{A} = \{k, \mathbf{C}, k', \mathbf{C}'\}$ and a

End

End

5 Finite element simulations of the circular cup

5.1 Finite element model

The numerical simulations of the cup drawing are performed with the in-house implicit finite element code DD3IMP (Menezes and Teodosiu, 2000), which has been specifically developed to simulate sheet metal forming processes (Oliveira et al., 2008). The kinematic description of the blank large deformation and rotation is described by an updated Lagrangian formulation. The forming tools are considered rigid bodies with its surfaces modeled by Nagata patches (Neto et al., 2014), while the nodal normal vectors required for the contact surfaces smoothing approach are evaluated through the IGES file using the algorithm proposed by Neto et al. (2013). Due to geometrical and material

symmetries, only a quarter of the global structure is modeled. The sheet is discretized with 8-node hexahedral finite elements, combined with a selective reduced integration technique (Hughes, 1980). The adoption of solid elements allowing an accurate evaluation of the contact forces and through-thickness stress and strain gradients during deformation in the can-making process (Teodosiu et al., 1995). The contact with friction conditions are described by the classical Coulomb's law. The sheet's in-plane discretization is presented in Figure 3, which considers three layers of finite elements in the thickness direction.

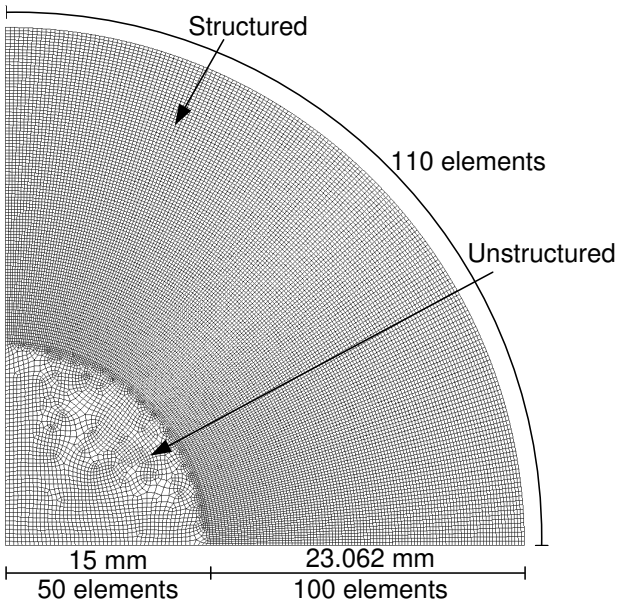

Figure 3. In-plane blank sheet discretization (3 layers of finite elements), comprising 84120 nodes and 62367 finite elements.

5.2 Material constitutive behavior model

The mechanical behavior of the AA3104 aluminum alloy is assumed to be isotropic in the elastic regime, being described by the Young's modulus, E, and the Poisson ratio, υ, with the corresponding values presented in Table 1. An associated flow rule is considered, meaning that the plastic strain increment vector is normal to the yield surface.

Note that the CPB06ex2 formulation guarantees that the yield stress, Y_0, considered is always equal to the one obtained for the uniaxial tensile test performed along the rolling direction. Therefore, previous results indicate that the value proposed for Y_0 defined by the hardening law should be in accordance with the yield stress in tension for the RD (σ_0^T), to enable an accurate description of the in-plane yield stress directionalities (Barros et al., 2015b).

The weighting coefficients considered for the CB2001 are $w_{r_\theta} = 0.1$ for $\theta \in [0,45]$, $w_{r_\theta} = 0.3$ for $\theta \in [60,90]$ and $w_{r_b} = 0.2$ for the anisotropy coefficients. For the yield stresses, $w_{\sigma_\theta^T} = 2.0$ for $\theta \in [0,45]$, $w_{\sigma_{60}^T} = 10$, $w_{\sigma_{75}^T} = w_{\sigma_{90}^T} = 20$ and $w_{\sigma_b} = 2.0$. In the case of the CPB06ex2, the weighting coefficients are $w_{r_\theta} = 0.1$ for $\theta \in [0,90]$, $w_{\sigma_\theta^T} = 2.0$ for $\theta \in [0,90]$, $w_{r_b} = 0.1$ and $w_{\sigma_b} = 1.0$. This set of weighting coefficients was tested for each integer value $a \in [2,20]$, leading to the selection of the exponent value $a = 12$.

Figure 4 presents the comparison between the experimental and predicted in-plane distributions for the *r*-values and yield stresses, for the considered yield criteria. The predicted *r*-values evolution presents negligible differences between both yield criteria for angles between the RD and 45º, with slight difference between 45º and 90º. In fact, although the CB2001 presents a very good prediction, the CPB06ex2 prediction is more accurate. Regarding the yield stresses directionalities, globally both yield criteria reproduce the evolution of the experimental results. Again, as for the *r*-values, the CPB06ex2 yield criterion is able to more faithfully represent the yield stresses directionalities. From the authors' experience, these slight differences are not expected to have a significant impact on the trend predicted for the earing profiles.

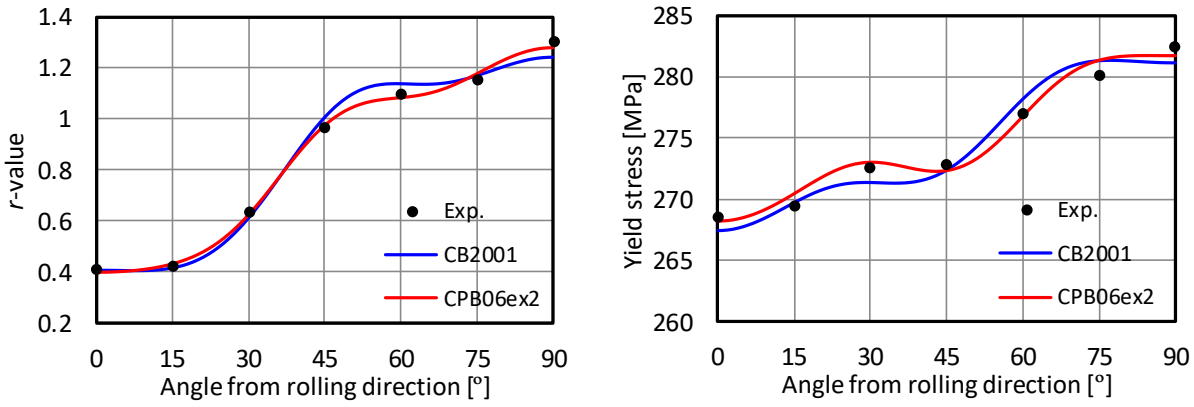

Figure 4. Experimental and predicted: (a) *r*-values and (b) yield stresses for the 3104 aluminum alloy considering the best fit for the CB2001 and CPB06ex2.

Figure 5 (a) presents the yield surfaces predicted for both yield criteria in the $\sigma_1 - \sigma_2$ plane (with $\sigma_3 = 0$), for increasing values of the shear stress σ_{12} component. For the surfaces corresponding to a null value of the shear stress ($\sigma_{12} = 0$), both yield criteria present approximate shapes, with the major differences occurring in the first quadrant,

between 45º and 90º, and in the fourth quadrant, around 215º. With increasing values of the shear stress, the differences between the corresponding surfaces become less pronounced except in the fourth quadrant, again at around 215º. Figure 5 (b) presents the yield surfaces predicted for both yield criteria in the $\sigma_1 - \sigma_3$ plane (with $\sigma_2 = 0$), highlighting that the major differences occur in the first and third quadrant. Regarding the biaxial values, Table 3 presents the comparison between the experimental and the numerically predicted values for the AA3104 aluminum alloy. In fact, both yield criteria show a good agreement with the experimental results for both the σ_b and the r_b values, which is visible when comparing the outermost surfaces represented in Figure 5 (a).

Table 3. Experimental and numerically predicted biaxial yield stress and anisotropy coefficient values for the AA3104 aluminum alloy.

	σ_b	r_b
Experimental	310.00	0.620
CB2001	308.48	0.620
CPB06ex2	310.50	0.620

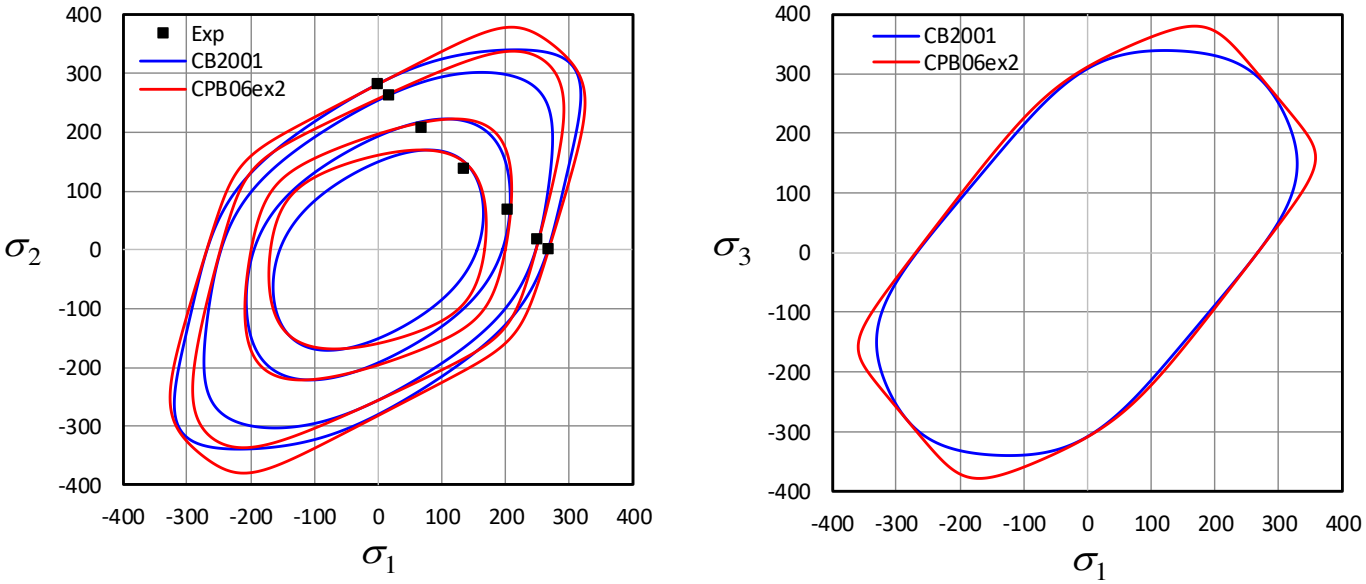

Figure 5. Predicted yield surfaces for both yield criteria in the: (a) $\sigma_1 - \sigma_2$ plane (with $\sigma_3 = 0$), for increasing values of the shear stress σ_{12}, such that: $\sigma_{12} = 0$; $\sigma_{12} = 0.250Y_0$; $\sigma_{12} = 0.433Y_0$ and $\sigma_{12} = 0.50Y_0$ and (b) $\sigma_1 - \sigma_3$ plane (with $\sigma_2 = 0$). Note that this corresponds to the material frame: $1 \equiv \text{RD}$, $2 \equiv \text{TD}$ and $3 \equiv \text{ND}$.

A resume of the parameters obtained for both yield criteria can be found in Table 4, together with the parameters for the Voce hardening law, which were used for the numerical simulation of the cup drawing. The exponent value used for the CPB06ex2 yield criterion was considered $a = 12$.

Table 4. Identified parameters for the AA3104 aluminum alloy for both yield criteria (a_5, a_6 and b_k $(k = 6, 7, 8, 9, 11) = 1.0$) and $C_{11} = C_{44} = C_{55} = C'_{11} = C'_{44} = C'_{55} = 1.0$), and material parameters of the Voce isotropic hardening law

CB2001	a_1	a_2	a_3	a_4			c
	1.0880	0.7545	1.1437	0.983174			0.4509
	b_1	b_2	b_3	b_4	b_5	b_{10}	
	4.8059	-0.1392	0.741261	-2.0292	-1.5681	0.6667	
CPB06ex2 ($a = 12$)	C_{22}	C_{33}	C_{66}	C_{23}	C_{13}	C_{12}	k
	1.0346	1.1889	1.1271	0.2065	0.2911	0.1758	0.0000
	C'_{22}	C'_{33}	C'_{66}	C'_{23}	C'_{13}	C'_{12}	k'
	1.1488	0.7752	-0.9834	0.1332	-0.2791	0.0427	0.0000
Voce (isotropic)	Y_0 [MPa]		Y_{sat} [MPa]		C		
	268.25		340.05		18.251		

Previous studies indicate that the cylindrical cups earing profile is dictated by the *r*-values and yield stresses directionalities, based on the knowledge of the stress states present in the rim, as shown in Figure 6 (Yoon et al., 2011). Assuming a cylindrical coordinate system (r, θ, z), it can be assumed that the outer surface of the rim is submitted to a compression stress state in the circumferential direction θ, when neglecting the influence of the blank-holder force. This means that, when considering a symmetric behavior for tension and compression stress states, the behavior of the rim in the direction defined by θ (to the RD) is controlled by the material tensile properties in the direction defined by $90 - \theta$, as highlighted in Figure 6. On the other hand, the inner surface of the rim is submitted to a tensile stress state in the radial direction r, while the in-between material points are submitted to stress states located in the second and fourth quadrant in the $\sigma_1 - \sigma_2$ plane (with $\sigma_3 = 0$), as exemplified in Figure 6 (b). Based on these assumptions, Yoon et al. (2011) proposed an analytical function to estimate the cup height evolution. It was also shown that these assumptions are helpful to understand the influence of the contact conditions in the stress state in the rim and, consequently, in the earing profile (Barros et al., 2015a). Based on this knowledge and in the analysis of

Figure 5 (a), small differences between both yield criteria in the predicted earing profile are expected.

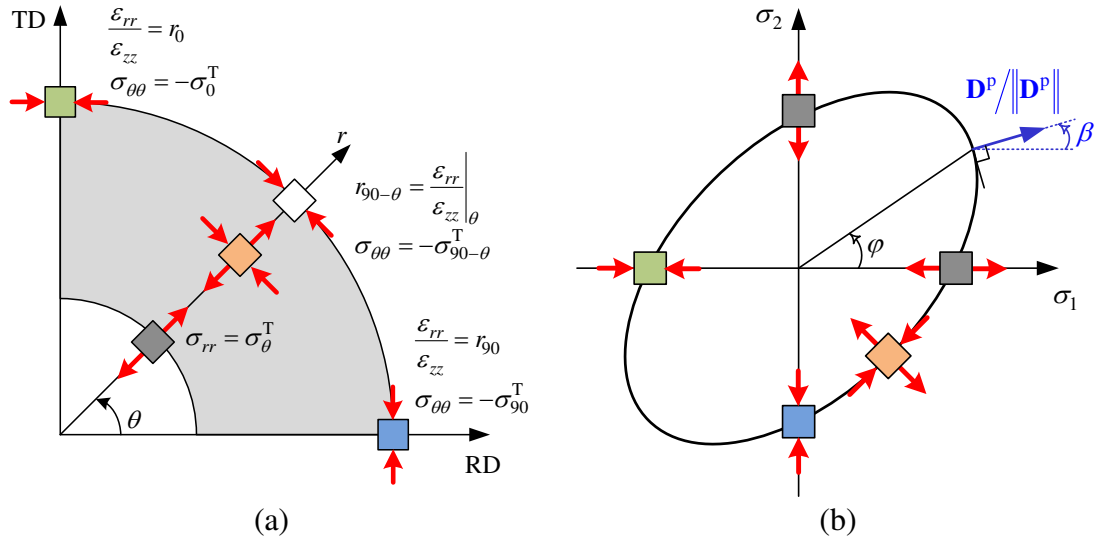

Figure 6. (a) Stress states on the rim and (b) stress states on the element on the yield surface (adapted from Yoon et al. (2011)).

In the following section, the comparison between experimental and numerical results is performed. This analysis is complemented with the study of the stress and strain states in the cup's rim, in order to understand the influence of the yield *locus* in the numerical predictions.

6 Results and discussion

In this section, the comparison between experimental and numerical predictions for both yield criteria is presented, for both punch force evolution and earing profiles. Thickness evolutions are also presented along some pre-determined planes, for further highlighting the differences between both yield criteria. Three friction coefficients, $\mu = 0.05$, $\mu = 0.03$ and $\mu = 0.00$ are considered for the contact between the sheet and the tools, labeled as "$\mu 0.05$", "$\mu 0.03$" and "$\mu 0.00$", respectively. This enables also an analysis of the blank-holder force distribution to understand the influence of the friction conditions during the cup forming.

6.1 Earing profile

The earing profile is measured for the fully drawn cup considering the height measured from the cup's bottom. The comparison between experimental and numerical profiles is presented in Figure 7. The total number of ears is correctly predicted by both yield criteria, confirming the expected results based on the similar in-plane *r*-values and yield stress

directionalities. For angles between the rolling direction and 45º, the earing profile is globally very well predicted in both amplitude and location of the ears, again for both yield criteria. The CB2001 yield criterion overpredicts the earing profile for all the friction conditions, from the RD to the TD. With the decrease of the friction coefficient, the profile height between 45º and the TD tends to decrease, becoming closer to the experimental results. Regarding the CPB06ex2 yield criterion, the profile height is slightly underpredicted for angles between the RD and 45º. The decrease of the friction coefficient, as in the CB2001 case, tends to lower the profile height for angles between 45º and the TD. In any case, the numerical predictions from the CPB06ex2 are more accurate than the ones for the CB2001, mainly for the friction condition "μ0.03".

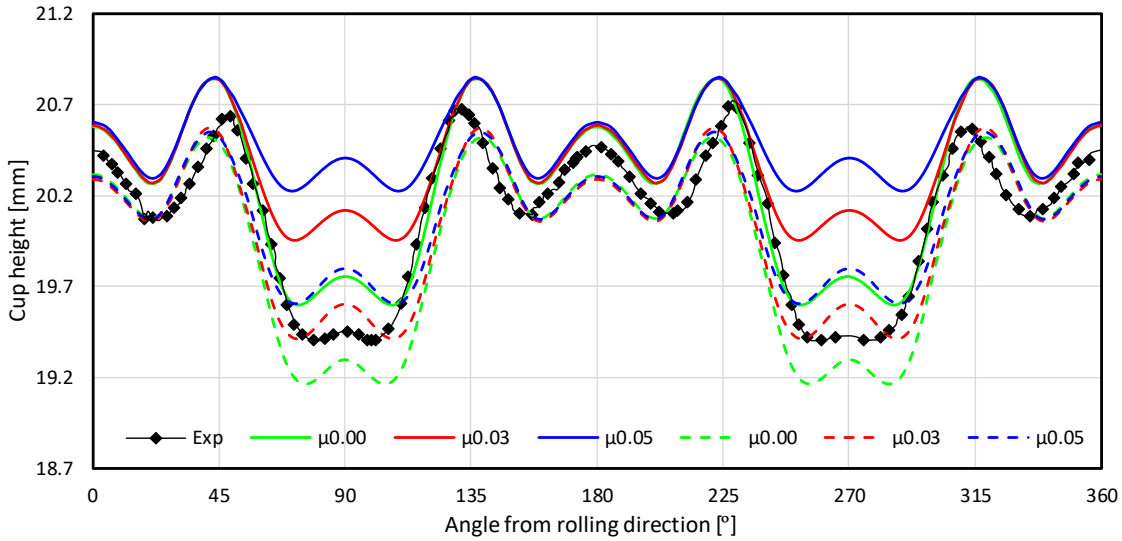

Figure 7. Comparison between experimental and numerically predicted earing profiles for the CB2001 (solid lines) and CPB06ex2 (dashed lines) yield criteria considering three values of the friction coefficient.

6.2 Punch force evolution

The comparison between experimental and numerically predicted punch force evolution for both yield criteria is presented in Figure 8. Globally, both yield criteria correctly predict the evolution of the punch force with its displacement, including the instant were loss of contact between the sheet and the blank-holder occurs, which is at around 19 mm. For the same friction conditions, the CB2001 predicts a lower punch force throughout the punch displacement, when compared with the CPB06ex2. This is in agreement with the fact that the CB2001 yield surfaces are always located in the interior of the ones defined by the CPB06ex2, as shown in Figure 5. As expected, lower friction coefficients yields lower punch force evolutions. Note that, with the decrease of the friction coefficient, the difference between punch force evolutions between both yield criteria becomes smaller.

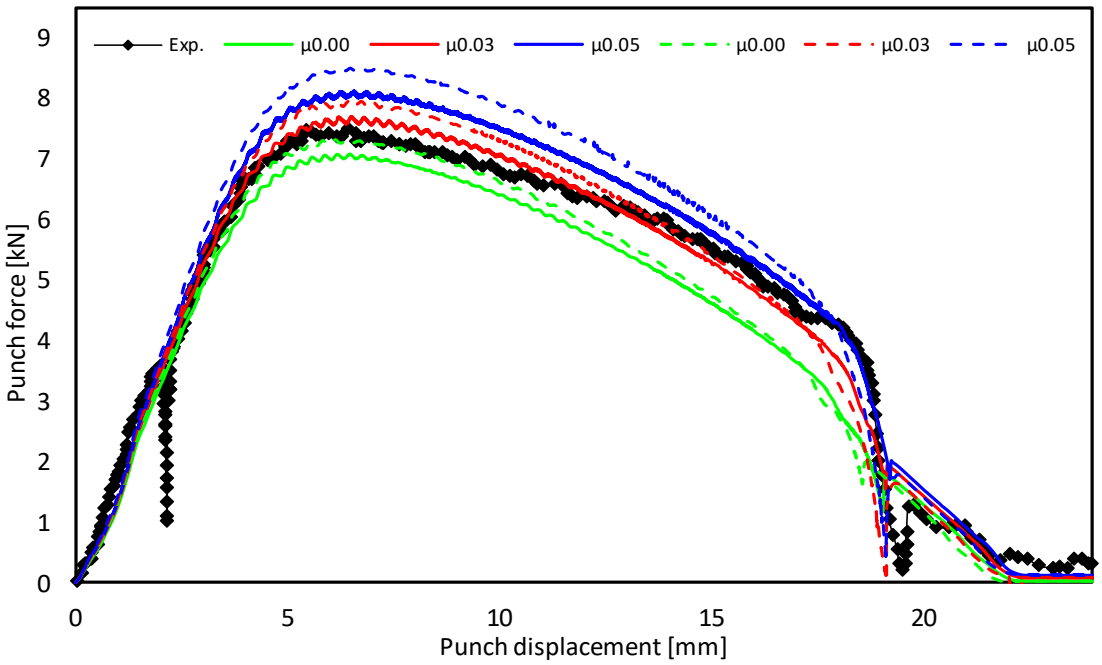

Figure 8. Comparison between experimental and numerically predicted punch force evolutions for the CB2001 (solid lines) and CPB06ex2 (dashed lines) yield criteria considering three values of the friction coefficient.

6.3 Thickness profiles

In this section, the thickness profiles for some predetermined planes are analyzed for the fully drawn cup. Figure 9 presents the planes considered for the thickness analysis. The thickness evolution with the angle from the RD, for the plane $z = 16.5$ mm, is presented in Figure 10 for both yield criteria considering the three friction conditions. The evolution is similar for both the CB2001 and CPB06ex2 yield criteria, with a lower thickness for angles closer to the RD and higher for angles closer to the TD. The CB2001 predicts lower thickness values when comparing with the CPB06ex2. This is related to the earing profiles predicted (Figure 7) since to a higher cup's height corresponds a lower wall thickness. The friction conditions influence both yield criteria in the same manner, *i.e.* to a lower friction coefficient corresponds higher thickness values and, as shown before, lower cup heights. The global trend is consistent with the experimental results.

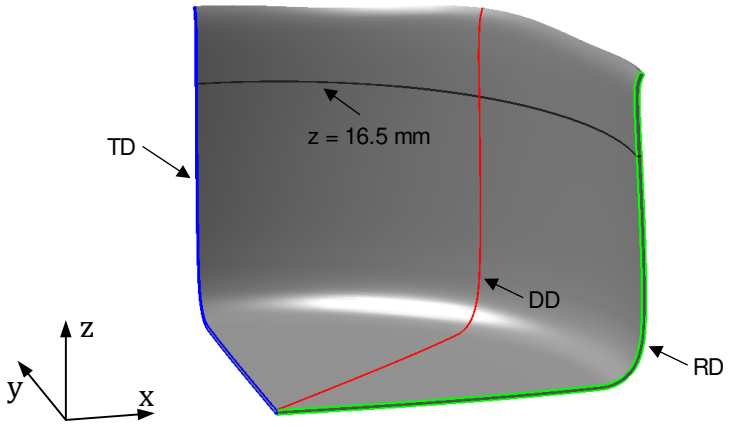

Figure 9. Planes considered for the thickness analysis, with correspondence as RD – green line, DD – red line; TD – blue line; and $z = 16.5$ mm – black line.

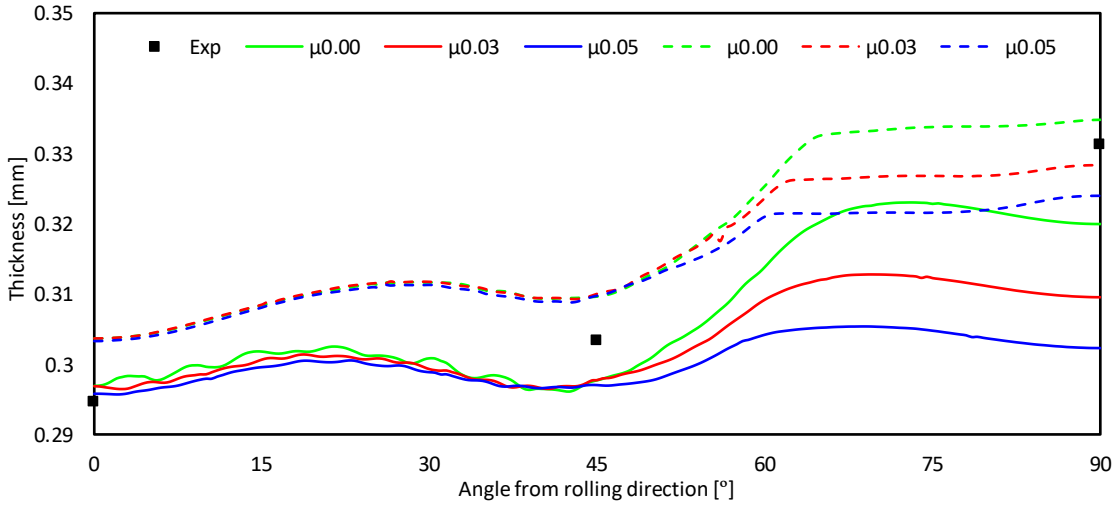

Figure 10. Thickness evolution with the angle from the rolling direction, measured for a plane $z = 16.5$ mm from the bottom of the cup, for the CB2001 (solid lines) and CPB06ex2 (dashed lines) yield criteria considering three values of the friction coefficient.

In order to further analyze the differences in thickness distributions for both yield criteria and friction conditions, the thickness evolution for the RD, DD and TD are shown. Figure 11, Figure 12 and Figure 13 present the thickness evolution considering a friction coefficient $\mu = 0.05$, $\mu = 0.03$ and $\mu = 0.00$, respectively. The differences between the yield criteria are small for both the RD and the DD. The major difference appears for the TD direction, with the thickness being higher for the CPB06ex2 yield criterion. This is consistent with the lower cup height, for this criterion, than the one with the CB2001 for the same conditions. This trend is consistent with the experimental thickness evolution data. The differences occurring for the TD are more pronounced for higher frictions. Moreover, the CPB06ex2 yield criterion presents a smaller sensitivity to the friction

coefficient for the TD, with the higher thickness value always reaching about 0.37 mm. The lower thickness value corresponds to the transition between the punch radius and the vertical wall (about 26 mm), whatever the considered conditions.

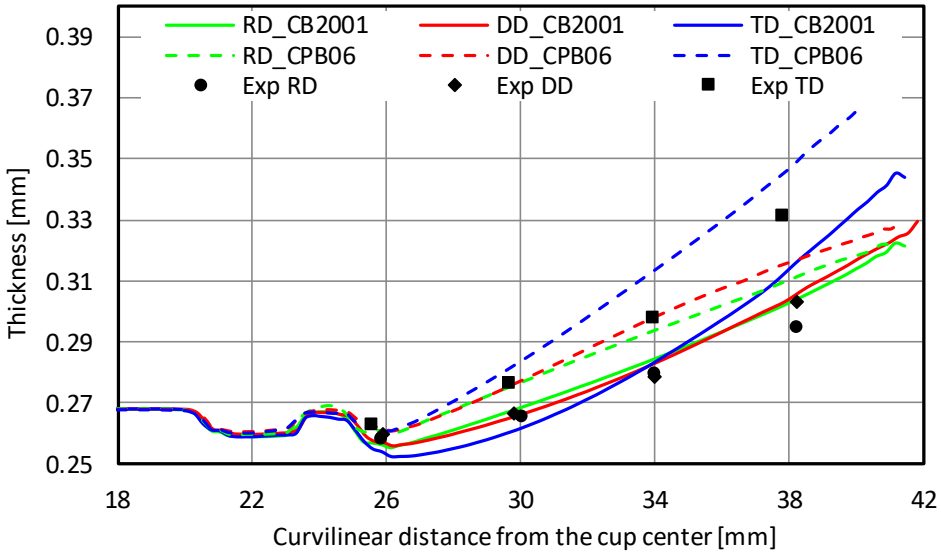

Figure 11. Thickness evolution with the initial material position for the CB2001 (solid lines), CPB06ex2 (dashed lines) yield criteria and experimental data (friction coefficient $\mu = 0.05$).

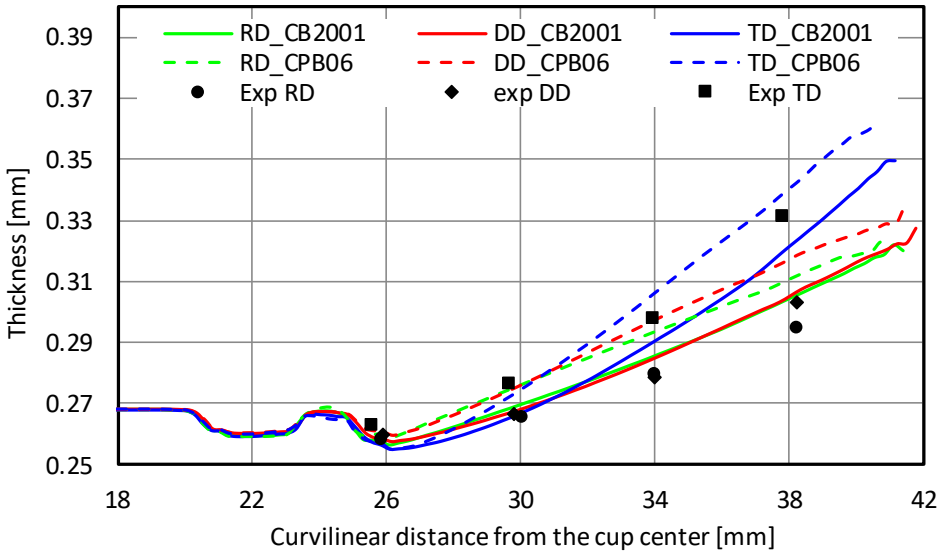

Figure 12. Thickness evolution with the initial material position for the CB2001 (solid lines), CPB06ex2 (dashed lines) yield criteria and experimental data (friction coefficient $\mu = 0.03$).

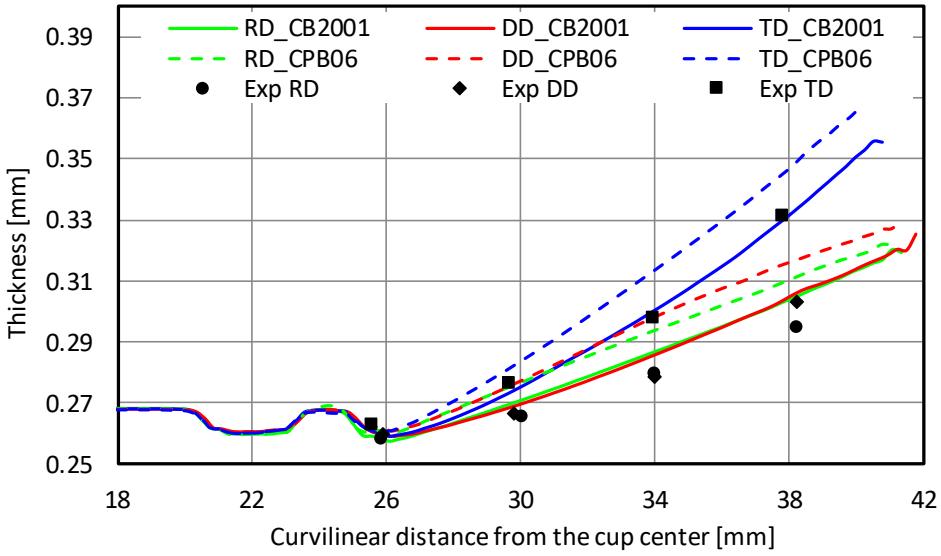

Figure 13. Thickness evolution with the initial material position for the CB2001 (solid lines), CPB06ex2 (dashed lines) yield criteria and experimental data (friction coefficient $\mu = 0.00$).

6.4 Blank-holder force distribution

In order to understand the interdependence between the process conditions and the material's orthotropic behavior, the blank-holder force distribution for an instant corresponding to a punch displacement of 15 mm is considered for analysis. Figure 14 shows these results for both yield criteria and the three friction conditions considered. Common for all the cases under analysis is the concentration of the force for angles between 60º and 90º to the RD. This can be related to the lower *r*-values (lower than 1.0) for angles between 0º and 45º to the RD, as seen in Figure 4. In fact, the behavior of the rim for an angle θ is dictated by the material properties in the direction defined by $90-\theta$. Note that the blank-holder is controlled by an imposed force, *i.e.* the total force should be equal for any case. For all friction conditions, the CB2001 yield criterion presents a smoother distribution of the contact forces. Since the blank-holder force is concentrated over the same area, the friction coefficient will have a direct impact in the material flow mainly in that zone, meaning that for a lower friction coefficient the material flow will be higher and, consequently, the cup's height will be lower. This is consistent with the earing profiles shown in Figure 7. Figure 15 further highlights the blank-holder's force concentration for angles between 60º and 90º. Whatever the yield criterion adopted, the small values of contact force between 0º and 60º seem to corroborate the small influence of the friction coefficient for angles between 0 and 45º,

for both the cup height (see Figure 7) and the thickness evolution (see Figure 10). Note that the force distribution highlights the existence of small frequency wrinkles in the circumferential direction of the rim, which are visible in the experimental cup (see Figure 2).

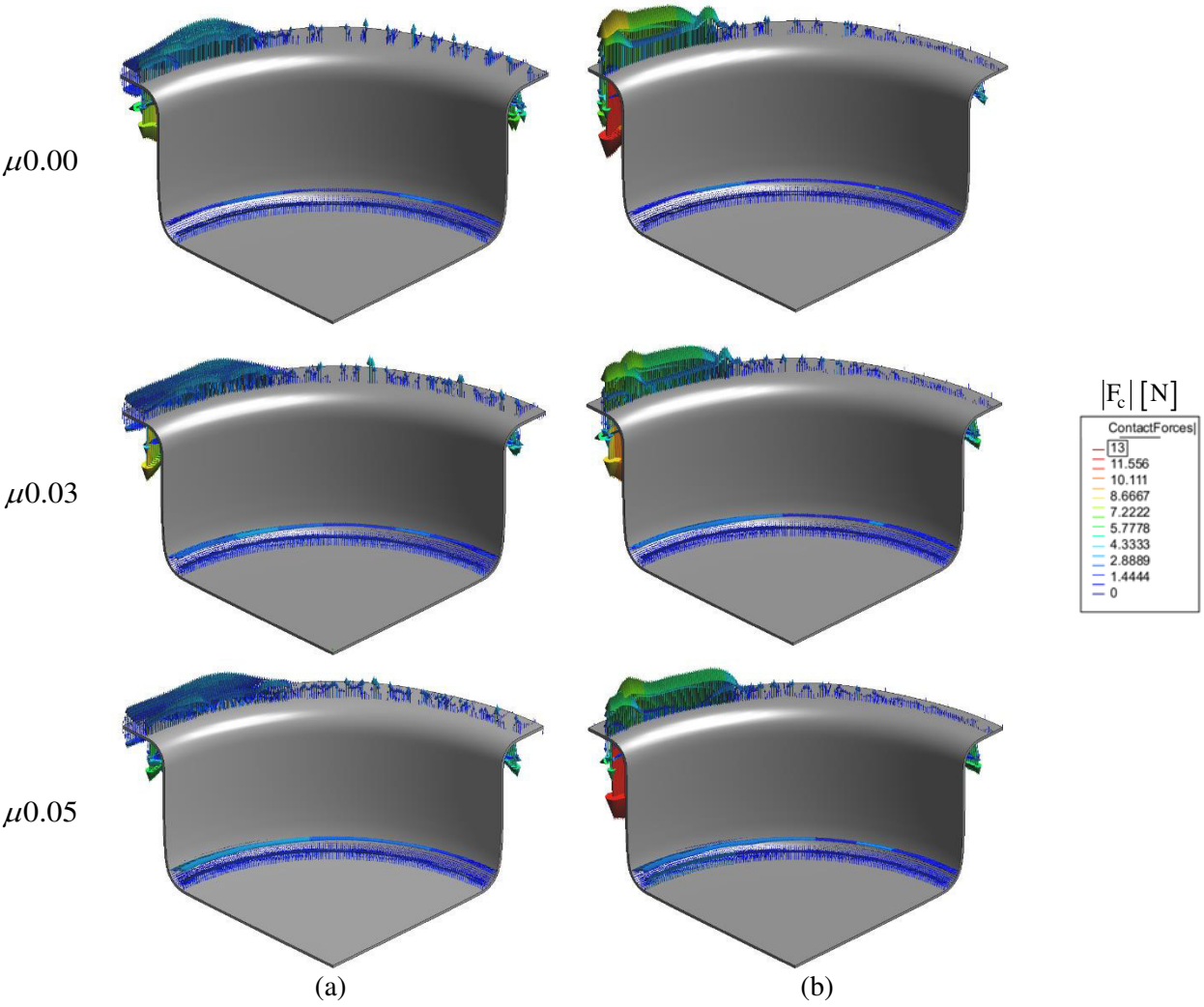

Figure 14. Numerical blank holder force distribution (F_c) for (a) CB2001 and (b) CPB06ex2 yield criteria considering three values of the friction coefficient. Punch displacement of 15 mm. Force in [N].

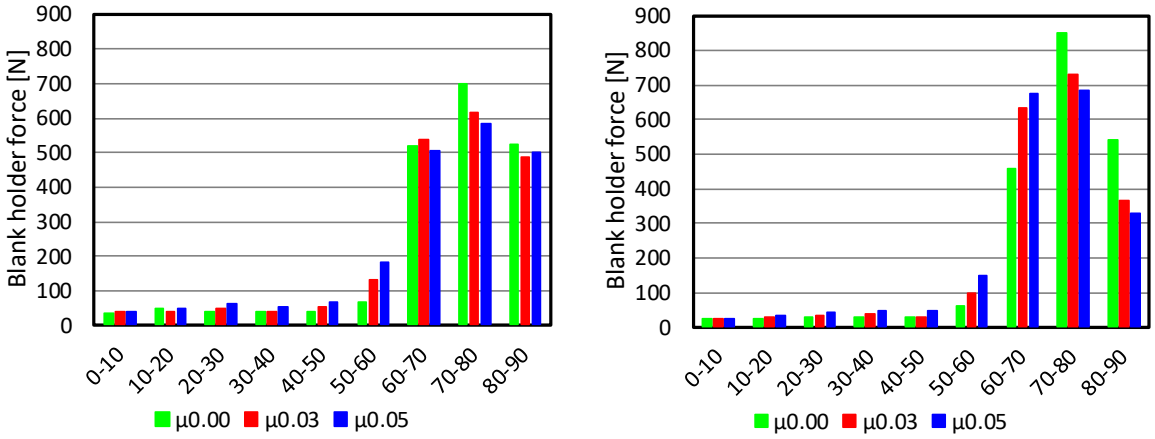

Figure 15. Numerical blank holder force, in 10º intervals, for the (a) CB2001 and (b) CPB06ex2 yield criteria considering three values of the friction coefficient. Punch displacement of 15 mm.

6.5 Stress and strain distributions in the rim

Figure 16 presents the stress distribution in the rim for both yield criteria, considering a cylindrical coordinate system (r, θ, z). The results presented correspond to the ones obtained for the friction coefficient of 0.03 and a punch displacement of 5 mm. The stress components shown in the rim are the circumferential, $\sigma_{\theta\theta}$, the radial, σ_{rr} and the axial, σ_{zz}, since the other components can be neglected. The results show that the distributions are quite similar for both yield criteria, particularly between 0º and 60º, for which the σ_{zz} component is very small. These results are in agreement with the ones presented in Figure 14, showing that the force distribution maintains a similar trend throughout the forming process.

Based on the stress state analysis presented in Figure 6, strain ratios were analyzed along two circumferential lines in the rim, which are schematically represented in Figure 17. Considering that the strain along the radial direction corresponds to ε_{22} (minor in-plane strain) and along the thickness direction to ε_{33}, the ratio between them is shown in Figure 18 for three values of punch displacement.

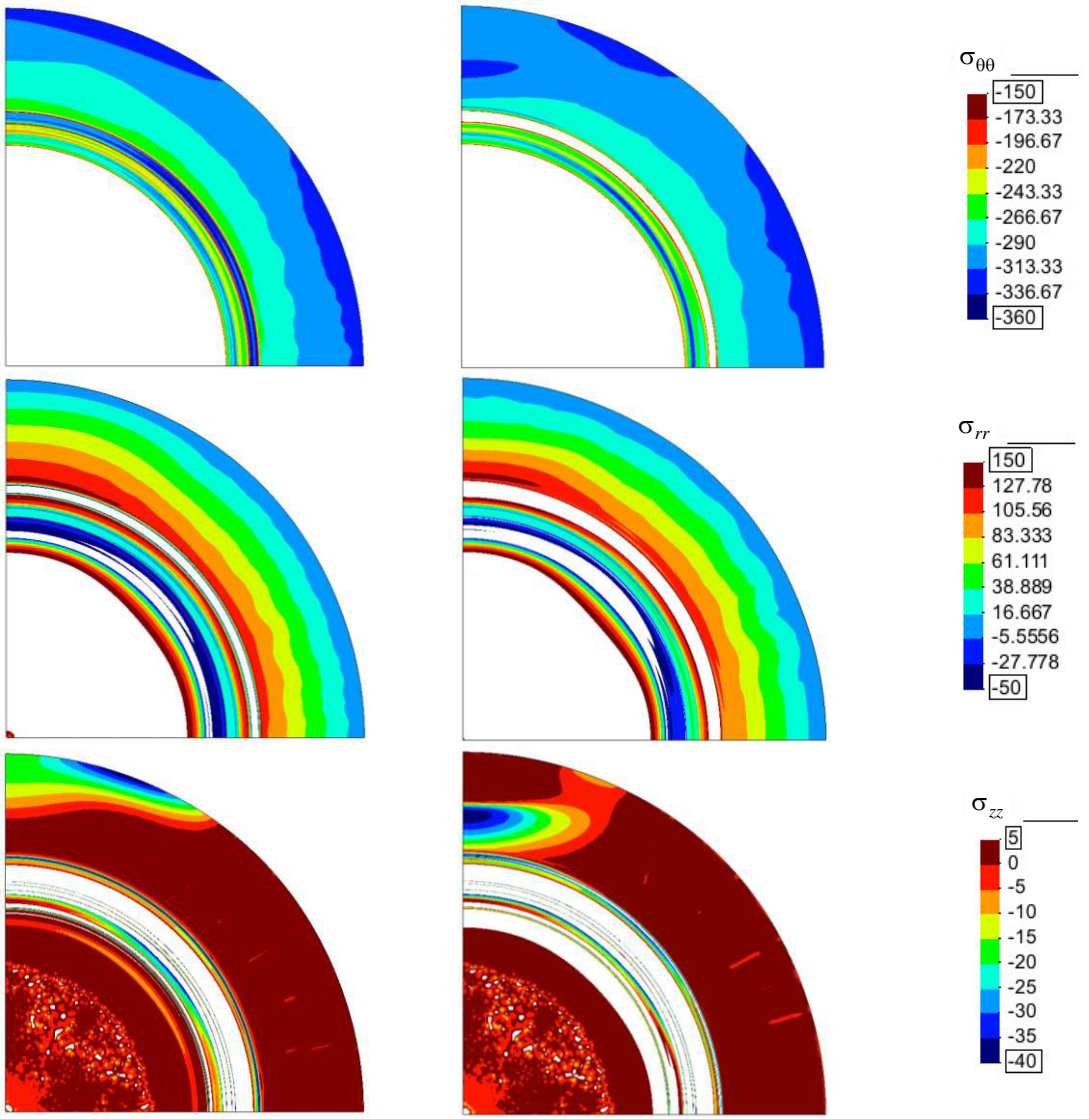

Figure 16. Numerically predicted stress distribution for (a) CB2001 and (b) CPB06ex2 yield criteria considering the friction coefficient value of 0.03. Punch displacement of 5mm. Stress range expressed in [MPa].

This figure also shows the numerical predictions for the in-plane distribution of the *r*-values, with the yield criterion under analysis (see Figure 4 (a)). These results were transformed, considering that the behavior of the rim in the direction defined by θ (to the RD) is controlled by the material tensile properties in the direction defined by $90-\theta$ (see Figure 6). Regarding the outer line of the rim (R1), the comparison between the model's *r*-values and the numerically predicted strain ratios confirms that these material points are subjected to a compression stress state in the circumferential direction θ. This is particularly evident for the CPB06ex2, for which the same trend is recovered, which correlates with the stress distributions shown in Figure 16. The same is valid for the CB2001, but only between 0º and about 50º. From this value until 90º, the numerically

predicted strain ratio is higher. This may be explained by the influence of the compression stress component σ_{zz}, as shown in Figure 16 (see also Figure 14). This changes the position of the material points from a compression stress state $(\sigma_1 = -\sigma_{\theta\theta}; 0)$ to $(\sigma_1 = -\sigma_{\theta\theta}; \sigma_3 = -\sigma_{zz})$, *i.e.* on the third quadrant of the yield surface shown in Figure 5 (b). This influence of the compression stress component has been previously reported in Barros et al. (2015a).

Regarding the inner line of the rim (R2), the comparison between the modeled *r*-values and the numerically predicted strain ratios lead to the same evolution for the CPB06ex2, although this line is submitted to a radial stress component σ_{rr} (see Figure 16). For this yield criterion, the stress components σ_{rr} or σ_{zz} seem to have a negligible impact in the strain ratios. For the CB2001 there is a positive shift of the strain ratios, even for material points in the area where σ_{zz} is null, *i.e.* between 0º and 60º (see Figure 16). In fact, these material points are submitted to a tensile stress component σ_{rr}, as shown in Figure 16. This changes the position of the material point at RD from the compression stress state $(0; \sigma_2 = -\sigma_{\theta\theta})$ to $(\sigma_1 = \sigma_{rr}; \sigma_2 = -\sigma_{\theta\theta})$, *i.e.* to the fourth quadrant of the yield surface shown in Figure 5 (a). On the other hand, the tensile stress component σ_{rr} changes the position of the material point at TD from the compression stress state $(\sigma_2 = -\sigma_{\theta\theta}; 0)$ to $(\sigma_1 = -\sigma_{\theta\theta}; \sigma_2 = \sigma_{rr})$, *i.e.* to the second quadrant of the yield surface.

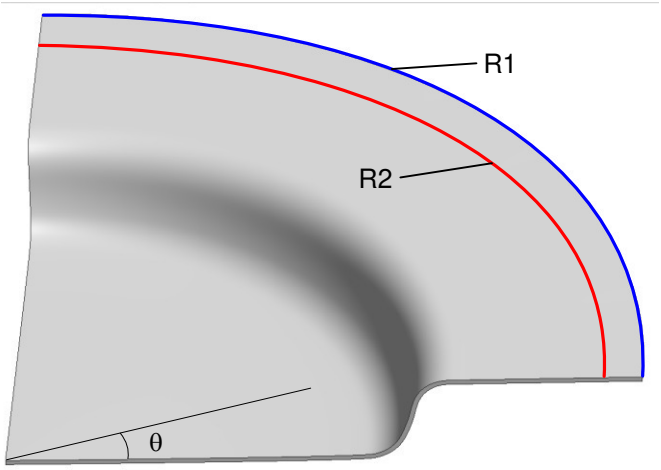

Figure 17. Lines considered for the strain ratio analysis, with correspondence as outer rim (R1) – blue line and inner rim (R2) – red line.

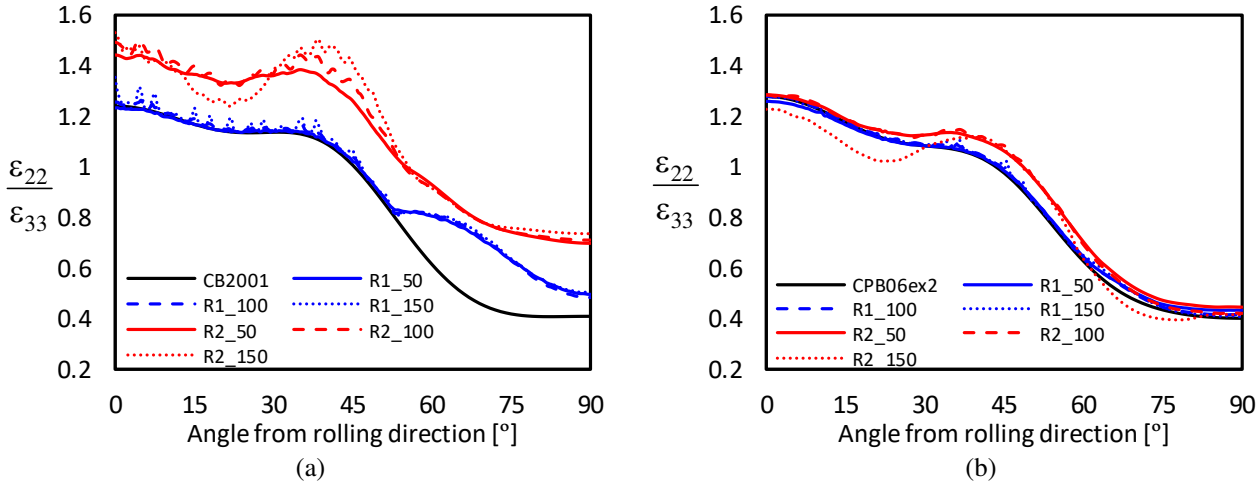

Figure 18. Numerical strain ratio $\varepsilon_{22}/\varepsilon_{33}$ with the angle from the rolling direction for the (a) CB2001 and (b) CPB06ex2 yield criteria, considering a friction coefficient of 0.03 and values of the punch displacement of 5, 10 and 15 mm.

The results show that the stress distribution for material points located in an area of the rim between 0º and 60º to RD is similar for both yield criteria (see Figure 16), but there are non-negligible differences in the strain distributions (see Figure 18). To understand these differences, the direction of the plastic strain rate β was calculated for each loading direction φ, following the definitions given in Figure 6 and commonly adopted by Kuwabara (2007). This analysis was performed for both yield surfaces shown in Figure 5. Figure 19 (a) shows a comparison between the measured directions of the plastic strain rate (evaluated from r_0 and r_{90} in Table 1) with those of the local outward vectors normal to the theoretical yield *locus* in the $\sigma_1-\sigma_2$ plane (with $\sigma_3=0$) for both the CB2001 and CPB06ex2. Figure 19 (b) shows the local outward vectors normal to the theoretical yield *locus* in the $\sigma_1-\sigma_3$ plane (with $\sigma_2=0$) also for both yield criteria. The results highlight that the CPB06ex2 yield *locus* presents zones with a null slope, which can be related with the sharper global shape of the yield surface, when compared with the CB2001 (see also Figure 5). The strain ratios can also be evaluated based on the local outward vectors normal to the theoretical yield *locus*. In order to determine $\varepsilon_{22}/\varepsilon_{33}$, it is important to consider that ε_{22} is always the in-plane minor strain and impose the volume conservation condition. Figure 20 presents $\varepsilon_{22}/\varepsilon_{33}$, as predicted for both yield criteria, for the two yield *loci* analyzed in Figure 19. The range considered for the loading direction for the two yield *loci* is distinct.

For a material point located in the outer rim in the TD, the reference stress state is the compression along RD, corresponding to $\varphi = 180^{\circ}$ in Figure 19 (b). As previously mentioned, for this material point the influence of the blank-holder results in a stress state located in the third quadrant of the yield surface in the $\sigma_1 - \sigma_3$ plane (with $\sigma_2 = 0$) (see Figure 5 (b)). This corresponds to a slight increase of the loading direction φ. As shown in Figure 20 (b), both yield criteria predict an increase of the ratio $\varepsilon_{22}/\varepsilon_{33}$, but the CB2001 presents a higher variation for the same loading direction. This may explain the slight increase of $\varepsilon_{22}/\varepsilon_{33}$ predicted by the CB2001 for the outer rim (R1), for 90º to the RD (see Figure 18).

In case of an inner rim element (R2), the influence of the tensile radial stress component leads to different quadrants, depending on the material location. Considering a material point located in RD, the reference stress state is the compression along TD, corresponding to $\varphi = 270^{\circ}$ in Figure 19 (a). Thus, the tensile radial stress component contributes to a slight increase of the loading direction φ, *i.e.* a stress state located in the fourth quadrant. For a material point located in TD, the reference stress state is compression along RD, corresponding to $\varphi = 180^{\circ}$ in Figure 19 (a). Thus, the tensile radial stress component contributes to a slight decrease of the loading direction φ, *i.e.* a stress state located in the second quadrant. As shown in Figure 20 (a), in either case, the CPB06ex2 shows almost constant strain ratios, while for the CB2001 the strain ratio increases. This explains why, for the CPB06ex2, similar strain ratios are predicted whatever the radial position in the rim For the CB2001, a positive shift of the strain ratios is observed (see Figure 18). This analysis was performed only for material points located at RD and TD, but the yield l*ocus* predicted by both yield criteria for different locations in the rim presents a similar behavior, *i.e.* the CPB06ex2 leads to a sharper global shape when compared with the CB2001 (see also Figure 5). This explains the higher influence of the friction coefficient for the CB2001 than for the CPB06ex2 in the numerically predicted thickness evolution with the angle from the RD (see Figure 10). The increase of the friction coefficient leads to an increase of the tensile radial stress component, particularly in the rim area submitted to the compression stress induced by the blank-holder. The results analysis indicates that this leads to an increase of the ratio $\varepsilon_{22}/\varepsilon_{33}$, *i.e.* there is a decrease of the through thickness strain.

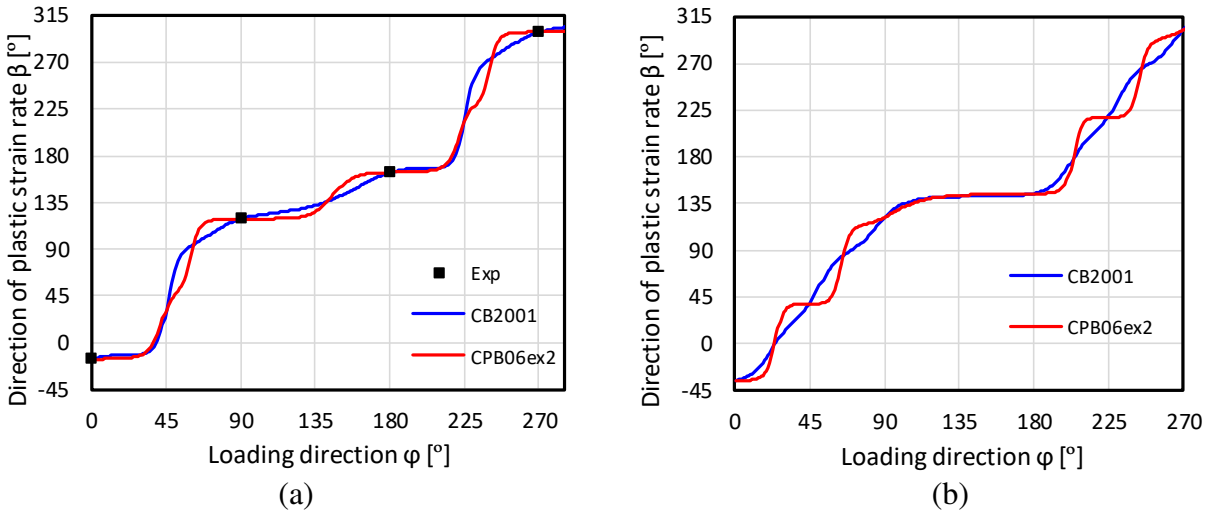

Figure 19. Directions of the plastic strain rates in function of the loading direction for the CB2001 and CPB06ex2 yield criteria in the: (a) $\sigma_1 - \sigma_2$ plane (with $\sigma_3 = 0$) (the black squares correspond to the experimental values); (b) $\sigma_1 - \sigma_3$ plane (with $\sigma_2 = 0$).

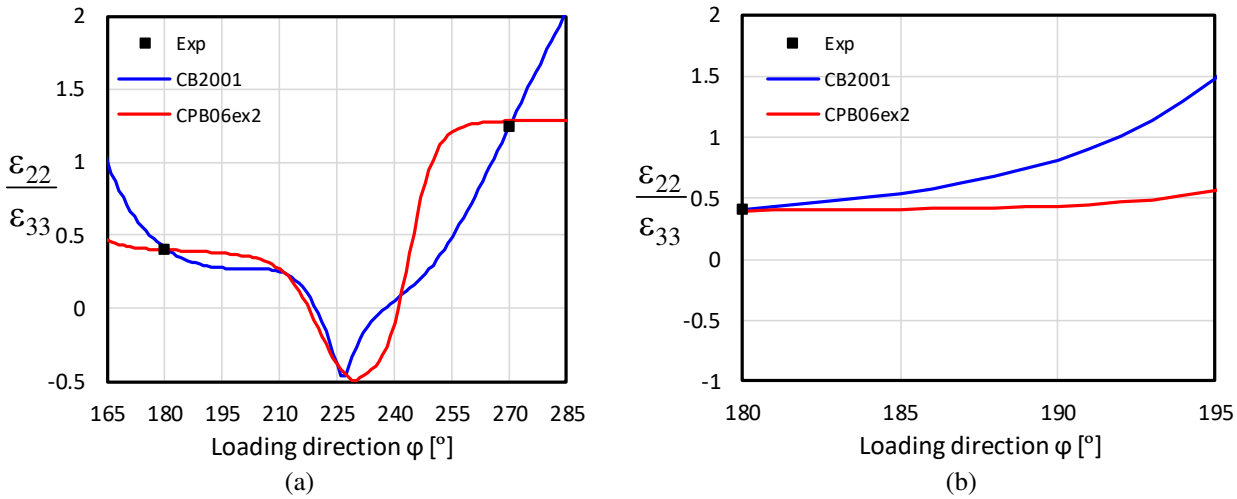

Figure 20. Strain ratio $\varepsilon_{22}/\varepsilon_{33}$ in function of the loading direction for the CB2001 and CPB06ex2 yield criteria in the: (a) $\sigma_1 - \sigma_2$ plane (with $\sigma_3 = 0$); (b) $\sigma_1 - \sigma_3$ plane (with $\sigma_2 = 0$) (the black squares correspond to the experimental values).

7 Conclusions

The cup drawing of an Alcoa AA3104 aluminum alloy was analyzed in this study, based on the knowledge of the experimental earing profiles and the thickness and punch force evolutions. Two highly flexible yield criteria are considered for describing the yielding of the material and its orthotropic behavior: CB2001 and CPB06ex2. The main details regarding the implementation of the CPB06ex2 in the finite element code DD3IMP are presented. The anisotropy parameters for both yield criteria were identified using the

DD3MAT in-house code. In this context, the strategy developed for the anisotropy parameters identification of the CPB06ex2 is also presented.

The numerical results show that the yield criterion selected influences the earing prediction, even though they predict similar in-plane yield stresses and *r*-values directionalities. This leads to a similar trend for the earing profile, with the same number of ears, but different average height and amplitude. In this context, three different values for the friction coefficient were studied: 0.00, 0.03 and 0.05. The results show that the increase of the friction coefficient leads to a higher cup for angles between 45º and TD, while the profile is unaffected for the remaining angles. The increase of the friction coefficient also leads to a smaller increase of the cup wall thickness observed only between 45º and TD, in agreement with the increase of the cup height. As a result of the material orthotropic behavior, it is shown that the blank-holder force is concentrated in a region between 60º to 90º, regardless of the yield criterion. Therefore, it is expected that the friction coefficient will have impact mainly in that region of the cup. Although the trend for the earing profile and for the thickness evolution is similar between both yield criteria, the influence of the friction coefficient is more remarked for the CB2001. Moreover, the thickness predicted for the cup wall is always lower in the results obtained with the CB2001. The results' analysis highlights that both yield criteria predict similar stress distributions in the cups' rim, but different strain ratios between the radial and the thickness direction. The yield *locus* defined by the CPB06ex2 yield criterion presents a sharper shape than the one defined by the CB2001, which means that in the later there are more regions in the stress space with a constant slope. This is highlighted by the comparison of the directions of the plastic strain rates, in function of the loading direction, predicted by both yield criteria. This explains the lower sensitivity of the CPB06ex2 yield criterion to small changes of the friction coefficient. The evaluation of the directions of the plastic strain rates also helps to evaluate the influence of small changes in the stress state in the strain ratio between the radial and the thickness direction. In this example, the increase of this strain ratio predicted by the CB2001 helps to explain why the predicted average cup height is always higher than the one obtained with the CPB06ex2, which presents a more constant value for this strain ratio.

The results confirm that the trend of the earing profile is mainly dictated by the in-plane yield stresses and *r*-values directionalities (Yoon et al., 2011). In fact, the *r*-values control the general trend of the earing (peaks, valleys) and the in-plane yield stresses control its magnitude. For a material presenting a strong orthotropic behavior, this

requires a flexible yield criterion and, consequently, a sufficiently large set of experimental results. Nevertheless, in case of components with a rim subjected to circumferential compression stress states, the experimental set available should not only cover the first quadrant of the stress space, corresponding to the biaxial tension stress state. In fact, it is important to accurately capture the directions of the plastic strain rates in the tension-compression stress states, in order to be able to predict the cup height. A yield criterion that is flexible enough to describe both the yield stresses and *r*-values directionalities, including the ones in compression, allows the description of the plastic strain rates also in compression-compression stress states, when experimental data is available.

Acknowledgements

This work was sponsored by national funds from the Portuguese Foundation for Science and Technology (FCT) via the project with reference PTDC/EMS-TEC/6400/2014 (POCI-01-0145-FEDER-016876) and by UE/FEDER funds through the program COMPETE 2020 under the projects CENTRO-01-0145-FEDER-000014 (MATIS) and UID/EMS/00481/2013-FCT under CENTRO-01-0145-FEDER-022083. The first author was also supported by a Ph.D. grant provided by the Portuguese Foundation for Science and Technology (FCT) with reference SFRH/BD/98545/2013. All supports are gratefully acknowledged. Moreover, the authors acknowledge Gabriela Vincze, Abel Dias dos Santos and Rui Amaral for the mechanical characterization and their help in some of the experimental procedures.

Appendix A: analytical expressions of the derivatives of the CPB06ex2 yield criterion

A. 1. This section is related to the calculations of the following quantities

$$\beta, \quad \mathbf{V} = \frac{\partial \bar{\sigma}}{\partial \boldsymbol{\sigma}}, \quad \mathbf{Q} = \frac{\partial^2 \bar{\sigma}}{\partial \boldsymbol{\sigma}^2}, \tag{16}$$

specifically related with the numerical implementation of the CPB06ex2 yield criterion in the FE solver DD3IMP.

The scalar β has to be evaluated whenever the effective stress state at the beginning of the time increment is elastic. It is determined with the consistency condition, such that

$$\Phi(\beta) = \bar{\sigma}(\boldsymbol{\sigma}'_0, \Delta\boldsymbol{\varepsilon}', \beta) - Y_I = 0\,, \tag{17}$$

where subscript I is the flow stress at the beginning of the time increment. β is the only unknown of this non-linear equation. Thus, the Newton-Raphson method is used to iteratively determine β, given by the relation

$$\beta^{i+1} = \beta^i - \frac{\Phi^i}{\Phi^{i\prime}}, \tag{18}$$

where i defines the iteration number. A schematic representation of the stress update algorithm is shown in Figure 21, where $\boldsymbol{\sigma}'^{trial}$ corresponds to the one obtained from Eq. (17), and subscripts 0 and F denote the deviatoric stress tensor at the beginning and at the end of the time increment $[t, t+\Delta t]$, respectively.

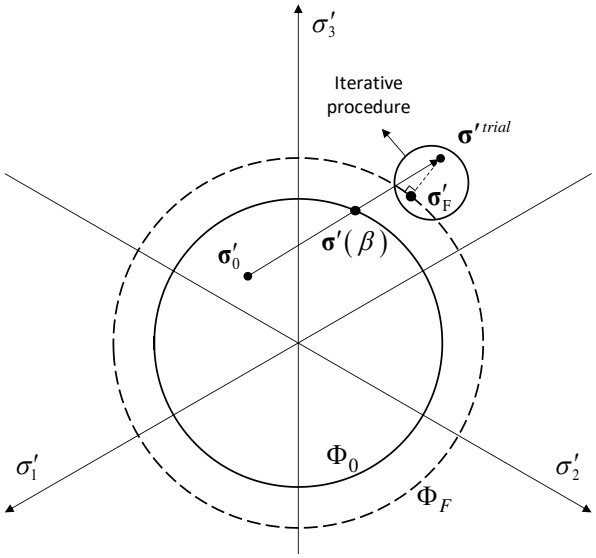

Figure 21. – Schematic representation of the stress update algorithm, with subscripts 0 and F denoting the quantities at the beginning and at the end of the time increment $[t, t+\Delta t]$.

The scalar quantities Φ^i and $\Phi^{i\prime}$ are required, being the first one given by Eq. (17) and the second one by

$$\Phi^{i\prime} = \frac{\partial\bar{\sigma}(\boldsymbol{\sigma}'_0, \Delta\boldsymbol{\varepsilon}', \beta)}{\partial\beta^i} = \frac{\partial\bar{\sigma}}{\partial\boldsymbol{\sigma}^i}\frac{\partial\boldsymbol{\sigma}^i}{\partial\beta^i} = \mathbf{V}^i : (2\mu\Delta\boldsymbol{\varepsilon}')\,. \tag{19}$$

The tensor $\mathbf{V}$ is given by

$$\mathbf{V}_{ij} = \frac{1}{2}\left(\frac{\partial}{\partial \boldsymbol{\sigma}_{ij}} + \frac{\partial}{\partial \boldsymbol{\sigma}_{ji}} \right) F = \frac{\partial \bar{\sigma}}{\partial s_p} \frac{\partial s_p}{\partial H_m} \frac{\partial H_m}{\partial s_{rs}} \Bigg|^{sym} \frac{\partial s_{rs}}{\partial \boldsymbol{\sigma}_{ij}} \Bigg|^{sym}, \tag{20}$$

while the tensor $\mathbf{Q}$ is given by,

$$\begin{aligned}
\mathbf{Q}_{ijkl} &= \frac{1}{2}\left(\frac{\partial}{\partial \boldsymbol{\sigma}_{kl}} + \frac{\partial}{\partial \boldsymbol{\sigma}_{lk}} \right) \mathbf{V}_{ij} = \frac{1}{2}\left(\frac{\partial}{\partial \boldsymbol{\sigma}_{kl}} + \frac{\partial}{\partial \boldsymbol{\sigma}_{lk}} \right) \left(\frac{\partial \bar{\sigma}}{\partial s_p} \frac{\partial s_p}{\partial H_m} \frac{\partial H_m}{\partial s_{rs}} \Bigg|^{sym} \frac{\partial s_{rs}}{\partial \boldsymbol{\sigma}_{ij}} \Bigg|^{sym} \right) \\
&= \frac{\partial^2 \bar{\sigma}}{\partial s_p \partial s_q} \left(\frac{\partial s_q}{\partial H_n} \frac{\partial H_n}{\partial s_{uv}} \Bigg|^{sym} \frac{\partial s_{uv}}{\partial \boldsymbol{\sigma}_{kl}} \Bigg|^{sym} \right) \left(\frac{\partial s_p}{\partial H_m} \frac{\partial H_m}{\partial s_{rs}} \Bigg|^{sym} \frac{\partial s_{rs}}{\partial \boldsymbol{\sigma}_{ij}} \Bigg|^{sym} \right) \\
&+ \frac{\partial \bar{\sigma}}{\partial s_p} \frac{\partial^2 s_p}{\partial H_m \partial H_n} \left(\frac{\partial H_n}{\partial s_{uv}} \Bigg|^{sym} \frac{\partial s_{uv}}{\partial \boldsymbol{\sigma}_{kl}} \Bigg|^{sym} \right) \left(\frac{\partial H_m}{\partial s_{rs}} \Bigg|^{sym} \frac{\partial s_{rs}}{\partial \boldsymbol{\sigma}_{ij}} \Bigg|^{sym} \right) \\
&+ \frac{\partial \bar{\sigma}}{\partial s_p} \frac{\partial s_p}{\partial H_m} \frac{\partial^2 H_m}{\partial s_{rs} \partial s_{uv}} \Bigg|^{sym} \frac{\partial s_{uv}}{\partial \boldsymbol{\sigma}_{kl}} \Bigg|^{sym} \frac{\partial s_{rs}}{\partial \boldsymbol{\sigma}_{ij}} \Bigg|^{sym}
\end{aligned} \tag{21}$$

The initial effective stress state is then updated to the initial yield surface as

$$\left(\boldsymbol{\sigma}'_0\right)^* \leftarrow \boldsymbol{\sigma}'_0 + \beta\left(2\mu \Delta \boldsymbol{\varepsilon}'\right) \tag{22}$$

A.2. First derivatives

In the following expressions, the superscript (i) with $i = 1, 2$ refers to the first and second linear transformations of the stress tensor $\mathbf{s}$, respectively.

a) Expressions for $\partial \bar{\sigma} / \partial s_p^{(i)}$

$$\begin{aligned}
\frac{\partial \bar{\sigma}}{\partial s_p^{(i)}} &= \frac{\partial}{\partial s_p^{(i)}} \left[B \cdot \left(\left(\left| s_1^{(1)} \right| - k^{(1)} s_1^{(1)} \right)^a + \left(\left| s_2^{(1)} \right| - k^{(1)} s_2^{(1)} \right)^a + \left(\left| s_3^{(1)} \right| - k^{(1)} s_3^{(1)} \right)^a + \right) \right] \\
&\left(\left(\left| s_1^{(2)} \right| - k^{(2)} s_1^{(2)} \right)^a + \left(\left| s_2^{(2)} \right| - k^{(2)} s_2^{(2)} \right)^a + \left(\left| s_3^{(2} \right| - k^{(2)} s_3^{(2)} \right)^a \right) \\
&= \frac{B}{a} \left[\left(\left| s_1^{(1)} \right| - k^{(1)} s_1^{(1)} \right)^a + \left(\left| s_2^{(1)} \right| - k^{(1)} s_2^{(1)} \right)^a + \left(\left| s_3^{(1)} \right| - k^{(1)} s_3^{(1)} \right)^a + \right]^{\frac{1}{a}-1} \cdot \left[a \left(\left| s_p^{(i)} \right| - k^{(i)} s_p^{(i)} \right)^{a-1} \left(\frac{\left| s_p^{(i)} \right|}{s_p^{(i)}} - k^{(i)} \right) \right], \\
&\left(\left(\left| s_1^{(2)} \right| - k^{(2)} s_1^{(2)} \right)^a + \left(\left| s_2^{(2)} \right| - k^{(2)} s_2^{(2)} \right)^a + \left(\left| s_3^{(2} \right| - k^{(2)} s_3^{(2)} \right)^a \right) \\
&= R \cdot D\left(s_p^i \right)
\end{aligned} \tag{23}$$

with

$$R = \frac{B}{a} \left(A \right)^{\frac{1}{a}-1}, \tag{24}$$

and

$$A=\left[\begin{pmatrix}\left(\left|s_1^{(1)}\right|-k^{(1)}\ s_1^{(1)}\right)^a+\left(\left|s_2^{(1)}\right|-k^{(1)}\ s_2^{(1)}\right)^a+\left(\left|s_3^{(1)}\right|-k^{(1)}\ s_3^{(1)}\right)^a+\\ \left(\left|s_1^{(2)}\right|-k^{(2)}\ s_1^{(2)}\right)^a+\left(\left|s_2^{(2)}\right|-k^{(2)}\ s_2^{(2}\right)^a+\left(\left|s_3^{(2}\right|-k^{(2)}\ s_3^{(2)}\right)^a\end{pmatrix}\right]. \tag{25}$$

Also,

$$D\left(s_p^{(i)}\right)=\left[a\left(\left|s_p^{(i)}\right|-k^{(i)}\ s_p^{(i)}\right)^{a-1}\left(\frac{\left|s_p^{(i)}\right|}{s_p^{(i)}}-k^{(i)}\right)\right]. \tag{26}$$

b) Expressions for $\partial s_p/\partial H_m$

$$\frac{\partial s_p^{(i)}}{\partial H_m}=\frac{\partial}{\partial H_m}\left[H_1+2\sqrt{H_1^2+H_2}\cdot\cos\left(\frac{\theta}{3}+\beta_p^{(i)}\right)\right], \tag{27}$$

$$\frac{\partial s_p^{(i)}}{\partial H_1}=1+\frac{2H_1}{\sqrt{H_1^2+H_2}}\cdot\cos\left(\frac{\theta}{3}+\beta_p^{(i)}\right)-\frac{2}{3}\sqrt{H_1^2+H_2}\cdot\sin\left(\frac{\theta}{3}+\beta_p^{(i)}\right)\frac{\partial\theta}{\partial H_1}, \tag{28}$$

$$\frac{\partial s_p^{(i)}}{\partial H_2}=\frac{2H_1}{\sqrt{H_1^2+H_2}}\cdot\cos\left(\frac{\theta}{3}+\beta_p^{(i)}\right)-\frac{2}{3}\sqrt{H_1^2+H_2}\cdot\sin\left(\frac{\theta}{3}+\beta_p^{(i)}\right)\frac{\partial\theta}{\partial H_2}, \tag{29}$$

$$\frac{\partial s_p^{(i)}}{\partial H_3}=-\frac{2}{3}\sqrt{H_1^2+H_2}\cdot\sin\left(\frac{\theta}{3}+\beta_p^{(i)}\right)\frac{\partial\theta}{\partial H_3}, \tag{30}$$

with $\beta_1=0$, $\beta_2=\frac{4}{3}\pi$ and $\beta_3=\frac{2}{3}\pi$.

$$\frac{\partial\theta}{\partial H_1}=-\frac{3}{2}\frac{\left(2H_1^2+H_2\right)H_p-2H_qH_1}{H_p\sqrt{H_p^3+H_q^2}} \tag{31}$$

$$\frac{\partial\theta}{\partial H_2}=-\frac{3}{2}\frac{H_1H_p-2H_q}{H_p\sqrt{H_p^3+H_q^2}} \tag{32}$$

$$\frac{\partial\theta}{\partial H_3}=-\frac{H_p}{H_p\sqrt{H_p^3+H_q^2}} \tag{33}$$

c) Expressions for $\partial H_m/\partial s_{rs}$

$$\frac{\partial H_1}{\partial s_{kl}^{(i)}} = \frac{1}{2}\left(\frac{\partial}{\partial s_{kl}^{(i)}} + \frac{\partial}{\partial s_{lk}^{(i)}} \right) H_1 = \frac{1}{3}\delta_{kl} \tag{34}$$

$$\frac{\partial H_2}{\partial s_{kl}^{(i)}} = \frac{1}{2}\left(\frac{\partial}{\partial s_{kl}^{(i)}} + \frac{\partial}{\partial s_{lk}^{(i)}} \right) H_1 = \frac{1}{3}\begin{bmatrix} -s_{yy}^{(i)} - s_{zz}^{(i)} \\ -s_{xx}^{(i)} - s_{zz}^{(i)} \\ -s_{xx}^{(i)} - s_{yy}^{(i)} \\ \frac{1}{2}\left(s_{zy}^{(i)} + s_{yz}^{(i)} \right) \\ \frac{1}{2}\left(s_{zx}^{(i)} + s_{xz}^{(i)} \right) \\ \frac{1}{2}\left(s_{yx}^{(i)} + s_{xy}^{(i)} \right) \end{bmatrix} \tag{35}$$

$$\frac{\partial H_3}{\partial s_{kl}^{(i)}} = \frac{1}{2}\left(\frac{\partial}{\partial s_{kl}^{(i)}} + \frac{\partial}{\partial s_{lk}^{(i)}} \right) H_1 = \frac{1}{3}\begin{bmatrix} s_{yy}^{(i)} s_{zz}^{(i)} - s_{yz}^{(i)} s_{zy}^{(i)} \\ s_{xx}^{(i)} s_{zz}^{(i)} - s_{xz}^{(i)} s_{zx}^{(i)} \\ s_{xx}^{(i)} s_{yy}^{(i)} - s_{xy}^{(i)} s_{yx}^{(i)} \\ \frac{1}{2}\left(s_{xy}^{(i)} s_{zx}^{(i)} + s_{yx}^{(i)} s_{xz}^{(i)} - s_{xx}^{(i)} \left(s_{yz}^{(i)} + s_{zy}^{(i)} \right) \right) \\ \frac{1}{2}\left(s_{yx}^{(i)} s_{zy}^{(i)} + s_{xy}^{(i)} s_{yz}^{(i)} - s_{yy}^{(i)} \left(s_{xz}^{(i)} + s_{zx}^{(i)} \right) \right) \\ \frac{1}{2}\left(s_{yz}^{(i)} s_{zx}^{(i)} + s_{zy}^{(i)} s_{xz}^{(i)} - s_{zz}^{(i)} \left(s_{xy}^{(i)} + s_{yx}^{(i)} \right) \right) \end{bmatrix} \tag{36}$$

d) Expression for $\partial s_{kl}^{(i)} \big/ \partial \boldsymbol{\sigma}_{ij}$

$$\frac{\partial s_{kl}^{(i)}}{\partial \boldsymbol{\sigma}_{ij}} = \frac{\partial}{\partial \boldsymbol{\sigma}_{ij}} \left[\mathbf{L}_{ijkl}^{(i)} : \boldsymbol{\sigma}_{kl} \right] = \mathbf{L}_{ijkl}^{(i)} \frac{\partial \boldsymbol{\sigma}_{kl}}{\partial \boldsymbol{\sigma}_{ij}} = \mathbf{L}_{ijkl}^{(i)} \delta_{ki} \delta_{lj} \tag{37}$$

A.3. Second derivatives

The second order derivatives have a role in the state variables update and in the definition of the consistent elastoplastic modulus.

a) Expression for $\partial^2 \bar{\sigma} \big/ \partial s_p^{(i)} \partial s_q^{(i)}$

$$\frac{\partial^2 \bar{\sigma}}{\partial s_p^{(i)} \partial s_q^{(i)}} = \frac{1}{A} \cdot \left(\frac{1}{a} - 1 \right) \cdot \left[\frac{\partial \bar{\sigma}}{\partial s_p^{(i)}} \right] \cdot D\left(s_q^{(i)} \right) + R \cdot \frac{\partial}{\partial s_q^{(i)}} \left[\; D\left(s_p^{(i)} \right) \right] \tag{38}$$

with

$$D\left(s_q^{(i)}\right)=\left[a\left(\left|s_q^{(i)}\right|-k\ s_q^{(i)}\right)^{a-1}\left(\frac{\left|s_q^{(i)}\right|}{s_q^{(i)}}-k\right)\right] \tag{39}$$

b) Expressions for $\partial^2 s_p^{(i)}\big/\partial H_m H_n$

$$\frac{\partial^2 s_p^{(i)}}{\partial H_m H_n}=\frac{\partial}{H_n}\left(\frac{\partial s_p^{(i)}}{\partial H_m}\right) \tag{40}$$

$$\begin{aligned}\frac{\partial}{\partial H_n}\left(\frac{\partial s_p^{(i)}}{\partial H_1}\right)&=\cos\left(\frac{\theta}{3}+\beta_p^{(i)}\right)\cdot \mathrm{dA1(n)}-\frac{2}{3}\sin\left(\frac{\theta}{3}+\beta_p^{(i)}\right)\frac{\partial\theta}{\partial H_1}\mathrm{dA2(n)}\\&-\frac{1}{3}\sqrt{H_1^2+H_2}\left[\begin{array}{l}\dfrac{2H_1}{H_1^2+H_2}\sin\left(\dfrac{\theta}{3}+\beta_p^{(i)}\right)\\+\dfrac{2}{3}\cdot\cos\left(\dfrac{\theta}{3}+\beta_p^{(i)}\right)\dfrac{\partial\theta}{\partial H_1}\end{array}\right]\frac{\partial\theta}{\partial H_n}\\&-\frac{2}{3}\sqrt{H_1^2+H_2}\cdot\sin\left(\frac{\theta}{3}+\beta_p^{(i)}\right)\frac{\partial^2\theta}{\partial H_1\partial H_n}\end{aligned} \tag{41}$$

$$\begin{aligned}\frac{\partial}{\partial H_n}\left(\frac{\partial s_p^{(i)}}{\partial H_2}\right)&=\cos\left(\frac{\theta}{3}+\beta_p^{(i)}\right)\cdot \mathrm{dA3(n)}-\frac{2}{3}\sin\left(\frac{\theta}{3}+\beta_p^{(i)}\right)\frac{\partial\theta}{\partial H_2}\mathrm{dA2(n)}\\&-\frac{1}{3}\sqrt{H_1^2+H_2}\left[\frac{1}{H_1^2+H_2}\cdot\sin\left(\frac{\theta}{3}+\beta_p^{(i)}\right)+\frac{2}{3}\cos\left(\frac{\theta}{3}+\beta_p^{(i)}\right)\frac{\partial\theta}{\partial H_2}\right]\frac{\partial\theta}{\partial H_n}\\&-\frac{2}{3}\sqrt{H_1^2+H_2}\cdot\sin\left(\frac{\theta}{3}+\beta_p^{(i)}\right)\frac{\partial^2\theta}{\partial H_2\partial H_n}\end{aligned} \tag{42}$$

$$\begin{aligned}\frac{\partial}{\partial H_n}\left(\frac{\partial s_p^{(i)}}{\partial H_3}\right)&=-\frac{2}{3}\sin\left(\frac{\theta}{3}+\beta_p^{(i)}\right)\frac{\partial\theta}{\partial H_3}\mathrm{dA2(n)}-\frac{1}{3}\sqrt{H_1^2+H_2}\left[\frac{2}{3}\cos\left(\frac{\theta}{3}+\beta_p^{(i)}\right)\frac{\partial\theta}{\partial H_3}\right]\frac{\partial\theta}{\partial H_n}\\&-\frac{2}{3}\sqrt{H_1^2+H_2}\cdot\sin\left(\frac{\theta}{3}+\beta_p^{(i)}\right)\frac{\partial^2\theta}{\partial H_3\partial H_n}\end{aligned} \tag{43}$$

with

$$\mathrm{dA1(n)}=\frac{\partial}{\partial H_n}\left(\frac{2H_1}{\sqrt{H_1^2+H_2}}\right)=\left[\frac{2H_2}{\left(\sqrt{H_1^2+H_2}\right)^3}\quad-\frac{H_1}{\left(\sqrt{H_1^2+H_2}\right)^3}\quad 0\right] \tag{44}$$

$$\mathrm{dA2(n)} = \frac{\partial}{\partial H_n}\left(\sqrt{H_1^2 + H_2}\right) = \begin{bmatrix} \dfrac{H_1}{\sqrt{H_1^2 + H_2}} & \dfrac{1}{2\sqrt{H_1^2 + H_2}} & 0 \end{bmatrix} \tag{45}$$

$$\mathrm{dA3(n)} = \frac{\partial}{\partial H_n}\left(\frac{1}{\sqrt{H_1^2 + H_2}}\right) = \begin{bmatrix} -\dfrac{H_1}{\left(\sqrt{H_1^2 + H_2}\right)^3} & -\dfrac{1}{2\left(\sqrt{H_1^2 + H_2}\right)^3} & 0 \end{bmatrix} \tag{46}$$

$$\frac{\partial}{\partial H_n}\left(\cos\left(\frac{\theta}{3} + \beta_p^{(i)}\right)\right) = -\frac{1}{3}\sin\left(\frac{\theta}{3} + \beta_p^{(i)}\right)\frac{\partial \theta}{\partial H_n} \tag{47}$$

$$\frac{\partial}{\partial H_n}\left(\sin\left(\frac{\theta}{3} + \beta_p^{(i)}\right)\right) = \frac{1}{3}\cos\left(\frac{\theta}{3} + \beta_p^{(i)}\right)\frac{\partial \theta}{\partial H_n}\,. \tag{48}$$

Also,

$$\begin{aligned}\frac{\partial}{H_n}\left(\frac{\partial \theta}{\partial H_m}\right) = &-\frac{H_p\dfrac{\partial^2 H_q}{\partial H_m \partial H_n} + \dfrac{\partial H_q}{\partial H_m}\dfrac{\partial H_p}{\partial H_n} - \dfrac{3}{2}\left(\dfrac{\partial H_q}{\partial H_n}\dfrac{\partial H_p}{\partial H_m} + H_q\dfrac{\partial^2 H_p}{\partial H_m \partial H_n}\right)}{H_p\sqrt{H_p^3 - H^2{}_q}} \\ &+ \frac{\left(H_p\dfrac{\partial H_q}{\partial H_m} - \dfrac{3}{2}H_q\dfrac{\partial H_p}{\partial H_m}\right)}{2\left(H_p\sqrt{H_p^3 - H^2{}_q}\right)^2\sqrt{H_p^3 - H^2{}_q}}\left(\left(5H_p^3 - 2H_q^2\right)\frac{\partial H_p}{\partial H_n} - 2H_pH_q\frac{\partial H_q}{\partial H_n}\right)\end{aligned}, \tag{49}$$

with

$$\frac{\partial H_p^{(i)}}{\partial H_m} = \frac{\partial}{\partial H_m}\left(H_1^2 + H_2\right) = \begin{bmatrix} 2H_1 \\ 1 \\ 0 \end{bmatrix}, \tag{50}$$

$$\frac{\partial H_q^{(i)}}{\partial H_m} = \frac{\partial}{\partial H_m}\left[\frac{1}{2}\left(2H_1^3 + 3H_1H_2 + 2H_3\right)\right] = \frac{1}{2}\begin{bmatrix} 6H_1^2 + 3H_2 \\ 3H_1 \\ 2 \end{bmatrix}, \tag{51}$$

$$\frac{\partial^2 H_p^{(i)}}{\partial H_m \partial H_n} = \frac{\partial}{\partial H_n}\left(\begin{bmatrix} 2H_1 \\ 1 \\ 0 \end{bmatrix}\right) = \begin{bmatrix} 2 & 0 & 0 \\ 0 & 0 & 0 \\ 0 & 0 & 0 \end{bmatrix}, \tag{52}$$

$$\frac{\partial^2 H_q^{(i)}}{\partial H_m \partial H_n} = \frac{\partial}{\partial H_n}\left[\frac{1}{2}\begin{bmatrix} 6H_1^2 + 3H_2 \\ 3H_1 \\ 2 \end{bmatrix}\right] = \frac{1}{2}\begin{bmatrix} 12H_1 & 0 & 0 \\ 3 & 0 & 0 \\ 0 & 0 & 0 \end{bmatrix}. \tag{53}$$

Note that in the previous expressions, since $H_p^{(i)}$ and $H_q^{(i)}$ with $i = (1,2)$ also H_1, H_2 and H_3 will be different although not explicitly mentioned, for sake of simplicity.

c) Expressions for $\partial^2 H_m \big/ \partial s_{rs}^{(i)} \partial s_{uv}^{(i)}$

$$\frac{\partial^2 H_1}{\partial s_{kl}^{(i)} \partial s_{mn}^{(i)}} = \frac{1}{2}\left(\frac{\partial}{\partial s_{mn}^{(i)}} + \frac{\partial}{\partial s_{nm}^{(i)}}\right)\left[\frac{1}{3}\delta_{kl}\right] = \mathbf{0} \tag{54}$$

$$\frac{\partial^2 H_2}{\partial s_{kl}^{(i)} \partial s_{mn}^{(i)}} = \frac{1}{2}\left(\frac{\partial}{\partial s_{mn}^{(i)}} + \frac{\partial}{\partial s_{nm}^{(i)}}\right)\frac{\partial H_2}{\partial s_{kl}^{(i)}} = \frac{1}{3}\begin{bmatrix} 0 & -1 & -1 & 0 & 0 & 0 \\ -1 & 0 & -1 & 0 & 0 & 0 \\ -1 & -1 & 0 & 0 & 0 & 0 \\ 0 & 0 & 0 & \frac{1}{2} & 0 & 0 \\ 0 & 0 & 0 & 0 & \frac{1}{2} & 0 \\ 0 & 0 & 0 & 0 & 0 & \frac{1}{2} \end{bmatrix} \tag{55}$$

$$\frac{\partial^2 H_3}{\partial s_{kl}^{(i)} \partial s_{mn}^{(i)}} = \frac{1}{2}\begin{bmatrix} 0 & s_{zz}^{(i)} & s_{yy}^{(i)} & -s_{yz}^{(i)} & 0 & 0 \\ s_{zz}^{(i)} & 0 & s_{xx}^{(i)} & 0 & -s_{xz}^{(i)} & 0 \\ s_{yy}^{(i)} & s_{xx}^{(i)} & 0 & 0 & 0 & -s_{xy}^{(i)} \\ -s_{yz}^{(i)} & 0 & 0 & -\frac{1}{2}s_{xx}^{(i)} & \frac{1}{2}s_{xy}^{(i)} & \frac{1}{2}s_{xz}^{(i)} \\ 0 & -s_{xz}^{(i)} & 0 & \frac{1}{2}s_{xy}^{(i)} & -\frac{1}{2}s_{yy}^{(i)} & \frac{1}{2}s_{yz}^{(i)} \\ 0 & 0 & -s_{xy}^{(i)} & \frac{1}{2}s_{xz}^{(i)} & \frac{1}{2}s_{yz}^{(i)} & -\frac{1}{2}s_{zz}^{(i)} \end{bmatrix} \tag{56}$$

d) Expressions for $\partial\theta/\partial H_a$

For sake of simplicity, the following is considered

$$\theta = \arccos\left[\frac{H_q}{H_p^{3/2}}\right] = \arccos\left[C\right], \text{ with } C = \frac{H_q}{H_p^{3/2}} \tag{57}$$

Thus, the derivative for $\partial\theta/\partial H_a$

$$\frac{\partial \theta}{\partial H_a} = \frac{\partial \theta}{\partial H_p}\frac{\partial H_p}{\partial H_a} + \frac{\partial \theta}{\partial H_q}\frac{\partial H_q}{\partial H_a} \tag{58}$$

The terms for the above expression are given by

$$\frac{\partial \theta}{\partial H_q} = -\frac{1}{\sqrt{1-C^2}} \cdot \frac{1}{H_p^{3/2}} = K \cdot \frac{1}{H_p^{3/2}}, \tag{59}$$

$$\frac{\partial \theta}{\partial H_p} = -\frac{1}{\sqrt{1-C^2}} \cdot C \cdot \left(-\frac{3}{2}\frac{1}{H_p} \right) = K \cdot C \cdot \left(-\frac{3}{2}\frac{1}{H_p} \right), \tag{60}$$

$$\frac{\partial H_q}{\partial H_a} = \begin{bmatrix} 3H_1^2 + \frac{3}{2}H_2 \\ \frac{3}{2}H_1 \\ 1 \end{bmatrix}, \tag{61}$$

$$\frac{\partial H_p}{\partial H_a} = \begin{bmatrix} 2H_1 \\ 1 \\ 0 \end{bmatrix}, \tag{62}$$

with

$$K = -\frac{1}{\sqrt{1-C^2}} \tag{63}$$

e) Expressions for $\partial^2\theta / \partial H_a \partial H_b$

$$\begin{aligned} \frac{\partial^2 \theta}{\partial H_a \partial H_b} &= \frac{\partial}{\partial H_b}\left(\frac{\partial \theta}{\partial H_p}\frac{\partial H_p}{\partial H_a} + \frac{\partial \theta}{\partial H_q}\frac{\partial H_q}{\partial H_a} \right) = \\ &= \left(\frac{\partial^2 \theta}{\partial H_p \partial H_p}\frac{\partial H_p}{\partial H_b} + \frac{\partial^2 \theta}{\partial H_p \partial H_q}\frac{\partial H_q}{\partial H_b} \right)\frac{\partial H_p}{\partial H_a} + \frac{\partial \theta}{\partial H_p}\left(\frac{\partial^2 H_p}{\partial H_a \partial H_b} \right), \\ &+ \left(\frac{\partial^2 \theta}{\partial H_q \partial H_q}\frac{\partial H_q}{\partial H_b} + \frac{\partial^2 \theta}{\partial H_q \partial H_p}\frac{\partial H_p}{\partial H_b} \right)\frac{\partial H_q}{\partial H_a} + \frac{\partial \theta}{\partial H_q}\left(\frac{\partial^2 H_q}{\partial H_a \partial H_b} \right) \end{aligned} \tag{64}$$

with

$$\frac{\partial^2 H_q}{\partial H_a \partial H_b} = \begin{bmatrix} 6H_1 & \frac{3}{2} & 0 \\ \frac{3}{2} & 0 & 0 \\ 0 & 0 & 0 \end{bmatrix} \quad \text{and} \quad \frac{\partial^2 H_p}{\partial H_a \partial H_b} = \begin{bmatrix} 2 & 0 & 0 \\ 0 & 0 & 0 \\ 0 & 0 & 0 \end{bmatrix}, \tag{65}$$

$$\frac{\partial^2 \theta}{\partial H_q \partial H_q} = \frac{\partial K}{\partial H_q} \cdot \left(\frac{1}{H_p^{3/2}} \right) \tag{66}$$

$$\frac{\partial^2 \theta}{\partial H_q \partial H_p} = \frac{\partial K}{\partial H_p} \cdot \left(\frac{1}{H_p^{3/2}} \right) + K \cdot \left(\frac{1}{H_p^{3/2}} \right) \cdot \left(-\frac{3}{2} \frac{1}{H_p} \right) \tag{67}$$

$$\frac{\partial^2 \theta}{\partial H_p \partial H_q} = \frac{\partial K}{\partial H_q} \cdot C \cdot \left(-\frac{3}{2} \frac{1}{H_p} \right) + K \cdot \frac{\partial C}{\partial H_q} \cdot \left(-\frac{3}{2} \frac{1}{H_p} \right) \tag{68}$$

$$\frac{\partial^2 \theta}{\partial H_p \partial H_p} = \frac{\partial K}{\partial H_p} \cdot C \cdot \left(-\frac{3}{2} \frac{1}{H_p} \right) + K \cdot \frac{\partial C}{\partial H_p} \cdot \left(-\frac{3}{2} \frac{1}{H_p} \right) - K \cdot C \cdot \left(-\frac{3}{2} \frac{1}{H_p} \right) \frac{1}{H_p} \tag{69}$$

A.4. Principal values

The principal values are calculated by solving the characteristic equation

$$\det\left(\mathbf{s} - s\mathbf{I}\right) = 0, \tag{70}$$

where s represents the principal values of $\mathbf{s}$ and $\mathbf{s}$ is a tensor whose trace is zero,

$$\mathbf{s} = \begin{bmatrix} s_{xx} & s_{xy} & s_{xz} \\ s_{xy} & s_{yy} & s_{yz} \\ s_{xz} & s_{yz} & s_{zz} \end{bmatrix}. \tag{71}$$

x, y and z denote an orthogonal frame attached to the material (*i.e.* sheet rolling, transverse and normal directions, respectively).

This equation reduces to

$$s^3 - H_1 s^2 - 3H_2 s - 2H_3 = 0, \tag{72}$$

with

$$H_1 = \frac{1}{3} I_1 = \frac{1}{3}\left(s_{xx} + s_{yy} + s_{zz}\right), \tag{73}$$

$$H_2 = \frac{1}{3} I_2 = \frac{1}{3}\left(s_{yz}^2 + s_{zx}^2 + s_{xy}^2 - s_{yy}s_{zz} - s_{zz}s_{xx} - s_{xx}s_{yy} \right), \tag{74}$$

$$H_3 = \frac{1}{2} I_3 = \frac{1}{2}\left(2s_{yz}s_{zx}s_{xy} + s_{xx}s_{yy}s_{zz} - s_{xx}s_{yz}^2 - s_{yy}s_{zx}^2 - s_{zz}s_{xy}^2 \right). \tag{75}$$

Through a change of variables (Barlat et al., 2005),

$$s = s + H_1, \tag{76}$$

the characteristic equation becomes

$$\overline{s}^3 - 3H_p\overline{s} - 2H_q = 0, \tag{77}$$

with

a) $$H_{\mathrm{p}} = H_1^2 + H_2, \tag{78}$$

b) $$H_{\mathrm{q}} = \frac{1}{2}\left(2H_1^3 + 3H_1H_2 + 2H_3 \right), \tag{79}$$

c) $$\theta = \arccos\left[\frac{H_{\mathrm{q}}}{H_{\mathrm{p}}^{3/2}} \right], \tag{80}$$

Cardan's solutions to the characteristic equation are

a) $$\overline{s}_1 = z^{1/3} + \overline{z}^{1/3}, \tag{81}$$

b) $$\overline{s}_2 = \omega z^{1/3} + \overline{\omega}\overline{z}^{1/3}, \tag{82}$$

c) $$\overline{s}_3 = \overline{\omega} z^{1/3} + \omega\overline{z}^{1/3}, \tag{83}$$

where z is a complex number. ω is a complex constant ($\mathrm{e}^{-2\mathrm{i}\pi/3}$), and $\overline{z}$ and $\overline{\omega}$ are their conjugate quantities.

$$z = H_q + \mathrm{i}\sqrt{H_p{}^3 - H_q{}^2}, \tag{84}$$

The principal values of s can be written as

$$\begin{cases} s_1 = H_1 + 2\sqrt{H_1^2 + H_2}\cos\left(\theta/3\right) \\ s_2 = H_1 + 2\sqrt{H_1^2 + H_2}\cos\left(\dfrac{\theta + 4\pi}{3}\right), \\ s_3 = H_1 + 2\sqrt{H_1^2 + H_2}\cos\left(\dfrac{\theta + 2\pi}{3}\right) \end{cases} \tag{85}$$

These values are ordered as (Barlat et al., 2005)

$$s_1 \geq s_2 \geq s_3\,, \qquad s_1 > s_3\,. \tag{86}$$

References

Banabic, D., 2010. Sheet Metal Forming Processes, Springer. Springer-Verlag Berlin Heidelberg. doi:10.1007/978-3-540-88113-1

Banabic, D., Aretz, H., Comsa, D.S., Paraianu, L., 2005. An improved analytical description of orthotropy in metallic sheets. Int. J. Plast. 21, 493–512. doi:10.1016/j.ijplas.2004.04.003

Banabic, D., Balan, T., Comsa, D.S., 2000. A new yield criterion for orthotropic sheet metals under plane stress conditions. 7th Cold Met. Form. Conf. 217–224. doi:10.1016/S0020-7403(03)00139-5

Barlat, F., Aretz, H., Yoon, J.W., Karabin, M.E., Brem, J.C., Dick, R.E., 2005. Linear transfomation-based anisotropic yield functions. Int. J. Plast. 21, 1009–1039. doi:10.1016/j.ijplas.2004.06.004

Barlat, F., Brem, J.C., Yoon, J.W., Chung, K., Dick, R.E., Lege, D.J., Pourboghrat, F., Choi, S.H., Chu, E., 2003. Plane stress yield function for aluminum alloy sheets - Part 1: Theory. Int. J. Plast. 19, 1297–1319. doi:10.1016/S0749-6419(02)00019-0

Barlat, F., Lege, D.J., Brem, J.C., 1991a. A six-component yield function for anisotropic materials. Int. J. Plast. 7, 693–712. doi:10.1016/0749-6419(91)90052-Z

Barlat, F., Lege, D.J., Brem, J.C., Warren, C.J., 1991b. Constitutive behavior for anisotropic materials and application to a 2090 Al±Li alloy., in: Lowe, T.., Rollett, A.., Follansbee, P.., Daehn, G.. (Eds.), TMS Annual Meeting,. TMS, New Orleans, LA, pp. 189–203.

Barlat, F., Maeda, Y., Chung, K., Yanagawa, M., Brem, J.C., Hayashida, Y., Lege, D.J., Matsui, K., Murtha, S.J., Hattori, S., Becker, R.C., Makosey, S., 1997. Yield function development for aluminum alloy sheets. J. Mech. Phys. Solids 45, 1727–1763. doi:10.1016/S0022-5096(97)00034-3

Barlat, F., Panchanadeeswaran, S., Richmond, O., 1991c. Earing in cup drawing face-centered cubic single crystals and polycrystals. Metall. Trans. A 22, 1525–1534. doi:10.1007/BF02667366

Barros, P.D., Alves, J.L., Oliveira, M., Menezes, L.F., 2016a. Tension-compression asymmetry modelling : strategies for anisotropy parameters identification., in: NUMIFORM 2016: The 12th International Conference on Numerical Methods in Industrial Forming Processes. MATEC Web of Conferences. doi:10.1051/matecconf/20168005002

Barros, P.D., Alves, J.L., Oliveira, M.C., Menezes, L.F., 2016b. Modeling of tension-compression asymmetry and orthotropy on metallic materials: Numerical implementation and validation. Int. J. Mech. Sci. 114, 217–232. doi:10.1016/j.ijmecsci.2016.05.020

Barros, P.D., Carvalho, P.D., Alves, J.L., Oliveira, M.C., Menezes, L.F., 2016. DD3MAT - A code for yield criteria anisotropy parameters identification. J. Phys. Conf. Ser. 734. doi:10.1088/1742-6596/734/3/032053

Barros, P.D., Carvalho, P.D., Alves, J.L., Oliveira, M.C., Menezes, L.F., 2016c. DD3MAT - a code for yield criteria anisotropy parameters identification., in:

Journal of Physics: Conference Series. doi:10.1088/1742-6596/734/3/032053

Barros, P.D., Neto, D.M., Alves, J.L., Oliveira, M., Menezes, L.F., 2015a. DD3IMP , 3D Fully Implicit Finite Element Solver : Implementation of CB2001 Yield Criterion. Rom. J. Tech. Sci. - Appl. Mech. 60, 105–136.

Barros, P.D., Oliveira, M.C., Alves, J.L., Andrade-Campos, A., Menezes, L.F., 2015b. Modelling of tension-compression asymmetry and orthotropic anisotropy in case of thin metallic sheets: identification procedure and case studies, in: Hora, P. (Ed.), . Institute of Virtual Manufacturing, ETH Zurich, Zurich, pp. 149–154.

Cazacu, O., Barlat, F., 2003. Application of the theory of representation to describe yielding of anisotropic aluminum alloys. Int. J. Eng. Sci. 41, 1367–1385. doi:10.1016/S0020-7225(03)00037-5

Cazacu, O., Barlat, F., 2001. Generalization of drucker's yield criterion to orthotropy. Math. Mech. Solids 6, 613–630. doi:10.1177/108128650100600603

Cazacu, O., Plunkett, B., Barlat, F., 2006. Orthotropic yield criterion for hexagonal closed packed metals. Int. J. Plast. 22, 1171–1194. doi:10.1016/j.ijplas.2005.06.001

Chung, K., Kim, D., Park, T., 2011. Analytical derivation of earing in circular cup drawing based on simple tension properties. Eur. J. Mech. A/Solids 30, 275–280. doi:10.1016/j.euromechsol.2011.01.006

Comsa, D.S., Banabic, D., 2007. Numerical simulation of sheet metal forming processes using a new yield criterion. Key Eng. Mater. 344, 833–840. doi:10.4028/www.scientific.net/KEM.344.833

Cooreman, S., Lecompte, D., Sol, H., Vantomme, J., Debruyne, D., 2008. Identification of mechanical material behavior through inverse modeling and DIC. Exp. Mech. 48, 421–433. doi:10.1007/s11340-007-9094-0

Dick, R.E., Yoon, J.W., 2018. Plastic anisotropy and failure in thin metal: Material characterization and fracture prediction with an advanced constitutive model and polar EPS (effective plastic strain) fracture diagram for AA 3014-H19. Int. J. Solids Struct. doi:10.1016/j.ijsolstr.2018.03.008

Drucker, D.C., 1949. Relation of experiments to mathematical theories of plasticity, Journal of Applied Mechanics. ASME 16, A349–A357.

Eggleston, 1958. General properties of convex functions, in: Convexity.

Engler, O., Kalz, S., 2004. Simulation of earing profiles from texture data by means of a visco-plastic self-consistent polycrystal plasticity approach. Mater. Sci. Eng. A 373, 350– 362.

Güner, A., Soyarslan, C., Brosius, A., Tekkaya, A.E., 2012. Characterization of anisotropy of sheet metals employing inhomogeneous strain fields for Yld2000-2D yield function. Int. J. Solids Struct. 49, 3517–3527. doi:10.1016/j.ijsolstr.2012.05.001

Hill, R., 1948. A Theory of the Yielding and Plastic Flow of Anisotropic Metals. Proc. R. Soc. A Math. Phys. Eng. Sci. 193, 281–297. doi:10.1098/rspa.1948.0045

Hosford, W.F., Duncan, J.L., 1994. The Aluminum Beverage can. Sci. Am. 271, 48–53. doi:10.1038/scientificamerican0994-48

Hughes, T.J.R., 1980. Generalization of selective integration procedures to anisotropic

and nonlinear media. Int. J. Numer. Methods Eng. 15, 1413–1418. doi:10.1002/nme.1620150914

Kuwabara, T., 2007. Advances in experiments on metal sheets and tubes in support of constitutive modeling and forming simulations. Int. J. Plast. 23, 385–419. doi:10.1016/j.ijplas.2006.06.003

Lee, J.Y., Xu, L., Barlat, F., Wagoner, R.H., Lee, M.G., 2013. Balanced Biaxial Testing of Advanced High Strength Steels in Warm Conditions. Exp. Mech. 53, 1681–1692. doi:10.1007/s11340-013-9758-x

Lege, D.J., Barlat, F., Brem, J.C., 1989. Characterization and modeling of the mechanical behavior and formability of a 2008-T4 sheet sample. Int. J. Mech. Sci. 31, 549–563.

Martins, B., Santos, A.D., Teixeira, P., Ito, K., Mori, N., 2013. Determination of flow curve using bulge test and calibration of damage for ito-goya models. Key Eng. Mater. 554–557, 182–189. doi:10.4028/www.scientific.net/KEM.554-557.182

Menezes, L.F., Teodosiu, C., 2000. Three-dimensional numerical simulation of the deep-drawing process using solid finite elements. J. Mater. Process. Technol. 97, 100–106. doi:10.1016/S0924-0136(99)00345-3

Mulder, J., Nagy, G.T., 2009. Earing and Wall Thickness in Cylindrical Deep Drawing. Complas X 1–8.

Neto, D.M., Oliveira, M.C., Menezes, L.F., Alves, J.L., 2014. Applying Nagata patches to smooth discretized surfaces used in 3D frictional contact problems. Comput. Methods Appl. Mech. Eng. 271, 296–320.

Neto, D.M., Oliveira, M.C., Menezes, L.F., Alves, J.L., 2013. Nagata patch interpolation using surface normal vectors evaluated from the IGES file. Finite Elem. Anal. Des. 72, 35–46.

Oliveira, M.C., Alves, J.L., Menezes, L.F., 2008. Algorithms and Strategies for Treatment of Large Deformation Frictional Contact in the Numerical Simulation of Deep Drawing Process. Arch. Comput. Methods Eng. 15, 113–162.

Pearce, R., 1968. Some aspects of anisotropic plasticity in sheet metals. Int. J. Mech. Sci. 10, 995–1004. doi:10.1016/0020-7403(68)90053-2

Plunkett, B., Cazacu, O., Barlat, F., 2008. Orthotropic yield criteria for description of the anisotropy in tension and compression of sheet metals. Int. J. Plast. 24, 847–866. doi:10.1016/j.ijplas.2007.07.013

Plunkett, B., Lebensohn, R. a., Cazacu, O., Barlat, F., 2006. Anisotropic yield function of hexagonal materials taking into account texture development and anisotropic hardening. Acta Mater. 54, 4159–4169. doi:10.1016/j.actamat.2006.05.009

Pöhlandt, K., Banabic, D., Lange, K., 2002. Equi-biaxial anisotropy coefficient used to describe the plastic behavior of sheet metal, in: ESAFORM 2002. Krakow, Poland., pp. 723–727.

Pottier, T., Vacher, P., Toussaint, F., Louche, H., Coudert, T., 2012. Out-of-plane Testing Procedure for Inverse Identification Purpose: Application in Sheet Metal Plasticity. Exp. Mech. 52, 951–963. doi:10.1007/s11340-011-9555-3

Prates, P.A., Oliveira, M.C., Fernandes, J. V., 2015. Identification of material parameters for thin sheets from single biaxial tensile test using a sequential inverse identification strategy. Int. J. Mater. Form. 547–571. doi:10.1007/s12289-015-

1241-z

Raabe, D., Wang, Y., Roters, F., 2005. Crystal plasticity simulation study on the influence of texture on earing in steel. Comput. Mater. Sci. 34, 221–234. doi:10.1016/j.commatsci.2004.12.072

Raemy, C., Manopulo, N., Hora, P., 2017. On the modelling of plastic anisotropy, asymmetry and directional hardening of commercially pure titanium: A planar Fourier series based approach. Int. J. Plast. 91, 182–204. doi:10.1016/j.ijplas.2017.02.010

Rockafellar, 1972. Convex Functions, in: Convex Analysis.

Teodosiu, C., Daniel, D., Cao, H.-L., Duval, J.-L., 1995. Modelling and simulation of the can-making process using solid finite elements. J. Mater. Process. Technol. 50, 133–143. doi:10.1016/0924-0136(94)01375-B

Tikhovskiy, I., Raabe, D., Roters, F., 2008. Simulation of earing of a 17% Cr stainless steel considering texture gradients. Mater. Sci. Eng. A 488, 482–490. doi:10.1016/j.msea.2007.11.063

Tikhovskiy, I., Raabe, D., Roters, F., 2007. Simulation of earing during deep drawing of an Al-3% Mg alloy (AA 5754) using a texture component crystal plasticity FEM. J. Mater. Process. Technol. 183, 169–175. doi:10.1016/j.jmatprotec.2006.10.006

Tritschler, M., Butz, A., Helm, D., Falkinger, G., Kiese, J., 2014. Experimental analysis and modeling of the anisotropic response of titanium alloy Ti-X for quasi-static loading at room temperature. Int. J. Mater. Form. 7, 259–273. doi:10.1007/s12289-013-1125-z

Walde, T., Riedel, H., 2007. Simulation of earing during deep drawing of magnesium alloy AZ31. Acta Mater. 55, 867–874. doi:10.1016/j.actamat.2006.09.007

Woodthorpe, J., Pearce, R., 1970. The anomalous behaviour of aluminium sheet under balanced biaxial tension. Int. J. Mech. Sci. 12, 341–347. doi:10.1016/0020-7403(70)90087-1

Yoon, J., Barlat, F., Dick, R., Karabin, M., 2006. Prediction of six or eight ears in a drawn cup based on a new anisotropic yield function. Int. J. Plast. 22, 174–193. doi:10.1016/j.ijplas.2005.03.013

Yoon, J.W., Dick, R.E., Barlat, F., 2008. Analytical prediction of earing for drawn and ironed cups., in: Hora, P. (Ed.), NUMISHEET2008 Proceeding. Interlaken, Switzerland, pp. 97–100.

Yoon, J.W., Dick, R.E., Barlat, F., 2011. A new analytical theory for earing generated from anisotropic plasticity. Int. J. Plast. 27, 1165–1184. doi:10.1016/j.ijplas.2011.01.002

Yoshida, F., Hamasaki, H., Uemori, T., 2013. A user-friendly 3D yield function to describe anisotropy of steel sheets. Int. J. Plast. 45, 119–139. doi:10.1016/j.ijplas.2013.01.010

Zhang, K., Holmedal, B., Hopperstad, O.S., Dumoulin, S., Gawad, J., Van Bael, A., Van Houtte, P., 2015. Multi-level modelling of mechanical anisotropy of commercial pure aluminium plate: Crystal plasticity models, advanced yield functions and parameter identification. Int. J. Plast. 66, 3–30. doi:10.1016/j.ijplas.2014.02.003

Zhao, Z., Mao, W., Roters, F., Raabe, D., 2004. A texture optimization study for

minimum earing in aluminium by use of a texture component crystal plasticity finite element method. Acta Mater. 52, 1003–1012. doi:10.1016/j.actamat.2003.03.001

Zidane, I., Guines, D., Léotoing, L., Ragneau, E., 2010. Development of an in-plane biaxial test for forming limit curve (FLC) characterization of metallic sheets. Meas. Sci. Technol. 21, 55701. doi:10.1088/0957-0233/21/5/055701

Chapter 5

Conclusions and Perspectives

This chapter highlights the main conclusions from this work and serves as a platform for future work concerning the use of constitutive models in the numerical simulation of sheet metal forming processes and the cares needed for the modeling of the material's orthotropic behavior.

(Page intentionally left blank)

5.1. Conclusions

Even though the deep-drawing of cylindrical cups has been extensively studied for more than sixty years (see *e.g.* Hill (1950) and Swift (1952)), still to this day it is a target of much attention since both the material's behavior and the process conditions have a strong impact in the final shape. Attesting to that is the fact that, for example, the Numisheet conference series present a benchmark related with cylindrical cup's forming in almost every meeting since 1999. In particular, the earing evolution and the wall thickness are known for being sensitive to both the material's yield stress and *r*-values in-plane directionalities.

In this context, the numerical simulation of the cylindrical cup's deep-drawing process was used to study the influence of the yield stresses on the material's behavior at the flange of the cup, *i.e.* submitted to blank holder action. For a sufficiently low blank holder force (sufficient only to avoid wrinkling), the flange material is subjected to an in-plane compression stress state. This means that, for an accurate modeling of the cup drawing, the material's mechanical behavior for compression stress states is important. Also, the process conditions play a major role in the numerical simulations results, since the stress state is also influenced by the friction coefficient and the type of control adopted for the blank-holder. This combined influence may contribute to improper conclusions concerning the ability of a yield criterion to properly describe the material behavior.

Taking into account the importance of the material's compression behavior, particular attention was given to the CPB06 yield criterion in order to analyze the role of the strength differential effect. In this context, anisotropy coefficients identification procedures were developed and implemented in the DD3MAT in-house code, for both the CB2001 and the CPB06 yield criteria. The procedure developed for the CPB06 was validated considering a 4-point beam bending test for both a zirconium and a magnesium alloy. The results highlight the ability of the CPB06 to describe the strain fields, including the shift of the neutral layer, which clearly results from the SD effect,

since the CB2001 is unable to capture it. The results clearly show that the CPB06 yield criterion is able to accurately describe both the in-plane anisotropy and tension–compression asymmetry, as well as different anisotropic behavior in tension and compression.

The combination of the knowledge obtained previously lead to the description of the mechanical behavior of a 2090-T3 aluminum alloy with two yield criteria which consider (CPB06), or not (CB2001), tension-compression asymmetry. Different sets of parameters were also identified for the CPB06, taking or not into account the strength differential effect. The results highlight the importance of an accurate description of the material yield stresses and *r*-values in-plane directionalities, for compression stress states, in order to have more accurate predictions of both the earing profile and the thickness distributions, even for a material presenting a small SD effect. In fact, the compression yield stresses directionalities seem to play a major role in the thickness prediction. The adoption of a flexible yield criterion, such as the CB2001, allows a proper prediction of the earing profile, but fails to capture the trend for the thickness distribution, since it imposes the same trend for the tensile and compression yield stresses directionalities. However, the CPB06 is not flexible enough to allow the simultaneous description of both the *r*-values and yield stresses, including the ones in compression.

In this context, the CPB06 with two linear transformations (CPB06ex2) was implemented in DD3IMP in-house code and a strategy for its anisotropy parameters identification was developed and implemented in DD3MAT. The analysis of the deep drawing of a cylindrical cup using an Alcoa 3104 commercial bodystock aluminum alloy was performed. The results highlight that this yield criterion is flexible enough to describe both the yield stresses and *r*-values directionalities, with the advantage that convexity can be guaranteed, as opposed to the CB2001 yield criterion. The comparison between the CPB06ex2 and the CB2001 yield criteria demonstrates the interconnection between the process conditions and the yield criteria adopted, particularly the influence that small changes in the stress state have in the directions of the plastic strain rates predicted.

In brief, this work contributes to raise awareness of some issues related with the correct modeling and use of more complex yield criteria, highlighting also the fact that

even metallic materials with cubic structure may present tension-compression asymmetry and that this experimental behavior should be taken into account.

5.2. Recommendations and Perspectives

This work contributes to the rise and better definition of some issues that deserve to be further analyzed in future research. These issues are related to both experimental and numerical details, as follows:

- The first is related with the availability of experimental results for uniaxial compression stress states. Even though some works try to address the difficulties related to compression test of metal sheet specimens, more reliable results are needed, if possible for higher strain values. This would allow the evaluation of the *r*-values for this compression stress state, in order to take them into account when performing the anisotropy parameters identification. Alternatively, in order to circumvent the necessary assumption of similarity between the tension and compression *r*-values, these can be estimated using crystal plasticity models.
- As highlighted in this study, the cylindrical cup geometry is very sensitive to the yield criteria adopted. In this context, some authors suggested its use for developing inverse procedures for the identification of the constitutive model parameters. The main difficulties associated with this approach result from the strong correlation between the constitutive model and the friction conditions, which dictate the material flow. However, as highlighted in this work, the impact of this interconnection can be minimized by using a proper control of the blank-holder. In that case, the experimental results from the cylindrical cup's deep drawing could be explored as a way to reduce the number of tests required for the identification of parameters of advanced yield criteria. Also in the experimental field, the contact conditions between tools and blank, in particular the friction conditions, should be better studied.
- This work was developed under the assumption that an associated flow rule is adopted. However, the results highlight that this assumption can impose additional difficulties in the accurate description of both the *r*-values and the yield stresses in plane directionalities. In this context, it would be interesting to compare the results

obtained with a non-associated flow rule coupled with a yield criterion capable of describing tension-compression asymmetry.

- The DD3MAT in-house code is specifically developed for the identification of anisotropy parameters using a classical approach. In this context, it constitutes an excellent laboratory for testing other optimization algorithms, or even the combination with other inverse analysis procedures, resorting to objective functions based on other type of experimental results. This could also involve the development of strategies that allow the simultaneous identification of the parameters for both the hardening law and the yield criteria.
- Lastly, this work was developed under the assumption that the yield surface shape remains unchanged during plastic deformation. However, in order to improve the numerical results, mainly for materials with HCP structure, it is recommended to take into account the evolution of the asymmetric yield surface, due to the relevant twinning effects present in these materials.

Appendix A

Cazacu and Barlat (2001) yield criterion anisotropy parameters identification

This appendix presents the main strategy implemented in the DD3MAT in-house code to improve the identification procedure of the anisotropy parameters of the Cazacu and Barlat (2001) yield criterion, taking into account the necessity to perform the assessment of the convexity condition.

(Page intentionally left blank)

A.1 Introduction

The Cazacu and Barlat (2001) yield criterion is known for being highly flexible, enabling the description of the behavior of strongly orthotropic metallic materials. The downfall of this yield criterion is that the conditions that guarantee the convexity of the yield surface are not established. In fact, the mathematical description of the yield surface in the three-dimensional space of the principal stresses must be closed, smooth and convex, following the Drucker's stability postulate. Thus, it is necessary to evaluate if the selected set of anisotropy parameters allows guaranteeing this condition. The strategy adopted to check the yield surface convexity, in some predefined planes, is based on the geometrical analysis of its shape as proposed by Soare et al. (2007). However, from the author's experience, the convexity test is a very time-consuming procedure. In this context, an algorithm is proposed which tries to improve the computational efficiency, while assuring the estimation of a proper set of anisotropy parameters.

A.2 Yield surface convexity test

The convexity test incorporated in the anisotropy parameters identification procedure is performed for several planes: (i) three defined by $\sigma_1 - \sigma_2$ (with $\sigma_3 = 0$), $\sigma_2 - \sigma_3$ (with $\sigma_1 = 0$) and $\sigma_1 - \sigma_3$ (with $\sigma_2 = 0$), and (ii) in the $\sigma_1 - \sigma_2$ plane for different values of shear stress, σ_{12}, such that $\sigma_{12} = x\sigma_1$ with $x = [0.1, 0.2, 0.3, 0.4, 0.5, 0.55]$. Figure A..1 schematically represents the geometrical analysis enabling the convexity test procedure. For each plane, the coordinates the points defining the yield surface is calculated for angles $\varphi \in [-2,182]$ as schematically shown in Figure A.1 (a) for $\varphi = -2$. This allows the definition of a set of points, with each point, P_φ, corresponding to an angle. The range for the angles φ assumes the condition that the yield surface is always symmetric. Moreover, increments of 1º are considered since it allows a good balance between accuracy and computational cost. In fact, the convexity check is

performed for each point P_φ considering two neighboring points, as schematically shown in Figure A.1 (b).

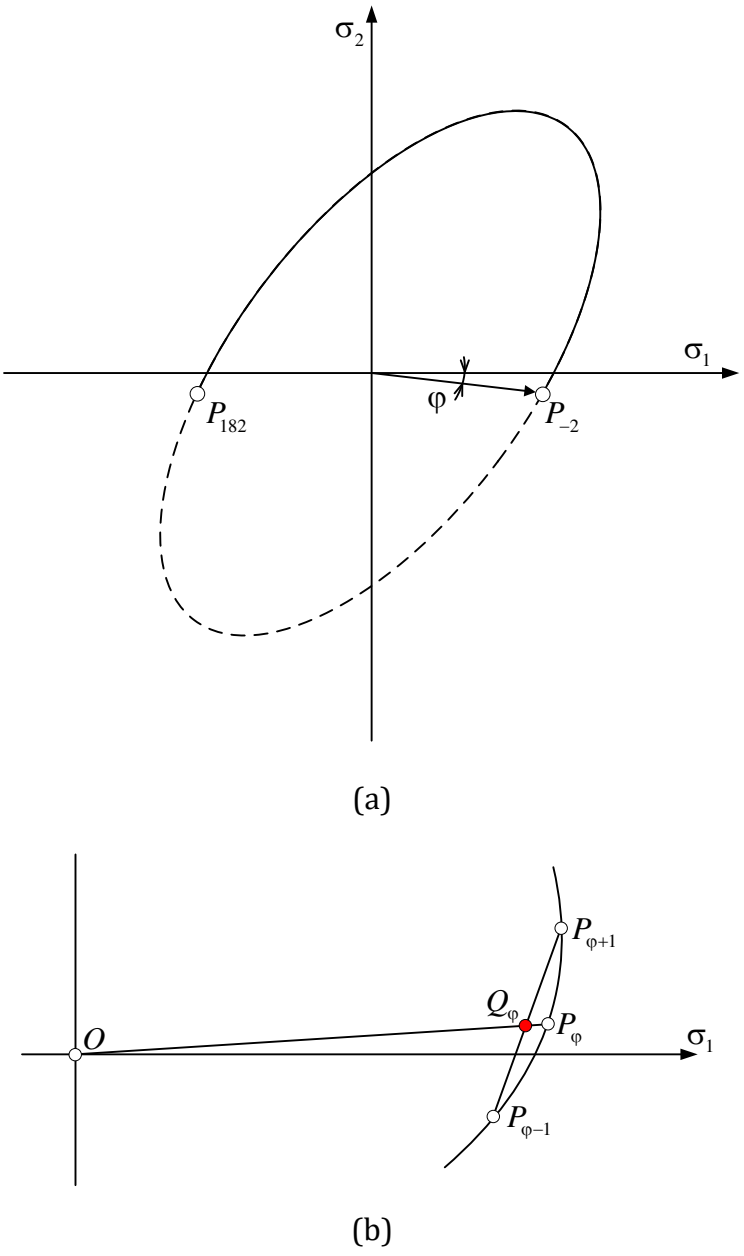

Figure A.1. Schematic representation of the convexity test for the $\sigma_1 - \sigma_2$ plane: (a) points of the yield surface used for the convexity test defined and (b) geometrical analysis for the convexity test.

The first step is to calculate the equation of the line segment defined by the two extreme points $\left[P_{\varphi-1} P_{\varphi+1} \right]$. In the second step, the equation of the line segment defined by the origin of the plane and the point under analysis, $\left[OP_\varphi \right]$, is defined. Afterwards,

the coordinates of the intersection point Q_φ, between the two previously mentioned line segments, are calculated. Finally, the length of the lines $\left[OP_\varphi\right]$ and $\left[OQ_{\varphi-1}\right]$ is calculated based on the Euclidean distance. The condition for convexity is given by

$$\left[OP_\varphi\right]_{lenght} \geq \left[OQ_\varphi\right]_{lenght}. \tag{A.1}$$

The general structure adopted for the convexity test algorithm is presented in Table A.1. Note that if the convexity condition is not verified at any point P_φ, no more checks are performed.

Table A.1. General scheme for the convexity test algorithm.

```
Begin
    Read A
    Do φ = −2 to 182
        Generate yield surface points, P_φ, for the plane in test
    End Do
    Do φ = −1-1 to 181
        Calculate equations for the two line segments [P_{φ−1}P_{φ+1}] and [OP_φ]
        Calculate intersection point Q_φ
        Calculate length of the two line segments [OP_φ] and [OQ_φ]
            If [OP_φ]_lenght ≥ [OQ_φ]_lenght Then
                The surface is convex
            Else
                The surface is not convex in the tested point
                Exit
            End If
    End Do
End
```

A.3 General algorithm implemented in DD3MAT

The general structure adopted for the integration of the convexity test algorithm with the downhill simplex method is presented in Table A.2. As shown in this table, the identification procedure can be performed without performing the convexity test. This

feature was adopted since, from the author's experience: (i) it enables a faster identification of the set of optimal anisotropy parameters, while retaining the possibility to evaluate *a posteriori* if it is convex and (ii) the convexity check makes the identification procedure sensitive to the initial solution. Thus, the optimal non-convex solution can be used as initial solution and to try to minimize its effect in the final solution. Therefore, the algorithm allows the user to use a pre-defined initial solution (defined in the mater1.dat file). Otherwise, it starts with the isotropic solution. The downhill simplex method is then applied as usual, to generate a new set of vertices in each iteration, I, named $\mathbf{A}_{\mathrm{v}}^{\mathrm{I}}$. When the convexity check is active, the selection of the optimal solution is performed taking into account if the anisotropy parameters set, $\mathbf{A}_{\mathrm{v}_{\min}}^{\mathrm{I}}$, passes the test. To help in this selection, large penalization value is assigned to the objective function, to each set that does not pass the test.

Table A.2. Scheme of the anisotropy parameters identification procedure implemented in DD3MAT, highlighting the integration of the convexity test algorithm.

Begin

Define the maximum number of iterations, *ItnMAX*

Convexity test? (On – Off)

Read initial solution from file mater1.dat? (Yes – No)

If convexity test is active **Then**

If initial solution is to be read from mater1.dat **Then**

Read file mater1.dat

Else

Initialize $\mathbf{A}$ to the isotropic solution

End if

Else

Initialize $\mathbf{A}$ to the isotropic solution

End if

Do While $\left| F\left(\mathbf{A}^{\mathrm{I}}_{\mathrm{v}_{\min}}\right) - F\left(\mathbf{A}^{\mathrm{I\text{-}1}}_{\mathrm{v}_{\min}}\right)\right| > 10^{-14}$ or $\mathrm{I} \le ItnMAX$

Apply the downhill simplex method to generate a new set of vertices, $\mathbf{A}^{\mathrm{I}}_{\mathbf{v}}$

Select the $\min F\left(\mathbf{A}^{\mathrm{I}}_{\mathbf{v}}\right) \rightarrow$ define $\mathrm{v}_{\min}$

If convexity test is active **Then**

Check convexity for $F\left(\mathbf{A}^{\mathrm{I}}_{\mathrm{v}_{\min}}\right)$

If $F\left(\mathbf{A}^{\mathrm{I}}_{\mathrm{v}_{\min}}\right)$ not convex **Then**

$F\left(\mathbf{A}^{\mathrm{I}}_{\mathrm{v}_{\min}}\right) = 10^{10}$

Select next vertice $\min F\left(\mathbf{A}^{\mathrm{I}}_{\mathbf{v}}\right) \rightarrow$ define $\mathrm{v}_{\min}$

End If

End if

End Do

End

(Page intentionally left blank)

Appendix B

Other publications resulting from the presented work

This appendix presents the resume of other scientific contributions that have been published in international scientific journals as well as in conference proceedings, including the oral presentation of the main results. The majority of the works correspond to examples of applications of numerical simulation to predict forming defects, highlighting the importance of advance yield criteria in the results accuracy.

(Page intentionally left blank)

B.1 Introduction

Within the framework of this thesis, the strategies and algorithms developed were tested using different sheet metal forming geometries, including the ones proposed within the Numisheet conferences. In this context, a list of these publications is presented to highlight the dissemination of the work performed and its contribution to the research field.

B.2 Journal articles

Neto, D.M., Oliveira, M.C., Dick, R.E., **Barros, P.D.**, Alves, J.L., Menezes, L.F. **(2017)**, Numerical and experimental analysis of wrinkling during the cup drawing of an AA5042aluminium alloy. International Journal of Material Forming, 10:34–7. http://dx.doi.org/10.1007/s12289-015-1265-4.

Abstract

The recent trend to reduce the thickness of metallic sheets used in forming processes strongly increases the likelihood of the occurrence of wrinkling. Thus, in order to obtain defect-free components, the prediction of this kind of defect becomes extremely important in the tool design and selection of process parameters. In this study, the sheet metal forming process proposed as a benchmark in the Numisheet 2014 conference is selected to analyse the influence of the tool geometry on wrinkling behaviour, as well as the reliability of the developed numerical model. The side-wall wrinkling during the deep drawing process of a cylindrical cup in AA5042 aluminium alloy is investigated through finite element simulation and experimental measurements. The material plastic anisotropy is modelled with an advanced yield criterion beyond the isotropic (von Mises) material behaviour. The results show that the shape of the wrinkles predicted by the numerical model is strongly affected by the finite element mesh used in the blank discretization. The accurate modeling of the

plastic anisotropy of the aluminium alloy yields numerical results that are in good agreement with the experiments, particularly the shape and location of the wrinkles. The predicted punch force evolution is strongly influenced by the friction coefficient used in the model. Moreover, the two punch geometries provide drawn cups with different wrinkle waves, mainly differing in amplitude.

Barros, P.D., Oliveira, M.C., Alves, J.L. and Menezes L.F. (**2013**), Earing Prediction in Drawing and Ironing Processes Using an Advanced Yield Criterion, Key Engineering Materials, 554–557, 2266–2276.
http://dx.doi.org/10.4028/www.scientific.net/KEM.554-557.2266.

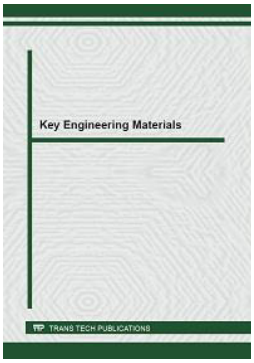

Abstract

This work aims to contribute to the understanding of the role/influence of advanced yield criteria on the earing profile prediction after drawing and ironing, for a cylindrical cup benchmark proposed at the NUMISHEET 2011 conference. Two typical materials used for can-making were considered and studied: an AA5042 aluminum alloy and an AKDQ steel. The drawing and ironing operations are performed on a special die which allows drawing and ironing in one single punch stroke in order to simplify the real process. The benchmark results report include, for each material: (i) the earing profile after drawing and ironing, presenting the cup height evolution with the angle from the rolling direction, and (ii) the evolution of punch force with punch stroke. This work presents a comparison between experimental and numerical results obtained for the aforesaid benchmark with DD3IMP in-house solver, using two sets of parameters for the Cazacu and Barlat 2001 yield criterion, identified based on uniaxial tensile, equi-biaxial tension and disc compression test results. The first set uses the initial yield stress values while the second one used the flow stress values for an accumulated plastic work of 20 MPa. The results highlight the different impact of the experimental data in the earing prediction for both materials: the results for the second set are

slightly improved for the AKDQ steel while for AA5042 the effect is negligible. The improved earing prediction obtained with the second set for the AKDQ steel seems to result from a better description of the stress states that occur in the flange zone.

B.3 Conference proceedings

Barros P.D., Amaral R.R., Oliveira M.C., Santos A.D., Alves J.L. and Menezes L.F. **(2017)**. Formability assessment of a cup drawing under complex nonlinear strain paths, Proceedings of CMN 2017 - Congress on Numerical Methods in Engineering, International Center for Numerical Methods in Engineering (CIMNE) Valencia, Spain, 3-5 July, ISBN: 978-84-947311-0-5

(With oral presentation)

Abstract

This work presents a study on the numerical prediction of failure of a can after drawing, reverse redrawing and expansion, as proposed under the NUMISHEET 2016 conference. Since this forming operation induces complex nonlinear strain paths on the material, a good description of the plastic anisotropy coupled with an accurate failure model is mandatory. Therefore, in order to assess the accuracy of the orthotropic behaviour of the material, the earing and the thickness profiles, after the reverse redrawing operation are also evaluated. Two different materials are considered: a TH330 steel and an AA5352 aluminium. The orthotropic behaviour of both materials is modelled considering the Cazacu and Barlat 2001 (CB2001) yield criterion, aiming for an accurate description of both yield stresses and *r*-values directionalities. In this context, a sensitivity study is performed, on the material parameter identification, to evaluate the impact of small variations of the experimental *r*-values. Regarding the failure model, the strain based Forming Limit Diagrams (FLD) is analysed as well as a thinning rate approach. The results show that the CB2001 can accurately predict the earing profile for both materials, as well as the thickness profile, confirming the importance of an accurate prediction of both yield stresses and *r*-values

directionalities. Also, the numerical results show that the failure timing and location are dependent on the set of anisotropy parameters used, while also influencing the thinning rate.

Barros, P.D., Carvalho, P.D., Alves, J.L., Oliveira, M.C., Menezes, L.F. **(2016)**. DD3MAT - a code for yield criteria anisotropy parameters identification. Journal of Physics: Conference Series, 734 032053 IOP Publishing, http://dx.doi.org/10.1088/1742-6596/734/3/032053.

(With oral presentation)

Abstract

This work presents the main strategies and algorithms adopted in the DD3MAT in-house code, specifically developed for identifying the anisotropy parameters. The algorithm adopted is based on the minimization of an error function, using a downhill simplex method. The set of experimental values can consider yield stresses and *r*-values obtained from in-plane tension, for different angles with the rolling direction (RD), yield stress and r -value obtained for biaxial stress state, and yield stresses from shear tests performed also for different angles to RD. All these values can be defined for a specific value of plastic work. Moreover, it can also include the yield stresses obtained from in-plane compression tests. The anisotropy parameters are identified for an AA2090-T3 aluminum alloy, highlighting the importance of the user intervention to improve the numerical fit.

Barros, P.D., Alves, J.L., Oliveira, M., Menezes, L.F. **(2016)**. Tension-compression asymmetry modelling: strategies for anisotropy parameters identification. NUMIFORM 2016: The 12th International Conference on Numerical Methods in Industrial Forming Processes. MATEC Web of Conferences http://dx.doi.org/10.1051/matecconf/20168005002.

(With oral presentation)

Abstract

This work presents details concerning the strategies and algorithms adopted in the fully implicit FE solver DD3IMP to model the orthotropic behavior of metallic sheets and the procedure for anisotropy parameters identification. The work is focused on the yield criterion developed by Cazacu, Plunkett and Barlat, 2006, which accounts for both tension–compression asymmetry and orthotropic plastic behavior. The anisotropy parameters for a 2090-T3 aluminum alloy are identified accounting, or not, for the tension-compression asymmetry. The numerical simulation of a cup drawing is performed for this material, highlighting the importance of considering tension-compression asymmetry in the prediction of the earing profile, for materials with cubic structure, even if this phenomenon is relatively small.

Barros, P.D., Oliveira, M.C., Alves, J.L., Andrade-Campos, A., Menezes, L.F. **(2015)**. Modelling of tension-compression asymmetry and orthotropic anisotropy in case of thin metallic sheets: identification procedure and case studies. In: Hora, P. (Ed.), Institute of Virtual Manufacturing. ETH Zurich, Zurich, pp. 149–154.

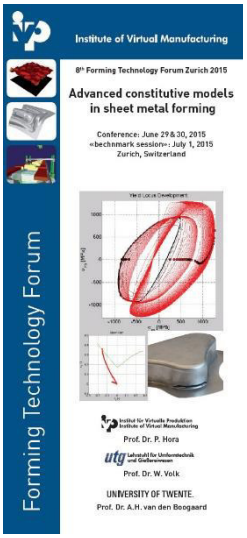

(With oral presentation)

Abstract

This work presents some details concerning the implementation of the yield criterion developed by Cazacu et al. (2006), which accounts for both tension–compression asymmetry and orthotropic anisotropy in plastic flow, in the implicit DD3IMP finite element solver. The work mainly focuses on the sensitivity analysis of the constitutive parameters of the yield criterion, and on an identification procedure when applied to thin metallic sheets. The identification procedure is exemplified for two materials, a magnesium and a zirconium alloy, taking into account the uniaxial tension and compression results as well the *r*-values, in several directions from the rolling direction. Due to the experimental difficulties on uniaxial compression tests in case of thin metallic sheets, an identification procedure that takes into account only uniaxial tensile data and the biaxial stress value is proposed, based on the equivalence between the equibiaxial and the through-thickness uniaxial compression stress states. The results show that it is possible to characterize the orthotropic behavior and the strength differential effects, even if uniaxial compression data is not available, using the proposed procedure.

Barros, P.D., Oliveira, M.C., Alves, J.L., Menezes, L.F. **(2014)**. Forming limits predictability under nonlinear strain paths: A classical approach using FLC, FLC 2014 workshop documentation, ETH Zurich, Switzerland, p.11.

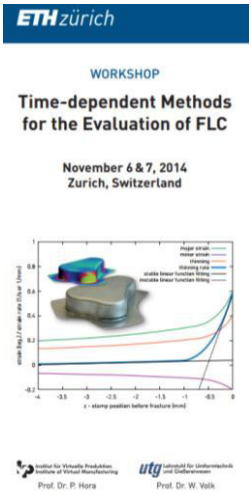

(With oral presentation)

Abstract

This work presents a study on the predictability of forming limits under nonlinear strain paths for a draw panel with a non-axisymmetric reversed dome-shape at the center, proposed under the NUMISHEET 2014 conference [1]. In order to predict the failure timing and location, a classical approach using the FLC's provided by the Benchmark committee was used. The finite element analysis was performed with DD3IMP in-house code. Thus, this approach considers the strain forming limits as though they were static during the deformation process. The numerical model considers all stages including the coupons preformed and springback between preforming and clamping as well as the one resulting from the deformation induced by the axisymmetric and the elliptical tools. This work presents the comparison between experimental and numerical results obtained for the DP600 steels. Globally, the results indicate a good agreement between the experimental and the predicted punch force evolution, for the different process conditions. Also, good agreement was observed for failure location, timing and strain path evolution for some predefined points. The results highlight that a proper material and process modelling, including numerical parameters, are important for predicting the punch force evolution and, consequently, the strain paths evolution, whatever the method used for failure analysis.

Barros, P.D., Simões, V.M., Neto, D.M., Oliveira, M.C., Alves, J.L., and Menezes, L.F. **(2013)**. On the influence of the yield parameters identification procedure in cylindrical cups earing prediction. AIP Conference Proceedings, 1567:512–515. http://dx.doi.org/10.1063/1.4850024

(With oral presentation)

Abstract

This work presents a study concerning the deep drawing process of a cylindrical cup, following the process conditions defined on the BENCHMARK 1 - Earing Evolution During Drawing and Ironing Processes, of NUMISHEET 2011. The deep drawing operation is analyzed for an AA5042 aluminum alloy, which orthotropic behavior is described using the Cazacu and Barlat, 2001 yield criterion. The constitutive parameters were determined based on the experimental data obtained from tensile tests, with different orientations to the rolling direction, disk compression test and the equibiaxial tension test, using DD3MAT in-house code. An analytical approach that relates the earing profile with the ones of both *r*-values and yield stresses is used to understand the influence of the identification procedure on the analytically and numerically predicted earing profile. The numerical simulations of the forming process were performed using DD3IMP in-house code. The analysis shows that, although earing is generally assumed as being coupled to the *r*-values profile, it is also important that the yield criterion captures the relative differences of the yield stress profile.

Barros, P.D., Oliveira, M.C., Alves, J.L., Menezes, L.F., **(2013)**. Influence of the yield parameters identification procedure in earing prediction, Proceedings of CMN 2013 - Congress on Numerical Methods in Engineering, Spanish Society for Numerical Methods in Engineering (SEMNI), Bilbao, Spain, 25-28 June. Complete article in electronic format.

(With oral presentation)

Abstract

This work concerns the deep drawing and ironing processes involved in the production of a cylindrical cup. The process conditions considered are the ones of the BENCHMARK 1 - Earing Evolution During Drawing and Ironing Processes, proposed under the NUMISHEET 2011 conference. The operations are performed considering two typical body stock materials: AA5042 aluminum alloy and AKDQ steel. The results analyzed are the cup heights after both drawing and ironing processes as well as the punch force evolution. In this work, two yield criteria were considered: Hill'48 and Cazacu and Barlat, 2001. The constitutive parameters for both yield criteria were determined using DD3MAT in-house code based on the benchmark experimental data, which includes results for tensile tests, with different orientations to the rolling direction, for the disk compression test and for the equibiaxial tension test. Different strategies are adopted for estimating the objective function weights coefficients. The numerical simulations of the forming process are performed using DD3IMP in-house code. The numerical results are compared with the experimental ones reported in the NUMISHEET 2011 conference proceedings. Globally, the numerical results highlight the sensitivity of the earing prediction to the yield criterion selected and the strategy used to identify the yield parameters.

Barros, P.D., Alves, J.L., Oliveira, M.C., Menezes, L.F. **(2012)**. Earing evolution during drawing and ironing processes, WCCM 10th World Congress on Computational Mechanics, Sao Paulo, pp. 3954–3973.

Abstract

This work presents a study concerning both the deep drawing and ironing processes. The process conditions considered are the ones of the BENCHMARK 1 - Earing Evolution During Drawing and Ironing Processes, proposed under the NUMISHEET 2011 conference. The deep drawing and ironing operations are performed considering two typical body stock materials: AA5042 aluminum alloy and AKDQ steel. The results analyzed are the average cup heights after drawing and ironing processes as well as the required punch load. Two yield criteria were considered: Hill'48 and Cazacu and Barlat, 2001. The constitutive parameters for the Hill'48 and the Cazacu and Barlat, 2001 were determined based on the experimental results for tensile tests with different orientations to the rolling direction, disk compression test and the equibiaxial tension test, using DD3MAT in-house code. The numerical simulations of the forming process are performed using DD3IMP in-house code. The blank sheet is discretized using 3D solid elements, allowing the accurate description of the contact conditions during the ironing process. The numerical results are compared with the experimental and numerical ones reported in the NUMISHEET 2011 conference proceedings. Globally, the numerical results show that the earing prediction is sensitive to the blank holder modeling, the yield criterion selected, the work hardening law and the strategy used to identify the materials parameters.

Overall list of references

Alart, P., Curnier, A., 1991. A mixed formulation for frictional contact problems prone to Newton like solution methods. Comput. Methods Appl. Mech. Eng. 92, 353–375.

Alves, J.L., Bouvier, S., Oliveira, M.C., Menezes, L.F., 2005. Drawbeads : to Be or Not to Be 655–660.

Alves, J.L.D.C.M., 2003. Simulação numérica do processo de estampagem de chapas metálicas - Modelação mecânica e métodos numéricos 403.

Andrade-Campos, A., De-Carvalho, R., Valente, R.A.F., 2012. Novel criteria for determination of material model parameters. Int. J. Mech. Sci. 54, 294–305. doi:10.1016/j.ijmecsci.2011.11.010

Aretz, H., Barlat, F., 2013. New convex yield functions for orthotropic metal plasticity. Int. J. Non. Linear. Mech. 51, 97–111. doi:10.1016/j.ijnonlinmec.2012.12.007

Armstrong, P.J., Frederick, C.O., 1966. A Mathematical Representation of the Multi Axial Bauschinger Effect.

Avril, S., Bonnet, M., Bretelle, A.S., Grédiac, M., Hild, F., Ienny, P., Latourte, F., Lemosse, D., Pagano, S., Pagnacco, E., Pierron, F., 2008. Overview of identification methods of mechanical parameters based on full-field measurements. Exp. Mech. 48, 381–402. doi:10.1007/s11340-008-9148-y

Ayres, R.A., Brazier, W.G., Sajewski, V.F., 1978. Evaluating the GMR-Limiting Dome Height Test as a new measure of press formability near plane strain. J. Appl. Metalwork. 1, 41–49. doi:10.1007/BF02833958

Banabic, D., 2010. Sheet Metal Forming Processes, Springer. Springer-Verlag Berlin Heidelberg. doi:10.1007/978-3-540-88113-1

Banabic, D., Aretz, H., Comsa, D.S., Paraianu, L., 2005a. An improved analytical description of orthotropy in metallic sheets. Int. J. Plast. 21, 493–512. doi:10.1016/j.ijplas.2004.04.003

Banabic, D., Comsa, D.S., Sester, M., Selig, M., Kubli, W., Mattiasson, K., Sigvant, M., 2008. Influence of constitutive equations on the accuracy of prediction in sheet metal forming simulation. Numisheet 2008 2–6.

Banabic, D., Vulcan, M., Siegert, K., 2005b. Bulge Testing under Constant and Variable Strain Rates of Superplastic Aluminium Alloys. CIRP Ann. - Manuf. Technol. 54, 205–208. doi:10.1016/S0007-8506(07)60084-5

Banu, M., Bouvier, S., Castelnau, O., Haddadi, H., Gardey, B., Girjob, C., Levee, P., Maier, C., Tabacaru, V., Teodosiu, C., 2001. Selection and identification of elastoplastic models for the materials used in Benchmarks, Digital Die Design Systems (3DS), WP3, Task 1, 18-Months progress report. LPMTM - CNRS.

Baptista, A., 2006. Modelação Mecânica e Simulação Numérica do Processo de Estampagem Multi-Etapas Modelação Mecânica e Simulação Numérica do Processo de Estampagem Multi-Etapas – Aplicação ao processo de estampagem de chapas soldadas –.

Barlat, F., Aretz, H., Yoon, J.W., Karabin, M.E., Brem, J.C., Dick, R.E., 2005. Linear transfomation-based anisotropic yield functions. Int. J. Plast. 21, 1009–1039. doi:10.1016/j.ijplas.2004.06.004

Barlat, F., Becker, R.C., Hayashida, Y., Maeda, Y., Yanagawa, M., Chung, K., Brem, J.C., Lege, D.J., Matsui, K., Murtha, S.J., Hattori, S., 1997a. Yielding description for solution strengthened aluminum alloys. Int. J. Plast. 13, 385–401. doi:http://dx.doi.org/10.1016/S0749-6419(97)80005-8

Barlat, F., Brem, J.C., Yoon, J.W., Chung, K., Dick, R.E., Lege, D.J., Pourboghrat, F., Choi, S.H., Chu, E., 2003. Plane stress yield function for aluminum alloy sheets - Part 1: Theory. Int. J. Plast. 19, 1297–1319. doi:10.1016/S0749-6419(02)00019-0

Barlat, F., Gracio, J.J., Lee, M.G., Rauch, E.F., Vincze, G., 2011. An alternative to kinematic hardening in classical plasticity. Int. J. Plast. 27, 1309–1327. doi:10.1016/j.ijplas.2011.03.003

Barlat, F., Lege, D.J., Brem, J.C., 1991a. A six-component yield function for anisotropic materials. Int. J. Plast. 7, 693–712. doi:10.1016/0749-6419(91)90052-Z

Barlat, F., Lege, D.J., Brem, J.C., Warren, C.J., 1991b. Constitutive behavior for anisotropic materials and application to a 2090 Al±Li alloy., in: Lowe, T.., Rollett, A.., Follansbee, P.., Daehn, G.. (Eds.), TMS Annual Meeting,. TMS, New Orleans, LA, pp. 189–203.

Barlat, F., Maeda, Y., Chung, K., Yanagawa, M., Brem, J.C., Hayashida, Y., Lege, D.J., Matsui, K., Murtha, S.J., Hattori, S., Becker, R.C., Makosey, S., 1997b. Yield function development for aluminum alloy sheets. J. Mech. Phys. Solids 45, 1727–1763. doi:10.1016/S0022-5096(97)00034-3

Barlat, F., Yoon, J.W., Cazacu, O., 2007. On linear transformations of stress tensors for the description of plastic anisotropy. Int. J. Plast. 23, 876–896. doi:10.1016/j.ijplas.2006.10.001

Barros, P.D., Carvalho, P.D., Alves, J.L., Oliveira, M.C., Menezes, L.F., 2016. DD3MAT - a code for yield criteria anisotropy parameters identification., in: Journal of Physics: Conference Series. doi:10.1088/1742-6596/734/3/032053

Belytschko, T., 1977. Explicit integration of structural problems. Finite Elem. nonlinear Mech. 2, 697–720.

Bleck, W., Blumbach, M., 2005. Laser-aided flow curve determination in hydraulic bulging. Steel Res. Int. 76, 125–130.

Bonte, M.H.A., 2007. Optimisation strategies for metal forming processes 254.

Bourne, L., Hill, R., 1950. LX. On the correlation of the directional properties of boiled shee in tension and cupping tests. Philos. Mag. Ser. 7 41, 671–681. doi:10.1080/14786445008560998

Bouvier, S., Alves, J.L., Oliveira, M.C., Menezes, L.F., 2005. Modelling of anisotropic work-hardening behaviour of metallic materials subjected to strain-path changes. Comput. Mater. Sci. 32, 301–315. doi:10.1016/j.commatsci.2004.09.038

Bouvier, S., Haddadi, H., Levée, P., Teodosiu, C., 2006. Simple shear tests: Experimental techniques and characterization of the plastic anisotropy of rolled sheets at large strains. J. Mater. Process. Technol. 172, 96–103. doi:10.1016/j.jmatprotec.2005.09.003

Bridgman, P.W., 1952. Studies in Large Plastic Flow and Fracture: With Special Emphasis on the Effects of Hydrostatic Pressure, 1st ed. McGraw Hill, New York.

Bridgman, P.W., 1947. The Effect of Hydrostatic Pressure on the Fracture of Brittle Substances 246. doi:10.1063/1.1697610

Bron, F., Besson, J., 2004. A yield function for anisotropic materials Application to aluminum alloys. Int. J. Plast. 20, 937–963. doi:10.1016/j.ijplas.2003.06.001

Cazacu, O., Barlat, F., 2004. A criterion for description of anisotropy and yield differential effects in pressure-insensitive metals. Int. J. Plast. 20, 2027–2045. doi:10.1016/j.ijplas.2003.11.021

Cazacu, O., Barlat, F., 2001. Generalization of drucker's yield criterion to orthotropy. Math. Mech. Solids 6, 613–630. doi:10.1177/108128650100600603

Cazacu, O., Plunkett, B., Barlat, F., 2006. Orthotropic yield criterion for hexagonal closed packed metals. Int. J. Plast. 22, 1171–1194. doi:10.1016/j.ijplas.2005.06.001

Chaboche, J.L., 2008. A review of some plasticity and viscoplasticity constitutive theories 24, 1642–1693. doi:10.1016/j.ijplas.2008.03.009

Chaparro, B., 2006. Comportamento plástico de materiais metálicos: identificacao e optimizacao de parâmetros.

Chaparro, B.M., Thuillier, S., Menezes, L.F., Manach, P.Y., Fernandes, J. V., 2008. Material parameters identification: Gradient-based, genetic and hybrid optimization algorithms. Comput. Mater. Sci. 44, 339–346. doi:10.1016/j.commatsci.2008.03.028

Cooreman, S., Lecompte, D., Sol, H., Vantomme, J., Debruyne, D., 2008. Identification of mechanical material behavior through inverse modeling and DIC. Exp. Mech. 48, 421–433. doi:10.1007/s11340-007-9094-0

Dick, R.E., Yoon, J.W., Huh, H.S., Bae, G., 2011. BM1 – Earing Evolution During Drawing and Ironing processes, Part C Benchmark Problems and Results, in: 8th International Conference and Workshop on Numerical Simulation of 3D Sheet Metal Forming Processes. pp. 171–226.

DIN8582, 2003. Fertigungsverfahren Umformen, in: DIN Deutsches Institut Für Normung. Beuth Verlag GmbH, Berlin, Germany.

Drucker, D.C., 1949. Relation of experiments to mathematical theories of plasticity,

Journal of Applied Mechanics. ASME 16, A349–A357.

Eggertsen, P.-A., Mattiasson, K., Hertzman, J., 2011. A Phenomenological Model for the Hysteresis Behavior of Metal Sheets Subjected to Unloading/Reloading Cycles. J. Manuf. Sci. Eng. 133, 61021. doi:10.1115/1.4004590

Eggleston, 1958. General properties of convex functions, in: Convexity.

Galster, E.M. and D., 1963. A method for producing a defined uniform biaxial tensile stress field. Br. J. Appl. Phys. 14, 810.

Gelin, J.C., Delassus, P., Fontaine, J.F., 1994. Experimental and numerical modelling of the effects of process parameters in the aquadraw deep drawing 329–334.

Gelin, J.C., Ghouati, O., 1995. The Inverse Approach for the Determination of Constitutive Equations in Metal Forming. CIRP Ann. - Manuf. Technol. 44, 189–192. doi:10.1016/S0007-8506(07)62304-X

Genevois, P., 1992. Etude expérimentale et modélisation du comportement plastique anisotrope de tôles d'acier en grandes transformations. Institut national polytechnique de Grenoble, Grenoble, FRANCE.

Gotoh, M., Ishisé, F., 1978. A finite element analysis of the rigid-plastic deformation of the flange in a deep-drawing process based on a fourth-degree yield function. Int. J. Mech. Sci. 20, 423–435. doi:https://doi.org/10.1016/0020-7403(78)90032-2

Grytten, F., Holmedal, B., Hopperstad, O.S., Børvik, T., 2008. Evaluation of identification methods for YLD2004-18p. Int. J. Plast. 24, 2248–2277. doi:10.1016/j.ijplas.2007.11.005

Guery, A., Hild, F., Latourte, F., Roux, S., 2016. Identification of crystal plasticity parameters using DIC measurements and weighted FEMU. Mech. Mater. 100, 55–71. doi:10.1016/j.mechmat.2016.06.007

Güner, A., Soyarslan, C., Brosius, A., Tekkaya, A.E., 2012. Characterization of anisotropy of sheet metals employing inhomogeneous strain fields for Yld2000-2D yield function. Int. J. Solids Struct. 49, 3517–3527. doi:10.1016/j.ijsolstr.2012.05.001

Heleno, R., 2012. Desenvolvimento de uma plataforma interactiva para a utilização do DD3IMP.

Héripré, E., Dexet, M., Crepin, J., Gélébart, L., Roos, A., Bornert, M., Caldemaison, D., 2007. Coupling between experimental measurements and polycristal finte element calculations for micromechanical study of metallic materials.

Hershey, A.V., 1954. The plasticity of an isotropic aggregate of anisotropic face centered cubic crystals. J. Appl. Mech. 21, 241–249.

Hill, R., 1950. The mathematical theory of plasticity, 1st Editio. ed. Oxford University press, Oxford.

Hill, R., 1948. A Theory of the Yielding and Plastic Flow of Anisotropic Metals. Proc. R. Soc. A Math. Phys. Eng. Sci. 193, 281–297. doi:10.1098/rspa.1948.0045

Hockett, J.E., Sherby, O.D., 1975. Large strain deformation of polycrystalline metals at low homologous temperatures. J. Mech. Phys. Solids 23, 87–98. doi:10.1016/0022-

5096(75)90018-6

Hollomon, J.H., 1945. Tensile deformation. Trans. Metall. Soc. AIME 162, 268–290.

Hosford, W.F., 1972. A Generalized Isotropic Yield Criterion. J. Appl. Mech. 39, 607–609.

Hußnätter, W., Merklein, M., 2008. Characterization of material behavior under pure shear condition. Int. J. Mater. Form. 1, 233–236. doi:DOI 10.1007/s12289-008-0 - 3 59 7 #

ISO, 2004. Metallic materials — Sheet and strip — Determination of biaxial stress-strain curve by means of bulge test with optical measuring systems.

Karafillis, A.P., Boyce, M.C., 1993. A general anisotropic yield criterion using bounds and a transformation weighting tensor. J. Mech. Phys. Solids 41, 1859–1886. doi:10.1016/0022-5096(93)90073-O

Khalfallah, A., Luís, J., Cristina, M., Filipe, L., 2015. Simulation Modelling Practice and Theory Influence of the characteristics of the experimental data set used to identify anisotropy parameters. Stimul. Model. Pract. THEORY 53, 15–44. doi:10.1016/j.simpat.2015.02.007

Khan, A.S., Huang, S., 1995. Continuum theory of plasticity. Wiley, New York.

Klinger, L.J., Sachs, G., 1948. Plastic flow characteristics of aluminum alloy plates. J. Aero. Sci. 15, 590–604.

Knezevic, M., Beyerlein, I.J., Brown, D.W., Sisneros, T.A., Tomé, C.N., 2013. A polycrystal plasticity model for predicting mechanical response and texture evolution during strain-path changes: Application to beryllium. Int. J. Plast. 49, 185–198. doi:10.1016/j.ijplas.2013.03.008

Koç, M., Billur, E., Cora, Ö.N., 2011. An experimental study on the comparative assessment of hydraulic bulge test analysis methods. Mater. Des. 32, 272–281. doi:10.1016/j.matdes.2010.05.057

Kuwabara, T., 2007. Advances in experiments on metal sheets and tubes in support of constitutive modeling and forming simulations. Int. J. Plast. 23, 385–419. doi:10.1016/j.ijplas.2006.06.003

Kuwabara, T., Ikeda, S., Kuroda, K., 1998. Measurement and analysis of differential work hardening in cold-rolled steel sheet under biaxial tension. J. Mater. Process. Technol. 80–81, 517–523. doi:10.1016/S0924-0136(98)00155-1

Kuwabara, T., Saito, R., Hirano, T., Oohashi, N., 2009. Difference in tensile and compressive flow stresses in austenitic stainless steel alloys and its effect on springback behavior. Int. J. Mater. Form. 2, 499–502. doi:10.1007/s12289-009-0520-y

Kuwabara, T., Van Bael, A., Iizuka, E., 2002. Measurement and analysis of yield locus and work hardening characteristics of steel sheets wtih different r-values. Acta Mater. 50, 3717–3729. doi:10.1016/S1359-6454(02)00184-2

Lagarias, J.C., Reeds, J.A., Wright, M.H., Wright, P.E., 1998. Convergence Properties of the Nelder--Mead Simplex Method in Low Dimensions. SIAM J. Optim. 9, 112–147. doi:10.1137/S1052623496303470

Lăzărescu, L., Comşa, D.S., Banabic, D., 2011. Analytical and Experimental Evaluation of the Stress-Strain Curves of Sheet Metals by Hydraulic Bulge Tests. Key Eng. Mater. 473, 352–359. doi:10.4028/www.scientific.net/KEM.473.352

Li, H., Fu, M.W., Lu, J., Yang, H., 2011. Ductile fracture: Experiments and computations. Int. J. Plast. 27, 147–180. doi:10.1016/j.ijplas.2010.04.001

Lim, H., Battaile, C.C., Carroll, J.D., Boyce, B.L., Weinberger, C.R., 2015. A physically based model of temperature and strain rate dependent yield in BCC metals: Implementation into crystal plasticity. J. Mech. Phys. Solids 74, 80–96. doi:10.1016/j.jmps.2014.10.003

Lippmann, H., 1970. Matrixungleichungen und die Konvexität der Fließfläche. ZAMM - J. Appl. Math. Mech. 50, 134–137.

Logan, R.W., Hosford, W.F., 1980. Upper-bound Anisotropic Yield Locus Calculations Assuming (111)-Pencil Glide. Int. J. Mech. Sci. 22, 419–430.

Ludwik, P., 1909. Elemente der Technologischen Mechanik. doi:10.1007/978-3-662-40293-1

Martins, B., Santos, A.D., Teixeira, P., Ito, K., Mori, N., 2013. Determination of flow curve using bulge test and calibration of damage for ito-goya models. Key Eng. Mater. 554–557, 182–189. doi:10.4028/www.scientific.net/KEM.554-557.182

Martins, B., Teixeira, P., Santos, A.D., 2012. Study on the flow stress determination using hydraulic bulge test, in: Andrade-Campos, A., Lopes, N., Valente, R.A.., Varum, H. (Eds.), Proceedings of the First ECCOMAS Young Investigators Conference Computational Methods in Applied Sciences. Aveiro, Portugal.

Meinders, T., Burchitz, I.A., Bonte, M.H.A., Lingbeek, R.A., 2008. Numerical product design: Springback prediction, compensation and optimization. Int. J. Mach. Tools Manuf. 48, 499–514. doi:10.1016/j.ijmachtools.2007.08.006

Menezes, L.F., Teodosiu, C., 2000. Three-dimensional numerical simulation of the deep-drawing process using solid finite elements. J. Mater. Process. Technol. 97, 100–106. doi:10.1016/S0924-0136(99)00345-3

Miyauchi, K., 1984. A proposal of a planar simple shear test in sheet metals. Sci Pap. Inst Phys Chem 78, 27–40.

Montay, G., François, M., Tourneix, M., Guelorget, B., Vial-Edwards, C., Lira, I., 2007. Strain and strain rate measurement during the bulge test by electronic speckle pattern interferometry. J. Mater. Process. Technol. 184, 428–435. doi:10.1016/j.jmatprotec.2006.12.013

Mulder, J., Vegter, H., Aretz, H., Keller, S., Van Den Boogaard, A.H., 2015. Accurate determination of flow curves using the bulge test with optical measuring systems. J. Mater. Process. Technol. 226, 169–187. doi:10.1016/j.jmatprotec.2015.06.034

Mulder, J., Vegter, H., Aretz, H., van den Boogaard, A.H., 2013. Accurate evaluation method for the hydraulic bulge test. Key Eng. Mater. 554–557, 33–40. doi:10.4028/www.scientific.net/KEM.554-557.33

Narasimhan, N., Lovell, M., 1999. Predicting springback in sheet metal forming: An

explicit to implicit sequential solution procedure. Finite Elem. Anal. Des. 33, 29–42. doi:10.1016/S0168-874X(99)00009-8

Nasser, A., Yadav, A., Pathak, P., Altan, T., 2010. Determination of the flow stress of five AHSS sheet materials (DP 600, DP 780, DP 780-CR, DP 780-HY and TRIP 780) using the uniaxial tensile and the biaxial Viscous Pressure Bulge (VPB) tests. J. Mater. Process. Technol. 210, 429–436. doi:10.1016/j.jmatprotec.2009.10.003

Neto, D.M., 2014. Numerical simulation of frictional contact problems using Nagata patches in surface smoothing 350.

Neto, D.M., Diogo, C.M.A., Neves, T.F., Oliveira, M.C., Alves, J.L., Menezes, L.F., 2016. Remapping algorithms: application to trimming operations in sheet metal forming. J. Phys. Conf. Ser. 734, 32046. doi:10.1088/1742-6596/734/3/032046

Neto, D.M., Oliveira, M.C., Menezes, L.F., 2015. Surface Smoothing Procedures in Computational Contact Mechanics. Arch. Comput. Methods Eng. doi:10.1007/s11831-015-9159-7

Neto, D.M., Oliveira, M.C., Menezes, L.F., Alves, J.L., 2014. Applying Nagata patches to smooth discretized surfaces used in 3D frictional contact problems. Comput. Methods Appl. Mech. Eng. 271, 296–320.

Neto, D.M., Oliveira, M.C., Menezes, L.F., Alves, J.L., 2013. Nagata patch interpolation using surface normal vectors evaluated from the IGES file. Finite Elem. Anal. Des. 72, 35–46.

Notta-Cuvier, D., Langrand, B., Lauro, F., Markiewicz, E., 2015. An innovative procedure for characterising a coupled elastoplastic damage model of behaviour using the Virtual Fields Method. Int. J. Solids Struct. 69–70, 415–427. doi:10.1016/j.ijsolstr.2015.05.009

Oliveira, M.C., Alves, J.L., Menezes, L.F., 2008. Algorithms and Strategies for Treatment of Large Deformation Frictional Contact in the Numerical Simulation of Deep Drawing Process. Arch. Comput. Methods Eng. 15, 113–162.

Pereira, A.F.G., Prates, P.A., Sakharova, N.A., Oliveira, M.C., Fernandes, J. V, 2015. On the identification of kinematic hardening with reverse shear test. Eng. Comput. 681–690. doi:10.1007/s00366-014-0369-7

Pilvin, P., 2003. SiDoLo Version 2.4495.

Plunkett, B., Cazacu, O., Barlat, F., 2008. Orthotropic yield criteria for description of the anisotropy in tension and compression of sheet metals. Int. J. Plast. 24, 847–866. doi:10.1016/j.ijplas.2007.07.013

Pottier, T., Vacher, P., Toussaint, F., Louche, H., Coudert, T., 2012. Out-of-plane Testing Procedure for Inverse Identification Purpose: Application in Sheet Metal Plasticity. Exp. Mech. 52, 951–963. doi:10.1007/s11340-011-9555-3

Prager, W., 1956. A new method of analyzing stresses and strains in work-hardening plastic solids. J. Appl. Mech. Trans. ASME 78, 493–496.

Prager, W., 1949. Recent developments in the mathematical theory of plasticity. J. Appl. Phys. 20, 235–241. doi:10.1063/1.1698348

Prager, W., 1945. Strain hardening under combined stresses. J. Appl. Phys. 16, 837–840. doi:10.1063/1.1707548

Prates, P., 2014. Inverse Methodologies.

Prates, P.A., Oliveira, M.C., Fernandes, J. V., 2015. Identification of material parameters for thin sheets from single biaxial tensile test using a sequential inverse identification strategy. Int. J. Mater. Form. 547–571. doi:10.1007/s12289-015-1241-z

Raabe, D., Wang, Y., Roters, F., 2005. Crystal plasticity simulation study on the influence of texture on earing in steel. Comput. Mater. Sci. 34, 221–234. doi:10.1016/j.commatsci.2004.12.072

Raemy, C., Manopulo, N., Hora, P., 2017. On the modelling of plastic anisotropy, asymmetry and directional hardening of commercially pure titanium: A planar Fourier series based approach. Int. J. Plast. 91, 182–204. doi:10.1016/j.ijplas.2017.02.010

Rauch, E.., 1998. Plastic anisotropy of sheet metals determined by simple shear tests. Mater. Sci. Eng. A 241, 179–183. doi:10.1016/S0921-5093(97)00486-3

Reis, L.C., Oliveira, M.C., Santos, A.D., Fernandes, J. V., 2016. On the determination of the work hardening curve using the bulge test. Int. J. Mech. Sci. 105, 158–181. doi:10.1016/j.ijmecsci.2015.11.009

Reis, L.C., Prates, P.A., Oliveira, M.C., Santos, A.D., Fernandes, J. V., 2017. Anisotropy and plastic flow in the circular bulge test. Int. J. Mech. Sci. 128–129, 70–93. doi:10.1016/j.ijmecsci.2017.04.007

Reis, L.C.D., Prates, P.A., Oliveira, M.C., Santos, A.D., Fernandes, J. V., 2015. Anisotropy and plastic flow in the circular bulge test. Int. J. Mech. Sci.

Rocha, A.B., Duarte, J.F., 1993. Tecnologia da embutidura. Associação Portuguesa das Tecnologias de Conformação Plástica.

Rockafellar, 1972. Convex Functions, in: Convex Analysis.

Roux, E., Bouchard, P.O., 2015. On the interest of using full field measurements in ductile damage model calibration. Int. J. Solids Struct. 72, 50–62. doi:10.1016/j.ijsolstr.2015.07.011

Safaei, M., Zang, S.L., Lee, M.G., De Waele, W., 2013. Evaluation of anisotropic constitutive models: Mixed anisotropic hardening and non-associated flow rule approach. Int. J. Mech. Sci. 73, 53–68. doi:10.1016/j.ijmecsci.2013.04.003

Sigvant, M., Mattiasson, K., Vegter, H., Thilderkvist, P., 2009. A viscous pressure bulge test for the determination of a plastic hardening curve and equibiaxial material data. Int. J. Mater. Form. 2, 235–242. doi:10.1007/s12289-009-0407-y

Soare, S., Yoon, J.W., Cazacu, O., Barlat, F., 2007. Applications of a Recently Proposed Anisotropic Yield Function to Sheet Forming, in: Advanced Methods in Material Forming. Springer Berlin Heidelberg, Berlin, Heidelberg, pp. 131–149. doi:10.1007/3-540-69845-0_8

Souto, N., Andrade-Campos, A., Thuillier, S., 2016. A numerical methodology to design

heterogeneous mechanical tests. Int. J. Mech. Sci. 107, 264–276. doi:10.1016/j.ijmecsci.2016.01.021

Spitzig, W.O., Richmond, O., 1984. The effect of pressure on the flow stress of metals 32, 457–463.

Stoughton, T.B., 2002. A non-associated flow rule for sheet metal forming. Int. J. Plast. 18, 687–714. doi:10.1016/S0749-6419(01)00053-5

Stoughton, T.B., Yoon, J., 2004. A pressure-sensitive yield criterion under a non-associated flow rule for sheet metal forming 20, 705–731. doi:10.1016/S0749-6419(03)00079-2

Stoughton, T.B., Yoon, J.W., 2009. Anisotropic hardening and non-associated flow in proportional loading of sheet metals. Int. J. Plast. 25, 1777–1817. doi:10.1016/j.ijplas.2009.02.003

Swift, H.W., 1952. Plastic instability under plane stress. J. Mech. Phys. Solids 1, 1–18. doi:10.1016/0022-5096(52)90002-1

Taherizadeh, A., Green, D.E., Ghaei, A., Yoon, J., 2010. A non-associated constitutive model with mixed iso-kinematic hardening for finite element simulation of sheet metal forming. Int. J. Plast. 26, 288–309. doi:10.1016/j.ijplas.2009.07.003

Tang, S.C., Chu, E., Samanta, S.K., 1982. Finite element prediction of the deformed shape of an automotive body panel furing preformed stage, in: Numiform'82. Swansea Pineridge Press, Swansea, pp. 629–640.

Teodosiu, C., Hu, Z., 1998. Microstructure in the continuum modeling of plastic anisotropy. proceeding 19th Risø Int. Symp. Mater. Sci. Roskilde, Denmark, Vol. Model. Struct. from Microscale to Prod. Eds. J.V. Carstensen, T. Leffers, T. Lørentzen, O.B. Pedersen, B.F. Sorensen G. Winther, Risø Na 285–290.

Teodosiu, C., Hu, Z., 1995. Evolution of the intergranular microstructure at moderate and large strains: Modelling and computational significance, in: Simulation of Materials Processing: Theory, Methods and Applications. pp. 173–182.

Thuillier, S., Manach, P.Y., 2009. Comparison of the work-hardening of metallic sheets using tensile and shear strain paths. Int. J. Plast. 25, 733–751. doi:10.1016/j.ijplas.2008.07.002

Toh, C.H., Kobayashi, S., 1983. Finite Element Process Modeling of Sheet Metal Forming of General Shapes, in: Grundlagen Der Umformtechnik --- Stand Und Entwicklungstrends / Fundamentals of Metal Forming Technique --- State and Trends: Vortr{ä}ge Des Internationalen Symposiums Stuttgart, 13./14. Oktober 1983 Teil I / Proceedings of the International Symposium Stu. Springer Berlin Heidelberg, Berlin, Heidelberg, pp. 39–56. doi:10.1007/978-3-642-82186-8_2

Tresca, H.-É., 1864. Mémoire sur l'écoulement des corps solides soumis à de fortes pressions. Comptes Rendus l'Académie des Sci. Paris 59, 754–758.

Tritschler, M., Butz, A., Helm, D., Falkinger, G., Kiese, J., 2014. Experimental analysis and modeling of the anisotropic response of titanium alloy Ti-X for quasi-static loading at room temperature. Int. J. Mater. Form. 7, 259–273. doi:10.1007/s12289-013-1125-z

Vial, C., Hosford, W.F., Caddell, R.M., 1983. Yield loci of anisotropic sheet metals. Int. J. Mech. Sci. 25, 899–915. doi:10.1016/0020-7403(83)90020-6

Voce, E., 1948. No TitleThe relationship between stress and strain for homogeneous deformation. J. Inst. Met. 74, 537–562.

von Mises, R., 1913. Mechanik der festen korper im plastic-deformablen zustand. Nachrichten vos der K. gellesschaft des winssenschaften zu Gottingen 582–592.

Wagoner, R.H., 1981. Comparison of plane-strain and tensile work hardening in two sheet steel alloys. Metall. Trans. A 12, 877–882. doi:10.1007/BF02648352

Wagoner, R.H., Li, M., 2007. Simulation of springback: Through-thickness integration. Int. J. Plast. 23, 345–360. doi:10.1016/j.ijplas.2006.04.005

Wagoner, R.H., Wang, N.M., 1979. An experimental and analytical investigation of in-plane deformation of 2036-T4 aluminum sheet. Int. J. Mech. Sci. 21, 255–264. doi:10.1016/0020-7403(79)90001-8

Wang, N.-M., Budiansky, B., 1978. Analysis of sheet metal stamping by a finite-element method. J. Appl. Mech. 45, 73. doi:10.1115/1.3424276

Wifi, A.S., 1976. An incremental complete solution of the stretch-forming and deep-drawing of a circular blank using a hemispherical punch. Int. J. Mech. Sci. 18, 23–31. doi:10.1016/0020-7403(76)90071-0

Woo, D.M., 1968. On the Complete Solution of the Deep Drwaing Problem. Int.J.Mech. Sci. 10, 83–94.

Woodthorpe, J., Pearce, R., 1970. The anomalous behaviour of aluminium sheet under balanced biaxial tension. Int. J. Mech. Sci. 12, 341–347. doi:10.1016/0020-7403(70)90087-1

Yin, Q., Zillmann, B., Suttner, S., Gerstein, G., Biasutti, M., Tekkaya, A.E., Wagner, M.F.X., Merklein, M., Schaper, M., Halle, T., Brosius, A., 2014. An experimental and numerical investigation of different shear test configurations for sheet metal characterization. Int. J. Solids Struct. 51, 1066–1074. doi:10.1016/j.ijsolstr.2013.12.006

Yoon, J.H., Cazacu, O., 2011. Anisotropic yield function capable of predicting eight ears. AIP Conf. Proc. 1383, 86–91. doi:10.1063/1.3623596

Yoon, J.W., Barlat, F., Gracio, J.J., Rauch, E., 2005. Anisotropic strain hardening behavior in simple shear for cube textured aluminum alloy sheets. Int. J. Plast. 21, 2426–2447. doi:10.1016/j.ijplas.2005.03.014

Yoon, J.W., Dick, R.E., Barlat, F., 2011. A new analytical theory for earing generated from anisotropic plasticity. Int. J. Plast. 27, 1165–1184. doi:10.1016/j.ijplas.2011.01.002

Yoon, J.W., Rolfe, B., Beynon, J.H., Hodgson, P., 2013. NUMISHEET 2014 : The 9th International Conference and Workshop on Numerical Simulation of 3D Sheet Metal Forming Processes : Part A Benchmark Problems and Results and Part B General Papers 1567.

Yoshida, F., Hamasaki, H., Uemori, T., 2013. A user-friendly 3D yield function to

describe anisotropy of steel sheets. Int. J. Plast. 45, 119–139. doi:10.1016/j.ijplas.2013.01.010

Yoshida, F., Uemori, T., 2003. A model of large-strain cyclic plasticity and its application to springback simulation. Int. J. Mech. Sci. 45, 1687–1702. doi:10.1016/j.ijmecsci.2003.10.013

Yoshida, F., Uemori, T., 2002. A model of large-strain cyclic plasticity describing the Bauschinger effect and workhardening stagnation 18, 661–686.

Yoshida, F., Uemori, T., Fujiwara, K., 2002. Elastic – plastic behavior of steel sheets under in-plane cyclic tension – compression at large strain 18, 633–659.

Yoshida, K., 2013. Evaluation of stress and strain measurement accuracy in hydraulic bulge test with the aid of finite-element analysis. ISIJ Int. 53, 86–95. doi:10.2355/isijinternational.53.86

Young, R.F., Bird, J.E., Duncan, J.L., 1981. An automated hydraulic bulge tester. J. Appl. Metalwork. 2, 11–18. doi:10.1007/BF02833994

Zhang, K., Holmedal, B., Hopperstad, O.S., Dumoulin, S., Gawad, J., Van Bael, A., Van Houtte, P., 2015. Multi-level modelling of mechanical anisotropy of commercial pure aluminium plate: Crystal plasticity models, advanced yield functions and parameter identification. Int. J. Plast. 66, 3–30. doi:10.1016/j.ijplas.2014.02.003

Zhao, Z., Mao, W., Roters, F., Raabe, D., 2004. A texture optimization study for minimum earing in aluminium by use of a texture component crystal plasticity finite element method. Acta Mater. 52, 1003–1012. doi:10.1016/j.actamat.2003.03.001

Zhou, P., Beeh, E., Friedrich, H.E., 2016. A Novel Testing Method for Uniaxial Compression of Thin-Sheet Magnesium Alloys. Exp. Mech. 56, 513–519. doi:10.1007/s11340-015-0095-0

Zidane, I., Guines, D., Léotoing, L., Ragneau, E., 2010. Development of an in-plane biaxial test for forming limit curve (FLC) characterization of metallic sheets. Meas. Sci. Technol. 21, 55701. doi:10.1088/0957-0233/21/5/055701

Zyczkowski, M., 1981. Combined Loadings in the Theory of Plasticity. PWN - Polish Scientific Publishers.